Search for pairs of scalar leptoquarks decaying into quarks and electrons or muons in $\sqrt{s} = 13$ TeV pp collisions with the ATLAS detector

UNIVERSITY OF LIVERPOOL

Thesis submitted in accordance with the requirements of the University

of Liverpool for the degree of Doctor of Philosophy by

Adam Elliott Jaspan

July, 2021

Abstract

A search for the pair production of scalar leptoquarks decaying into quarks and leptons is performed, considering final states containing two leptons, and two or more jets. Jet flavour tagging techniques are used to determine the flavour of quark from which the jet has fragmented, including b jet identification using the MV2c10 algorithm, and, for the first time in leptoquark searches, c jet identification using the DL1 algorithm.[1] This search uses 139 fb^{-1} of $\sqrt{s} = 13$ TeV pp collisions, recorded with the ATLAS detector in the years 2016 - 2018. This search is the first test of a new class of leptoquark models, which explicitly includes decay modes to leptons and quarks of differing generations. The number of observed events is found to be in good agreement with known Standard Model processes. Such leptoquark models are found to be incompatible with the observed data to within a 95% confidence level for leptoquark masses of up to 1.7 (1.8) TeV in the muon (electron) channels respectively, assuming a branching fraction (β) of 1 to charged leptons. These results are also expressed as limits on the branching fraction into charged leptons, with strong exclusions for values of $\beta > 0.1$. Full documentation of this search is presented in Part III, based on the analysis documented in Ref. [1].

[1] These are two supervised machine learning algorithms developed by dedicated flavour tagging working groups within the ATLAS collaboration that are capable of distinguishing the flavour origins of a jet to high accuracy.

Declaration

I hereby confirm this work is my own, except where other works are referenced. This work has not previously been submitted to any institute, including this one. This thesis does not exceed the relevant word count.

Adam Elliott Jaspan

Acknowledgements

I'd like to thank the immeasurable patience and invaluable guidance of my supervisors, Andrew Mehta and Monica D'Onofrio, and to thank my loving and supportive family for helping to see me through.

Contents

List of Figures

List of Tables

Introduction

The Standard Model (SM) of particle physics is the principal theoretical framework used in the description of particle interactions via three of the four known fundamental forces, namely the electromagnetic force, the weak nuclear force, and the strong force. This model has been shown to accurately describe the physical properties of its constituent particles and their interactions to a remarkable degree of precision. Moreover, the SM was able to predict the existence of previously unknown particles that have subsequently been observed. Collider experiments allowed the discovery of the W boson [2], the Z boson [3], the gluon [4], the top and charmed quarks [5–8], and most recently, the Higgs boson [9, 10]. With each successive confirmed prediction, confidence in the SM increased. Despite the many successes of the SM, however, various observations have been made which the SM is unable to explain. To develop a model that can incorporate our experimental observations requires us to introduce New Physics (NP), taking us beyond the SM (BSM). Examples of such phenomena are the hierarchy problem, the cosmological inferences of dark matter, and the perhaps existentially problematic matter-antimatter asymmetry.

In addition to these, the SM has not (as of yet) been able to provide a particle description of gravity. For this, our most precise theory is that of General Relativity. The SM is not a complete theory, in that it does not give a full description of the universe, but instead, it provides the most precise description of particle interactions that we have to date.

The Large Hadron Collider (LHC), constructed in Geneva, is a circular particle accelerator, a full description of which is provided in Section II. The LHC was built with the intention of better understanding the fundamental constituents of our universe. This includes making high-precision measurements of the known particles of the standard model, and detecting the last particle predicted by the Standard Model that had yet to be discovered (the Higgs Boson), as well as attempting to observe the signatures of physics processes outside the predictions of the Standard Model. In addition to this, the LHC collides heavy ions together, enabling us to study the nature of the quark-gluon plasma. As such, several experiments were constructed around interaction points (IPs) placed along the LHC. The design of each is unique to the physics signatures that it predominantly studies. Two of these experiments, however, are intended to be "general purpose detectors", a kind of catch-all detector, which retains sensitivity to the largest possible regions of phase space. These are the ATLAS and CMS detectors. It is these two experiments which, in 2012, achieved

one of the primary design ambitions of the LHC; the discovery of the Higgs Boson.

This thesis pertains to expanding our knowledge of what exists "Beyond the Standard Model". The simplest and most elegant way of doing so, is to consider what areas of the SM could be naturally extended, and what new particles and properties these extensions might entail. As I shall argue in Part I, leptoquarks are one of the primary and most natural candidates by which to extend the SM. They enable interactions between the leptons and quarks of the fermionic sector, and are primary candidates in the explanation for the matter-antimatter asymmetry that we observe in the universe, as well as resolving many long-standing anomalous observations.

This thesis is organised as follows :

Part I presents an overview of the standard model, and discusses the need to introduce extensions to this theory. It then continues to discuss the motivations and phenomenology of leptoquark physics.

Part II presents a brief discussion of the Large Hadron Collider, and the ATLAS experiment, as well as a description of the full Run II ATLAS dataset. Also presented are the methods used in the modelling of pp collision events using advanced Monte Carlo techniques, and some of the challenges involved in doing so.

Part III presents the analysis of ATLAS data, performed to search for the pair-production of scalar leptoquarks in 139 fb^{-1} of $\sqrt{s} = 13$ TeV proton-proton collisions.

In this work, I was the lead analyst, having developed and implemented the tools and the selection used to identify leptoquark candidates in all channels. Doing so involved validating and requesting the simulation of all signal samples, performing the full analysis of systematic uncertainties, and implementing the statistical analysis. All of this was done within well maintained analysis frameworks used across multiple ATLAS searches.

In addition, I performed the studies on $t\bar{t}$ modeling documented in Section 4.5, performed in service to the ATLAS collaboration. Throughout this work I was guided and assisted by my supervisors Andrew Mehta and Monica D'Onofrio.

Part I

Theory and Motivation

Chapter 1

The Standard Model

This Chapter outlines the formulation of the Standard Model of particle physics. For a more comprehensive review of some of the concepts introduced, please refer to Refs. [11–16]. The SM is a relativistic Quantum Field Theory (QFT) described by the non-abelian gauge[1] symmetry group $\mathrm{SU}(3)_c \otimes \mathrm{SU}(2)_L \otimes \mathrm{U}(1)_Y$, composed of the gauge invariant groups of unitary and special unitary[2] transformations. In Section 1.1, a discussion of the meaning of these gauge groups will be presented, as well as the physics that we can learn from these symmetries. In Section 1.2, a full description of the fundamental particles of the SM is presented, and finally, Sections 1.3 - 1.4 present a description of the fundamental forces that govern the dynamics of this theory.

1.1 Physics of the SM

The SM gauge group, $\mathrm{SU}(3)_c \otimes \mathrm{SU}(2)_L \otimes \mathrm{U}(1)_Y$ is constructed from the group product ($\otimes$) of each set of gauge transformations under which the SM is invariant. Here, each subscript refers to a symmetry of the respective gauge group, and as such, tells us about the conserved quantity that is governed by that group. To study these symmetries, we first formulate a Lagrangian description of our theory, denoted $\mathcal{L}$.[3] We can then demonstrate the conservation of these group transformations by studying the invariance of the Lagrangian under their action by the following theorem, as proposed by Noether in her 1918 work [18, 19]; "*If*

[1] A gauge is a local choice of a coordinate basis. As such, a gauge group is a group of localised smooth transformations (that can be applied to the basis vectors of a system) under which the system remains invariant. This group of transformations between different local choices of gauge form a Lie group, following Lie algebra [17]. For each generator of this group, there arises a corresponding gauge field. These fields must be included in the Lagrangian to ensure its gauge invariance. The quanta of such fields are the gauge bosons.

[2] The unitary group, "$U(n)$" consists of all $n \times n$ unitary matrices, with $(n^2 - 1)$ generators. Matrix "U" is unitary if its conjugate transpose U^* is also its inverse; $UU^* = U^*U = I$ (where I is the identity matrix). The special unitary group is a sub-group of this, for which the determinant of each matrix equals 1.

[3] Lagrangian mechanics is a useful mathematical framework, used in describing complex multivariate systems through a reduced set of generalised parameters. This is achieved by exploiting the underlying symmetries of the system.

the action, S is invariant under a finite dimensional continuous group of transformations depending smoothly on the independent parameters, ω_α, then the current,

$$j^\mu_\alpha = -\sum_i \frac{\partial \mathcal{L}}{\partial(\partial_\mu \psi_i)} \frac{\partial \delta\psi_i}{\partial(\Delta\omega_\alpha)} \tag{1.1.1}$$

is conserved"

$$\partial_\mu j^\mu_\alpha = 0 \tag{1.1.2}$$

As such, the symmetries of each gauge group that comprise the SM can tell us about the quantities that are conserved under that group. For example, the $\mathrm{SU}(3)_c$ group remains invariant under transformations of *colour* charge. This means that the colour quantum number must be a conserved value. Similarly, the $\mathrm{SU}(2)_L$ and $\mathrm{U}(1)_Y$ gauge groups preserve symmetry under transformations of the weak *isospin* (Y_W) and weak *hypercharge* (T) respectively. As such, contractions under these two groups preserve the quantity Q, the electric charge. This arises as a linear combination of Y_W and the z component of weak isospin (T_3); $Q = T_3 + Y_W$. $\mathrm{U}(1)_{EM}$ (the gauge group of electromagnetism) is the group generated by this combination.

This simple formulation of the gauge groups of the SM already presents us with the symmetries which govern three for the four fundamental forces of nature. These are colour, which governs the strong interaction, and the weak isospin and hypercharge that govern the electroweak interaction.

The SM is a mathematically self-consistent, and renormalizable QFT. The fields that it describes are defined by their representation under the local symmetries of the gauge group, $\mathrm{SU}(3)_c \otimes \mathrm{SU}(2)_L \otimes \mathrm{U}(1)_Y$ as well as their invariance under the global symmetries of the Poincaré group of spatial and relativistic transformations. Through introducing small perturbations to a quantum field, we can derive qualitative predictions of the interactions of said field. The field Lagrangian can be deconstructed into components that describe a *free field* ($\mathcal{L}_0$) and an *interaction* ($\mathcal{L}_I$); $\mathcal{L} = \mathcal{L}_0 + \mathcal{L}_I$. A free field describes a particle in isolation, in a non-evolving quantum state, such as the field description of a free particle in a true vacuum. The interactions of this field with other quantum fields are then described in the *interaction* Lagrangian, which can be treated by perturbation theory.

In addition to the gauge and Poincaré symmetry requirements, it is also imposed that the SM is renormalizable. This restriction is not a fundamental requirement of the theory, as the symmetry groups are, but instead renormalisation is used to tell us about the limitations of the SM, and to ascribe boundaries to it. Renormalizability is the requirement that effects coming from processes occurring at energies above a cut off scale of the theory can be safely ignored. As such, it assumes that the theory is successful at describing all processes within this energy scale. This therefore is a useful measure of what might be missing from a theory; if we are successful at accurately describing processes at all accessible energy regimes, then

we learn that the scale of any new physics must be large. Conversely, if a non-renormalizable theory is required, then we learn that this theory misses some fundamental components. The application of this requirement means that when imagining complex processes, with divergent, higher order effects, we must attempt to renormalize them to converge on real and finite predictions.

A compact formulation of the SM Lagrangian can be written as follows;

$$\mathcal{L} = \underbrace{-\frac{1}{4}F_{\mu v}F^{\mu v}}_{\substack{\text{gauge boson}\\ \text{interactions}}} + \overbrace{i\bar{\Psi}\not{\mathcal{D}}\Psi}^{\substack{\text{fermion}\\ \text{interactions}}} + \underbrace{\Psi_i y_{ij}\Psi_j\Phi}_{\substack{\text{fermion mass}\\ \text{terms}}} + \overbrace{h.c.}^{\substack{\text{hermitian}\\ \text{conjugate}}} + \underbrace{|\mathcal{D}_\mu\Phi|^2}_{\substack{\text{gauge boson}\\ \text{mass terms}}} - \overbrace{V(\Phi)}^{\substack{\text{Higgs field}\\ \text{potential}}} . \tag{1.1.3}$$

Here, the notation *h.c.* denotes the hermitian conjugate of the preceding term, which accounts for the anti-fermions. A discussion shall later be provided on how each of these terms is derived from the aforementioned symmetry requirements.

1.2 Particles of the SM

The SM consists of 25 fundamental[4] elementary particles. Of these, 12 have half-integer spin, known as fermions. These particles follow Fermi-Dirac [20, 21] statistics, a consequence of which is the Pauli exclusion principle.[5] A full discussion of these particles is provided in Section 1.2.1. The remaining 13 particles have integer spin, meaning that they obey Bose-Einstein statistics [22], which allows for indistinguishable particles to coalesce into a Bose-Einstein Condensate (BEC).[6] Again, a discussion of these particles is presented in Section 1.2.2. Fermions and bosons are the two distinct classes into which all elementary particles fit.

1.2.1 Fermions

A summary of the fermions of the SM is presented in Table 1.1. These 12 fermions are the building blocks of all conventional macroscopic structures observed in the Universe. They can be divided into two groups; the quarks, and the leptons. Quarks form composite states such as protons and neutrons, which in turn are the basis of atomic structure, while leptons enable the formation of inter-atomic bonds, giving us complex molecular structures. These groups both seemingly come in three "generations" that are ordered in mass (although it is not yet known if the neutrinos follow this ordering). It is only through the charged current

[4] A fundamental particle is an indivisible elementary particle with no substructure.

[5] This is the mechanism that prevents electrons in atomic orbitals from all collapsing to the lowest state.

[6] A BEC is a unique state accessible only to Bosons, where all particles in the condensate may occupy the same state. In this state you can add or remove one of its constituents, without changing the condensate as a whole. This forms a useful definition of a bosonic field.

weak interactions that these fermions can decay into the lighter generations, while the first generation is stable and does not decay. Each generation consists of a pair of quarks, which can be described as "*up*" type (up-, charm- or top-quark), with $T_3 = +\frac{1}{2}$ and "*down*" type (down-, strange- or bottom-quark) with $T_3 = -\frac{1}{2}$ and a pair of leptons of similar structure. These two types differ in their charge, Q and weak isospin, T_3, by ± 1 unit. T_3 must be conserved under the weak interaction. Therefore the only allowed decay mode between the fermions is via the charged current weak interaction, where the W boson mediates a change of $T_3 \pm 1$. No process will allow a direct decay into a quark of the same T_3. Conversely, the right-handed fermions have $T = T_3 = 0$, forming singlets under the weak isospin, which do not partake in the weak interaction.

Generation	Particle	Q [e]	T_3	Mass [GeV]
		Quarks		
I	up (u)	$+\frac{2}{3}$	$+\frac{1}{2}$	$2.16^{+0.49}_{-0.26} \times 10^{-3}$
	down (d)	$-\frac{1}{3}$	$-\frac{1}{2}$	$4.67^{+0.48}_{-0.17} \times 10^{-3}$
II	charm (c)	$+\frac{2}{3}$	$+\frac{1}{2}$	1.27 ± 0.02
	strange (s)	$-\frac{1}{3}$	$-\frac{1}{2}$	$9.3^{+1.1}_{-0.5} \times 10^{-2}$
III	top (t)	$+\frac{2}{3}$	$+\frac{1}{2}$	172.76 ± 0.03
	bottom (b)	$-\frac{1}{3}$	$-\frac{1}{2}$	$4.18^{+0.04}_{-0.02}$
		Leptons		
I	electron (e)	-1	$-\frac{1}{2}$	$5.11 \times 10^{-4} \pm 0.31 \times 10^{-12}$
	electron neutrino (v_e)	0	$+\frac{1}{2}$	$< 1.1 \times 10^{-6}$
II	muon (μ)	-1	$-\frac{1}{2}$	$1.05 \times 10^{-1} \pm 0.24 \times 10^{-10}$
	muon neutrino (v_μ)	0	$+\frac{1}{2}$	$< 1.7 \times 10^{-4}$
III	tauon (τ)	-1	$-\frac{1}{2}$	$1.78 \pm 0.12 \times 10^{-3}$
	tau neutrino (v_τ)	0	$+\frac{1}{2}$	$< 1.8 \times 10^{-2}$

Table 1.1: A summary of the Fermionic constituents of the SM. All values are taken from PDG [23]. Values of the neutrino masses are quoted as upper limits at the 90% CL.

The SM is a chiral[7] theory, due to the $SU(2)_L$ gauge group. This means that left- and right-handed fermion fields transform differently under this gauge group. Transformations of handedness are called parity transforms. It was first observed in Chien-Shiung Wu's experiment [24] that parity symmetry is violated in the weak interaction, by observing an excess of left handed electrons produced in the decay of ^{60}Co atoms, for which Tsung-Dao Lee and Chen-Ning Yang received the Nobel prize in 1957.[8] From this experiment, it was deduced that the weak force only mediates interactions with left chiral fermions (and right chiral anti-fermions), demonstrating that we observe no right handed SU(2) gauge

[7]The chirality of a particle is a quality that emerges from its mass and spin. Chirality is determined by whether a particle transforms in a right- or left-handed representation of the Poincaré group. For a massless particle, there is no Lorentz transformation that can change the helicity of a particle, meaning that chirality is equivalent to helicity in this case.

[8]One of many failings of the Nobel committee to recognise the contributions of women in Physics. A field in which only three women have been awarded the Nobel prize throughout its 120 year history, these being: Marie Curie (1903), Maria Goeppert-Mayer (1963) and Donna Strickland (2018)

symmetry group ($SU(2)_R$), and that all right handed fermions transform as singlets of the $SU(2)_L$ group.

The fermions of the SM may all be described as Dirac spinors.[9] These are the plain wave solutions to the Dirac equation;

$$\begin{aligned}(i\gamma^\mu\partial_\mu - m)\Psi = 0 \\ \Psi(x^\mu) = u(p^\mu)e^{-ipx}\end{aligned} \tag{1.2.1}$$

where u are the eigenspinors;

$$u^1 = \begin{pmatrix}1\\0\\0\\0\end{pmatrix}, \quad u^2 = \begin{pmatrix}0\\1\\0\\0\end{pmatrix}, \quad u^3 = \begin{pmatrix}0\\0\\1\\0\end{pmatrix}, \quad u^4 = \begin{pmatrix}0\\0\\0\\1\end{pmatrix}, \tag{1.2.2}$$

which describe spin $\frac{1}{2}$ particles using 4-component column vectors. The 4 components describe the spin state in both the positive (u^1, u^2) or negative (u^3, u^4) energy states. These can be interpreted as the matter and anti-matter particles respectively.

The left- and right-handed fermions can be related using the left- and right-handed chirality projection operations;

$$\begin{aligned}L = \frac{1}{2}(1-\gamma^5), \qquad R = \frac{1}{2}(1+\gamma^5), \\ \Psi_L = L\Psi, \qquad \Psi_R = R\Psi, \\ \Psi = \Psi_L + \Psi_R,\end{aligned} \tag{1.2.3}$$

where the matrix, γ^5 has the properties;

$$\begin{aligned}\gamma_5 = i\gamma^0\gamma^1\gamma^2\gamma^3, \qquad \{\gamma^5, \gamma^\mu\} = 0, \\ \gamma_5^\dagger = \gamma_5, \qquad (\gamma_5)^2 = 1.\end{aligned} \tag{1.2.4}$$

A gauge invariant field description of the fermionic fields can be written as;

$$\mathcal{L} = \frac{1}{2}(\partial^\mu\Psi\partial_\mu\Psi) - \frac{1}{2}m^2\Psi^2. \tag{1.2.5}$$

[9] The possible exception to this are neutrinos, for which it is hypothesised that they may be Majorana spinors. These are particles that are their own anti-particle. This is unconfirmed, but an observation of neutrino-less double-beta decay [25] would support this hypothesis.

Quarks

The up- and down-type constituents of the three quark generations amounts to 6 "*flavours*" of quarks, each of which has its own flavour quantum number. The conservation of this quantum number can only be violated in the charged current weak interaction. This process enables the decay of heavy quarks into the lighter generations. The quark sector of the SM can have either left or right handed chirality. The representation of these multiplets within the $\mathrm{SU}(3)_c \otimes \mathrm{SU}(2)_L \otimes \mathrm{U}(1)_Y$ gauge group can be written as follows;

$$\begin{aligned} \mathcal{Q}_L = \begin{pmatrix} u_L \\ d_L \end{pmatrix} &= \left(3, 2, \frac{1}{6}\right), \\ u_R &= \left(\bar{3}, 1, \frac{2}{3}\right), \\ d_R &= \left(\bar{3}, 1, -\frac{1}{3}\right). \end{aligned} \tag{1.2.6}$$

Therefore, it follows from equation 1.2.1, that the left- and right-handed quarks transform as doublets and singlets of the $\mathrm{SU}(2)_L$ group respectively, but that all quarks transform as triplets of the $\mathrm{SU}(3)_c$ gauge group. This means that all quarks are charged under the $\mathrm{SU}(3)_c$ gauge symmetry. The term denoted for this charge is the "*colour*" charge. Colour, governed by the rules of Quantum Chromodynamics (QCD) is a quantum charge, the analog of the electric charge of Quantum Electro Dynamics (QED), and is mediated by the gluon.[10] Colour comes in three base states, but due to the asymptotic freedom of the gluon, these states are described as having *colour confinement*,[11] meaning that a colour singlet state cannot exist in isolation. The term colour was defined analogously to the three primary colours, 'red' (r), 'green' (g) and 'blue' (b). In addition to the three base colour states, there respective anti-states, 'antired ($\bar{r}$)', 'antigreen ($\bar{g}$)' and 'antiblue ($\bar{b}$)', and the mixing of the above, there arises a total of 9 unique colour combinations. Singlet states are formed by combining either a colour and its anti-colour (e.g. $r\bar{r}$), or an equal mix of the three colours (e.g. rbg), which is analogous to the colour white. Each quark possesses one of the possible colour charges listed. Due to the confinement of colour, it is impossible for a quark to exist in isolation. As such, quarks form composite states such as mesons (a quark and its anti-quark) and baryons (a combination of three of more quarks). These are collectively known as hadrons. The formation of these states is governed by the

[10] Gluons also possess colour charge, meaning that they can both mediate interactions between quarks, as well as self-interacting.

[11] Asymptotic freedom refers to a property of the strong force, whereby the effects of the strong interaction become asymptotically weaker as the length scale decreases (energy scale increases). Therefore, as two colour charges are separated, the pair production of a new quark-anti-quark pair becomes energetically favorable. This property results in the confinement of colour charged partons to exist only within colour neutral states. These concepts are discussed in more detail in Section 1.5.

conservation of baryon number (B), under which quarks are also charged, possessing $B = \frac{1}{3}$ for quarks, and $B = -\frac{1}{3}$ for anti-quarks. All hadronic states are required to have an integer baryon number.

As well as possessing colour charge, quarks have fractional electric charge, meaning that they are also governed by QED, and the left-handed multiplets are charged under the weak hypercharge and weak isospin, meaning that they can partake in the weak interaction. Because of this, quarks interact with each of the gauge bosons, W, Z, g and γ, which are discussed in more detail in Section 1.2.2.

Leptons

The leptonic constituents of the SM can be subdivided into the neutral and the charged leptons. The charged leptons, namely the electron (e), muon (μ) and tauon (τ) are all massive particles, with a hierarchy in their mass in the order given above. These particles obtain their mass through interaction with the Higgs field, as will be discussed in Section 1.4. Meanwhile, the neutral leptons, neutrinos (v), are described as massless particles within the SM. This is because the right handed neutrino (v_R) is not a requirement of the SM and thus far, only left handed neutrinos have been observed in nature. As such, there are no mass terms for neutrinos within the minimal construction of the SM. It is observed however, that neutrinos do have a small, but non-zero mass due to evidence of flavour oscillations [26–28]. However, the SM's lack of a right handed counter term for the neutrino precludes the Higgs mechanism as the method by which neutrinos acquire mass.[12] In fact, the origins of the neutrino masses remains an open question within physics.

Both the charged and neutral leptons are assigned a lepton number of $+1$, and their corresponding anti-particles have a lepton number of -1. This value is conserved within the SM. Each individual lepton can also be considered to have its own flavour. This flavour is preserved within the electromagnetic interaction, but violated in the weak interaction. However, within each generation of lepton, each doublet of T_3 can be assigned a lepton flavour that remains a conserved quantity within the SM.[13] These flavours take the name of the charged lepton of that doublet. Therefore, the charged and neutral leptons of the first generation have an electron flavour that they conserve in their interactions. This conservation has been observed to be violated however, in neutral current interactions, by neutrino flavour oscillations as mentioned above. These remain some of the most significant measurements of the effects of BSM physics to date. The violation of charged lepton flavour is also heavily suppressed,[14] and so, any observation of such a process would also constitute

[12] This is because interactions with the Higgs field induces a change in chirality, meaning that such interactions for neutrinos are not predicted within the SM.

[13] Note that it is the flavour of the doublet that remains conserved, and not the flavour of the individual leptons.

[14] Such processes are only possible via neutrino mixings, and so are suppressed by the small neutrino masses with a rate of $\ll 10^{-50}$ [29, 30].

new physics. The representation of these multiplets within the $\mathrm{SU}(3)_c \otimes \mathrm{SU}(2)_L \otimes \mathrm{U}(1)_Y$ gauge group can be written as follows;

$$\mathcal{L}_L = \begin{pmatrix} \upsilon_L \\ \ell_L \end{pmatrix} = \left(1, 2, -\frac{1}{2}\right), \qquad (1.2.7)$$
$$\ell_R = (1, 1, -1).$$

In the left handed doublets of weak isospin, the neutrinos are "*up*" -type and have $T_3 = \frac{1}{2}$, while the charged leptons are "*down*" -type, and have $T_3 = -\frac{1}{2}$. As can be seen from Equation 1.2.7, these particles are all singlets of the $\mathrm{SU}(3)_c$ gauge group, meaning that these particles have no interaction with the strong force. Instead, their dynamics within the SM are entirely governed by the electroweak interaction, or $\mathrm{SU}(2)_L \otimes \mathrm{U}(1)_Y$ gauge group. As previously discussed, $\mathrm{SU}(2)_L$ is a chiral gauge group that only mediates interactions between left handed particles (and right handed anti-particles). Therefore, the right-chiral lepton multiplet (ℓ_R) does not partake in this interaction, and transforms as a singlet of this gauge group.

1.2.2 Bosons

The SM also includes 13 bosonic particles, with integer spin values. Twelve of these are vector bosons of spin 1, which mediate the three forces that the SM describes. These are the photon (γ), Z boson, the W^+ and W^- bosons, and the 8 gluons (g). These vector bosons are the gauge bosons, which originate from the quantization of the vector fields associated with each gauge symmetry. The vector bosons, and the forces that they mediate, are the electromagnetic (γ), weak ($Z, W^\pm$) and strong (g) forces. A summary of these is provided in Sections 1.3 and 1.5 respectively. Additionally, the SM requires one scalar boson of spin 0, the Higgs Boson (H). This boson originates from the Higgs mechanism, which is discussed in Section 1.4. The Higgs is not a gauge boson, and does not define a gauge symmetry. Instead, the Higgs Boson provides a mechanism through which the global symmetry of the electroweak group can be spontaneously broken, providing mass to both fermions and gauge mediators. Beyond those mentioned, there exist many composite bosons that are predicted by the SM. These arise from the combination of multiple fermions to arrive at integer spin composite particles such as mesons (which have been mentioned previously). A summary of the fundamental bosons of the SM is presented in Table 1.2;

1.3 Electroweak Interaction

The electroweak interaction is the unification of the weak and electromagnetic forces. This interaction is described by Glashow-Weinberg-Salam (GWS) theory [31–33], which proposes a Lagrangian that is invariant under the $\mathrm{SU}(2)_L \otimes \mathrm{U}(1)_Y$ gauge group of transformations.

Force	Name	Q [e]	Mass [GeV]
	Vector		
EM	photon (γ)	0	0
Strong	gluon (g)	0	0
Weak	Z boson (Z)	0	91.187 ± 0.002
	W bosons ($W^{\pm}$)	± 1	80.379 ± 0.012
	Scalar		
Higgs boson (H)		0	125.10 ± 0.14

Table 1.2: A summary of the Bosons of the SM. All values are taken from PDG [23].

These gauge groups introduce four vector gauge fields, the quanta of which form three vector bosons that gauge the $\mathrm{SU}(2)_L$ group, denoted W^i_μ (for $i = 1, 2, 3$) (that transform as a triplet of the weak isospin, with $T = 1$). The quanta of the fourth field is an additional vector boson which gauges the U(1) group, and transforms as a singlet of $T = 0$. This is denoted B_μ, with gauge couplings g and g', respectively. The dynamics of these fields are described by the kinetic term of the Lagrangian;

$$\mathcal{L} = -\frac{1}{4} B_{\mu v} B^{\mu v} - \frac{1}{4} W^i_{\mu v} W^{\mu v}_i, \tag{1.3.1}$$

where the field strength tensors are:

$$\begin{aligned} B_{\mu v} &= \partial_v B_\mu - \partial_\mu B_v, \\ W^i_{\mu v} &= \partial_v W^i_\mu - \partial_\mu W^i_v + g \epsilon_{ijk} W^j_\mu W^k_v. \end{aligned} \tag{1.3.2}$$

Here, ϵ_{ijk} is the Levi-Citiva symbol.[15]

These bosons are not, however, the mediators of the weak and electromagnetic interactions that we directly observe in nature, namely the $W^{\pm}$, Z and γ bosons. Instead, the charged W bosons are constructed as a linear combination of the W^1 and W^2 fields, as follows;

$$W^{\pm}_\mu = \frac{1}{\sqrt{2}} W^1_\mu \pm i W^2_\mu. \tag{1.3.3}$$

Finally, the neutral bosons, Z_μ and A_μ are formed by mixing W^3 with the B field, via the Weinberg angle (also termed the weak mixing angle), θ_W:

[15] This is defined to take the value of "0" when at least two of the labels i, j or k are the same, and "1" ("-1") if i, j or k forms an even (odd) permutation of "1, 2, 3".

$$\begin{pmatrix} A_\mu \\ Z_\mu \end{pmatrix} = \begin{pmatrix} \cos(\theta_W)\sin(\theta_W) \\ -\sin(\theta_W)\cos(\theta_W) \end{pmatrix} \begin{pmatrix} B_\mu \\ W^3_\mu \end{pmatrix} \tag{1.3.4}$$

where the weak mixing angle can be expressed in terms of the weak isospin (g) and weak hypercharge (g') couplings:

$$\cos(\theta_W) = \frac{g'}{\sqrt{g^2 + g'^2}}, \tag{1.3.5}$$

$$\sin(\theta_W) = \frac{g}{\sqrt{g^2 + g'^2}}. \tag{1.3.6}$$

The GWS model therefore adequately provides a gauge invariant Lagrangian that describes the electroweak interactions. Unfortunately though, this predicts all of the electroweak gauge mediators to be massless, as no mass terms are permissable within this Lagrangian. This is in direct contradiction with the experimental evidence. To reconcile our theory with experiment, we must break the $\mathrm{SU}(2)_L$ symmetry via the Brout-Englert-Higgs mechanism, as documented in Section 1.4.

1.4 The Brout-Englert-Higgs (BEH) mechanism

We have shown, in Section 1.3 how the electromagnetic and weak forces are unified through GWS theory. We find, however, that the symmetry that governs this electroweak interaction, namely $\mathrm{SU}(2)_L \otimes \mathrm{U}(1)_Y$, is spontaneously broken, resulting in the electromagnetic subgroup. Furthermore, we have shown that the electroweak symmetry group produces the mediators of the weak and electromagnetic interactions through a mixing of the quantization of the $\mathrm{SU}(2)_L$ and $\mathrm{U}(1)_Y$ gauge groups. However, we have stated that this formulation of the electroweak interaction is not sufficient to describe the mass of these particles.

Before we proceed to explain this discrepancy, it is useful to first consider what *mass* is. From Albert Einstein's famous equation, $E = mc^2$, we know that mass is the equivalent of energy. From this, we can consider that the intrinsic mass of a particle is related to its intrinsic energy, or the energy of which that particle will have when at rest, and without interaction with the outside world. However, a particle's energy is precisely defined by its interactions. This would mean, therefore, that a particle would have to be interacting with itself. We see, for the fermions, that this is exactly what happens. As they have the same electromagnetic charges, the left-handed and right-handed multiplets are free to oscillate between themselves (more detail is provided on this subject in Section 1.4.1). Such oscillations would, however, violate the conservation of the weak isospin. It is clear that something else is involved in this process, which carries off these conserved values to enable such oscillations. As such, for an isolated particle at rest, we find that there must still be

some field for it to interact with that must acquire a non-zero expectation value when in a vacuum. Furthermore, from this description, we learn that mass can also be thought of as a polarisation in a new direction, introducing an additional degree of freedom; a mode in which a particle can spin, such as the right and left-handed fermions. As such, we can look to introduce masses to the W and Z bosons by introducing additional polarisation's. Following on from this, we can see that a massless particle can only have two polarisations, as it cannot spin in the direction of its motion (not without travelling faster than the speed of light). Since particles with a spin carry at least two degrees of freedom, we know that we will have to introduce a field which interacts with the W and Z that has no intrinsic spin (is a scalar) to allow for just a single additional longitudinal degree of freedom. With this in mind, we can proceed to discuss the Brout-Englert-Higgs (BEH) mechanism [34–38].

Robert Brout, François Englert and Peter Higgs proposed a mechanism through which masses could be explained. It requires the introduction of a new complex scalar field, the Higgs field (ϕ), that forms a doublet under the $\mathrm{SU}(2)_L$ gauge group, which can be written as;

$$\Phi = \begin{pmatrix} \phi^+ \\ \phi^0 \end{pmatrix} = \frac{1}{\sqrt{2}} \begin{pmatrix} \phi_1 + i\phi_2 \\ \phi_3 + i\phi_4 \end{pmatrix} \tag{1.4.1}$$

where we introduce four real scalar fields (ϕ_i), corresponding to four additional degrees of freedom. This doublet has weak charges of $T_3 = \pm\frac{1}{2}$ and $Y = 1$, leading to charges of $Q = 1(0)$ for $T_3 = +(-)\frac{1}{2}$. Next, we must add an additional term to the SM Lagrangian for this field;

$$\mathcal{L}_H = (\mathcal{D}_\mu \Phi)^\dagger (\mathcal{D}^\mu \Phi) - \overbrace{\mu^2 \Phi^\dagger \Phi - \lambda (\Phi^\dagger \Phi)^2}^{V(\Phi)}, \tag{1.4.2}$$

where we have written out the scalar potential ($V(\Phi)$) where μ^2 and λ are real constants. We can now consider how this potential might look. To ensure that this potential has a ground state, it must be bounded from below, by setting $\lambda > 0$. We can then find the trivial local minima of this potential at $\phi^+ = \phi^0 = 0$. However, if we set $\mu^2 < 0$, then we find that there is a degenerate set of global minima on the ϕ^+, ϕ^0 plane. This potential with one local, and infinitely degenerate global minima is shown in the real and complex planes in Figure 1.1.

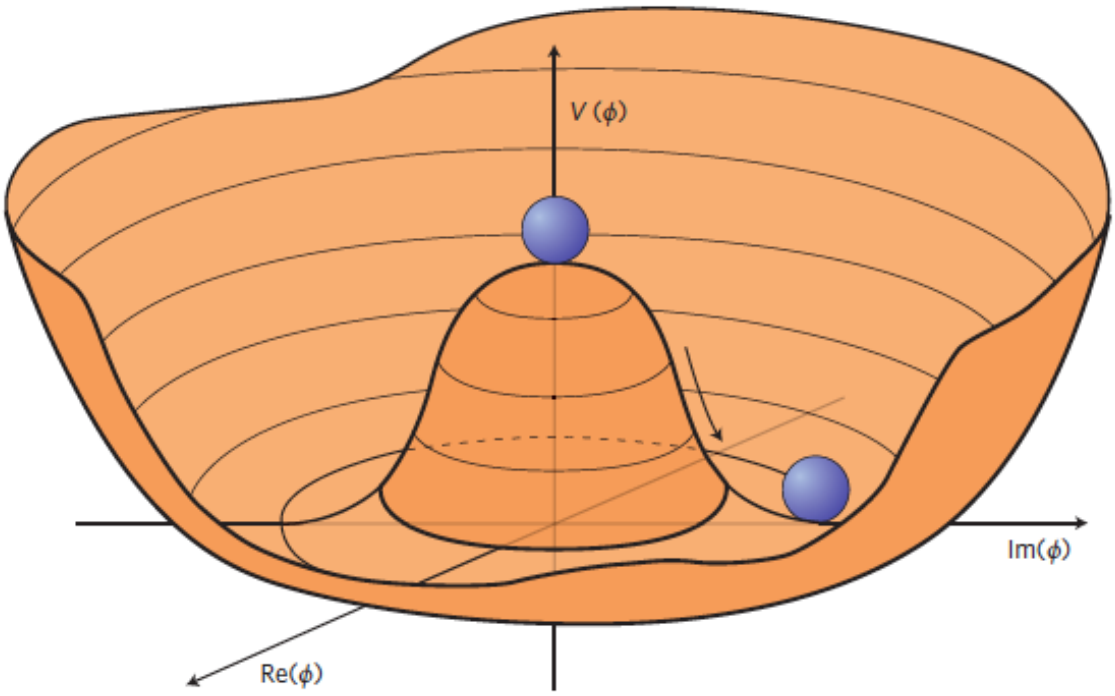

Figure 1.1: [39] Schematic of the Higgs potential ($V(\Phi)$) for either part of the Higgs doublet, as written in Equation 1.4.1.

Looking at Equation 1.4.2, we find that the minima of this potential occurs at $\frac{\mu^2}{\lambda}$. Due to gauge invariance, we can choose to work in any such configuration of the fields ϕ_i that satisfies this constraint. By choosing the vacuum expectation values (v) of each field to be zero, apart from the real component of ϕ^0, we arrive at;

$$\phi_{1,2,4} = 0 \quad \phi_3 = \frac{\mu^2}{\lambda} = v^2 \tag{1.4.3}$$

And as such, we can write the Higgs doublet as;

$$\Phi = \frac{1}{\sqrt{2}} \begin{pmatrix} 0 \\ v \end{pmatrix} \tag{1.4.4}$$

we can then expand Φ by setting $\phi_0 = \phi_3 = H + v$ (with H being the scalar Higgs field). In this way, the Higgs field can be written as:

$$\Phi = \frac{1}{\sqrt{2}} \begin{pmatrix} 0 \\ H + v \end{pmatrix} \tag{1.4.5}$$

The four real fields that comprise the complex Higgs doublet relate to oscillations of this potential. Angular oscillations within the degenerate ground state form massless

Goldstone Bosons,[16] while oscillations around the ground state (with changing $V(\Phi)$) form the massive Higgs field. The Goldstone bosons are then absorbed by the $W^{\pm}$ and Z bosons through gauge transformations. This introduces an additional longitudinal polarisation component of the weak bosons (one for each Goldstone boson that is absorbed) and as such, introduces terms for their mass. These can be derived by calculating the kinetic term of its Lagrangian as it acts on the vacuum state $(\mathcal{D}_\mu\Phi_0)^\dagger(\mathcal{D}^\mu\Phi_0)$, where $\mathcal{D}_\mu$ is the covariant derivative:

$$\mathcal{D}_\mu = \partial_\mu + \frac{ig'Y}{2}B_\mu + \frac{ig}{2}\sigma^i W^i_\mu. \tag{1.4.6}$$

Here, the σ_i are the Pauli matrices. By operating with this derivative on our equation for the Higgs field from Equation 1.4, we find the kinetic term of the Higgs field to be:

$$(\mathcal{D}_\mu\Phi_0)^\dagger(\mathcal{D}^\mu\Phi_0) = -\frac{g^2v^2}{8}(2W^+_\mu W^\mu + \frac{1}{\cos^2\theta_W}Z_\mu Z^\mu). \tag{1.4.7}$$

therefore, by substituting in our descriptions of the weak gauge bosons, from Equations 1.4 & 1.4, we find mass terms of:

$$M_Z = \frac{v}{2}\sqrt{g^2+g'^2} = \frac{m_W}{\cos\theta_W}, \tag{1.4.8}$$

and

$$M_W = \frac{gv}{2} = \frac{e_0 v}{2\cos\theta_W}, \tag{1.4.9}$$

with e_0 being the coupling constant of the photon:

$$e_0 = \frac{gg'}{\sqrt{g^2+g'^2}} = g\sin\theta_W. \tag{1.4.10}$$

It can be seen that the weak bosons acquire mass terms that are linearly proportional to the vacuum expectation value of the Higgs field, with a magnitude that is determined by their gauge couplings. This tells us that as the *v.e.v.* of the Higgs field tends to zero, so too do the masses of the weak gauge mediators. Fortunately, this value, v, is a fixed constant of nature that is connected to the Fermi constant (G_F) by the equation:

$$v = (\sqrt{2}G_F)^{-\frac{1}{2}} \approx 246\text{GeV}. \tag{1.4.11}$$

Finally, by considering the action of the Higgs potential on the doublet of scalar fields, $V(\Phi)$, we find a term for the Higgs mass of:

[16] These are massless as there is no restorative force applied to them in this potential.

$$m_H = 2\sqrt{2\lambda}v. \tag{1.4.12}$$

we therefore find that the only remaining free parameter in the Higgs sector is m_H, or λ, the Higgs self-coupling. A measurement of this free parameter by the ATLAS and CMS experiments in June 2012 found its value to be $m_H = 125.10 \pm 0.14$ GeV [9, 10]. This searched for a mass resonance in the $H \to \gamma\gamma$ channel.[17] This observation marked a milestone in the field of particle physics; no additional particles are required to make the SM self-consistent. We will go on to discuss in the next Chapter however, some tensions between the SM and experimental observation, and the motivation for possible extensions to account for them.

1.4.1 Fermionic masses

Fermions acquire their bare (non-interacting) mass from the Higgs field also.[18] This mass is proportional to the rate of interaction with the Higgs field (the Higgs coupling strength). Couplings are described by Yukawa interactions, and are introduced into the SM Lagrangian in the form;

$$g_f \bar{\psi_L} \phi \psi_R, \tag{1.4.13}$$

where g_f governs the strength of the Yukawa coupling between the fermion and the Higgs field. As such, the mass of these particles comes from their interaction with the Higgs field, and is governed by the strength of their Yukawa couplings. This can be illustrated as in Figure 1.2. In this diagram, Higgs particles are shown to terminate (ending with an "X"). This is to represent these particles being absorbed into the BEC. This process therefore allows for the oscillation between the right and left chiral fermions, resulting in a bare mass term, which is governed by the strength of their Yukawa couplings. Precise measurement of both the mass of the Higgs boson, and the Yukawa coupling terms, have been one of the crowning achievements of experimental tests of the Standard Model in the past decade.

[17] This channel, although only produced with a relatively low branching fraction, provides a very clean signature with a very uniform background, which helps to emphasise the mass resonance.

[18] However this accounts for only a small portion of their observed mass

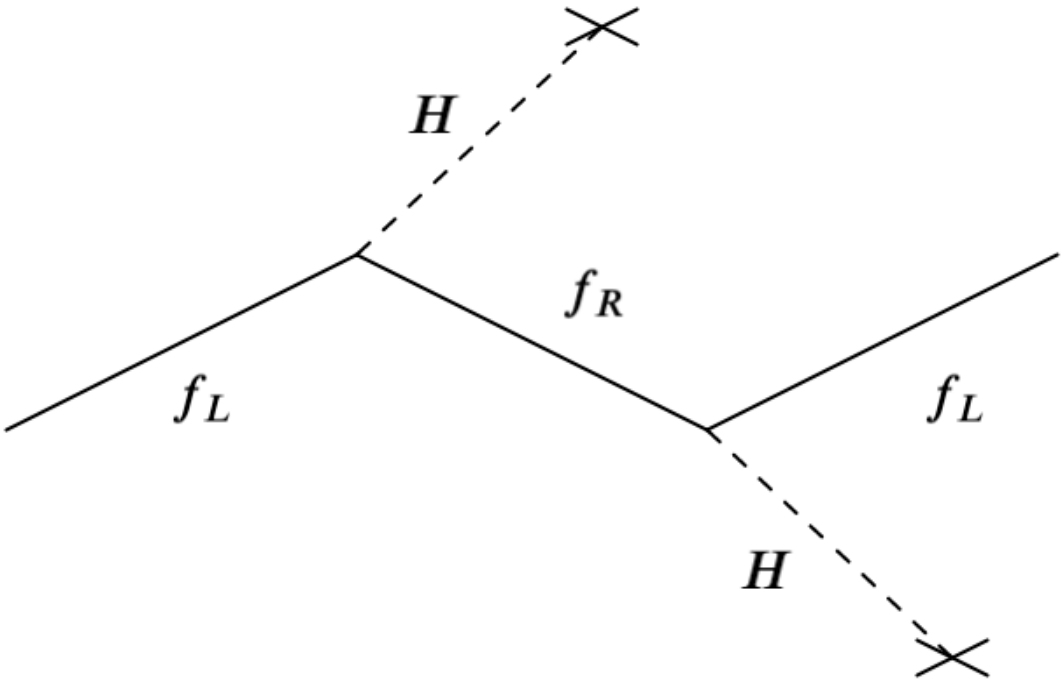

Figure 1.2: Schematic of the mechanism producing fermion masses, where f_L (f_R) are the left (right) handed fermion multiplets, and H is the Higgs boson.

1.5 Strong Interaction

The strong interaction is described by QCD. As previously mentioned, QCD conserves a "*colour*" charge in all interactions of quarks and gluons. There are 8 types of gluons, which possess a mixture of the colours. This requires us to describe the fermion wave functions using a three-component vector of the Dirac spinors:

$$\Psi_f = \begin{pmatrix} \Psi_r \\ \Psi_g \\ \Psi_b \end{pmatrix}. \tag{1.5.1}$$

We shall also introduce new vector potentials, $A_{\mu,v}$ which represent the gluon fields. The generators of this gauge group are the Gell-Mann matrices λ^a (for $a = 1, ..., 8$), which have the relation $[\lambda^a, \lambda^b] = 2if^{abc}\lambda^c$, where f^{abc} are the completely anti-symmetric structure constants of SU(3).

Following a similar procedure to the derivation of the QED Lagrangian outlined in Section 1.3, we can construct a QCD Lagrangian that is based upon a non-abelian SU(3) Yang-Mills theory [40], of the form[19]:

[19]Here we introduce the "$\not{X}$" notation, which indicates that variable X is a co-variant vector: $\not{X} \overset{def}{=} \gamma^\mu X_\mu$.

$$\mathcal{L} = -\frac{1}{4}F^a_{\mu v}F^{\mu v}_a + \sum_f \bar{\Psi}^f_i(i\not{\mathcal{D}}_{ij} - m_f\delta_{ij})\Psi^f_j. \tag{1.5.2}$$

where δ_{ij} is the Kronecker delta function.[20] The QCD Lagrangian is then summed over the quark flavours (f) and the colour charges (a). Additionally, the field strength tensor and co-variant derivative are defined to be:

$$\begin{aligned} F^a_{\mu v} &= \partial_\mu A^a_v - \partial_v A^a_\mu - g_S f_{abc} A^b_\mu A^c_v, \\ \mathcal{D}^\mu_{ij} &= \partial^\mu \delta_{ij} + i g_S \lambda^a_{ij} A^\mu_a. \end{aligned} \tag{1.5.3}$$

It is this latter term in the expression for the field strength tensor which enables the self interaction of gluons. Here, the gauge coupling terms (g_s) determines the strong coupling constant, $\alpha_S = 4\pi g_S^2$, and is related to the momentum transfer of a process, Q^2, as:

$$g_S^2(Q^2) = \frac{4\pi}{\beta_0 \ln\left(\frac{Q^2}{\Lambda^2_{QCD}}\right)}, \tag{1.5.4}$$

with the QCD, or *hadronization scale*, Λ_{QCD}. we find from Equation 1.5, that as the coupling term, g_S tends to 0, the momentum transfer tends to infinity, and similarly, in the low energy regime, where Q^2 tends to the hadronization scale ($Q^2 \to \Lambda_{QCD}$), the strong coupling tends to infinity. This is known as the asymptotic limit, and allows for the asymptotic freedom of quarks, whereby they behave as quasi-free particles in the high energy limit, but are confined at low energies. This relation between the coupling strength and the momentum transfer is shown in Figure 1.3, where the coupling constant, $\alpha_S(Q^2)$ is measured as a function of the energy scale Q, through a combination of precision measurements at HERA. This combination reports a combined value of $\alpha_S(M_Z^2) = 0.1198 \pm 0.0032$ when Q^2 is set to the Z mass scale, however a wider combination reported by the Particle Data Group (PDG) reports the world average of this value to be $\alpha_S(M_Z^2) = 0.1179 \pm 0.0010$ [41].

[20] $\delta_{ij} = 1$ if $i = j$ and $\delta_{ij} = 0$ if $i \neq j$, which equates to the identity matrix.

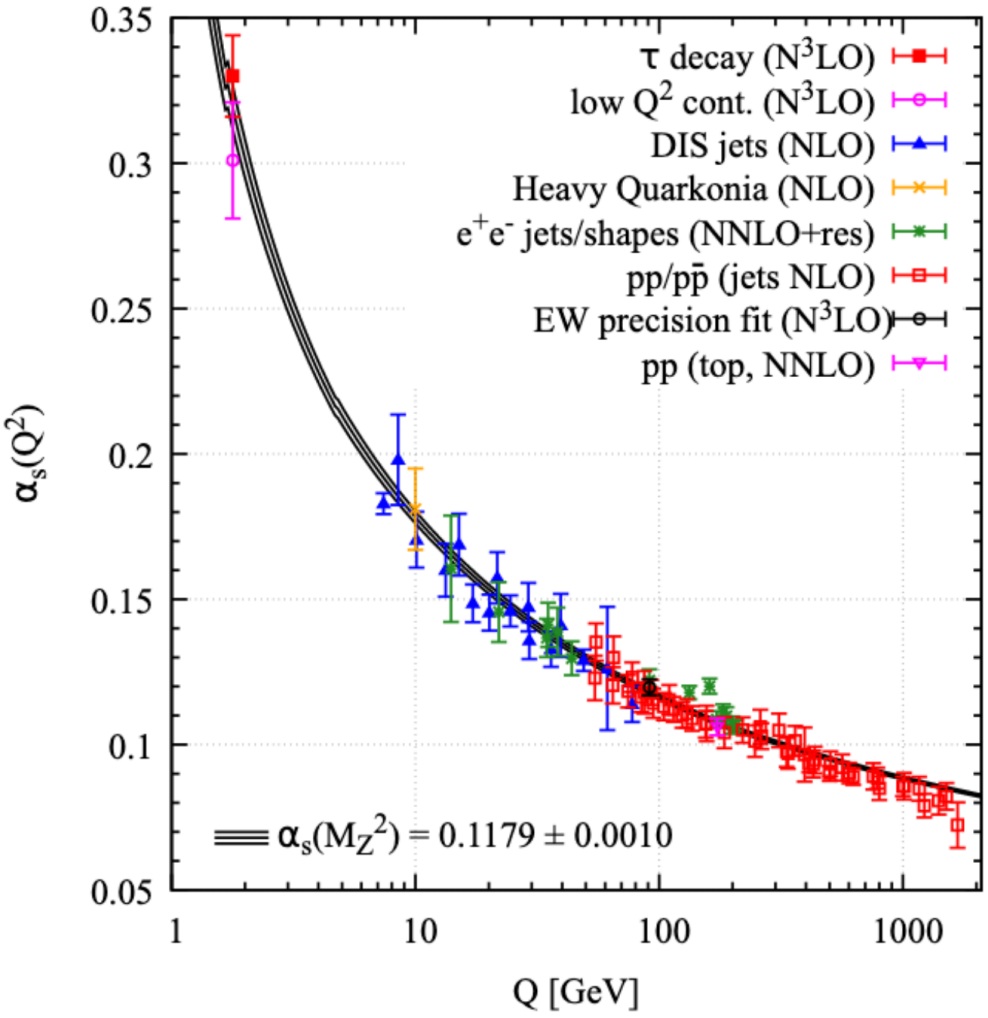

Figure 1.3: [41, 42] A summary of precision measurements of α_S as a function of the energy scale, Q. Measurements are derived from NLO fits to inclusive jet cross sections in neutral current Deep Inelastic Scattering (DIS) at high Q^2.

The confinement of the colour charge is a consequence of the asymptotic freedom of the strong interaction. As colour charged particles are separated, the potential energy in their colour interaction increases until it becomes energetically favorable for a quark–antiquark pair to form instead of extending the colour flux between the initial state particles. This means that colour charged particles are confined to exist within composite, colour neutral states. Because of this, individual quarks and gluons cannot be observed directly using particle detectors, since they hadronize[21] before interacting with our detectors. As a result of this, the strong force only has a direct effect inside hadrons at distances of the order; $\mathcal{O} \sim 10^{-17}$ m. Therefore, the strong nuclear force that is observed to bind hadrons together

[21] The exception to this is the top quark, which is heavy enough to decay via the weak process before it has sufficient time to hadronize.

is a residual effect, mediated by intermediate mesons, which act as the force carriers, the intensity of which diminishes with distance in the form of Yukawa potential [43].

1.6 Proton-proton collisions

Thus far the interactions of point-like free particles has been discussed and the key principles behind calculating the cross sections of different processes have been outlined. This model is highly informative, and provides a robust framework for describing the interactions of particles, however, it is insufficient for producing a meaningful description of the processes that occur during pp collisions and the objects that may be observed within our detectors. This is because protons are not point-like particles, but rather they are composite states. The proton has two "*up*" quarks and a "*down*" quark (uud). It is these three "*valence*" quarks that determine the quantum numbers of the proton, giving it a positive charge, and a half-integer spin. However, these only account for approximately 1% of the rest mass of the proton. The mass of the proton is instead dominated by the Quantum Chromodynamic Binding Energy (QCBE) of the strong interaction that holds the proton together. This constant flux of QCD interactions within the proton induces a "*sea*" of virtual quark anti-quark pairs, forming a complex and dynamic internal structure of the proton.

The cross-sections that we can derive for the interactions of point-like particles must therefore be modified to account for this rich internal structure of the protons from which the interacting partons originate. A method was postulated by Drell and Yan [44] for the weighting of specific sub-process cross sections to account for this internal structure.[22] This method breaks down, however, when accounting for perturbative corrections from real and virtual gluon emission, introducing large logarithmic terms arising from gluons produced collinear to the initial state quarks. These terms can be thought of as the "*far-out*" effects, that contribute potentially infinite low momentum corrections, that would cause our cross-section calculation to become non-renormalizable. It was found however, that these terms could be absorbed into the definition of the parton distribution function (PDF). A *factorization theorem* [45] was developed that shows this to be a general feature of hard scattering processes. The finite orders of perturbative corrections must however, still be applied. These effects can be thought of as the "*near-by*" effects of perturbative processes with larger effects on the momentum transfer of the process. As such, a *factorisation* scale, μ_F is introduced to provide a "*cut-off*" that separates these long- and short-distance processes.

As has been shown, when producing accurate predictions of the cross-sections of processes occurring in pp collisions, there must first be a model that accounts for this internal structure. In order to probe this, we can measure the Deep Inelastic Scattering (DIS) of high energy leptons in nucleons, which is discussed in Section 1.6.1. Subsequently, in

[22] The Drell-Yan process is discussed in detail in Section 2.7

Section 1.6.2, there is a discussion of how these initial states are evolved to reflect the observable final state recorded in our detectors.

1.6.1 Structure of the proton

The DIS of a lepton ℓ off a nucleon N is mediated via the exchange of a virtual gauge boson, γ^*, the wavelength of which is determined by the momenta transferred in the scattering (Q). At high enough momenta, the wavelength becomes small enough to resolve the internal structure of the nucleon. In DIS, the momentum exchanged is sufficient to break apart the nucleon into a hadronic final state, X, absorbing some of the energy of the incident lepton into the creation of final state particles. By measuring the energy loss of the scattered lepton, and the invariant mass of the system X, it is possible to determine the Bjørken variable, x, which is the fraction of momenta of nucleon, N, that is carried by each parton involved in the scattering. From these measurements, it is possible to derive the parton distribution function (PDF), $f_i(x)$ for each parton (i). The values of these PDFs cannot be evaluated from first principles, but can be measured experimentally by performing a fit to a large number of cross section data points, typically at some low value of $Q^2 = Q_0^2$. This fit can then be evolved through increasing Q^2 using the Dokshitzer-Gribov-Lipatov-Altarelli-Parisi (DGLAP) [46–48] equations,[23] to produce predictions at increasing orders of perturbation. This is shown in Figure 1.4, calculated at the *next-to-next-to-leading-order* (NNLO) for two different Q^2 scales. These fits are derived from a range of data sets, collected by the Tevatron, HERA and LHC colliders, combined into a global fit.

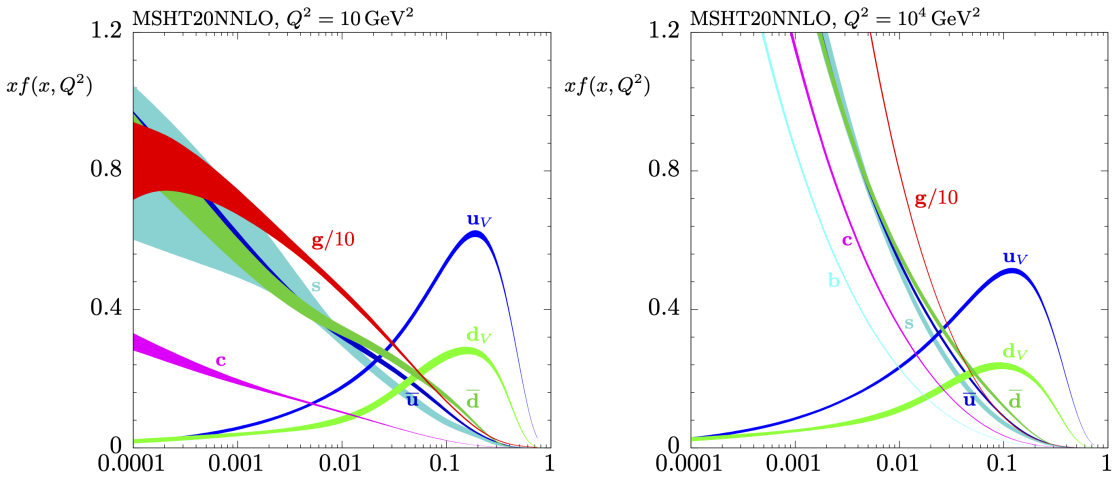

Figure 1.4: [49] PDFs of the proton, evaluated at NNLO for a momenta transfer of 10 GeV^2 (left) and 10^4 GeV^2 (right). Each line shows the contributions of the different quarks and gluons.

[23] These are splitting functions that describe the probability of a parton splitting over different energy scales.

1.6.2 Hadronization

The final states considered in tree-level cross-section calculations do not directly correspond to the final state objects observed by the ATLAS detector. This discrepancy occurs when the outgoing particles possess colour (quarks and gluons), which cannot exist in isolation due to the confinement of the colour charge. As such, these particles are un-stable, and so, to produce a full description of these processes, we must continue along the evolution of these particles through the process of hadronization, until they form more stable hadronic states that can be observed directly. This process of hadronization pertains to the non-perturbative regime of QCD, and describes the formation of colourless hadronic particles such as mesons. A phenomenological framework for describing this process is the Lund string model [50] which describes "*strings*" of self-interacting gluon field lines connecting color charged partons. As the separation of the colour charged partons increases, so does the potential energy of the *string*. Beyond a certain threshold, it will become energetically favorable for these *strings* to fragment into cascades of highly collimated hadrons termed "*jets*". There is additionally a QCD cluster model [51] which is often used.

Chapter 2

Beyond The Standard Model

The Standard Model of particle physics is certainly one of the greatest achievements of modern science. It is one of the most precise and rigorously tested theories, that offers extraordinary predictive capabilities. However, the SM is not a complete theory, and as we shall discuss in Section 2.1, it has many shortcomings. What the SM offers, however, is a robust mathematical and phenomenological framework upon which we can expand, in order to address these shortcomings. By modifying the SM, we are able to construct extensions that allow us to explain physical phenomena beyond its reach, in such a way that does not detract from its many successes.

In Section 2.2, we shall introduce one theoretical framework, which goes BSM and is the primary focus of this Thesis. This framework proposes a new class of particles, "*leptoquarks*" (LQ) which behave as the bound state of a lepton and a quark. LQs provide a natural extension to the SM and have a rich phenomenological background, dating back nearly 50 years to the unification of quarks and leptons in the SM [52]. LQs arise naturally in many extensions to the SM such as models with quark lepton compositeness [53], grand unified SU(5) models [54, 55], the SU(4) based Pati-Salam model [56], and R-parity violating (RPV) supersymmetry (SUSY) models [57]. There is an abundance of recent and in-depth reviews available, which cover the many varied facets of LQ theory [58–61]. This Chapter aims to first provide the reader with a broad overview of the subject, as presented in Section 2.2, and then present the detailed foundations of the theory that are significant to the primary focus of this Thesis "Search for pairs of scalar leptoquarks decaying into quarks and electrons or muons in $\sqrt{s} = 13$ TeV pp collisions with the ATLAS detector" as discussed in Chapter 6. Specifics relating to the phenomenological model, the W. Buchmüller, R. Rückl and D. Wyler (BRW) model, are then presented in Section 2.6 with a discussion of current experimental constraints being presented in Section 2.8.

2.1 Reasons to look Beyond the SM

In its current formulation, the SM only provides a description of three of the four fundamental forces in nature. It is quite possible that the SM is only a low-energy approximation of some more intrinsic theory [62–64]. As we have discussed previously, the formulation of the SM requires the unification of the weak nuclear force with quantum electrodynamics to form the Electroweak interaction, as described by the $SU(2)_L \otimes U(1)$ gauge groups. Many models also predict the unification of the electroweak and strong interactions in a "Grand Unified Theory" (GUT) [65]. Although the mass scale of such a unified theory is expected to be far beyond the scope of modern particle colliders ($\lambda_{GUT}\ \mathcal{O} \sim 10^{16}$ GeV [66]), there remain many indirect search channels which could probe this through effects such as proton decay. Some theories also unify a particulate description of gravity to the unified electroweak and strong interactions under a "Theory of Everything" (TOE) [67], which could perhaps provide a fuller understanding of the behaviour of our Universe.

2.1.1 Constrained Model

Within the SM, there are at least 25 physical parameters that must be experimentally determined, and which constrain the behavior of the SM to reflect the Universe that we see. There are many possible representations of these 25 degrees of freedom within the model. One such representation uses the mass of both the fermionic constituents of the SM, and of the Higgs boson, as well as the three mixing angles (θ_{12}, θ_{23} and θ_{13}), and CP violating phase (δ_{13}) of the Cabibbo-Kobayashi-Maskawa (CKM) matrix, the gauge couplings of the U(1), SU(2) and SU(3) gauge symmetries and the Higgs vacuum expectation value. Additionally, the inclusion of massive neutrinos introduces three additional mass terms, and the three mixing angles and CP-violating phase of the Pontecorvo-Maki-Nakagawa-Sakata (PMNS) matrix. In many extensions of the SM, additional parameters may also be required to characterize new properties, such as the CP symmetry violation in the strong interaction.

Although there is no inherent problem with a model that contains of so many undetermined values, it does introduce a degree of instability into our description of the Universe. Even a small variation of any of the aforementioned values could result in a completely un-recognisable Universe with distinctly different physical laws. Such a finely tuned set of parameters can be explained with the anthropic principle; "I think, therefore I am" (Descartes, 1644 [68]) or that; as we live in a Universe which is able to produce scientific observers capable of such measurements, it requires that the values of these parameters are such as to enable the existence of such observers. However, many theoretical models that go beyond the SM attempt to provide a more theoretically robust solution to the exact formulation of these parameters [62–64], to provide a more holistic description of our Universe.

2.1.2 The Hierarchy Problem

From this initial set of experimentally measured parameters, the SM enables the prediction of many additional values. This introduces additional tensions within the SM, when the measured value of a physical parameter greatly differs from its predicted value, requiring large corrections to the theory such as to reconcile it with experiment. It is these instances of such vast disparities in the theory, without theoretically understood origins, that are termed hierarchy problems, of which there are two pre-eminent examples within the SM. One is the large difference between the electroweak ($\mathcal{O} \sim$ GeV) and Planck ($\mathcal{O} \sim 10^{18}$ GeV) scales, which underpins the drastically different strengths of the weak and gravitational forces. The other relates to the Higgs mass which, when considering the possible radiative corrections, would be expected to diverge quadratically up to the cut-off scale of new physics, but we instead find to be of the same order as the electroweak scale. To understand the origin of this hierarchy problem, we must first understand the construction of the measured Higgs mass. It can be thought of as being composed of two terms; the bare mass (m_0), which can be thought of as the non-interacting mass of an isolated Higgs boson, and the additional mass contribution, which arises from its field interactions (δ_m), whereby the measured value is the sum, $m_H = m_0 + \delta_m$. This additional contribution which arises from the field interactions can be determined from the contribution of an infinite set of virtual one-loop diagrams. These divergences could be expected to produce a measured Higgs mass that is at the scale of the Plank mass (m_{Plank} $\mathcal{O} \sim 10^{18}$ GeV), at which our theory breaks down. In order to cancel out this divergence, there must be a degree of fine tuning, such as to derive a value of m_0, which precisely cancels these divergencies, allowing for a value of $m_0 + \delta_m = 125$ GeV. It is this high degree of fine tuning that could motivate the existence of TeV-scale physics, which may cancel some of the divergent corrections.

2.1.3 Origins of the Neutrino Masses

As has been discussed in Section 1.4, Dirac particles are thought to acquire their mass through interaction with the Higgs boson. However, this mechanism is not accessible in the neutrino sector without the existence of right-handed neutrinos, which have not been observed. As such, neutrinos are treated as massless Weyl spinors within the SM. However, direct observations of flavour mixing between the different generations of neutrinos from the Super-Kamiokande, Sudbury Neutrino Observatory (SNO) and KamLAND experiments [26–28], presents clear evidence that neutrinos do in fact possess intrinsic mass. This therefore, is conclusive evidence that the SM, in its current formulation, is not a complete description of our Universe.

These observations have motivated many BSM theories, often proposing the existence of right-handed neutrinos, which may hint at a left-right symmetric theory [69]. Another popular theory is that neutrinos may be Majorana fermions. These are fermions which form their own anti-particle. Such theories propose a "seesaw" mechanism [70–72] through which

the vanishingly small masses observed in neutrinos are explained by the large, possibly GUT scale, masses of their right-handed Majorana anti-particles.

One such test to determine the Dirac or Majorana nature of neutrinos is to study neutrino-less double beta decay, a process that is forbidden within the SM, and which, if found, would directly confirm lepton-number violation and the Majorana nature of neutrinos [25, 73].

2.1.4 Anomalous Magnetic Moment of the muon (g-2)$_\mu$

A long-standing discrepancy stands in the measurement of the muons' magnetic moment, μ. This is a vector along the spin (s) axis;

$$\mu = g\frac{Qe}{2m_\mu}s \tag{2.1.1}$$

where the factor, g, consists of the Dirac value of 2, and the factor $a_\mu = \frac{1}{2}(g-2)_\mu$, which arises from radiative corrections. Measurements of this value, a_μ, poses an interesting channel in which to probe beyond the SM, as it can be measured to an extremely high precision, with the final measurement from the Brookhaven National Laboratory (BNL) experiment E821 having a precision of 0.54 ppm [74]. Candidates from many BSM theories propose potential solutions to this anomalous measurement via virtual loop effects. This discrepancy is measured at the 3.7 σ level [75] to be;

$$a_\mu \equiv \frac{1}{2}(g-2)_\mu = \begin{cases} \text{Theory} : 116\ 591\ 810(43) \times 10^{-11}\ [76\text{˘}95] \\ \text{Experiment} : 116\ 592\ 089(63) \times 10^{-11}\ [74] \end{cases} \tag{2.1.2}$$

$$\therefore \Delta a_\mu = a_\mu^{exp} - a_\mu^{SM} = 279(76) \times 10^{-11} \tag{2.1.3}$$

While a less significant discrepancy of about 2.5 σ is also observed for the electron;

$$\Delta a_e = a_e^{exp} - a_e^{SM} = -88(36) \times 10^{-14}\ [96] \tag{2.1.4}$$

As such, the electrons anomalous magnetic moment is found to agree with prediction at a precision at the parts per trillion level. This measurement supports the measurement of Δa_μ, as the effects of new physics will affect the anomalous magnetic moment of these leptons in proportion to $(m_l/m_{BSM})^2$, meaning that a_μ is a much more useful probe of new physics.

While 3.7 σ is a significant discrepancy, it has not yet reached the 5 σ level that is set as the gold standard for a discovery. However, this may change in the near future, as it is expected that the experimental uncertainty will soon be greatly reduced via the new E-989 experiment that is currently in operation at Fermilab [97, 98], and a future J-PARC experiment [99, 100], which is expected to significantly reduce theoretical uncertainty to a level in line with experimental goals.

2.1.5 Dark Matter

Measurements of gravitational lensing [101], the rotation of galaxies [102–104] and the collisions of galaxy clusters [105] all provide strong empirical evidence for a non-luminous (dark) form of matter (DM). Based on Global fits of the Lambda Cold Dark Matter[1] Model (ΛCDM) [106] to the Cosmic Microwave Background[2] (CMB), it is found that the baryonic matter described by the SM approximately accounts for less than 5% of the total composition of the Universe [107–110]. This study of the CMB finds that dark matter accounts for roughly a further 27%, and the remaining 68% is made up of "*dark energy*".[3] Weakly Interacting Massive Particles (WIMPs) arise as strong candidates for a DM particle. These are massive particles that only interact via the weak nuclear force. WIMPs are a strong contender in BSM searches for dark matter, as the thermal production of WIMPs with weak scale cross-section will naturally lead to the observed DM relic abundance. Under this definition, neutrinos represent a form of hot DM, however, through simulation it can be shown that neutrinos are not sufficient to account for the DM density of galaxies [112] or the predicted energy density of DM in the Universe. Instead, it is thought that some new particle that is not predicted by the SM will constitute this WIMP DM. Such particles are predicted by many BSM theories, and searches for them are ongoing in various experiments where they can either be detected directly through their interaction with a scintillating detector substance [113, 114], or indirectly through evidence of DM interactions in galactic cores [115–117]. Finally, DM may also be produced in high-energy particle interactions and subsequently identified through various search channels such as the enhancement of high-precision electroweak observables, or in the missed transverse energy (E_T) reconstruction in an event or even in the on shell resonance of DM mediating SM processes. Such searches are actively pursued at three of the experiments running at the LHC [118–120].

2.1.6 Charge Parity Violation

The conventionally accepted model for the formation of our Universe is that there was a superdense initial state, which expanded into the Universe that we see today. In this hot, dense model of the early Universe, both matter and anti-matter were expected to be equally mixed and produced in abundance. In such a model, however, the matter and anti-matter constituents of the early Universe would be expected to interact and almost

[1] Cold dark matter refers to dark matter that was non-relativistic when decoupling from ordinary matter. This decoupling is thought to have occurred when the expanding Universe cooled to a "*freeze-out*" temperature. Additionally, dark matter can be "*warm*" (relativistic upon decoupling, but has since become non-relativistic as the Universe has expanded) or "*hot*" (particles that are light enough to remain relativistic today).

[2] This is a universally present background of low energy radiation, that is a relic from the formation of the early Universe.

[3] Dark energy is a proposed explanation for the expansion of the Universe. This theory proposes that a very small (7×10^{-30} g/cm^3) but homogeneous energy distribution pervades the Universe, which has often been associated to the cosmological constant Λ [111] that is accounted for in the ΛCDM.

fully annihilate. The amount of matter and anti-matter expected to remain in such a Universe can be calculated from the proton-antiproton annihilation cross section, where it can be shown that antinucleons "freeze out"[4] of thermal equilibrium with the Universe, when its expansion overtakes the annihilation rate, at a temperature of $\sim$ 20 MeV. This would predict a baryonic density of just $\Omega_{baryon} = 4 \times 10^{-11}$. However, as discussed in Section 2.1.5, studies of the CMB indicate that baryonic matter makes up around 4% of the closure density[5] of the Universe, or $\Omega_{baryon} = 4 \times 10^{-2}$ [121]. There is clearly, therefore, a vast divergence between the baryonic density predicted in a simplistic big-bang model, to that which we observe today. It was shown by Sakharov in 1966 [122], that these two pictures can be reconciled if we apply three conditions to baryogenesis, that if an interaction is: baryon number violating, C and CP-symmetry violating and out of thermal equilibrium, then matter and antimatter can be produced at different rates. These conditions can be understood implicitly, as a dominance of baryons over anti-baryons implies a positive (non-zero) baryon number, inferring that baryon number is violated. Additionally, the violation of both C and CP symmetries ensures that there are some sets of processes in which particles are treated differently from their anti-particles. Finally the third condition ensures that matter does not not achieve thermal equilibrium to antimatter, decreasing the frequency of pair-annihilation. These conditions provide a useful metric for understanding this asymmetry that we observe.

2.2 Phenomenology of Leptoquarks

LQ theory proposes a new class of colour-triplet bosons that can be either scalar or vector-like in nature. Carrying both non-zero baryon and lepton quantum numbers ($B \neq 0,\ L \neq 0$), LQs are able to couple simultaneously to both quarks and leptons. As such, rather than individually considering the conservation of either lepton or baryon number, these quantum numbers are combined into the definition of a new conserved value, the fermion number; $F = 3B + L$ [123]. The strength of this coupling is dependent on the branching ratio, β, into different charged and un-charged leptons, as well as on a single Yukawa coupling, λ. The coupling to the charged lepton is given by $\sqrt{\beta\lambda}$ and the coupling to the neutrino by $\sqrt{1-\beta\lambda}$. Since they couple either up-type ($Q = \pm 2/3$) or down-type ($Q = \pm 1/3$) quarks to either charged ($Q = \pm 1$) or neutral ($Q = 0$) leptons, there arise four possible charge assignments for LQs, of either $Q = \pm 5/3$, $\pm 4/3$, $\pm 2/3$, or $\pm 1/3$. In addition to this, it is possible for LQs to be either left- or right-handed, or even for them to posses a mixture of chiralities in their couplings. As a result of this, some LQ multiplets may enable couplings to left- and right-handed fermions simultaneously, while others may enable couplings to

[4] Meaning that their production mechanisms are no longer kinematically accessible from the ambient energy density of the Universe.

[5] Ω is defined as the ratio of the matter density, ρ_0, to the critical density ρ_{crit} ($\Omega = \frac{\rho_0}{\rho_{crit}}$) where $\Omega > 1$ would indicate a closed Universe that will collapse, and $\Omega < 1$ would indicate an open and monotonically expanding Universe.

either two left-handed or two right-handed fermions.

When constructing possible LQ extensions to the SM Lagrangian, we begin with the kinetic and mass terms for scalar LQs. These are constructed as seen in Equation 2.2.1.

$$\mathcal{L}^{\Phi}_{kinetic} = (\mathcal{D}_{\mu}\Phi)^{\dagger}(\mathcal{D}^{\mu}\Phi) - m^2_{LQ}\Phi^{\dagger}\Phi \tag{2.2.1}$$

where $\mathcal{D}$ is the appropriate co-variant derivative, and Φ is the relevant LQ multiplet, as defined in Table 2.1. Here, superscript † stands for conjugation. In this formulation of the Lagrangian, we have assumed that all the components of a given LQ multiplet (Φ) have the same mass when transforming non-trivially under $SU(2)$, an assumption that is motivated by electroweak precision measurements (as demonstrated in Section 4.2 of Ref. [59]).

Since the number of representations of quark and lepton fields in the SM is finite and small, it is possible to identify all valid LQ multiplets. This is shown (for those multiplets that do not mediate proton decay) in Table 2.1, which follows the notation outlined by W. Buchmüller, R. Rückl and D. Wyler [124] (an alternative notation, the *Aachen* [125] notation, is also often used within the literature). In total, Table 2.1 identifies 6 scalar and 6 vector LQ multiplets that are allowed in a global $SU(3)\otimes SU(2)\otimes U(1)$ gauge symmetry. This table also presents the chirality of the couplings, as well as the gauge representations, the electromagnetic charge and the fermion number of each possible scalar and vector LQ multiplet. Importantly, the fermion number, F, is well defined for each multiplet, and characterises the type of interactions that it may mediate. For example, multiplets of $|F| = 2$ will couple to ℓq, and multiplets of $|F| = 0$ will couple to $\bar{\ell} q$ or $\ell \bar{q}$ [126]. For an in-depth review of the interactions of each multiplet with the known matter particles, including a list of all couplings to the photon, Z boson, W boson, gluon and Higgs fields, please refer to Ref. [59]. If we include the right-handed neutrinos to our formulation of the SM, the number of possible LQ states increases above those from a purely left-chiral SM. For completeness, these are also included in Table 2.1. Of these, it is the $\overline{S_1}$ and $\overline{U_1}$ multiplets whose leptonic couplings are limited to the right-chiral neutrinos (which are not components of the SM field content).

Under $SU(3)_C$ gauge symmetry, all quarks transform as triplets and all leptons transform as singlets. As such, to ensure invariance under the $SU(3)$ group transformations, LQs must transform as 3-dimensional representations of $SU(3)$ to enable the contractions of the quark, lepton and LQ operators. One consequence of this property is that it is possible to construct a theory in which couplings to a quark-quark pair are possible, but there are no such couplings to a lepton–lepton pair (as leptons transform as singlets of $SU(3)$). Since both quarks and leptons are either singlets or doublets of $SU(2)$, the dimensionality assignment of LQs under the $SU(2)$ gauge symmetry is less trivial, as quark-lepton contractions can be of triplet, doublet, and singlet nature under the $SU(2)$ gauge symmetry. This dimensionality can therefore be used to identify the different LQ multiplets, denoted in the subscript of the multiplets symbol. Additionally, we distinguish multi-

leptoquark	Spin	$F = 3B + L$	Quantum Numbers	$Q_{em} = T_3 + Y_W$	Couples to
S_1	0	-2	$(\bar{3}, 1, \frac{1}{3})$	$\frac{1}{3}$	LL,RR
$\widetilde{S_1}$	0	-2	$(\bar{3}, 1, \frac{4}{3})$	$\frac{4}{3}$	RR
$\overline{S_1}$	0	-2	$(\bar{3}, 1, -\frac{2}{3})$	$-\frac{2}{3}$	$\overline{RR}$
S_3	0	-2	$(\bar{3}, 3, \frac{1}{3})$	$(\frac{4}{3}, \frac{1}{3}, -\frac{2}{3})$	LL
R_2	0	0	$(3, 2, \frac{7}{6})$	$(\frac{5}{3}, \frac{2}{3})$	RL,LR
$\widetilde{R_2}$	0	0	$(3, 2, \frac{1}{6})$	$(\frac{2}{3}, -\frac{1}{3})$	RL,$\overline{LR}$
U_1	1	0	$(3, 1, \frac{2}{3})$	$\frac{2}{3}$	LL,RR
$\widetilde{U_1}$	1	0	$(3, 1, \frac{5}{3})$	$\frac{5}{3}$	RR
$\overline{U_1}$	1	0	$(3, 1, -\frac{1}{3})$	$-\frac{1}{3}$	$\overline{RR}$
U_3	1	0	$(3, 3, \frac{2}{3})$	$(\frac{5}{3}, \frac{2}{3}, -\frac{1}{3})$	LL
V_2	1	-2	$(3, 2, \frac{5}{6})$	$(\frac{4}{3}, \frac{1}{3})$	RL,LR
$\widetilde{V_2}$	1	-2	$(3, 2, -\frac{1}{6})$	$(\frac{1}{3}, -\frac{2}{3})$	RL,$\overline{LR}$

Table 2.1: The full set of scalar and vector-like leptoquarks with $SU(3) \otimes SU(2) \otimes U(1)$ invariant couplings to quark-lepton pairs (this omits di-quark couplings due to constraints on proton decay). The names of each multiplet are based on the notation outlined in Ref. [124]. Shown are the fermion number, calculated as $F = 3B + L$, and the hypercharge, Y_W, which is normalized so that $Q_{em} = T_3 + Y_W$, where Q_{em} is the electric charge operator and T_3 is the diagonal generator of $SU(2)$. Also shown are the chiralities of the quark and lepton fields that each leptoquark couples to. The first letter of each pair indicates the chirality of the quark field and the second letter indicates the lepton field. The over-line indicates that the right-handed lepton field is a right-handed neutrino.

plets with the same charge under $SU(2)$ but differing $U(1)$ (hypercharge), by affixing a tilde or a bar above the LQ symbol. An example of these rules is the $\widetilde{R_2}$ and R_2 scalar multiplets. Here, the subscript "2" denotes their $SU(2)$ charge, and the tilde indicates a change in $U(1)$ hypercharge. The LQ hypercharge is an additive quantity that can be determined by its contractions with the quark and lepton multiplets ($Q_L \equiv (3, 2, 1/6)$ and $L_L \equiv (1, 2, -1/2)$ respectively). As an example, a LQ that transforms as a triplet of both $SU(3)$ and $SU(2)$ would therefore yield a hypercharge of $-1/2 + 1/6 = -1/3$, i.e., $(1, 1, 0) \in (1, 2, -1/2) \otimes (3, 2, 1/6) \otimes (3, 3, 1/3)$.

2.3 Theoretical Motivation

The hallmark of a good theory is its ability to make precise predictions which can be experimentally verified. By this measure, the Standard Model performs exceedingly well as a theory of particle interactions, correctly predicting quantities such as the electromagnetic fine-structure constant, α [127] to a precision at the parts per trillion level [96]. As such, we are in an era of precision physics in which discoveries can be made in small deviations from theory. However, as discussed in Section 2.1.4, even in the aforementioned measurement, there exists a significant discrepancy with respect to the standard model at 12^{th} decimal place. This discrepancy as well as an even more significant discrepancy in the anomalous magnetic moment of the muon, have been proposed to be hints of LQ physics [128–130]. One other area in which high-precision tests of the SM have repeatedly presented discrepancy, is that of the rare decays of B mesons. B meson decays occur in the SM via various mechanisms. An example of some such diagrams with intermediate charged vector bosons is provided in the diagrams on the left of Figure 2.1. The rates of these B meson decays are well understood in the SM, however, these SM predictions are in disagreement with the rates observed at various experiments. The diagrams on the right of Figure 2.1 present BSM mechanisms that result in the same final states. This would provide an enhancement of the observed decay rates, that could explain the anomalous measurements.

These processes have been repeatedly observed by several completely independent experiments including LHCb [132–140], BaBar [141–143] and Belle [144, 145], and tensions with the SM predictions still remain. Included in this list are tests of several rare decay channels of the B meson, such as the $B^+ \to K^+\ell^+\ell^-$ [146] and $B^{*0} \to K^{*0}\ell^+\ell^-$ [133] channels. These are studied via their ratio to the different flavour of lepton, as stated in Equation 2.3.1.

$$R_{K^{(*)}} = \frac{\mathcal{B}(B \to K^{(*)}\mu^+\mu^-)}{\mathcal{B}(B \to K^{(*)}e^+e^-)} \tag{2.3.1}$$

Another result is reported in the channel $\overline{B^0} \to D^{(*)+}\tau^-\bar{\nu}$ [141–145, 147], which can be expressed in the ratio in Equation 2.3.2.

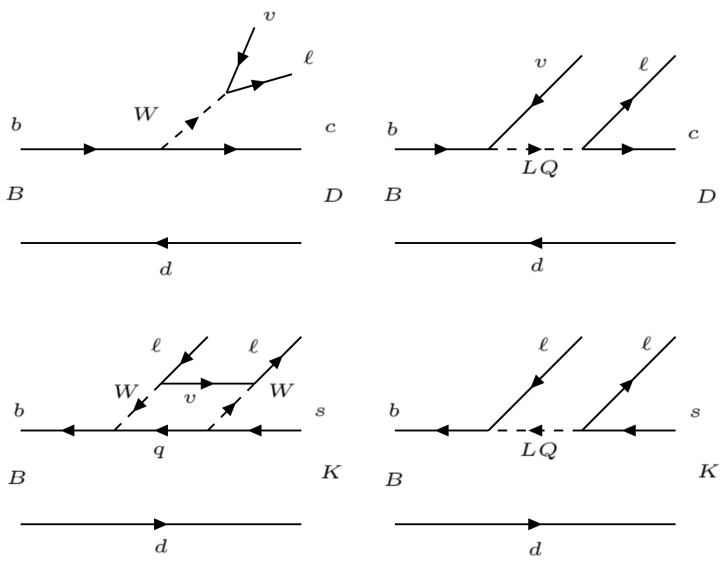

Figure 2.1: Diagram of $B \to D^{(*)}v\ell$ decay (top) and $B \to K^{(*)}\ell\ell$ decay (bottom), with the SM decay channels (left) and the proposed LQ involved channels shown (right). Further discussions of LQ solutions to the $R_{K^{(*)}}$ and $R_{D^{(*)}}$ anomalies can be found in Ref. [131]

$$R_{D^{(*)}} = \frac{\mathcal{B}(B \to D^{(*)}\tau^-\bar{\nu})}{\mathcal{B}(B \to D^{(*)}\ell^-\bar{\nu})}, \qquad (\ell = e/\mu) \tag{2.3.2}$$

LHCb reports measurements for these values as follows[6];

$$R_K = 0.84^{+0.044}_{-0.041} \quad \text{for } 1.1 < q^2 < 6 \text{ GeV}^2 \tag{2.3.3}$$

$$R_{K^{*0}} = \begin{cases} 0.660^{+0.110}_{-0.070}(\text{stat}) \pm 0.024(\text{syst}) & \text{for} \quad 0.045 < q^2 < 1.1 \text{ GeV}^2 \\ 0.685^{+0.113}_{-0.069}(\text{stat}) \pm 0.047(\text{syst}) & \text{for} \quad 1.1 < q^2 < 6.0 \text{ GeV}^2 \end{cases} \tag{2.3.4}$$

$$R_{D*} = 0.310 \pm 0.016(\text{stat}) \pm 0.022(\text{syst}) \tag{2.3.5}$$

These findings are in tension with the predictions of the SM, which expects these values of R_{D*} and $R_{K^{(*)}}$ to be 0.252 ± 0.003 [149] and 1.00 ± 0.01 [150–153] respectively. Such measurements are highly unexpected in a SM only model, with LHCb reporting statistically significant deviations from the SM at the 2.2, 3.1 and 2.6 σ levels for the measurements of R_{D*}, R_K and $R_{K^{*0}}$ respectively [133, 146, 147]. To explain these measurements, hypothetical extensions to the SM are proposed, often introducing new mass terms to the SM

[6] Although it should be noted that a similar measurement of R_{D*} by ATLAS, which tested lepton flavour non-universality in the ratio of decays to τ and μ (documented in Ref. [148]), found the ratio to be in agreement with the SM.

Lagrangian. LQs are one such candidate particle that satisfactorily describes the anomalous measurements reported. As seen in Figure 2.1, the anomaly reported by LHCb [132] can be adequately described by the introduction of a new boson mediating the lepton-quark transition. This would have to enable the transition between mixed lepton and quark generations, and mixed LQ decay modes. This requirement has lead to the adaptation of traditional, fixed generation, LQ models to relax this requirement, and allow for these cross-generational LQ decay modes. Specifically, it has been shown that these observations can be resolved by introducing either one scalar (S_3) or vector (U_3) LQ multiplet [154], or two scalar multiplets ($R_2 + U_1$) together [155].

In addition to the B anomalies, LQs can be used to explain the origins of the neutrino masses [156–159], as well as the origins of CP violation, explaining the matter/anti-matter asymmetry observed in the Universe [160–162]. There is, therefore, significant experimental and empirical evidence to motivate searches for leptoquark production at the LHC.

2.4 Leptoquark Production mechanisms at the LHC

Leptoquarks can be both singly and pair-produced in pp collisions with cross-sections that are proportional to their mass and the strong coupling constant, α_S. Some examples of on-shell scalar LQ single production are presented in Figure 2.2. For LO single LQ production, the cross-sections also have a dependence on a model dependent coupling parameter (λ). For LQs on the TeV scale, these couplings are constrained to be below the electromagnetic coupling ($\lambda_{em} \approx 0.3$) [163, 164], meaning that limits on single LQ production are to be presented as combined limits on the LQ mass and coupling parameter.

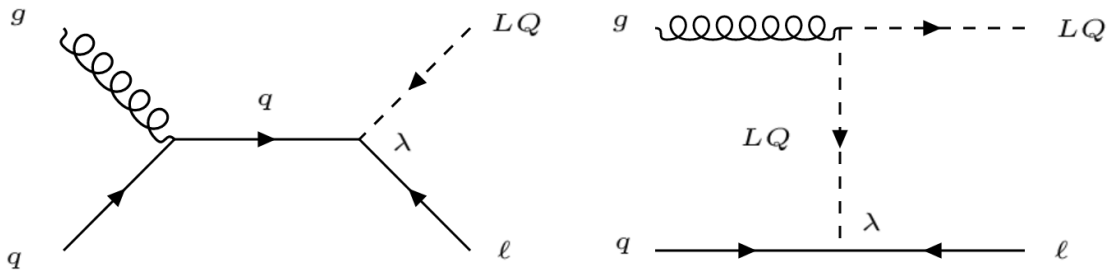

Figure 2.2: Leading order single scalar leptoquark production mechanisms available at the LHC.

Because LQs possess colour charge, they can also exhibit large pair production cross-sections at the LHC. These mechanisms serve as the focus of the search documented in this Thesis. These production modes include gluon-gluon and quark-quark mechanisms, and are dominated by gluon-gluon fusion processes as shown in Figure 2.3. These leading contributions from gluon fusion imply that low energy constraints on fermionic couplings do

not significantly effect pair production cross-sections. This independence from any coupling parameter means that for pair production, the cross-section limits may be presented as a function of the LQ mass only.

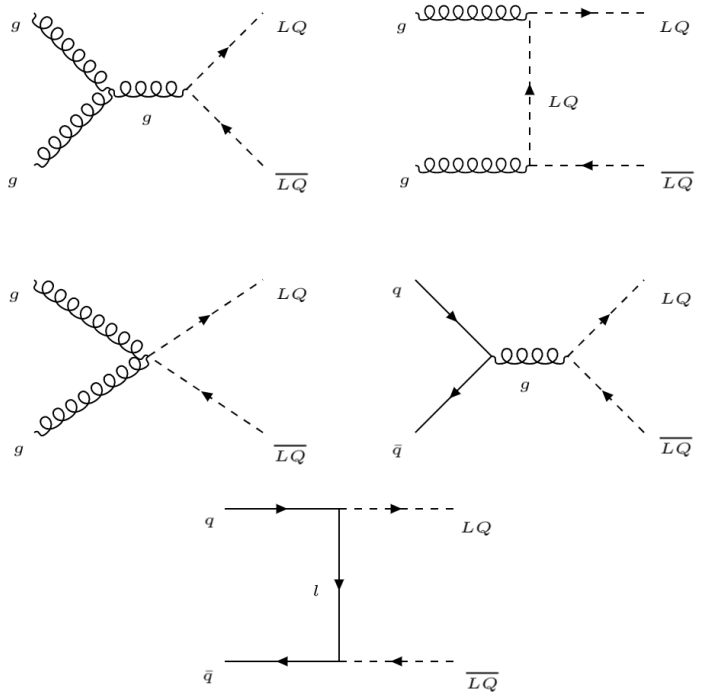

Figure 2.3: Leading order scalar leptoquark pair production mechanisms available at the LHC, of which gluon-gluon and quark-quark initiated are dominant. Also shown is a t-channel lepton exchange mechanism in which there is some model dependence on the strength of the Yukawa coupling term λ. This model dependence is minimal for values of $\lambda < 1$ however.

Additionally, vector leptoquark models predict large single and pair produced LQ cross sections, that are parameterised by two additional model-dependent parameters, κ_G and λ_G that can have significant impact on both pair- and single-production mechanisms. In this way, vector LQ models become heavily model dependent, and can typically produce much larger cross-sections than scalar models [165]. As such, scalar LQ bounds can be interpreted as conservative limits on vector interpretations also.

2.5 Leptoquark Decay modes

Within the BRW model, LQs may couple to lepton-quark pairs with decay widths proportional to the mass of the leptoquark and the Yukawa coupling term, λ. For values of $\lambda < 1$, and LQ masses at the TeV scale, these decay widths are found to be small in comparison to our experimental resolutions. The branching fraction of these decays to quarks

and leptons, β, is a free parameter of the model, with the assumption that the branching ratios to charged and neutral leptons sum to unity ($BR(LQ \to \ell q) + BR(LQ \to \nu q) = 1$). Their arises, therefore, three distinct final states that may be produced in the decay of pair-produced LQs; $q\nu q\nu$, $q\ell q\ell$ and $q\nu q\ell$. The parameter β determines the branching ratios of the different decay modes.

In the case of decays to the heavy flavours of quarks, however, β is not exactly equivalent to the branching ratio, as these decays also exhibit strong dependence on the LQ mass. This is due to the large masses of the top and bottom quarks, meaning that the phase space for decays to these final states is constrained. For small LQ masses, this can result in large differences between β and the branching ratio, as shown in Figure 2.4. The effect is found to be small however, with $\beta \to$ BR as $m_{LQ} \to 1$ TeV. The equations used to describe this relationship for the model used in this search are based on those outlined in Refs. [59, 166]:

$$\Gamma(LQ^u \to t\nu) = \frac{(M_{LQ}^2 - M_t^2)^2 3\lambda^2(1-\beta)}{48\pi M_{LQ}^3} \tag{2.5.1}$$

$$\Gamma(LQ^u \to b\ell) = \frac{(M_{LQ}^2 - M_\ell^2 - M_b^2)\sqrt{M_{LQ}^4 + M_b^4 + M_\ell^4 - 2(M_{LQ}^2 M_b^2 + M_{LQ}^2 M_\ell^2 + M_b^2 M_\ell^2)} \times 3\lambda^2\beta}{48\pi M_{LQ}^3} \tag{2.5.2}$$

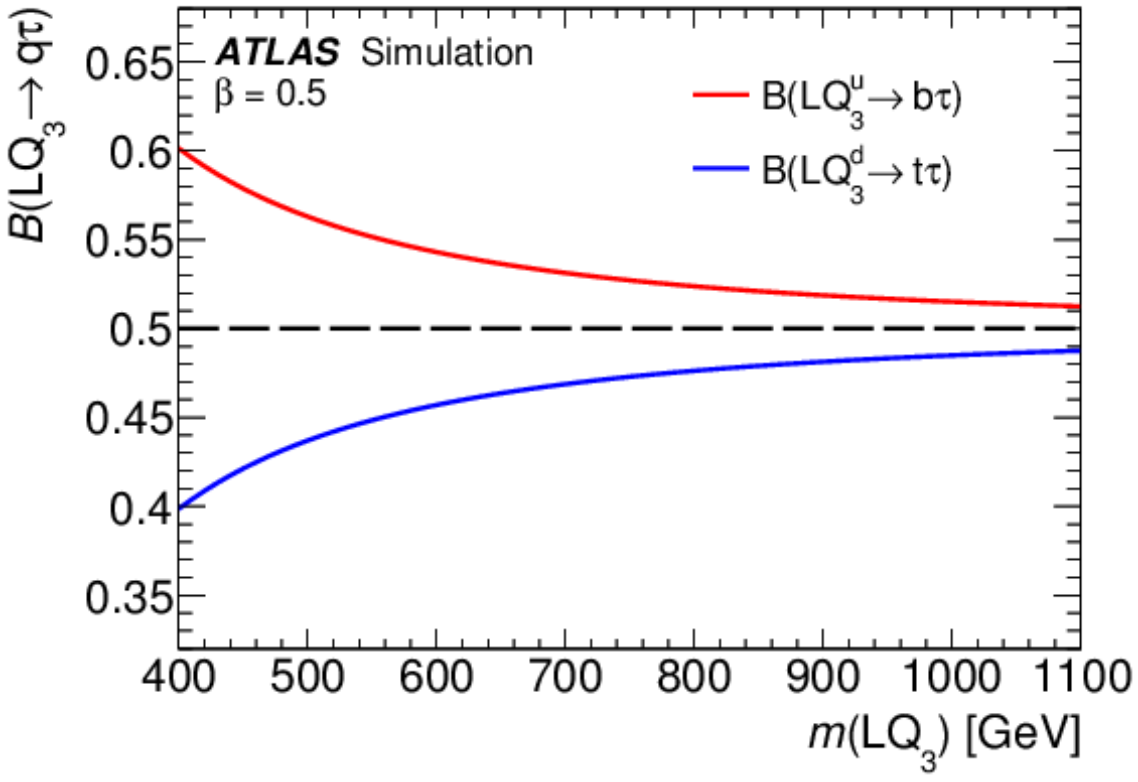

Figure 2.4: [166] Plot of BR to charged leptons for $\beta = 0.5$ for $LQ_3^u \to b\tau/t\nu$ & $LQ_3^d \to t\tau/b\nu$.

2.6 The Minimal Buchmüller-Rückl-Wyler Model

A minimal implementation of the general, effective Lagrangian for LQ interactions with lepton-quark pairs as formulated by W. Buchmüller, R. Rückl and D. Wyler [124], has been implemented into a UNIVERSAL FEYNRULES OUTPUT (UFO) [167] for use in the NLO MC simulation of LQ decays by Mandal *et al* in Ref. [168]. This formulation of the Lagrangian is shown, for the case of scalar LQ interactions, in Equation 2.6.1.

$$\begin{aligned}\mathcal{L}_s = (g_{1L}\bar{q}_L^c i\tau_2 \ell_L + g_{1R}\bar{u}_R^c e_R)\cdot S_1 + \tilde{g}_{1R}\bar{d}_R^c e_R \cdot \widetilde{S}_1 \\ +g_{3L}\bar{q}_L^c i\tau_2 \tau \ell_L \cdot S_3 + (h_{2L}\bar{u}_R \ell_L + h_{2R}\bar{q}_L i\tau_2 e_R)\cdot R_2 \\ +\tilde{h}_{2L}\bar{d}_R \ell_L \cdot \widetilde{R}_2\end{aligned} \tag{2.6.1}$$

Here, the scalar LQ multiplets, $S_1,\ \widetilde{S}_1,\ S_3,\ R_2$ and $\widetilde{R}_2$ are those outlined in Table 2.1, while $\ell_L,\ q_L$ ($e_R,\ d_R,\ u_R$) are the lepton and quark doublets (singlets) as outlined in Section 1.2.[7] This formulation of the LQ interaction Lagrangian is designed to have some key traits in order to conform with the SM, requiring the Lagrangian to be,

- renormalizable;
- invariant under the $SU(3)_C \otimes SU(2)_L \otimes U(1)_Y$ SM gauge group;
- have only interactions separately conserving L and B quantum numbers, preserving proton stability

In addition to these basal constraints on the Lagrangian, additional requirements are imposed based on experimental observation. For example, it is observed in leptonic pion decays and $(g-2)_\mu$ measurements that the LQs must be chiral [61, 163]. Meaning that within this implementation, the S_1 and R_2 multiplets could have left-handed or right-handed couplings but not both. Additionally, multiplets that require right-handed neutrinos are also dropped from this formulation, which may be noticed by the omittance of $\overline{S_3}$ from Equation 2.6.1. These constraints on chirality are in part what establish this as the minimal W. Buchmüller, R. Rückl and D. Wyler model (mBRW). Additionally, the original formulation of the mBRW model imposed the requirement that LQs couple to a single lepton-quark generation. The notion of leptoquarks conforming to decays within the fermionic generations stems from constraints on Flavour Changing Neutral Currents (FCNCs), as outlined in Ref. [61]. However, as discussed, recent anomalies in the rare decays of B mesons has hinted at signs of lepton flavour non-universality, enabling the propagation of FCNCs. As such these traditional constraints on the decay products being of the same generation are relaxed in this interpretation of the BRW model, allowing for

[7] Additionally, τ_i are the Pauli matrices and g_x, h_x, $\tilde{g}_x$ and $\tilde{h}_x$ are coupling constants. Here, the subscript denotes both the dimensionality of the coupling LQ's representation under $\mathrm{SU}(2)_L$ (1, 2, 3), as well as the chirality of the coupled lepton (L,R).

the introduction of cross-generational leptoquark decay modes, a process which has not previously been explicitly studied. Additionally, in the construction of the UNIVERSAL FEYNRULES (UFO) model in Ref. [168], the 4 possible charge assignments outlined in Section 2.2 are reduced to a simplified model for scalar LQs with charge, -1/3 and 2/3. The final state observed at a hadron collider such as the LHC is insensitive to the discrepancies between the different multiplets outlined in Table 2.1, and as such constraints placed on LQ decays can be considered as conservative constraints on all multiplets.

2.7 Decay Signature

The analysis documented in this thesis targets the pair production of scalar LQs, each of which decays to a quark and a charged lepton, in which both charged leptons are of the same flavour. As such, the event topology considered contains 2 leptons and 2 jets, which can originate from the fragmentation of either a light, charm or bottom quark. These mechanisms are the same as those shown in Figure 2.3, but with the exception that the lepton mediated t- and u-channel mechanisms, which depend on the strength of the Yukawa coupling term λ can be neglected in this analysis by setting $\lambda < 1$. Additionally, single LQ production terms are also possible, but these are not considered in this analysis.
In this analysis, several different possible flavour compositions of the final state are considered, specifically, a final state containing $q\ell q\ell$, $c\ell c\ell$ or $b\ell b\ell$, where ℓ represents either an electron or a muon, b is a beauty quark, c is a charm quark, and q represents the up, down and strange quarks. As the Z/Drell-Yan (DY)+jets and $t\bar{t}$ processes are dominant background processes with similar final states to those considered in this analysis, it is worth explicitly discussing how these processes can occur in pp collisions.

Z/DY+jets The production and subsequent decay of electroweak mediators, such as the Z or W bosons are well understood at proton-proton colliders. This process involves the annihilation of a quark anti-quark pair or a gluon gluon pair originating from incident protons in the pp collision. This process, first outlined by Sidney D Drell and Tung-Mow Yan [44], and observed by by J.H. Christenson *et al* [169] is known as Drell-Yan production. The subsequent gauge boson can be either a virtual off-shell photon (γ) or Z boson (as these bosons have the same quantum numbers). These electroweak mediators may then subsequently decay into a pair of charged leptons. As shown in Figure 2.5, there are various channels through which this process can occur, in association with multiple high p_T jets. This process will then present a signal-like topology of two leptons and two or more jets. These processes occur with large cross-sections at the LHC, measured to be 300 ± 12 pb [170].

$t\bar{t}$ The large centre of mass energies available at the LHC enable the pair production of top quarks at large rates. The dominant mode for $t\bar{t}$ production at the LHC is gg fusiuon.

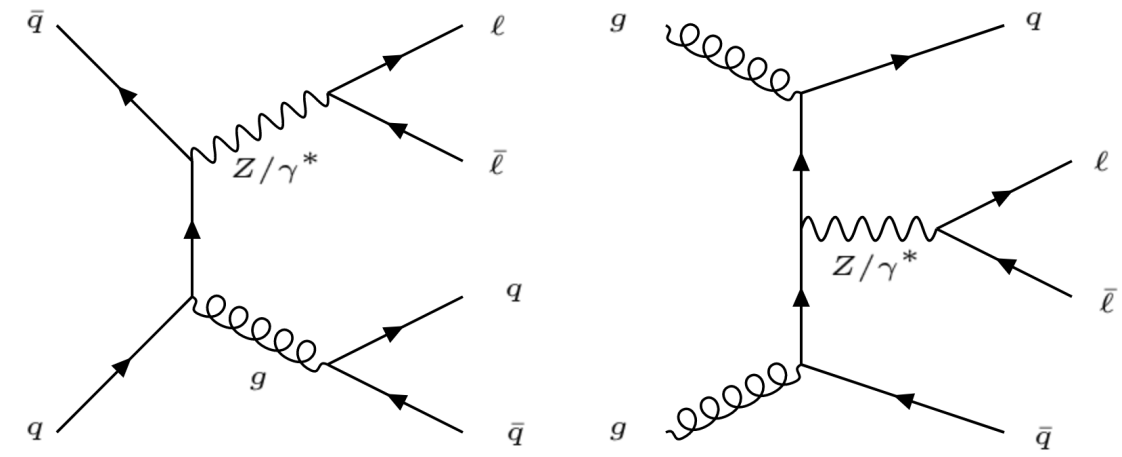

Figure 2.5: Depiction of Z+jets production modes in ATLAS.

This is possible when a gluon, produced in the hard scattering of quarks from the incident pp collision, transforms into a top, anti-top pair, via the strong interaction. It is expected that each produced top-quark will decay into both a b quark, and a W boson. This process is therefore written as $gg \to t\bar{t} \to bb + WW$. This becomes signal-like in the event that each boson decays leptonically, in the process $W \to \ell\nu_\ell$. This would therefore produce the final state of $bb + \ell\ell + \nu\nu$, that is simalar to the final state of this analysis. As both top quarks decay via a b-quark, this process is a dominant background when flavour tagged jets are required.

Single top There are three dominant mechanisms in which a single top quark is produced in association with a W boson, as presented in Figure 2.6. These are Wt, t-channel, and s-channel production.

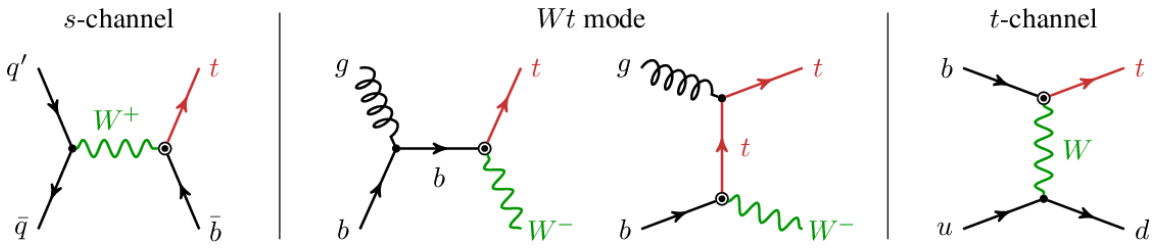

Figure 2.6: [171] Feynman diagrams for single top quark production, shown at leading order (LO) in the t-channel, Wt associated production and s-channel mode.

Of these processes, the Wt-mode single top production is signal-like when considered at NLO, with initial state gluon splitting, in the case where both the top quark and W boson decay semi-leptonically, as shown in Figure 2.7.

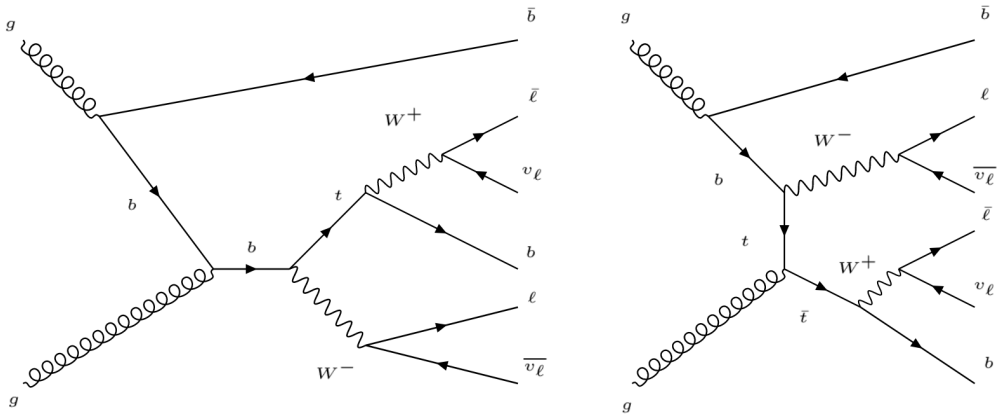

Figure 2.7: Single top quark production in the Wt-mode, considered at NLO with initial state gluon splitting, in the case where both the top-quark and $W^{+/-}$ boson decay semi-leptonically.

2.8 Current Limits

Searches for the pair production of leptoquarks are one of the primary focuses of BSM searches, and have been repeatedly studied from a range of experiments, and throughout the operational lifetime of the LHC. This section shall address the most recent (and most stringent) results from the ATLAS and CMS [172] experiments at the LHC, both of which have analyses recently published at 13 TeV pp collisions.

CMS has several early Run II analyses recently published, at 35.9 fb^{-1}, which search for both 1^{st} [173], and 2^{nd} generation LQs [174], both published in 2019. These two results follow the same methodology, where they require 2 high-p_T leptons ($p_T(\mu) > 35$) GeV and $p_T(e) > 50$ (53) GeV for the 1^{st} (2^{nd}) generation search, and 2 high-p_T jets ($p_T(j) > 50$ GeV) in the final state, with no jet-flavour requirements. These set limits on 1^{st} (2^{nd}) generation LQs at $B = 0.5$ at 1270 (1285) GeV, and for $B = 1$ these increase to 1435 (1530) GeV. A more recent CMS result is also available using the full Run II data set recorded by CMS of 137 fb^{-1}, which searches for the pair production of $\tilde{t}$ and $\tilde{b}$ (the super symmetric top and bottom quarks) [175]. An interpretation of this analysis is also presented when considering a LQ model. This search only considers decays to neutrinos. Here, limits are set at 1140 - 1185 GeV based on the flavour of the leading hadronised quark.

ATLAS has also searched for both 1^{st} and 2^{nd} generation LQs in a combined result using 36.1 fb^{-1} of ATLAS pp collision data [176]. This search set limits on this decay mode at 1290 GeV and 1230 GeV for first- and second-generation leptoquarks respectively, for a branching ratio of $B = 0.5$, and limits at around 1400 GeV for $B = 1$. ATLAS has also performed a comprehensive search for the production of third generation LQs

through a combination of several results. This work establishes limits for all possible decays to third generation quarks and leptons (t, b, τ, ν) through a series of re-interpretations using 36.1 fb^{-1} of ATLAS pp collision data [166]. This search set limits on LQ masses below 800 GeV for both LQ_3^u and LQ_3^d independently of branching ratio, with these limits extending to 1000 GeV and 1030 GeV (970 GeV and 920 GeV) being excluded for the cases of B equal to zero and one for LQ_3^u (LQ_3^d). Additionally, in a similar method to the CMS search, an ATLAS search for the pair-production of $\tilde{t}$ decaying to neutrinos has been recast with a LQ interpretation using the full Run II dataset [177]. This search puts limits on this process at 1240 GeV for a branching ratio of B=0. Finally, as the production cross-section and decay modes of top squarks are equivalent to those of LQs, an ATLAS search using 36.1 fb^{-1} of Run 2 data targeting $B-L$ R-parity-violating supersymmetric models, and top squarks [178], with a final state consisting of ℓ+b-jets, can be directly interpreted as lower limits on the LQ mass. This search excludes top squarks with masses between 600 and 1500 GeV depending on the branching ratio into charged leptons and b-quarks.

Each of the results aforementioned by both ATLAS and CMS focus on the traditional model of LQs that decay to SM particles within the different generations observed in the fermionic sector. However, as has been discussed previously, there are strong motivations to search for leptoquarks decaying via cross-generational decay modes, as is the subject of this thesis. As such recent studies following the publication documented herein, have begun to test such cross-generational mechanisms. These studies were performed in conjunction with the analysis presented in this thesis to provide an increased coverage of the possible decay products that may be searched for. One of these is a search for LQs decaying to either an electron or a muon, and a boosted top quark [179]. This analysis is optimised in the high m_{LQ} region ($m_{LQ} > 1$ TeV), in which the produced top quarks are highly boosted, and are reconstructed as a single large radius jet. A boosted decision tree (BDT) classifier is trained in the signal region using the XGBoost [180] framework. This search employs the full Run II data set recorded at ATLAS, of 139 fb^{-1}. and sets mass limits on this model at around 1480 (1470) GeV in the electron (muon) channel for a branching ratio to charged leptons of $B = 1$, and limits at around 1300 GeV for a branching ratio of $B = 0.5$.

Another ATLAS analysis searches for the 3^{rd} generation of LQs, decaying to the top quark and the τ lepton, using the full Run II dataset [181]. Here multiple configurations of the final state leptons are considered, to maximise the acceptance, each of which requires at least 1 fully hadronically decaying τ. This search places mass limits on this decay mode at 1430 GeV for a branching ratio of $B = 1$, and 1220 GeV for $B = 0.5$. This is roughly a 480 GeV increase in sensitivity on the early Run II ATLAS analysis that searched for this decay channel using only 36.1 fb^{-1} [166]. For a branching ratio of $B = 0.5$, the limit on this model was placed at 1200 GeV.

Of the searches mentioned, it is Refs. [173, 174, 176] that have the closest final state signatures to those of this thesis, the results of which can be seen in Figures 2.8 - 2.10. It

is to these that a comparison of the results of this thesis should be made. From these, it is shown that this search increases the sensitivity of previous ATLAS and CMS results by around 300 - 400 GeV for B=1.

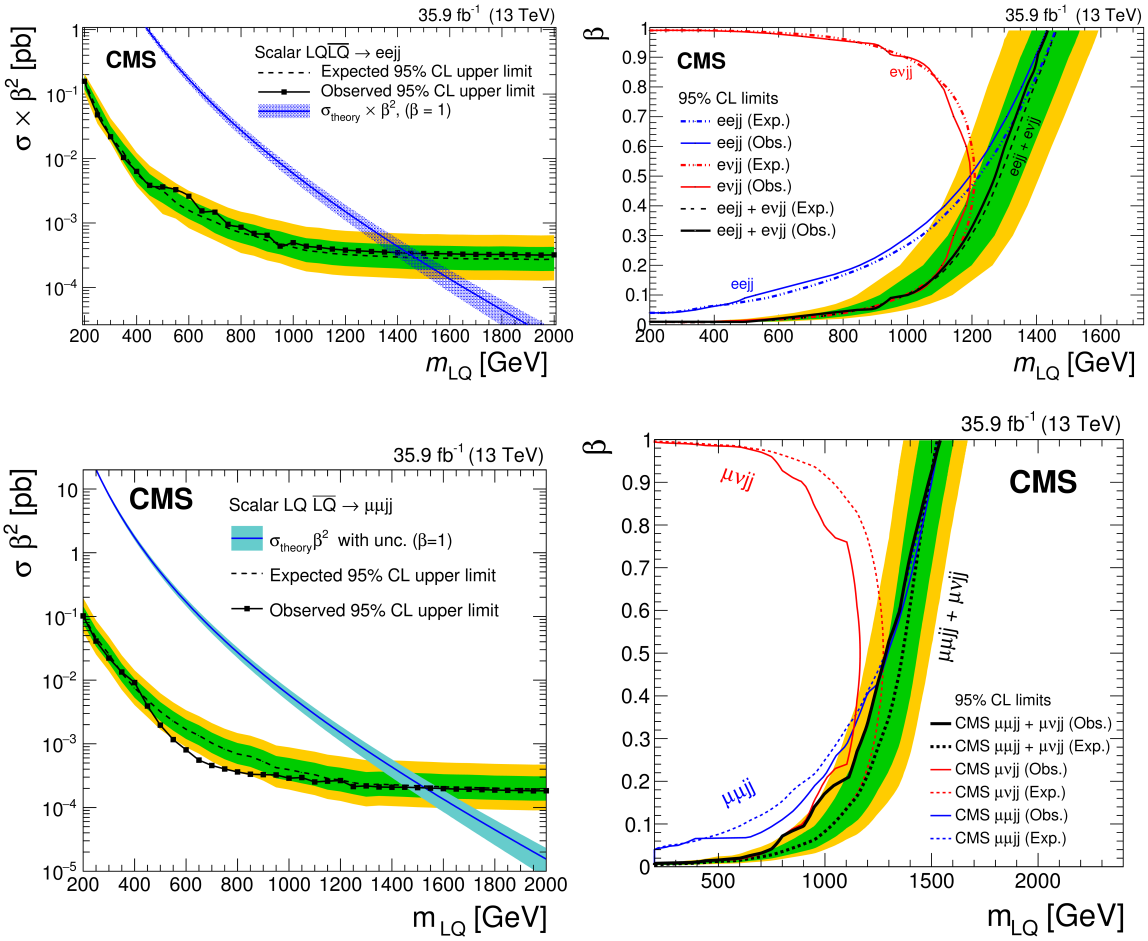

Figure 2.8: [173, 174] Observed upper limits for scalar LQ pair-production cross-section times β^2 (left) and the upper limits in the m_{LQ} β plane (right). These limits are obtained in the $\ell\ell jj$ channel (left), and a combined channel (combined with ℓvjj) (right). The solid (dashed) black line represents the observed (median expected) exclusion. Exclusions are shown at a 68% (95%) CL in the green (yellow) band.

Summary This chapter has illustrated some of the reasons why we need to look beyond the SM to explain our universe, and more specifically, why scalar LQ models, with cross-generational decay modes might provide an interesting channel of new physics. However, if such processes do occur in nature, it is clear from the cross section and branching ratio limits reported in Section 2.8 that we do not yet have either sufficient statistics to make a meaningful observation of such rare processes, or that our colliders have not yet reached

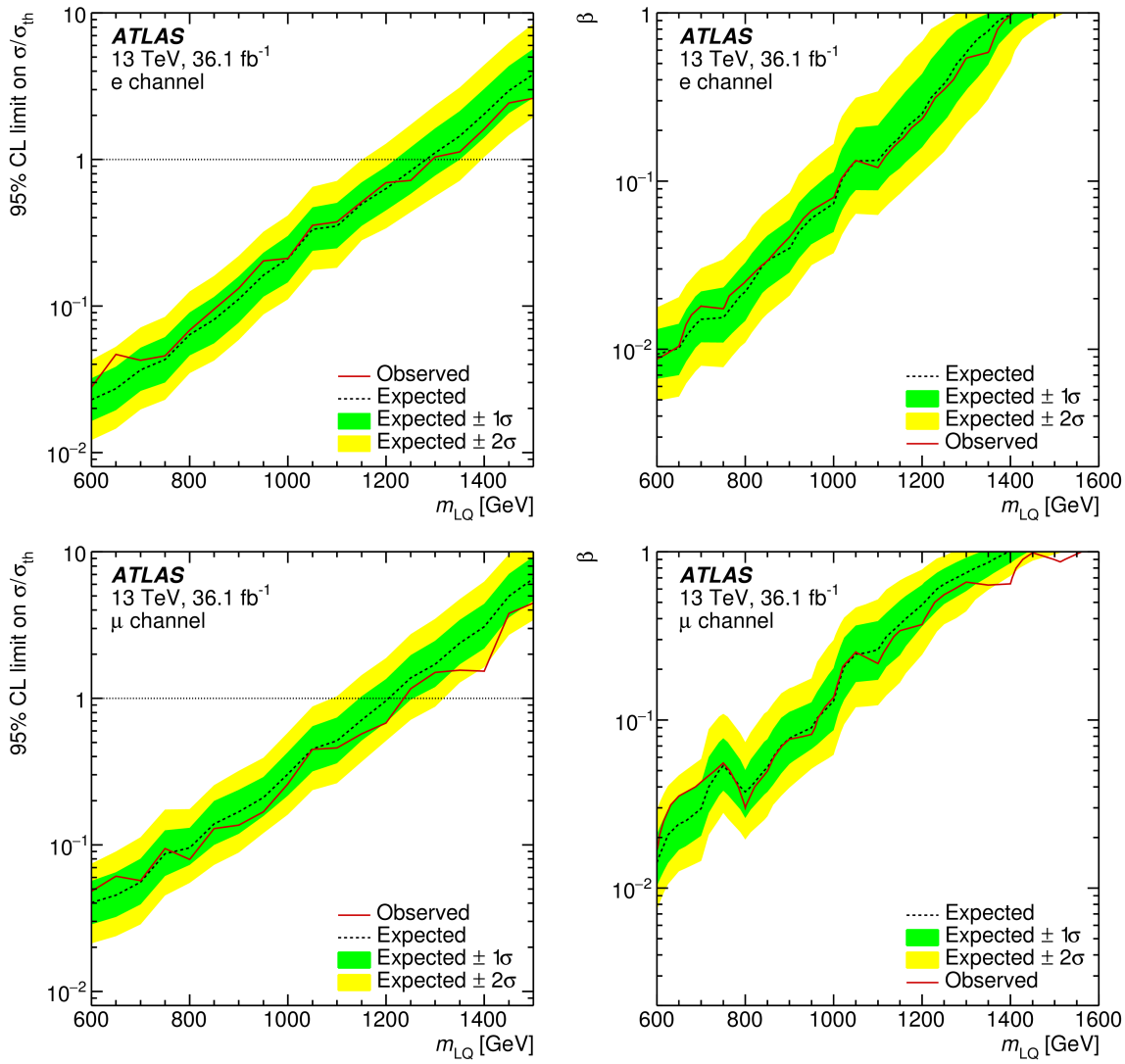

Figure 2.9: [176] Observed upper limits for scalar LQ pair-production cross-section normalised to the predicted cross-section (σ/σ_{th}) (left) and the upper limits in the m_{LQ} β plane (right). Limits are shown for 1^{st} (top) and 2^{nd} (bottom) generation LQs, in the high mass ($m_{LQ} > 600$ GeV) region. The solid (dashed) black line represents the observed (median expected) exclusion. Exclusions are shown at a 68% (95%) CL in the green (yellow) band.

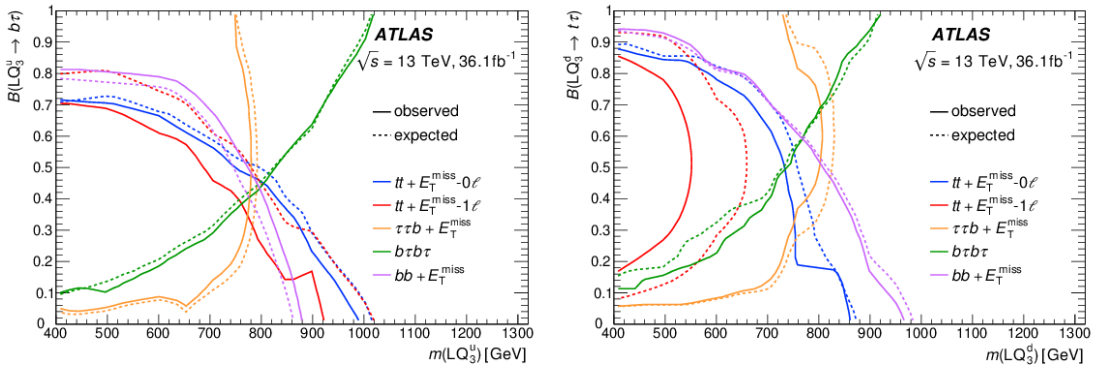

Figure 2.10: [166] Limits on the branching ratio into charged leptons for scalar third-generation up-type (left) and down-type (right) leptoquark pair production, produced using the early Run II dataset of the ATLAS detector, recorded in the years 2015 and 2016.

high enough energies to produce them. Many searches are ongoing, however, and it is expected that this will remain a valuable branch of BSM phenomenology that will continue to be actively studied.

Part II

The LHC and ATLAS

Chapter 3

The LHC and the ATLAS Detector

The data presented in this thesis was recorded by the ATLAS detector [182] during Run II of the LHC [183, 184]. The ATLAS detector is one of the four main experiments located along the LHC beam-pipe. The LHC is a hadronic particle accelerator, constructed maintained and operated by the European Organization for Nuclear Research (CERN). In this chapter, we will discuss the LHC and CERN accelerator complex in Section 3.1, as well as the key details of the Run II data set in Section 3.2. Finally, we shall discuss the design of the ATLAS detector in Section 3.3.

3.1 The LHC

The LHC (currently producing the world's highest-energy proton-proton collisions) is located outside of Geneva, on the Franco-Swiss border. The LHC is the primary beam ring of the CERN accelerator complex, which is illustrated in Figure 3.1. In tunnels placed approximately 100 m underground,[1] sit two rings of pipeline of 27 km in circumference, encased in super-conducting magnets. Inside each pipeline is an extremely high-quality vacuum chamber, with an atmospheric pressure of 10^{-13} atmospheres. Into each pipeline, groups of protons,[2] supplied by the Super Proton Synchrotron (SPS) accelerator, are injected in clusters (termed "bunches") in opposite directions, at close to the speed of light. The trajectory of these two counter-rotating beams is precisely controlled using 1232 superconducting dipole magnets, with an additional 392 superconducting quadrupole magnets used to focus the beam. Each beam is also further accelerated by 8 Radio-Frequency (RF) cavities per beam-ring to the collision energy of 6.5 TeV. These two beams are then overlaid so that the proton beams collide in a direct collision at each of the 4 detector experiments (ATLAS [182], CMS [172], LHCb [186] and ALICE [187]) depicted in Figure 3.1.

[1] These were initially constructed in the 1980s for the Large Electron Positron (LEP) collider [185].

[2] The LHC is also used for heavy ion collisions including Pb+Pb, Xe+Xe and p+Pb, at various collision energies [183].

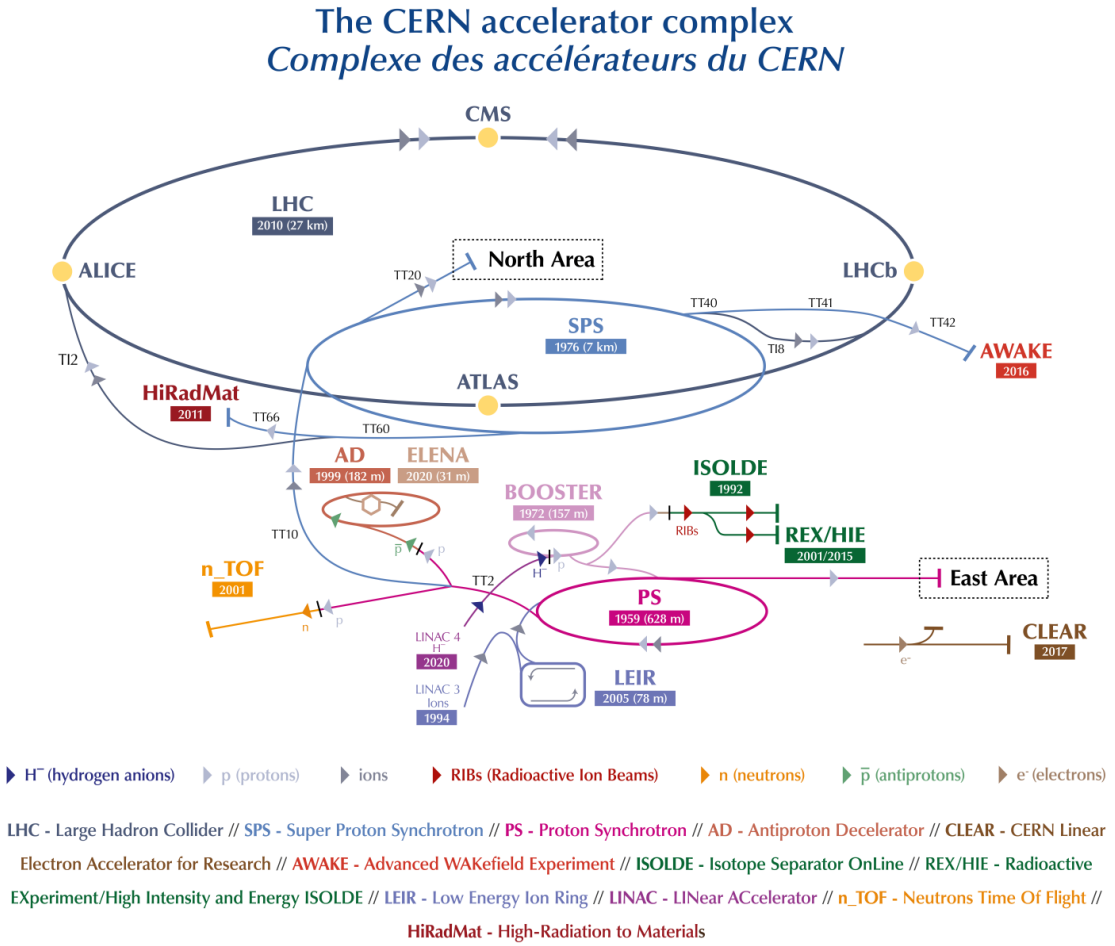

Figure 3.1: [188] A schematic of the LHC main ring and delivery system. Hydrogen gas is stripped of its electrons in an electric field. The free protons are then injected into the linear accelerator (Linac 2) (in the injection of heavy ions, the Linac 3 accelerator is instead used) and accelerated to an energy of 50 MeV using a series of Radio-Frequency (RF) cavities. These are then injected into the Proton Synchrotron Booster (PSB), which accelerates them to 1.4 GeV, and then the Proton Synchrotron (PS), which accelerates them to 25 GeV. Here the protons are split into discrete bunches. Finally, the Super Proton Synchrotron (SPS) accelerates these bunches to an energy of 450 GeV, before they are injected into the two beam pipes that form the main ring of the LHC.

3.2 The Run II dataset

Data events used in this analysis correspond to the full Run II dataset of proton-proton collisions observed at a centre of mass energy of $\sqrt{s} = 13$ TeV, as recorded by the ATLAS detector in the years 2015 - 2018. In full, the dataset considered "good for physics" corresponds to an integrated luminosity of 139 fb^{-1}.

In the years 2015-2018, up to 2556 proton bunches were injected into each of the LHC beam pipes, with a 25 ns bunch spacing. Due to this extremely small separation of the proton bunches, it is possible for the ATLAS detector to be sensitive to interactions from the preceding or following bunch collision due to the limited detector response time. This effect is known as "out of time" pileup, where pileup, denoted μ, is simply the term for multiple pp collisions being simultaneously recorded by the ATLAS detector. Similarly, due to the high density of these proton bunches, there are multiple protons interacting within each bunch crossing, with an average of 33 pp interactions per bunch crossing. This effect is known as "in time" pileup. The pileup distributions for these data-sets are shown in Figure 3.2.

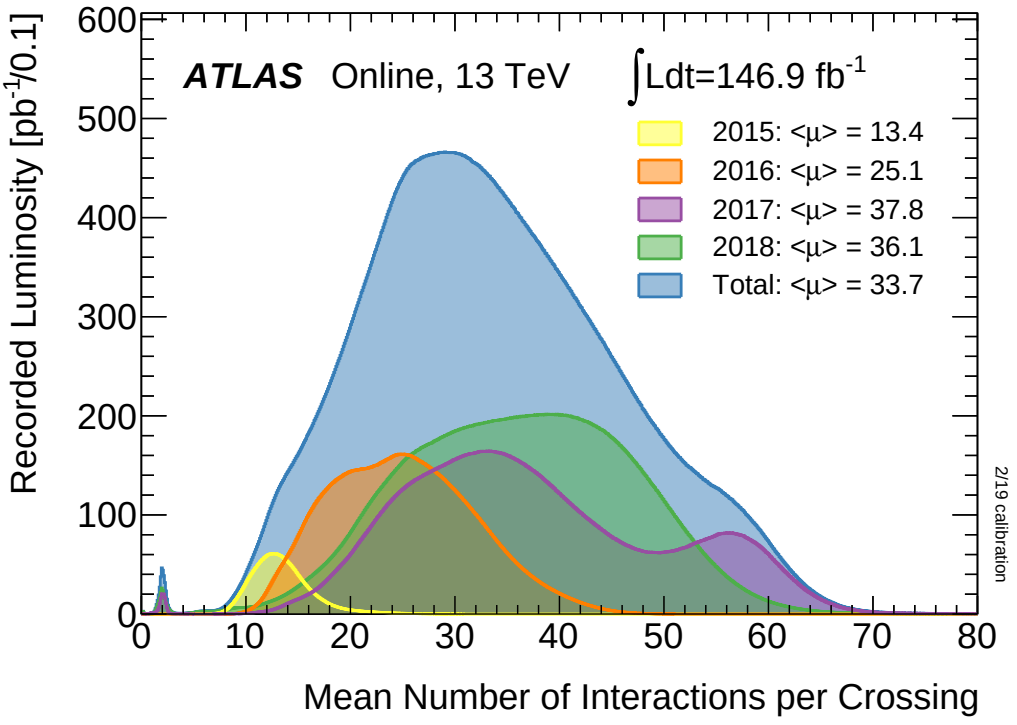

Figure 3.2: [189] Luminosity-weighted distribution of the average pileup ($\langle\mu\rangle$) per bunch crossing is shown for the full Run II dataset.

3.2.1 Luminosity

The luminosity recorded by the ATLAS detector is measured by the upgraded version of the dedicated online "LUminosity Cherenkov Integrating Detector" (LUCID)-2 [190] for the primary luminosity measurements. This measurement is dependent on several variables; the number of bunches (n_b), the number of protons per bunch in the interaction ($N_{1,2}$), the revolution frequency (f_{rev}) and the beam profile at the collision point. The beam profile is then described by both the normalised emittance of the beam, given by ϵ_n and the amplitude function, β^*, which describes by how much the beam is squeezed[3,4] Also contributing to the luminosity is a geometric factor that is dependent on the crossing angle of the two beams[5] (θ_c) and the length of the bunches (σ_s). The theoretical calculation of the luminosity is then given in Equation 3.2.1.

$$\mathcal{L} = \frac{n_b \times N_1 \times N_2 \times \gamma \times f_{rev}}{4\pi \times \beta^* \times \epsilon_n} \times F(\theta_c, \beta^*, \epsilon, \sigma_s) \tag{3.2.1}$$

The analysed luminosity is then further reduced by selecting only events recorded during periods when the relevant detector components were operating normally. These are listed in the "All Good" Good Run List (GRL). With the end of the Run II operation of the LHC on the 3^{rd} of December, 2018, ATLAS has recorded 147 fb^{-1} of pp collision data, with a data taking efficiency of 95.6% [193],[6] which amounts to the largest pp collision data set recorded to date. The remaining integrated luminosity that is considered good for physics stands at 139 fb^{-1}. The total integrated luminosity that is delivered, recorded and considered good for physics is subsequently shown for each month of the Run II data taking period in Figure 3.3 and is also presented, along with the data quality (DQ) efficiency, peak instantaneous luminosity, $\mathcal{L}_{Peak}$, pile up ($\langle\mu\rangle$) and peak pile up ($\langle\mu_{Peak}\rangle$) in Table 3.1.

Year	$\mathcal{L}$ [fb^{-1}]	$\mathcal{L}_{Peak}$ [cm^{-2}s^{-1}]	$\langle\mu\rangle$	$\langle\mu_{Peak}\rangle$	ϵ_{Data}
2015	4.0	5 $\times 10^{33}$	13	16	88.8%
2016	38.5	13 $\times 10^{33}$	25	41	93.1%
2017	50.2	16 $\times 10^{33}$	38	60	95.7%
2018	63.4	19 $\times 10^{33}$	36	55	97.5%

Table 3.1: [189, 193] The exact break-down of the integrated luminosity $\mathcal{L}$, peak instantaneous luminosity, $\mathcal{L}_{Peak}$, average pile up ($\langle\mu\rangle$), peak pile up ($\langle\mu_{Peak}\rangle$) and the data taking efficiency ϵ_{Data} for each year of data-taking used in Run II.

[3] At the collision point, bunches are squeezed into an hour-glass shape, where the highest density occurs at the crossing point, with the value of β^* being reduced to as low as 25 cm [191].

[4] By reducing these two factors, the size of the beam at the collision point can be reduced to as low as 15 μm [191].

[5] To ensure collisions occur only at the crossing point, the beams are crossed at an angle of at least 120 microradians [192].

[6] Where the Data Quality (DQ) is defined as the luminosity-weighted fraction of good quality data recorded during stable beam periods. Only periods during which the recorded data were intended to be used for physics analysis are considered for the DQ efficiency

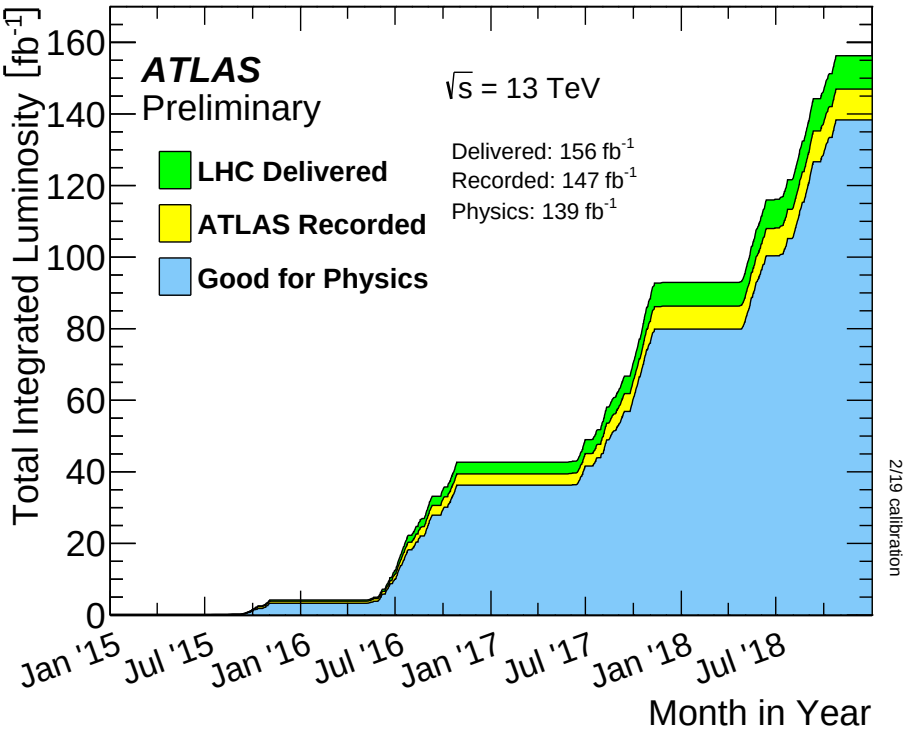

Figure 3.3: [189, 193] Cumulative integrated luminosity delivered to and recorded by ATLAS between 2015 and 2018 during stable beam pp collision data-taking at $\sqrt{s} = 13$ TeV. This includes machine commissioning periods, special runs for detector calibration, and LHC fills with a low number of circulating bunches or bunch spacing greater than 25 ns. It is worth noting that the total integrated luminosity recorded for the standard $\sqrt{s} = 13$ TeV pp collision data set corresponds to 147 fb^{-1}. It is this number that is used in the denominator when calculating the data quality efficiency of the standard $\sqrt{s} = 13$ TeV pp collision data set.

3.3 The ATLAS Detector

ATLAS (A Toroidal LHC ApparatuS) [194] is a general-purpose particle detector, maintained and operated by the ATLAS collaboration. ATLAS is designed to record a high luminosity of collision events, measuring decay signatures over a large solid angle, and wide p_T range. This makes ATLAS useful for a range of SM and BSM applications. ATLAS is designed to accommodate the high collision rates and extreme radiation levels produced by the LHC.

ATLAS employs a right-handed coordinate system, who's origin is located on the nominal interaction point. The z-axis is then defined as being along the beam pipe (note that this differs from the beam axis due to the slight crossing angle). The x-axis is then defined to point from the beam-spot to the centre of the LHC ring, while the y-axis points vertically upwards. The $x-y$ plane is then defined as the *transverse* plane. A cylindrical coordinate system (R, ϕ) can then be used to define this plane, where ϕ is the azimuthal angle around the beam pipe and R is a measure of the radial distance from the interaction point. The polar angle, θ, is then defined as the angle from the positive z-axis.

The polar angle θ is a poorly defined variable however, as it does not maintain invariance under lorentz transformations along the beam line. As such, a more robust choice would be the lorentz-invariant variable, rapidity, defined as;

$$y = \frac{1}{2}\ln\left[\frac{E+p_z}{E-p_z}\right] \tag{3.3.1}$$

where E is the energy of the particle and p_z is the z-component of its three-momentum. However, this variable is dependent on the particle's momentum, which can be poorly reconstructed in the high p_T region. To avoid this, we can, in the ultra-relativistic limit where the energy approximates to the momenta, define the pseudorapidity (η);

$$\eta = -\ln\,\tan\left(\frac{\theta}{2}\right). \tag{3.3.2}$$

This equates to the rapidity in the ultra-relativistic limit, but depends only on the polar angle θ, which suffers no such reduction in its resolution. The value of η will vary from 0 when in the transverse plane, to $\pm\infty$ when along the beam pipe ($\pm z$). The distance ΔR, as defined in $\eta-\phi$ space is;

$$\Delta R = \sqrt{\Delta\eta^2 + \Delta\phi^2} \tag{3.3.3}$$

3.3.1 ATLAS Sub-Systems

ATLAS is comprised of several sub-detector systems and a complex system of magnets. Each sub-detector is placed concentrically around the beam pipe. These are (in order of radial separation from the beam pipe) the Inner Detector (ID), the Electromagnetic, and

Hadronic Calorimeters (EMCAL, HCAL), and the Muon Spectrometer (MS). A visualisation of the layout of ATLAS is shown in Figure 3.4. Through the aforementioned systems, ATLAS attempts to provide a precise reconstruction of each pp collision event.

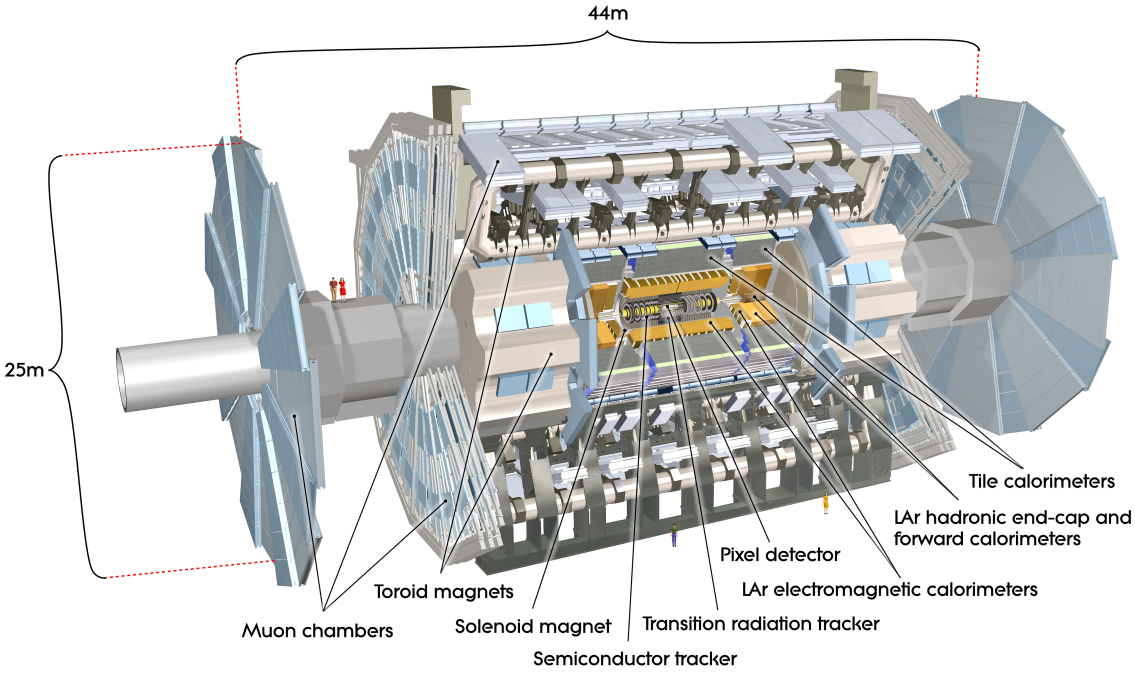

Figure 3.4: [195] Schematic of the ATLAS detector, listing its many sub-systems.

Magnet System

Across these detector systems are strong magnetic fields, designed to bend the trajectory of charged particles as they pass through the various layers of the ATLAS detector. These strong magnetic fields are produced by a superconducting magnetic system [196], comprised of three toroidal (one barrel, and 2 end-caps) and one solenoid magnet. The inner-most of these is the solenoid magnet. Aligned along the beam pipe, the solenoid magnet is a thin, superconducting coil, delivering a 2 T magnetic field across the ID. The barrel and end-cap toroids each consist of 8 radially symmetric coils, providing a toroidal magnetic field across the muon spectrometer (MS), ranging in field strength from a 0.2 to 3.5 T. A schematic of this system is shown in Figure 3.8.

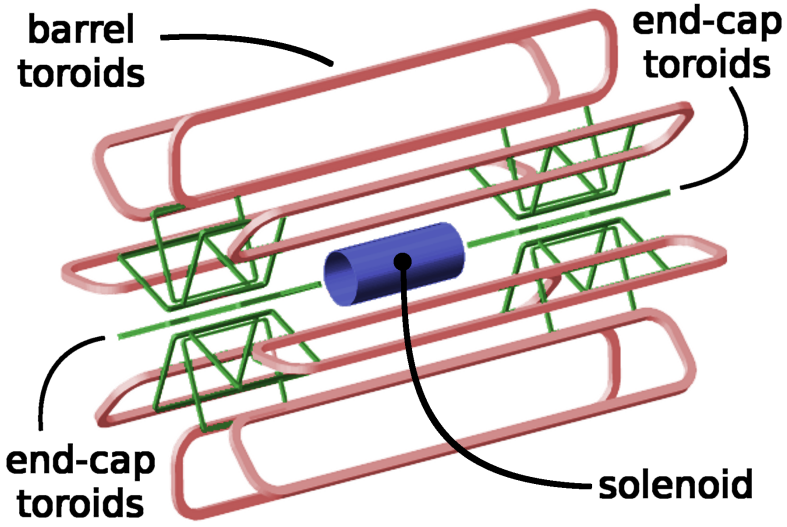

Figure 3.5: [196] Schematic of the ATLAS magnet system.

Inner Detector (ID)

The ATLAS Inner Detector (ID) is the innermost shell of the ATLAS detector subsystems and is constructed concentrically around the interaction point. At the interaction point a *pp* collision produces a high density of high energy radiation which disperses throughout the detector and beyond, meaning that the ID is exposed to the highest density of charged particle tracks. To provide accurate momentum and vertex reconstruction it is therefore required to provide a highly granular spatial resolution, provided by the silicon tracking detectors. These consist of a concentric cylindrical geometry in the barrel region, and end-cap disks perpendicular to the beam pipe; this layout is presented in Figure 3.6.

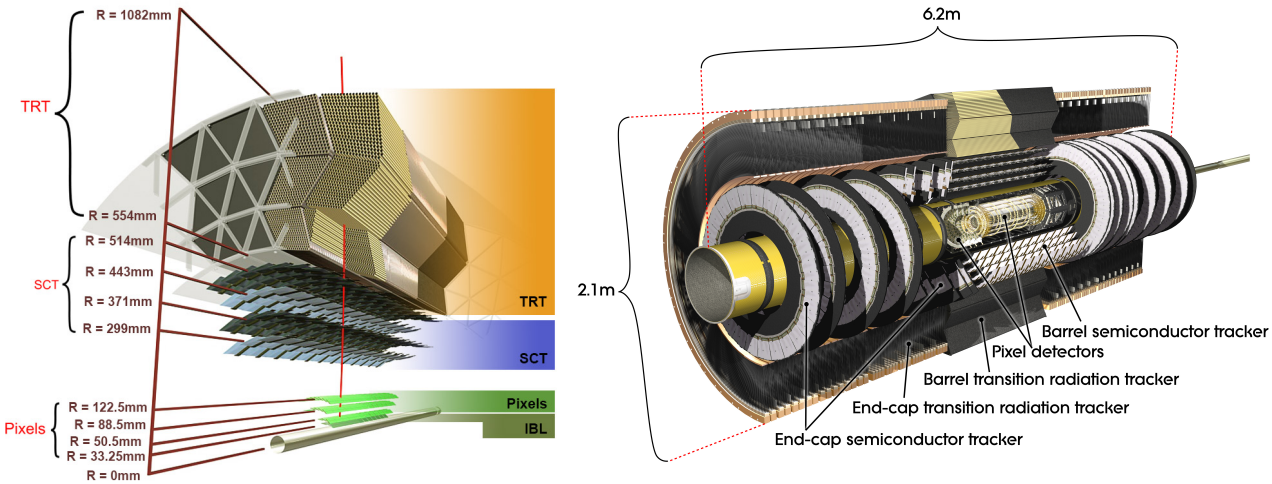

Figure 3.6: [197] Schematic of the ATLAS inner detector sub-systems, with a detailed breakdown of the silicone and TRT detectors in the barrel region also provided (right) [198].

This detector provides tracking resolution in the region $|\eta| < 2.5$. The highest granularity of the silicon detectors are the Pixel [199] and the Insertable B-Layer (IBL) [200] detectors, with a reduced granularity in the Semi-Conductor Tracker (SCT) [201]. These detectors are located in the barrel region around the vertex, and so are closest to the IP. Radially outwards from these is the Transition Radiation Tracker (TRT) [202], providing coverage in the region $|\eta| < 2$. This is a straw tube gaseous detector, providing both particle identification information, and a reduced granularity of spatial and momentum resolution.

The Pixel detector The Pixel detector consists of three barrel layers, and three end cap disks, with 1744 pixel modules between them. In total, this consists of 47 232 pixels, resulting in 80.4 million readout channels. Each pixel has a typical size of 50×400 μm^2, and thickness of 250 μm. The Pixel detector can provide an intrinsic spatial resolution of 10 μm in the $R - \phi$ plain, and 115 μm in the z (R) direction in the barrel (end-cap).

The Insertable B-Layer (IBL) The IBL was inserted during the Long Shutdown 1 (LS1).[7] The IBL is comprised of 14 carbon fibre staves, each containing 32 sensor modules with 26 880 pixels in each module, resulting in 12 million readout channels. Each pixel in the IBL has a cell size of 50×250 μm^2, providing a spatial resolution of 8 μm in the $R - \phi$ plain, and 40 μm in the z direction. The IBL upgrade improves the reconstruction of tracks and vertices, and leads to improved b-jet identification, and recovers any lost sensitivity in the Pixel detector due to radiation damage.

The Semi-Conductor Tracker (SCT) The SCT lies between the Pixel detector and the TRT. This consists of four layers of silicon strips in the barrel region, and nine disks in each end-cap region. In total the SCT consists of 4088 modules, each of which measures 6.36×6.4 cm^2, and has a pitch of 80 μm. Each sensor is only capable of providing position measurements in one direction, and as such, each module is formed of pairs of sensors, mounted back-to-back with an angular separation of 40 mrad. The SCT can provide an intrinsic spatial resolution of 17 μm in the $R-\phi$ plain, and 580 μm along the z (R) direction in the barrel (end-cap) region.

The Transition Radiation Tracker (TRT) The TRT is a gaseous detector that measures the ionisation of Xenon (Xe) or Argon (Ar) present in thin cathode tube drift chambers (straws). Thin anode wires present in the centre of each straw measures the drift current. These straws are parallel to the z-axis in the barrel region, and perpendicular to it in the end-cap. The TRT consists of 50 000 straw tubes in the barrel region, and 250 000 in each end-cap, each with a diameter of 4 mm. The TRT provides an intrinsic spatial resolution of

[7] Between operations of the LHC, the detector is shutdown, providing the opportunity to service and upgrade the detector. LS1 lasted 2 years, from 2013 - 2015, and was followed by the Run II operation of the ATLAS detector. In this time, the IBL layer was inserted, and has been in operation for the entirety of 13 TeV pp data taking.

$130\mu m$ in the $R-\phi$ plane, but provides no spatial measurement along the axis of the tube - in the z (R) direction in the barrel (end-cap) region. The ionisation of the gas present will occur when transition radiation is emitted. Transition radiation occurs when a charged particle crosses a boundary between two media of different refractive indices. The energy of such radiation is proportional to the Lorentz factor γ, which for a fixed momentum will be greater for lighter particles. As such, the TRT provides a useful discriminant in the isolation of the lightest charged particle; the electron.

Calorimetry Systems

ATLAS employs a series of sampling calorimeters, which collectively provide coverage in the region $|\eta| < 4.9$, as presented in Figure 3.7. The region $1.375 \leq |\eta| \leq 1.52$ is normally excluded as this is occupied by non-active materials required to cool and instrument the inner detector. The calorimetry systems can be sub-divided into the electromagnetic and hadronic calorimetry systems (EMCAL and HCAL), which between them, are designed to stop the passage of all particles, and in doing so to take a full measurement of their energies and positions. The exceptions to this are neutrinos and muons.

Electromagnetic showers induced in the EMCAL lose energy via bremsstrahlung and electron-positron pair production processes. This process is characterized by the radiation length, X_0, defined as either the distance at which the energy of particles has reached $1/e$ (the mean free path)[8] for electrons, or $7/9$ times the mean free path, for photons. Meanwhile hadronic showers, induced in the HCAL, typically lose energy via inelastic collisions with the dense material. These are measured in terms of their interaction length, λ, which is related to the inelastic interaction cross section of the material. It is important for the depth of each calorimetry system to greatly exceed λ and X_0 respectively, to ensure that the partonic showers are contained within the calorimetry system. λ is typically far larger than X_0 in high Z materials, meaning that the hadronic calorimeters must be much larger.

The resolution of these calorimeters is determined as a function of the total energy of the relevant partonic shower, in the form;

$$\frac{\sigma_E}{E} = \frac{N}{E} \oplus \frac{S}{\sqrt{E}} \oplus C, \tag{3.3.4}$$

where N is the noise of the measurement, S is a stochastic uncertainty and C is a constant, which reflects the non-uniformity of the detector, and $\oplus$ denotes the summation in quadrature.

[8] e here being the base of the natural logarithm: $e \approx 2.71828$

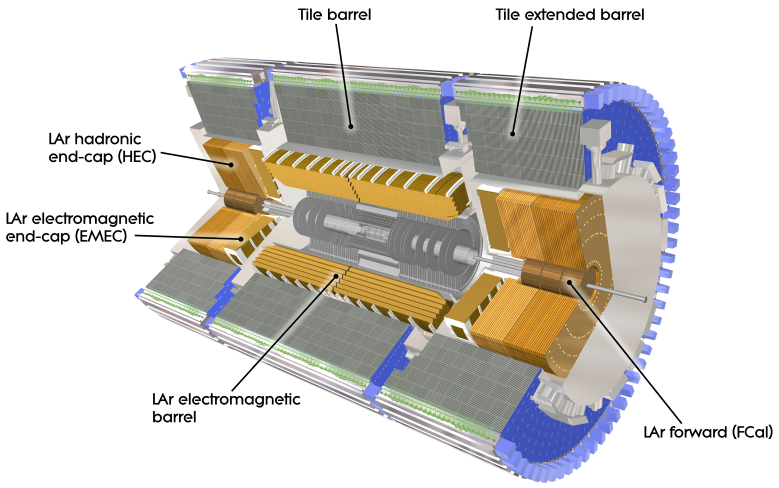

Figure 3.7: [203] Schematic of the ATLAS calorimetry systems, with components using LAr as the active medium shown in gold, and components using tile scintillators being shown in silver. The EMEC, EM barrel and copper plated FCal detectors make up the EMCAL, while the tile HEC and tungsten plated FCAL detectors make up the HCAL. Note that the EMCAL exclusively uses LAr as the active medium, while the HCAL uses a combination of LAr and tile scintillators.

In the electromagnetic barrel, electromagnetic end-caps, hadronic end-caps and forward calorimeters, ATLAS employs liquid argon (LAr) sampling calorimeters [204], which use LAr as the active medium and lead, copper or tungsten,[9] as the absorber material. Here, the absorber material induces an EM shower, which subsequently ionizes the liquid argon. Placed just before the innermost layer of these calorimeters is an active layer of liquid argon, to act as *presamplers* which can provide an estimation of energy loss "upstream" of the calorimeters (e.g. in the ID and solenoid magnet). Test-beam measurements have found the fractional energy resolution of the EMCAL to be;

$$\frac{\sigma_E}{E} = \frac{10.1\%}{\sqrt{E}} \oplus 0.2\%, \quad \text{and} \quad \frac{\sigma_E}{E} = \frac{12.1\%}{\sqrt{E}} \oplus 0.4\% \tag{3.3.5}$$

in the barrel [205] and end-cap [206] regions respectively.

In the outermost shell of the calorimetry system, in the barrel region, ATLAS employs the tile calorimeter system [207]. In this region, radiation density is lower, and reducing the width of the detector is a priority, which motivates the choice of this system. These calorimeters use scintillating plastic tiles as the active medium alternating with steel absorber. Here, ionizing radiation that passes through these tiles will induce ultra violet (UV) scintillation, where the amount of light produced is proportional to the energy deposited. Each tile module is then connected to wavelength-shifting fibers which guide the scintilla-

[9]The EMCAL primarily uses lead absorbers, but uses copper plates in the primary layer of the FCal, while tungsten plates are used in the latter two modules for hadronic measurements.

tion to photo multiplier tubes (PMTs), where a signal is recorded. The fractional energy resolution of the tile calorimetry system has been found to be;

$$\frac{\sigma_E}{E} = \frac{52.0\%}{\sqrt{E}} \oplus 3.0\% \tag{3.3.6}$$

while the fractional resolution of the hadronic end-cap and forward calorimetry systems are measured to be;

$$\frac{\sigma_E}{E} = \frac{70.6\%}{\sqrt{E}} \oplus 5.8\%, \quad \text{and} \quad \frac{\sigma_E}{E} = \frac{94.2\%\%}{\sqrt{E}} \oplus 7.5\%, \tag{3.3.7}$$

respectively.

Muon Spectrometer (MS)

The outermost layer of the ATLAS detector is the muon spectrometer (MS) system [208]. This consists of three successive layers termed "*stations*" in both the barrel and end-cap regions. The MS system employs a range of detector technologies; monitored drift tubes (MDTs) and cathode strip chambers (CSCs) are used to provide precision tracking,[10] while resistive plate chambers (RPCs) and thin gap chambers (TGCs) are chosen for triggering due to their fast response times. It is expected that all other interacting particles will have been fully adsorbed by the preceding calorimetry systems, and as such, any interacting particle observed in the MS is expected to be a muon.[11]

There are 1150 MDTs in the MS, which provide tracking information with a spatial resolution of 35 μm in the z-direction for each MDT. The CSCs provide precision tracking measurements in the end-caps, where the rates are expected to be larger. These provide a spatial resolution of 40 μm in R and 5 mm in ϕ. Momentum is then reconstructed from the curvature of muonic tracks due to the magnetic field. Curved tracks are detected as a circle segment, with a sagitta of the segment that is inversely proportional to the p_T of the muon. As such, the momentum reconstruction of the muons develops as a function of the p_T, with the fractional resolution,

$$\frac{\sigma_{p_T}}{p_T} = 3\%. \tag{3.3.8}$$

at around 100 GeV. At $p_T = 1$ TeV, this increases to 10%.

Due to the size of these detectors, understanding their relative alignment is crucial for the accurate reconstruction of a muon's momentum. An initial calibration of the precision

[10] Where CSCs are used on the innermost end-cap wheel, as they have a higher rate capability and better time resolution.

[11] The reason muons are not adsorbed by the EMCAL is due to their large mass (muons are 200x heavier that electrons). Electrons interact with the EMCAL due to Bremsstrahlung (breaking) radiation, which depends on the 4th power of the boost factor, γ. For equal energies, the boost factor of the muon will be about 200 times smaller than that of the electron (tauons would also not interact via Bremsstrahlung, but as they are unstable, they will almost always decay prior to the calorimeter).

chambers was first evaluated using a sample of cosmic ray tracks with toroid magnets turned off. However the muon chambers may then move by a few mm when the magnet is switched on. As such, 5,800 precision-mounted optical alignment sensors are employed to monitor the alignments of the MDTs. Additionally, pp collisions have been run with the toroid magnet switched off to validate the alignment system.

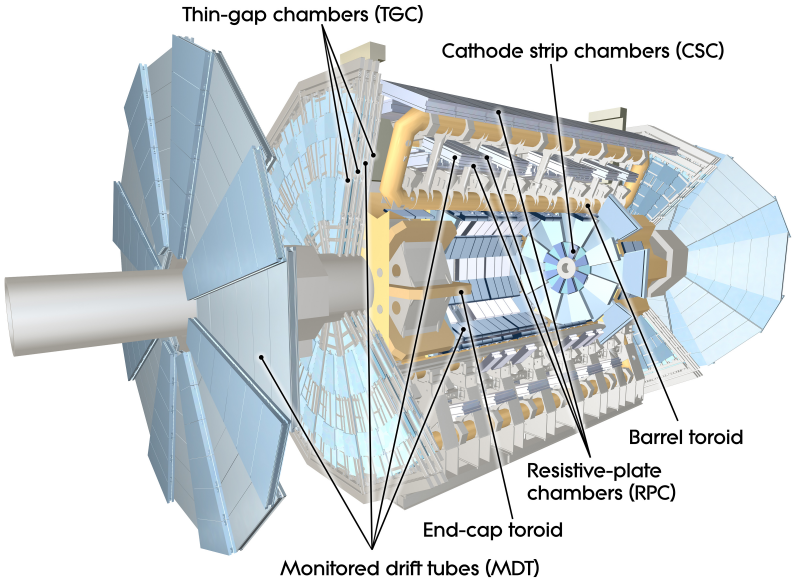

Figure 3.8: [209] Schematic of the ATLAS muon spectrometer

Trigger and Data Acquisition (TDAQ)

The low bunch spacing achieved by the LHC means that ATLAS records a new bunch crossing every 25 ns, leading to around 40 million bunch crossings per second. With an average Run II pileup of $\langle\mu\rangle = 33$, this means over 1 billion pp collisions are recorded by the ATLAS detector per second. With each data event requiring around 1.5 megabytes to store, the bandwidth and storage capacity available to the ATLAS experiment is significantly too small to keep all events. As such, the ATLAS Trigger and Data Acquisition (TDAQ) [210] system comprises a multi-level event triggering system designed to preserve only high-quality data that is of interest, where each successive layer of the trigger system results in a further reduction to the volume of data recorded. The first trigger is the hardware based Level-1 (L1) [211] trigger that reduces the incoming event rate by a factor of 400 [212]. This hardware based trigger uses custom electronics purpose built into the detector itself. These include the L1Calo trigger, the L1Muon trigger and the L1 topological (L1Topo) trigger [213] as well as trigger signals from several detector subsystems such as the Minimum Bias Trigger Scintillators (MBTS) [214] the LUCID Cherenkov counter [190] and the zero-degree calorimeter (ZDC) [215]. From these inputs, a trigger decision is formed by the Central Trigger Processor (CTP) [216] with a latency of just 2.5μs. This decision uses a

reduced granularity of the ATLAS detector information to make a trigger decision based on the presence of events containing high-p_T objects, or large amounts of E_T^{miss}.

Following a triggering decision from the L1 triggers, detector read-out (initially stored in on-detector pipeline memories) is passed to the data acquisition (DAQ) system. This is then responsible for the read-out of the detector, recording raw data to storage and providing information to successive triggers. The Regions of Interest (ROI) that reflects the decision of the L1 trigger object, will then be passed on both to a software based trigger system and to the DAQ system. The L1 ROIs are combined with additional data from the detector, such as tracks and calo clusters, allowing for a higher level trigger decision, that is processed in the software-based Higher Level Trigger (HLT) [217]. Here, a trigger decision is achieved using the L1 ROIs, as well as a full reconstruction of final state objects applying ATLAS reconstruction. This system is designed to make a trigger decision within a few hundred milliseconds. In the HLT, ATLAS reconstruction tools are applied, performing a full reconstruction of the event. Events can then be classified into physics streams, the main streams, developed and maintained by the combined performance (CP) groups, these being E/gamma, Muons, Tau and Jet/Etmiss. Fully processed events are then stored on CERN data storage at a maximum rate of 1 kHz, with each event having a data-size of around 1.5 MB. Events not passing the HLT criteria are then removed from the read-out system (ROS). A visualisation of this decision flow is presented in Figure 3.9.

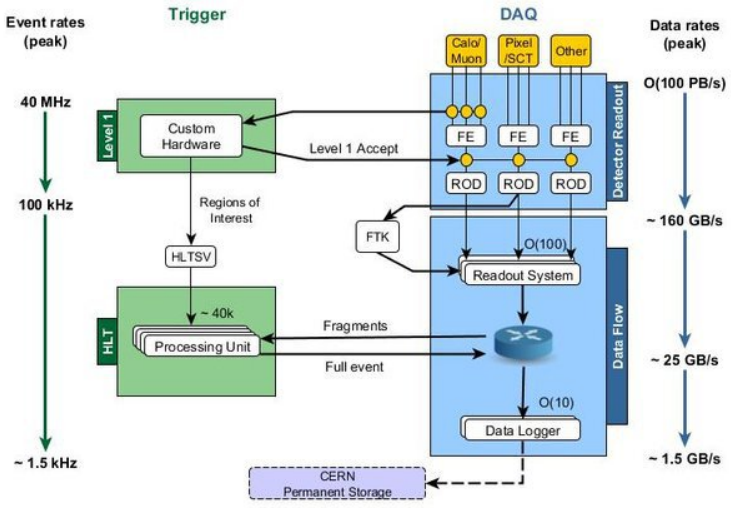

Figure 3.9: [218] ATLAS TDAQ System in Run 2.

Chapter 4

Monte Carlo Generators and Simulated Data

High energy physics (HEP) experiments attempt to make highly precise comparisons of experimental data against theoretical predictions. To do so, a highly complex simulation of both the known SM processes as well as the novel BSM model that is being tested, is required. This simulation of particle interactions and their evolution through the ATLAS detector is a complex, multi-faceted challenge.

This Chapter shall present the steps involved in simulating high energy proton-proton collisions. Section's 4.1 and 4.2 first outline the general work-flow of MC event simulation. Section 4.3 then provides a discussion of some of the state-of-the-art MC event generators. Finally, Section 4.4 provides a detailed discussion of the nominal SM MC samples used in ATLAS, and Section 4.5 documents a study performed in testing new methods to simulate the top-pair production process which also constitutes a significant background for the search presented in this Thesis.

4.1 Event Simulation

Predictions can be made of the final state products created in hard scattering interactions by implementing perturbations into a theoretical model of the unbound interactions of incident partons. From this, we can determine vectoral representations of the interacting partons by calculating the Matrix Element (ME) of the scattering process at a given order of perturbation. The decay products then undergo complex phase-transitions that bring them into the non perturbative regime. This hadronization of the final state constituents and any subsequent decays into long-lived particles that may go on to interact with the ATLAS detector is described by dedicated Parton Showering (PS) algorithms. On the resulting objects, we must then implement a simulation of the ATLAS detector, accounting for its geometry and its interaction with the final state objects. It is then, from the information re-constructed after detector interactions have been simulated, that we have meaningful

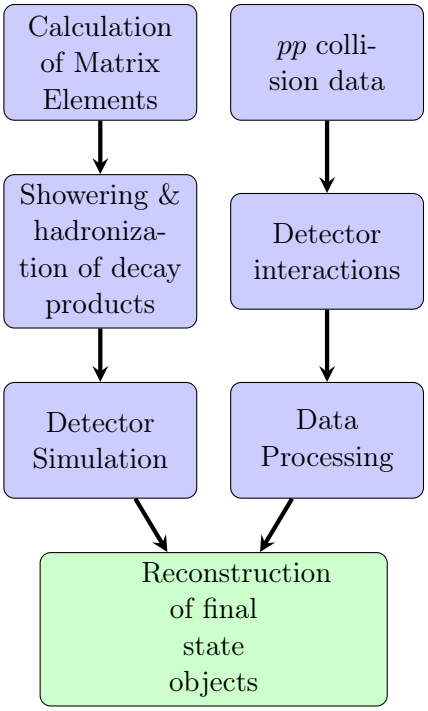

Figure 4.1: Diagrammatic representation of the sequence of steps involved in the simulation of MC events and recording of ATLAS data, to the equivalent states, as used in physics analysis.

event information which can be used in direct comparison to ATLAS data. This sequence of steps undergone in the simulation of events is illustrated in Figure 4.1.

The final state objects observed by the ATLAS detector do not always directly correspond to the decay products of the hard interaction. These partons will first undergo the process of hadronization as discussed in Section 1.6.2. This describes the formation of a particle shower, in which many, highly collimated collections of hadrons are produced, leading to clusters of energy deposits, collectively described as jets.

In a single pp collision occurring in the ATLAS detector, constituent partons from each of the incident protons interact. These interactions are often dominated by soft, low p_T interactions, but occasionally hard scatter collisions occur. It is important in ATLAS simulation to consider the soft terms produced in a pp collision to accurately assess the impact on physics backgrounds and detector performance. In most cases, the interaction of a single parton from each proton mediates a significant portion of the momentum transfer of the pp collision. However, multiple parton interactions (MPI) can occur, in which multiple, separate, 2-body interactions take place between constituent partons of the two incident protons. In such collisions, the sub-dominant interaction is often orders of magnitude lower in p_T than the leading interaction, however such processes still constitute an observable signature in the ATLAS detector. These additional processes occurring in the pp interaction

are denoted as part of the Underlying Event (UE). This is an umbrella term for all of the particles produced in a hard scattering event. This includes contributions from processes such as the beam-beam remnants (BBR), and the particles arising from MPIs. The emission of such surplus radiation can lead to complex detector signatures, with many processes originating from the same pp interaction. A depiction of the extent of the complexity of the UE is shown in Figure 4.2, where, as depicted in red, two gluons interact to form a $t\bar{t}$ pair and a Higgs boson, with many additional final state partons produced through initial state radiation (ISR), final-state radiation (FSR) and soft beam remnant processes as shown by the purple and blue elements of the schematic.

4.2 The Event Generation Workflow

4.2.1 Matrix Element (ME) Calculations

As illustrated in Figure 4.1, the process involved in simulating pp collision events begins with a theoretical determination of the cross-section for each process being considered. This cross-section is proportional to the square of the hard scattering matrix element (ME) of the specific process. A matrix element can be thought of as the summation of all Feynman diagrams contributing to the decay process. The accuracy of this calculation is often improved by considering the effects of increasing orders of perturbation added to the LO diagram. These consider the contribution of additional corrections to the tree-level diagram that constitute distinct processes that must also be considered in the calculation of the ME. As each additional process inherently introduces additional vertices and often massive particles, these processes are heavily suppressed, leaving the LO calculation to often serve as a good initial approximation. The calculation of such higher order corrections can now be efficiently computed using modern MC event generator software. However, as the order of perturbation is increased, there is an increasing number of higher-order effects such as divergences between real and virtual corrections, as well as soft and collinear effects that may lead to singularities in the ME calculation. These must all be corrected for by the generator, which is often non-trivial. The problem is compounded by an increasing number of final state constituents, as this vastly increases the number of contributing diagrams.

4.2.2 Parton Showering Algorithms (PS)

The calculation of MEs provides a prediction of the differential cross-section of the underlying hard scattering event for a given physical process at a fixed order of perturbation. As such, this is limited to a description of the, often un-stable and short-lived, leading final state partons. The hadronic final states observed at ATLAS arise from the calorimetric absorption of the energy of incident colour-neutral hadrons. The formation of these hadrons brings us beyond the perturbative regime of QCD (pQCD), and as such the techniques used to determine tree-level MEs are no longer valid when describing the formation

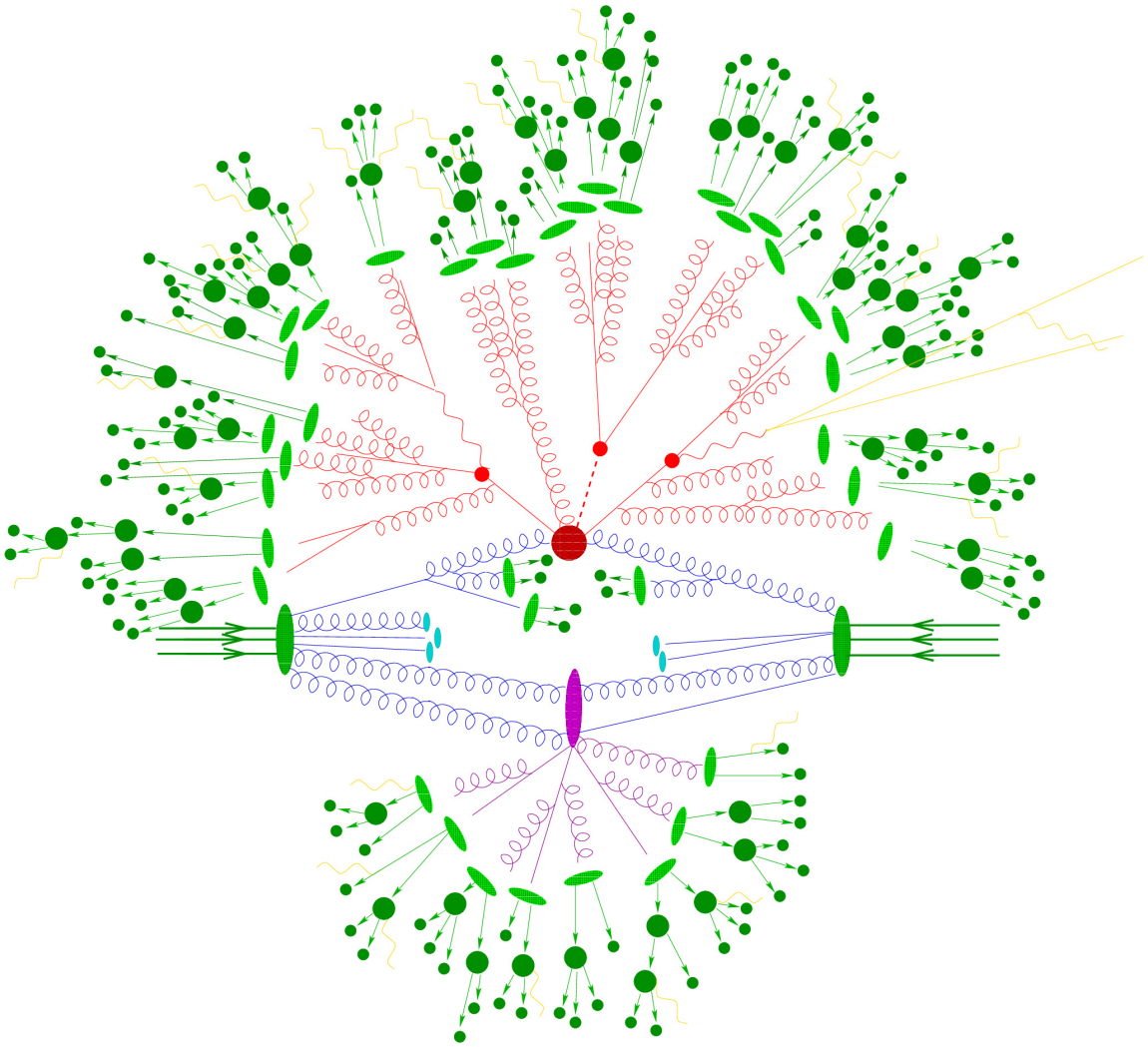

Figure 4.2: [219] Diagram of the total event composition of the UE for a MPI pp collision. Here shown as considered by the SHERPA event generator, when simulating the $gg \to t\bar{t}h$ process. The partonic composition of the incident protons is represented by the blue lines. Those terminating in blue ovals represent the beam remnants. The hard interaction is represented by the large red circle, and is subsequently followed by the decay of both top quarks and the Higgs boson (small red circles). The remaining red lines represent the additional hard QCD radiation, as simulated by the PS algorithm. Also shown is a secondary interaction, represented in the purple oval. The final state particles then hadronize, as shown by the light green circles, with hadrons shown as dark green circles. Photon radiation can also occur at any stage, and is shown in yellow.

of these states.

To be able to simulate such final states, we must instead adopt a separate approach. This begins by developing PS algorithms. These attempt to describe the evolution of final state objects, and account for the multitude of soft and collinear emissions, reconciling these elements into the formation of clusters of colour-neutral objects that may be directly observed. This is achieved by determining the probability amplitudes of sequentially and recursively splitting the initial- and final-state partons from one to two body states. The calculation of these probabilities can be performed using the DGLAP equations. The probabilities determined using this method provides an approximation of the real QCD Bremsstrahlung [220][1] emissions at each order in perturbation theory, and are accurate to leading logarithmic order. They work by considering a parton, produced at a scale t' and then determining the scale $t < t'$ at which it should branch into two daughter partons. There are several choices of scale, and this choice helps distinguish the many available PS algorithms available, however all are proportional to the invariant mass of the branching. In order to limit the probability of branching to ≤ 1 final state parton, it is necessary to modify the DGLAP equations, by introducing the probability of a parton *not* splitting within a set "evolution" scale, $\Delta(t, t')$, which is given by the Sudakov form factor [221].

In this way, we have evolved the high p_T particles from their initial states down to the non-perturbative regime, onto which we can apply a universal hadronization model independent of the hard scattering process. We denote this p_T scale as the hadronization scale, which then defines the lower bound on the implementation of the PS technique. It is here that the transition into the colour-neutral hadronic final states that are observed in the detector will occur. These hadronization models state that partons with virtualities[2] that are of the same order as this scale are considered to enter the non-perturbative regime, and must be described using hadronization models.

4.2.3 ME+PS (Matching and Merging)

The combination of matrix elements, calculated to a fixed order of perturbation, to the approximation of pQCD using the probabilistically determined parton showers, is a combination of two fundamentally distinct approaches to evaluating pQCD. There exist two main approaches to the combination of ME and PS, termed "matching" and "merging". The key difference is that matching methods simulate the entire phase space using the PS, but correct for the hardest emission using the ME. Meanwhile merging methods separate the hard and soft production, employing the predictions of the ME for emissions above a certain scale, and the PS below it.

The primary issue in the combination of higher order ME calculations to Shower Monte

[1] Bremsstrahlung is a Germanic term that roughly translates as "braking radiation". As the name suggests, it is the radiation emitted by a charged particle, decelerating as it interacts with matter.

[2] Taken as the square of there virtual mass, q^2, a measure used to describe how off shell the virtual particles are.

Carlo (SMC) simulations is in the appropriate treatment of the soft and collinear emissions. These can be reproduced in both the calculation of the hard ME as well as in the higher-order corrections provided by the SMC. This can lead to a double counting of NLO events, where events which are generated at LO+PS can also be recreated in NLO calculations. As such, the partons of the hard ME must be correctly combined with the PS by matching the hard and soft emissions. One approach to solve this issue of double counting, employed by the `MC@NLO` program [222], is to subtract the approximated cross section which is implemented in the SMC, from the exact NLO cross section. This subtraction scheme is highly SMC dependent, and can lead to the introduction of negative weights. Therefore an alternative method is developed, termed the POWHEG (Positive Weight Hardest Emission Generator)-method [223]. This is a multiplicative method, which determines NLO MEs that can be interfaced with any SMC. As the name suggests, this uses positive weights.

An additional method termed the "CKKW" algorithm [224, 225] that is used largely by the SHERPA [219] event generator works by separating the phase space of the NLO parton emission into either the hard contribution of jet production, or a softer regime of intra-jet evolution. The separation of these regimes is based on a $k_\perp$-type jet measure [226, 227]. In this way, the MEs for the different parton multiplicities describe the production of a corresponding number of jets, whereas the parton shower is constrained such that it does not produce any additional jets. Finally, a similar approach termed the "CKKW-L" method [228–230] has been developed which uses a dipole shower, as opposed to the more traditional parton cascade, to describe QCD radiation beyond fixed order. More details on this can be found in Appendix A. In this way we can merge the NLO precision of the matrix elements to the Leading Log approximation (LL) of the SMC.

4.2.4 Detector Simulation

Once the hard ME has been generated and effectively combined with the PS, the MC generated events will provide accurate theoretical predictions of the topology, kinematics and production rates of the targeted process shortly after the pp collision. Following the ordering described in Figure 4.1, we see that this information must now be passed into a sophisticated simulation of the ATLAS detector [231]. This is implemented in the GEANT4 (GEometry ANd Tracking) [232, 233] software, which describes the interactions of particles with the detector. This simulation reproduces the entire process of event detection in ATLAS, by reproducing the interactions of the final state particles with the volume of the detector. This is performed using a detailed description of the geometry and composition of the ATLAS detector, which imposes these constraints on the simulation. The output of this replicates the digitization of energy depositions into voltages and currents, and can then be directly compared to the raw data recorded by the detector. These digitized detector responses are then outputted into a Raw Data Object (`RDO`). The `RDO` is then reconstructed into its particle configuration using the same reconstruction algorithms that are used when

processing observed ATLAS data.

This precise simulation of all detector responses is extremely computationally expensive, as shown in Figure 4.3. As such, a parametric version of the calorimeter response simulation, FastCaloSim, has been developed [234, 235]. This uses a simplified geometry of the ATLAS calorimeters and a parametric model of the complex particle-material interactions and showers that is based on the Geant4 simulation of single particles in a fine grid of particle energies and directions. This simulation is then interfaced with a full simulation of the ID and muon system in Geant4, and termed "ATLFASTII". This parameterisation of the calorimeter simulation can reduce the computational load by 1 - 2 orders of magnitude, and yet still provides a highly precise replication of detector interactions.

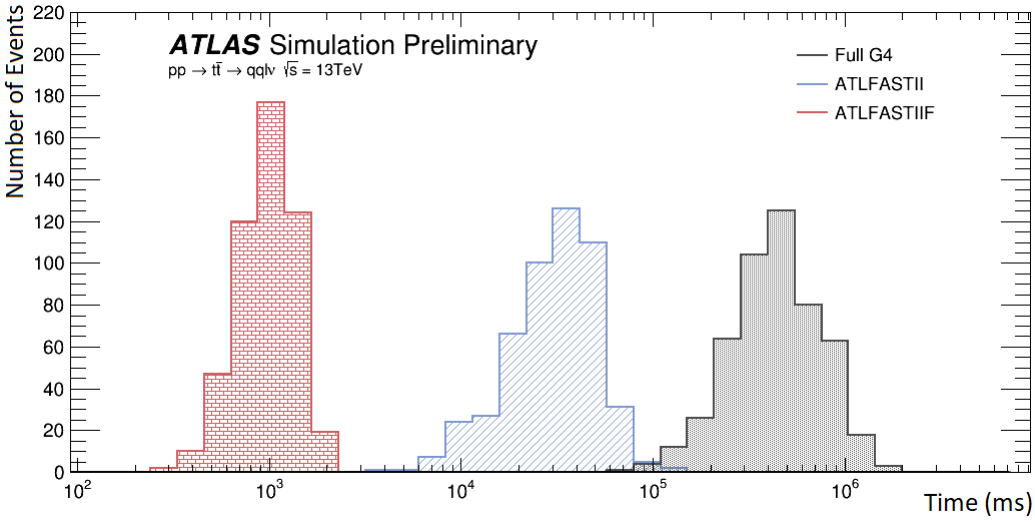

Figure 4.3: [236] Comparison between Geant4, ALTFAST-II and ALTFAST-IIF (this is a method to further reduce the computational load by combining the FastCaloSim with Fast Tracking Simulation) CPU performance of event processing time for a sample of semi-leptonic $t\bar{t}$ scattering events.

4.3 MC Generators

There exists a plethora of dedicated Monte Carlo event generators capable of simulating SM and BSM processes under the conditions produced at the LHC. Of note are four General Purpose MC generators (GPMC); Powheg-Box, Sherpa, Pythia and Herwig. Of these, the Pythia and Herwig generators have applications as both GPMC and SMC generators, that can provide sophisticated PS functionality to other ME generators. Also described is the MadGraph5_aMC@NLO generator, which is used in the simulation of various background and signal processes for the analysis documented in Part III.

4.3.1 SHERPA

SHERPA (Simulation for High Energy Reactions of PArticles) [219, 237–240] is able to quickly interface a range of NLO-accurate matrix elements for up to 2 partons, and LO-accurate matrix elements for up to 4 partons through interfacing with the Comix [237] and OPENLOOPS [238, 241, 242] libraries or to generate ME's via its matrix-element generator, AMEGIC++ (A Matrix Element Generator in C++) [243]. SHERPA consistently combines the ME to the PS following the schema of Catani, Krauss, Kuhn and Webber (CKKW) [224, 225], as is discussed in Section 4.2.3. The default shower generator for SHERPA is APACIC++ [244, 245], which evolves the PS with decreasing parton virtuality, and ordering of the opening angles in subsequent branchings by default.[3] Full spin correlations are accounted for in the decay of primary hadrons. The hadronization model used when constructing the parton shower in SHERPA is the AHADIC cluster model [246]. SHERPA evaluates MPI's such that PS produced in sub-leading interactions evolve independently.

4.3.2 PYTHIA

PYTHIA [247, 248] simulates hadronic events, interfacing to around 300 hard-coded $2 \rightarrow 1, 2, 3$ scattering processes at LO. Event generation is performed with full spin correlations accounted for in the primary hadronic decays. PYTHIA simulates the UE as a MPI, accounting for both the impact parameter between protons, and energy sharing between multiple partons in the beam remnants. The hadronization of particles in the PS is determined following the Lund string model [50, 249]. PYTHIA is capable of simulating both initial- and final-state parton showers. PYTHIA evolves these in order of a decreasing parton virtuality scale, Q^2, which provides a time ordering of the cascade. In addition, each splitting can be ordered in terms of the mass (m^2) or transverse momenta, $k_\perp$. PYTHIA 6.428 [248] is often used in conjunction with other generators to provide the PS.

4.3.3 HERWIG

HERWIG (Hadron Emission Reactions With Interfering Gluons) interfaces to a number of $2 \rightarrow n$ ME's of spin correlated SM and BSM hard scattering processes, as well as having the functionality to generate ME's using FEYNRULES outputs [167, 250]. The most recent iteration of HERWIG (HERWIG7) enables the use of either `MC@NLO`- or POWHEG-like combination of the ME and PS. HERWIG uses a QCD cluster model [51] of hadronization. The evaluation of the UE can be interfaced specially to a dedicated software package for the simulation of multiple parton interactions, JIMMY [251, 252].

[3] Although $k_\perp$ ordering is also available via the CSS SHERPA parton showering [239].

Process	Generator	PDF set	PS and fragmentation/hadronisation	UE tune	Cross-section order
Top pair ($t\bar{t}$)	Powheg-Box v2 [256]	NNPDF 3.0 [260]	Pythia 8	A14	NNLO+NNLL [247]
Single-top: t-channel	Powheg-Box v1	NNPDF 3.0	Pythia 8	A14	NNLO+NNLL [261]
Single-top: s- and Wt-channel	Powheg-Box v2	NNPDF 3.0	Pythia 8	A14	NNLO+NNLL [262, 263]
W+jets, Z/Drell–Yan+jets	Sherpa 2.2.1 [219, 237–240]	NNPDF 3.0	Sherpa	Default	NNLO [264]
Diboson	Sherpa 2.2.1 – 2.2.2	NNPDF 3.0	Sherpa	Default	NLO [219]

Table 4.1: List of generators used for the different background processes. Information is given about the underlying-event (UE) tunes, the PDF sets and the perturbative QCD highest-order accuracy (NLO, NNLO, and NNLL) used for the normalisation of the different samples.

4.3.4 MadGraph5_aMC@NLO and Powheg-Box

The MC@NLO [253, 254] and Powheg (POsitive Weight Hardest Emission Generator) [223, 255] programs are systems designed to handle the incorporation of NLO QCD matrix elements consistently into a parton shower Monte Carlo program. This improves the prediction of production rates, and the description of the hard parton emission. A description of the two methods is provided in Section 4.2.3. The Powheg-Box [256, 257] method constructs the Powheg implementation of a NLO process, given the hard ME's (which can be provided from an external ME provider), and interfaces to a shower MC program. Finally, the MadGraph5_aMC@NLO [258] generator is an on-the-fly (OTF) ME generator, which uses MadGraph to generate hard MEs, and implements the MC@NLO method of PS matching at NLO.

4.4 Standard Model MC Samples

In the analysis detailed in Part III, MC simulated events are used to evaluate the properties of both signals and backgrounds. A summary of the event generators used in the simulation of SM background processes for this analysis are summarised in Table 4.1. Shown are the accuracy of theoretical cross-sections, the underlying-event parameter tunes, and the PDF sets used in the simulation of these samples. For the simulation of the properties of the b- and c-hadron decays in all samples (except those generated using Sherpa [219, 237–240]), the EvtGen v1.2.0 [259] program was used.

A more detailed discussion of each sample follows:

- For the production of V+jets samples ($V = Z, W$), events were simulated using the Sherpa 2.2.1 generator. Here, the number of expected events in this sample is then rescaled using cross-sections calculated at NNLO [264]. To compensate for the diminishing cross-sections of such processes in the high p_T region, it is useful to split the production of these samples into separate "slices", using a cut at the generation level, on the variable $\max(H_T\ ,\ p_T^V)$ (where p_T^V is defined as the transverse momentum of the true lepton pair from the decay of the V boson, and H_T is the transverse momenta of the sum of all jets and leptons in the event). The sliced samples are then

further filtered into further sub-samples based on the presence of a heavy flavour bottom or charmed hadron in the final state. For the Z→ $\tau\tau$ samples that have the highest cross section, an additional event filter is applied to sub-divide these samples based on the leptonic or hadronic decays of the τ leptons. The Z sample includes contributions from off-shell Z production, allowing for final states with a large invariant mass of the dilepton system. The Z+jets events are categorised into three processes $Z+bX$, $Z+cX$ and Z+light. These are defined respectively as events with one or more reconstructed jets that contain a true b hadron (within a cone of radius 0.4), a c hadron or neither.

- Generation of the $t\bar{t}$ and single-top samples was performed using the POWHEG-BOX v2 generator, using the NNPDF 3.0 PDF interfaced to PYTHIA 8 [265] to provide the PS. The PS used the PERUGIA2012 [266] tune with CTEQ6L1 [267] PDF for the underlying event descriptions. The mass of the top quark is set to $m_t = 172.5$ GeV. In accordance with the di-leptonic final state of the considered model, only the di-lepton $t\bar{t}$ samples are considered. The cross section of $t\bar{t}$ is known to NNLO in QCD including the re-summation of next-to-next-to-leading logarithmic (NNLL) soft gluon terms. The reference value used in ATLAS is calculated using TOP++ 2.0 [247]. The parameter HDAMP [268], used to regulate the high-p_T radiation (above the scale defined by the HDAMP parameter) in POWHEG, is set to m_t for good data/MC agreement in the high p_T region [269]. Each process of single-top (t-channel, s-channel and Wt-channel) is generated separately. The cross section of single-top is calculated with the prescriptions in Ref. [261, 262].

- For the generation of the fully (semi) leptonic diboson processes (WW, WZ and ZZ), the SHERPA 2.2.2 (SHERPA 2.2.1) generator was used. These events were generated using the NNPDF 3.0 PDF set and by merging NLO and LO calculations as described in Ref. [270]. The diboson processes are normalised directly to the Sherpa prediction.

- Finally, minimum bias events generated with PYTHIA 8 are overlaid to model the effects of the pileup for all simulated events. MC samples with different numbers of pile-up interactions are re-weighted to match the conditions observed in each dataset between 2015 and 2018.

4.5 Additional Studies on $t\bar{t}$ Modelling with HERWIG7

In addition to the aforementioned MC samples, work was performed in studying the modelling of the $t\bar{t}$ process with HERWIG7 [271–273], with the aim of validating it for a future bulk MC sample production for ATLAS analysis. HERWIG7 was used to test the production of merged, multi-leg $t\bar{t}$ samples at the next-to-leading order accuracy, using it's new MATCHBOX [274] package, which enables the combination of LO and NLO ME's to the

PS in a fully integrated framework. The full documentation of this task is presented in Ref. [275].

Merged multi-leg MC samples at NLO accuracy have become baseline samples for many important processes in ATLAS. Problems arise, however, when one tries to combine these calculations, made at a fixed order of perturbation, to the approximation of pQCD used by the PS algorithms, as these represent two fundamentally distinct approaches to the evaluation of pQCD. As discussed in Section 4.2.3, there are two techniques developed to achieve the consistent combination of the ME and PS, termed "*matching*" and "*merging*". Essentially, matching techniques use the PS to evaluate the entire phase space, but correct for the hardest emission using the ME. The other technique, merging, is the subject of this study. Here, a Merging Scale (MS) is defined ($\kappa_{\perp MS}$), above which, exact matrix elements for the hard process are generated. A re-weighting is then applied to predict the PS correctly. The PS is then added below the $\kappa_{\perp MS}$ scale.

There is a limited set of MC generators that are able to perform this merging of the multi-leg matrix elements to the hard cross-section. Currently, multi-jet merging has been made available via an implementation of the CKKW-L scheme, as well as the unitarised matrix element + parton shower merging (UMEPS) [276] techniques. This has also been comprehensively extended by UNLOPS [228] merging (which provides multi-jet merging at NLO) and FxFx merging [277]. Most recently, this functionality has also been made available within Herwig7 via the Matchbox feature using a multi-jet merging algorithm detailed in Ref. [278], which is based on an improved, unitarised merging prescription set out in Ref. [279].

In order to perform the full calculation of cross-sections, Matchbox requires plugins to provide the tree level and one-loop amplitudes required for each process. For the purposes of the studies described herein, these plugins are used to provide both tree-level amplitudes (achieved using the MadGraph provider) and tree-loop interferences, by choosing one of the supported one-loop amplitude providers. Herwig7 currently supports interfaces to the GoSam [280], MadGraph, NJet [281], OpenLoops and VBFNLO [282] one-loop providers. This study focuses on the usage of the MadGraph and OpenLoops amplitude providers.

Currently, only Catani-Seymour dipole showering [239] is supported within the Matchbox framework. As a result of this, it is only possible to interface with a `MC@NLO` (subtractive) matching method. The design of this method emulates the design of a subtraction based NLO QCD cross-section calculation.

As stated in Section 4.2.3, merging methods separate the hard and soft production processes; employing the predictions of the ME for emissions above a certain scale, and the PS below it, where the scale separating these two regions of phase space is a controlled parameter in the merging procedure applied. The combination of the higher order ME calculations with the SMC must then be handled correctly to avoid the potential double

counting of soft and collinear emissions. Subtractive methods such as the MC@NLO procedure require the simulation of events that are negatively weighted to counteract this double counting. This method can be computationally expensive however, as it reduces the effective number of simulated events, requiring the simulation of many more events to compensate for those that are negatively weighted.

In the calculation of the hard ME, two forms of divergent processes must be prevented from distorting the cross-sectional calculation to either "0" or "∞". These can be either; ultraviolet (UV) divergencies that arise from large momentum of the loop corrections, or infrared (IR) divergencies, which arise from either particles reaching zero momenta,[4] or processes in which massless particles radiate other massless particles.

UV divergencies can be controlled by varying the strong coupling constant α_S as a function of the "*renormalisation*" scale (μ_R). Similarly, the IR divergencies arising from the radiation of massless particles from other massless particles can be controlled by varying the parton distribution and fragmentation functions as a function of a "*factorisation*" scale (μ_F). These parameters, μ_R and μ_F are therefore spurious parameters that are introduced to avoid potential divergencies from arising when restricting the ME calculations to a finite order or perturbation. It is expected these divergencies should begin to cancel at higher orders of perturbation but the effect is still expected to be non-negligible even at the next-to-next-to-leading order. Different choices arise for how to assign the scales μ_R and μ_F, such as fixing them to a physically meaningful value that is relevant to the process being simulated. A discussion of the choice of μ_R and μ_F in this study is presented in Section 4.5.1.

This study examines the production of merged multi-leg $t\bar{t}$ Monte Carlo samples at NLO accuracy, generated using Herwig 7.1.3, where the merging of the multi-leg matrix elements to the hard cross-section is performed using the Matchbox framework of Herwig7.

The key aims of this study are:

- Write base fragments and job options for NLO-merged $t\bar{t}$ in Herwig7.
- Investigate the speed of event generation and the fraction of negative weights.
- Explore and validate samples against ATLAS data using Rivet.

To do this, MC event samples are generated, as is documented in the Appendix A.3. These samples are then analysed using three different Rivet (Robust Independent Validation of Experiment and Theory) [285] routines, which are documented in the Appendix A.1. Rivet is an open source repository intended for the preservation and distribution of developed analyses. Rivet facilitates the comparison of measurements and theoretical calculations, within a defined fiducial region. Rivet can therefore be used for rapid "on-the-fly"

[4]However this type of correction is predicted to cancel by the Kinoshita-Lee-Nauenberg (KLN) theorem [283, 284], which states that IR divergencies coming from loop integrals will be canceled by IR divergences coming from phase space integrals.

comparisons of novel MC simulations to ATLAS data through a developed ATLAS analysis. Because of this, RIVET has many applications in tuning and developing MC generators, and in testing novel theoretical models. In this study, RIVET routines have been used to make comparisons to data and to access details of the performance of the HERWIG generator. The nominal samples considered are documented in Appendix A.2, and are also the same as some of the samples documented in Section 4.4.

4.5.1 Dedicated Studies

NLO Jet Multiplicity and total cross-section

For ATLAS standards, it is required that nominal $t\bar{t}$ samples replicate the underlying process to a high level of precision. However, to produce samples at higher orders of perturbation above the Born process requires an exponentially increasing amount of computations. To be competitive with already available samples used within ATLAS, it is required to simulate events to NLO accuracy, and to be able to merge at least 2 additional jets to the ME. This must be achievable with minimal consumption of ATLAS computing resources, and as such it is essential to keep the number of negatively weighted events to a minimum.

Table 4.2 reports the cross-section of the produced samples. These values are taken from the MC_XS RIVET routine, and are calculated with an average error of the order of 1%. The study compares the different multiplicities of NLO merged jets, and tested production with two different combinations of matrix element provider (MADGRAPH or OPENLOOPS). The generation of these samples uses the "`TopPairMass`" for setting the re-normalisation (μ_R) and factorisation (μ_F) scales. This sets these scales based on the momentum of the top and anti-top quarks, p_t ($p_{\bar{t}}$), as outlined in Equation 4.5.1.

$$\mu_R^2 \;=\; \mu_F^2 \;=\; (p_t \;+\; p_{\bar{t}})^2 \tag{4.5.1}$$

An alternative scale option is also provided in HERWIG, the "`TopPairMT`". This sets the re-normalisation and factorisation scales based on the transverse mass of the top and anti-top quarks, $m_{T,t}$ ($m_{T,\bar{t}}$), as outlined in Equation 4.5.2.

$$\mu_R^2 \;=\; \mu_F^2 \;=\; (m_{T,t}^2 + m_{T,\bar{t}}^2) \tag{4.5.2}$$

The cross-sections predicted by HERWIG 7 are significantly lower than the theoretical value. Increasing the order of perturbation (above the Born process) improves the HERWIG 7 prediction. This is as expected. However, as shown in Table 4.2, the predicted value for the "NLO 2, 2 merged Jets" setup is still 33% lower than the theoretical value.

The configurations in Table 4.2 all have used the `TopPairMass` scale. Changing the scale to the `TopPairMT` scale, the cross section was found for the configuration "NLO 2, 2 merged Jets" to be $\sigma = 822$ pb. This is for an inclusive sample, obtained using MADGRAPH as the one loop amplitude provider. These values can be compared to those from Table 4.2, of

Setup	All-Inclusive (OpenLoops)	All Inclusive (MadGraph)
NLO 0, 0 merged Jets σ [pb]	391	385
NLO 0, 1 merged Jets σ [pb]	374	386
NLO 0, 2 merged Jets σ [pb]	379	369
NLO 1, 0 merged Jets	N / A	N / A
NLO 1, 1 merged Jets σ [pb]	605	627
NLO 1, 2 merged Jets σ [pb]	630	622
NLO 2, 0 merged Jets	N / A	N / A
NLO 2, 1 merged Jets	N / A	N / A
NLO 2, 2 merged Jets σ [pb]	620	607

Table 4.2: Documentation of the cross-sections of the $t\bar{t}$ cross-section for different multiplicities of NLO merged jets, and different combinations of leptonic filter and matrix element provider. The cells listed as N / A (Not Applicable) are those configurations which are not possible to produce in Matchbox (discussion of this is provided in Ref. [275]). These samples are generated using the `TopPairMass`, which sets the renormalisation and factorisation scales as defined in Equation 4.5.1. Each sample is produced with 50k events.

$\sigma = 607$ pb. From this it can be seen that using the `TopPairMT` scale drastically improves the prediction of the cross-section. The time of event generation, however, is about 20% longer.

Sample statistics and negative weights

Table 4.3 documents the speed of generation, and fraction of negative weights produced, for two of the setups; NLO 0, 0 merged Jets and NLO 2, 2 merged Jets. These are All Inclusive samples, produced with MadGraph as the chosen ME provider and are produced with 50k events. For the latter setup, a comparison is also shown between the `TopPairMT` and `TopPairMass` scales.

Setup		σ [pb]	N_{events}	$frac_{Negative}$	$frac_{Positive}$	T_{Total} [min]
NLO 0, 0 merged Jets		385	5×10^4	23%	77%	117.25
NLO 2, 2 merged Jets	`TopPairMass`	607	5×10^4	39%	61%	870.71
	`TopPairMT`	822	5×10^4	40%	60%	1060.64

Table 4.3: Documentation of the speed of generation, and fraction of negative weights produced.

Although increasing the order of perturbation improves the prediction of the cross-section as seen in Table 4.2, it also significantly increases the fraction of negative weights. As such, for the desired accuracy of "NLO 2, 2 merged Jets", the fraction of negative weights is prohibitively large (39%). In the generation of samples, the user supplies Herwig with a requested number of events (N_{Req}). Herwig will then simulate this number of events, with various weightings. The simulation of negatively weighted events therefore reduces the total number of events that can be positively weighted, and also acts as a counter term

to the positively weighted events. Therefore, the combination of these two effects greatly reduces the effective number of events simulated (N_{Eff}). This can significantly increase the number of events that must be requested to produce a sample with an equivalent luminosity close to or above the size of the data. Equation 4.5.3 [286], can be used to determine the factor (x) by which one must increase N_{Req} by, in order to account for the fraction, f, of negative weights.

$$1/x = (1 - 2f)^2 \tag{4.5.3}$$

Therefore, for a fraction of negative weights, $f = 39\%$, one will only obtain a sample that has $\sim 5\%$ of the statistics that it was requested to have. Therefore, to make a fair comparison to a nominal sample of, for example, $N_{Eff} = 250k$ events, one will have to request $N_{Req} = 5$ million events.

This fraction of negative weights is (partly) why it is so important to use the dileptonic filtered samples, as these allow us to quickly increase the statistics. As documented in Ref. [275], the $t\bar{t}$ process has a branching ratio of $\beta = 0.108$ [23] to dileptonic, b-quark events[5] (the selection criteria of the "ATLAS_2017_I1495243" Rivet routine). Therefore, by producing only these events, there is a gain in statistics for dileptonic $t\bar{t}$ events by a factor of 10.

The full list of sample configurations that are produced with large statistics (and a summary of the number of events that are requested and expected) is provided in Table 4.4. The comparison of these samples to ATLAS data will then be provided in Section 4.5.2. These are all using the configuration of "NLO 2, 2 merged Jets" and use MadGraph as the external ME provider.

	All Inclusive (`TopPairMass`)	All Inclusive (`TopPairMT`)	Dileptonic (`TopPairMass`)	Dileptonic (`TopPairMT`)
N_{Req}	10 Million	10 Million	5 Million	5 Million
N_{Eff}	500 K	500 K	250 K	250 K

Table 4.4: Summary of the requested number of events for each final configuration, and the effective number of events after considering the fraction of negative weights, as taken from Table 4.3.

4.5.2 Comparisons to data

This section documents the Rivet outputs for the high-statistics run, and for the effect of changing the renormalisation and factorisation scales. This will be shown for both events generated with the dileptonic filter, and inclusive events generated with no filter. Comparisons are made to both ATLAS data obtained from the Rivet routine, and to nominal MC samples of the $t\bar{t}$ process denoted Powheg + Herwig7 or Powheg + Pythia8. The ME of these nominal samples is generated at NLO using the PowhegBox v2 generator, and

[5]This gives the branching fraction of both W bosons decaying leptonically.

then interfaced to either the HERWIG7 or PYTHIA8 SMC generators. A full documentation of these samples is provided in Appendix A.2

Single lepton RIVET routine Distributions taken from the "single lepton" RIVET routine (as described in Appendix A.1.1) for a sample of 10 million events generated without filters applied are shown. This routine was developed using 3.2 fb^{-1} of 13 TeV pp collisions as recorded by ATLAS. Measurements are then provided of the differential cross-sections of top-quark pair production as a function of the top-quark transverse momentum and rapidity, as well as the $t\bar{t}$ transverse momentum, rapidity and invariant mass. The analysis requires events with exactly one electron or muon and at least two b-tagged jets in the final state. The differential cross-sections of the top-quark pair production as a function of the p_T of the $t\bar{t}$ system is shown in Figure 4.4. This is shown for both samples produced with the `TopPairMass` scale and for samples produced with the `TopPairMT` scale.

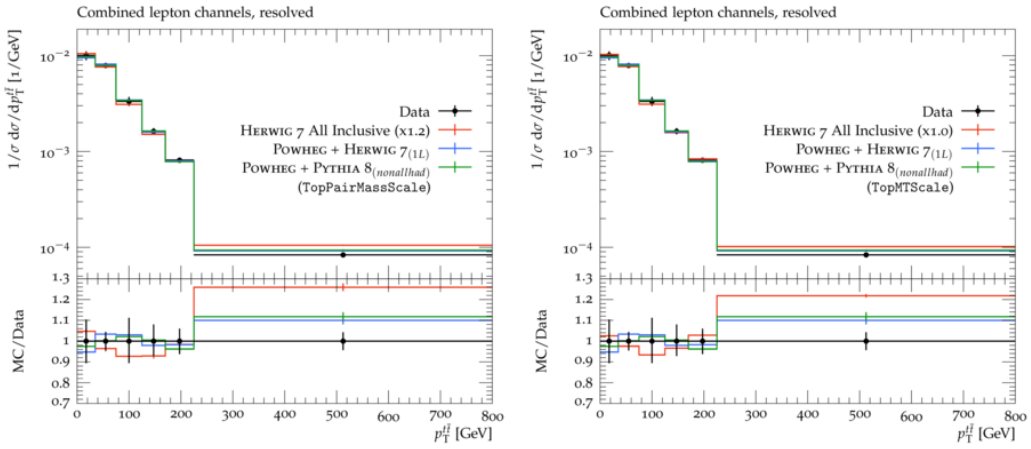

Figure 4.4: Predictions of the differential cross-sections of the top-quark pair production is shown as a function of the p_T of the $t\bar{t}$ system. These are shown for events generated with the `TopPairMass` scale (left) and the `TopPairMT` scale (right). In these plots, "HERWIG7 All Inclusive" represents the MADGRAPH+HERWIG samples produce as part of this study. Predictions are shown against 3.2 fb^{-1} of 13 TeV pp collision data, recorded by the ATLAS detector, and unfolded to particle level from the analysis described in Appendix A.1.1 (shown in black), as well as the two nominal $t\bar{t}$ samples described in Section A.2. The factor 'X' listed in the legend is a normalisation factor. The statistical uncertainties of the prediction are indicated by the error bars.

Dilepton RIVET routine Predictions of the differential cross-sections of the top-quark pair production are shown as a function of the rapidity, $|y|$ of the leading fragmented top quark for dileptonic samples in Figure 4.5 for both scale choices of the renormalisation and factorisation parameters. Predictions are shown against 3.2 fb^{-1} of ATLAS pp data unfolded to particle level from the analysis described in Appendix A.1.1 (shown in black), as well as the two nominal $t\bar{t}$ samples described in Appendix A.2. The statistical uncertainties

of the prediction are indicated by the error bars. This is shown using plots taken from the "dilepton" RIVET routine (as described in Appendix A.1.2) for a sample of 5 million events generated with the dileptonic filter. This routine selects oppositely charged e/μ events and two b-tagged jets to be in the final state.

Distributions of the number of additional jets after the lowest p_T cut of $p_T > 25$ GeV are shown. These are reported for samples produced with the `TopPairMass` scale and the `TopPairMT` scale in Figure 4.6.

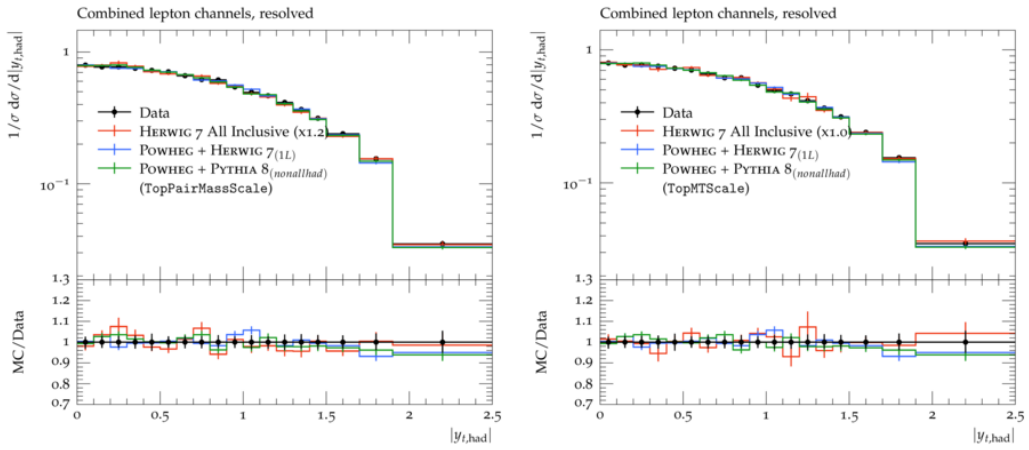

Figure 4.5: Predictions of the differential cross-sections of the top-quark pair production are shown as a function of the rapidity ($|y|$) of the leading fragmented top quark. These are shown for events generated with the `TopPairMass` scale (left) and the `TopPairMT` scale (right). In these plots, "HERWIG7 All Inclusive" represents the MADGRAPH+HERWIG samples produce as part of this study. Predictions are shown against 3.2 fb^{-1} of 13 TeV pp collision data, recorded by the ATLAS detector, and unfolded to particle level from the analysis described in Appendix A.1.1 (shown in black), as well as the two nominal $t\bar{t}$ samples described in Section A.2. The factor 'X' listed in the legend is a normalisation factor. The statistical uncertainties of the prediction are indicated by the error bars.

4.5.3 Findings

The production of merged, multi-leg $t\bar{t}$ Monte Carlo samples at the next-to-leading order accuracy, using the Matchbox framework of HERWIG 7 has been tested and validated. It is found from these distributions that throughout most of the phase space, the $t\bar{t}$ process is satisfactorily modelled, replicating the data for the distributions considered (within uncertainties), although in the high p_T regions, this is not so. It is expected that the data/MC agreement of the HERWIG 7 Matchbox samples could be improved by with more tuning, as has been performed in the nominal samples. It is also worth noting the large difference when using the different choices in scale setting, which may suggest that either one or both of the scales is not suitable for describing this process at the order of perturbation considered. Unfortunately, the performance of the HERWIG 7 generated samples performs slightly worse than the nominal throughout the distribution of the $p_T^{t\bar{t}}$, and performs worse

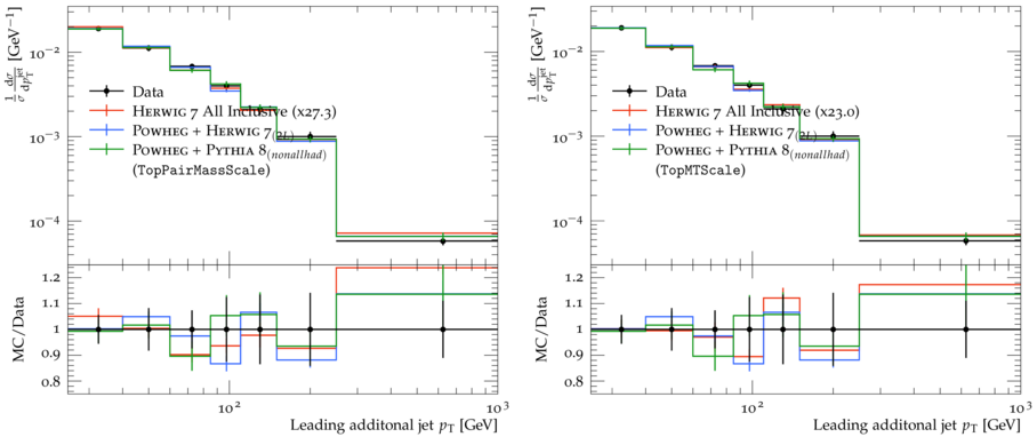

Figure 4.6: The p_T of the additional leading jet is shown for events generated with the `TopPairMass` scale (left) and the `TopPairMT` scale (right). In these plots, "Herwig7 All Inclusive" represents the MadGraph+Herwig samples produce as part of this study. Predictions are shown against 3.2 fb^{-1} of 13 TeV pp collision data, recorded by the ATLAS detector, and unfolded to particle level from the analysis described in Appendix A.1.2 (shown in black), as well as the two nominal $t\bar{t}$ samples described in Section A.2. The factor 'X' listed in the legend is a normalisation factor. The statistical uncertainties of the prediction is indicated by the error bars.

than the nominal in the region of high p_T of the leading jet. The primary motivation of this study was to determine the usefulness of the Matchbox Framework of Herwig 7 for the production of future bulk MC samples for ATLAS analysis. It is concluded, in part because of the large fraction of negative weights simulated by Herwig 7, that this is not viable for larger statistic samples.

Part III

A Search for LQ Pair Production

Chapter 5

Reconstructed Objects and Statistical Methods

In this Chapter we provide a detailed discussion of the reconstruction of final state objects, to be used in a search for pair-produced leptoquarks. As discussed in Part II, the ATLAS detector provides a vast quantity of detector output relating to the energy deposits of charged particles interacting with the various sub-detector components. In order to perform a high-level analysis of this raw data, it must be processed to reconstruct observable variables that relate to the final state constituents of the fundamental process occurring at the IP. To do so, highly robust reconstruction algorithms are developed and maintained by various sub-groups within the ATLAS Collaboration. In Section 5.1 is a discussion of how individual tracks and vertices are reconstructed within the ATLAS detector. Section 5.2 then proceeds to explain how higher-level variables can be built from this information, and discusses the baseline selection placed on objects used in the reconstruction of leptoquarks.

Finally, in Section 5.3 is a discussion of the statistical methods used in establishing limits or observations from the data, and in assigning levels of confidence to these statements. This section provides a general overview of the frequentist techniques used, while the specifics of how these techniques are implemented in the search for leptoquarks can be found in Section 7.1 of Chapter 7.

5.1 Tracks and Vertices

ATLAS reconstructs the tracks of charged particles passing through both the Inner Detector and the Muon Spectrometer independently. From well reconstructed tracks we can then determine a reliable measurement of their trajectory. This information then tells us about both the origin, and the initial momentum of the charged particle (based on a measurement of its curvature through a strong magnetic field). From this information we can then proceed to reconstruct the vertex and the energy at which the particle was produced.

The reconstruction of individual tracks and vertices within the ATLAS detector to a

high degree of certainty, with a low contribution of fake or mis-reconstructed tracks is a difficult task. These challenges are compounded by the high pile-up conditions present for the duration of Run II. This extreme environment means that the ATLAS detector is subject to an extremely high track density, as can be seen in Figure 5.1. It is worth noting that at present, this challenge is particularly relevant as we approach the high-lumi LHC. To suitably meet the demands posed by this upgrade in luminosity, efforts are being made to further improve our track and vertex performance in ever higher pileup conditions, see Ref. [287]. Additionally, for a detailed and comprehensive review of tracking in ATLAS, please refer to Ref. [288].

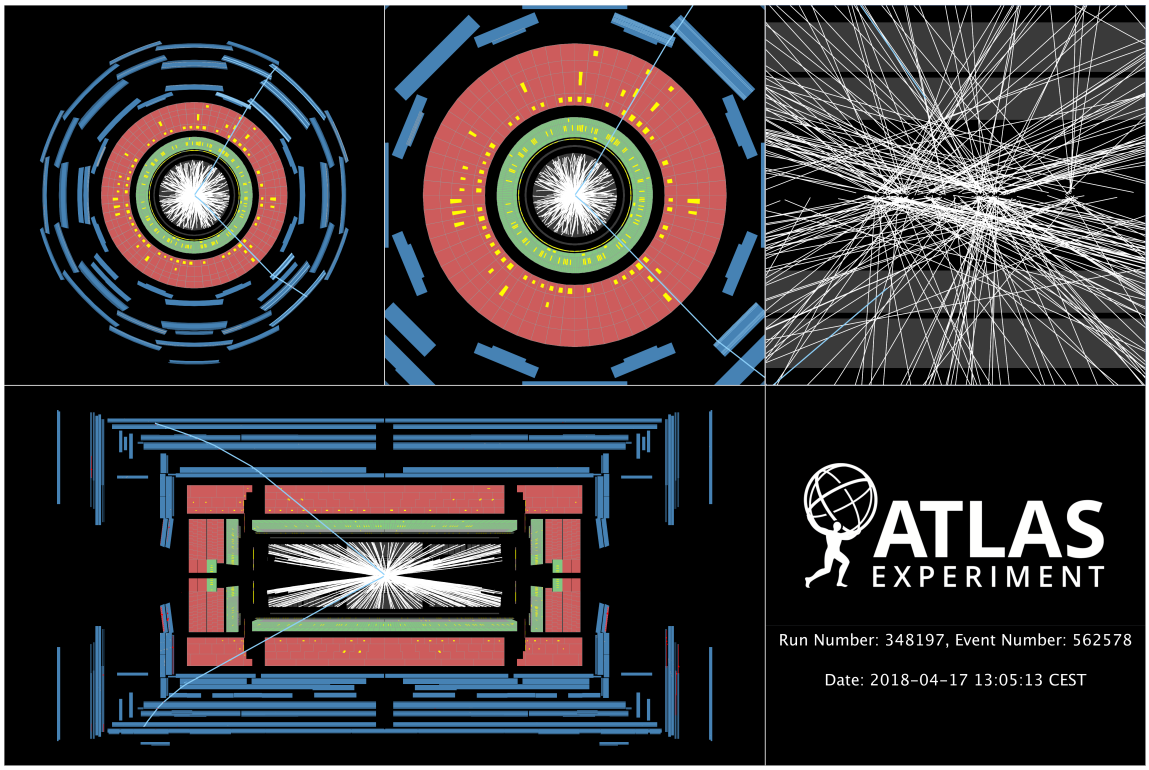

Figure 5.1: [289, 290] Event display taken from the first stable beam proton-proton collision run of 2018, recorded on April 17, as part of the 139 fb^{-1} $\sqrt{s} = 13$ TeV pp collision dataset. Here the high track multiplicity can be seen, originating from both the hard scatter and min-bias collisions.

5.1.1 Tracks

In the ID, the interaction of charged particles with the silicon strips in the Pixel or SCT results in a measured voltage output from the interacting cell termed a "hit". Using a three-dimensional mapping of the spatial location of each hit, we can then reconstruct the trajectory of charged particles in three-dimensions as they pass through the many layers of these detectors, where we call the sequence of hits deposited by a charged particle its track. To determine individual tracks, we provide the positions of measurements of individual hits

in our detector to a series of algorithms to reconstruct[1] individual tracks to a high degree of certainty.

ATLAS employs an "inside-out" tracking algorithm [291] to determine baseline reconstructed tracks. The reconstruction of these tracks is instigated by a *seed*, as reconstructed by the SiSPSeededTrackFinder [291]. A track seed is accepted when successive hits are recorded in at least 3 layers within either the pixel or silicone tracking detectors, given that they meet the fit requirements. Proceeding radially away from the IP, hits are sequentially added to the track if they are found along its fitted trajectory, as determined using a combinatorial Kalmann filter [292], with the successive hits being used to update the fit. This procedure continues sequentially until a completed track candidate passes beyond the SCT. If they conform with the existing fit, measurements in the TRT are then added to the track. Finally, a global fit is applied to all ID hits after the track ambiguities have been resolved.

Following the selection of these baseline tracks, ATLAS then employs an "outside-in" tracking method [291], designed to catch tracks previously missed. The main types of tracks that the "inside-out" method is likely to miss are those originating from secondary decays or photon conversions. As suggested in the name, the "outside-in" method begins by forming seed candidates from hits recorded in the TRT (the outermost component of the ID), using only those that are not already included in the extended baseline tracks. Again, using a Kalmann filter, the method proceeds radially inwards towards the IP.

5.1.2 Vertices

A vertex is the spatial position of a particle interaction, including both the production and decay of particles. Both *primary* and *secondary* vertices are used in the reconstruction of physics objects in this analysis. A primary vertex relates to the exact spatial position of the hard-scatter within the ATLAS detector, of which there is only 1 in an event. A secondary vertex is the location of the subsequent decay or interaction of a particle that was produced in a previous vertex. There can be many secondary vertices in a single event. One such source of observable secondary vertices that are used in physics analyses are the displaced secondary vertex produced in the decay of a B hadron. These are relatively stable states, and so the secondary vertex may occur at a distinguishable distance from the vertex at which the initial b quark originated.

The reconstruction of primary vertices can be decomposed into two main elements; vertex identification - in which tracks are associated to vertex candidates, and vertex fitting - in which the position of each candidate is reconstructed. Initially, a seed position for each

[1]It is worth mentioning that ATLAS performs both an *online* and an $offline$ reconstruction. The former is used in trigger decisions, and as such is developed for a minimal latency, while the latter, which is the subject of this section, is the more computationally expensive, and is developed to be used in physics-analysis.

vertex is selected based on the beam spot in the transverse plane.[2] An iterative fitting procedure is then performed [191]. This uses an adaptive fit with the seed position as the starting point, and reconstructed tracks as input measurements. Each track is assigned a weight according to it's compatibility to the vertex candidate, with the position and weightings being recalculated iteratively. The least compatible tracks are given the lowest weighting, and subsequently the least impact on the fitted vertex position. After the final iteration, the track weightings are evaluated, and tracks that are displaced from a fitted vertex position by more than 7 σ are rejected from the reconstruction of that vertex, and may instead be considered in the reconstruction of other vertices. The procedure repeats until all vertex candidates within the beam spot region are found. From the vertices reconstructed within the beam spot, the *primary* vertex is then identified as the one whose associated tracks have the maximal Σp_T^2.

5.2 Final State Objects

The composition of the final state targeted in the search for pair-produced leptoquarks consists of charged leptons (either electrons or muons), and jets, which can be flavour tagged via jet tagging algorithms. The acquisition of these objects from both ATLAS data and simulation is provided by the Combined Performance (CP) groups, who maintain tools that can be implemented within an ATLAS analysis in many different configurations, specific to different use-cases. This section outlines the tools and configurations chosen for this analysis, and the physical constraints imposed upon the selection due to these choices. The definition of signal electrons and muons is provided in Sections 5.2.1 and 5.2.2 respectively, and the definition of jets is provided in Section 5.2.3. A detailed discussion of the truth-tagging techniques, used to optimise the use of our Monte Carlo, is also provided in Section 5.2.3.

5.2.1 Electron Definition

Electrons are reconstructed from ID tracks, which are matched to clusters of energy deposits found in the EM Calorimeter. An object can then be identified as an electron after passing selections on the track quality, the quality and shape of the EM clusters, and the track-to-cluster matching. Measurements of the transition radiation (TR)[3] are also used to help distinguish electrons from charged hadrons over the energy range $1 < E < 200$ GeV [293].

[2] The x and y positions of the seed are taken as the center of the beam spot, and the z position is taken as the modal value of the z coordinates of all tracks at their point of closest approach to the center of the beam spot.

[3] TR is emitted when a highly relativistic charged particle with a Lorentz factor, γ, of $\mathcal{O} \gtrsim 10^3$ crosses the boundary between two materials of different dielectric constants. Transition radiation (in the form of soft X-rays) emitted from the radiator are then absorbed in the gas inside the straw tubes of the TRT. These then serve as detecting elements both for tracking and for particle identification.

The e/γ Combined Performance working group then provides a set of selection tools used for differing levels of electron identification in physics analysis, these include the Loose, Medium, and Tight Working Points (WPs). These WPs select prompt electrons in the central region of the detector ($|\eta| < 2.47$) and then apply a selection using a likelihood-based (LH) identification. The inputs to this identification include measurements from the tracking system, the calorimeter system, and variables that combine information from both. For a full discussion on the parameters used, see Refs. [294, 295]. Using these parameters, it is possible to apply a Loose, Medium, or Tight selection, where each category includes the events of all tighter selections. The Loose, Medium, and Tight WPs all require at least two hits in the pixel detector and seven hits total in the pixel and silicon-strip detectors combined. For the Medium and Tight operating points, one of these pixel hits must be in the innermost pixel layer (or in the next-to-innermost layer if the innermost layer is non-operational). This is done to reduce the background from photon conversions.

A summary of the requirements for electrons in this analysis is provided in Table 5.1.

Electron selection	
Feature	*Criteria*
Pseudorapidity range	$\|\eta\| < 2.47$ (and excluding $1.37 < \|\eta\| < 1.52$)
Transverse momentum	$p_T > 27$ GeV
Object quality	Not from a bad calorimeter cluster
	Remove clusters from regions with bad HV (2016 data only)
Track to vertex association	$\|d_0^{BL}(\sigma)\| < 5$
	$\|\Delta z_0^{BL} \sin\theta\| < 0.5$ mm
Identification	`MediumLH`
Isolation	`FixedCutLooseIso`

Table 5.1: Electron selection requirements

Where $d_0^{BL}(\sigma)$ and $|\Delta z_0^{BL}\sin(\theta)|$ are the transverse and longitudinal separation of the primary vertex of the electron track from the proton-proton interaction point (IP).

As stated in Table 5.1, electron candidates with $p_T > 27$ GeV, and in the region $|\eta| < 2.47$ (but excluding the transition region between the barrel and end cap EM calorimeters, $1.37 < |\eta| < 1.52$) are considered. These candidates are then required to pass the selection of the "Medium" WP, as discussed above, which achieves a reconstruction efficiency of 90%.

In order to increase the rejection of hadronic jets mis-identified as electrons, a Calorimeter-based isolation requirement is also applied [294], using the WP "`isFixedCutLooseIso`".

5.2.2 Muon Definition

Muons are initially reconstructed independently in both the ID and the MS. The Muon Spectrometer provides tracking resolution through a combination of the Monitored Drift

Tubes (MDTs) and Cathode Strip Chambers (CSCs).[4] In the MS, the construction of a muon track candidate using the outputs of these two sub detectors begins with a search for a segment in each muon chamber.[5] Segments formed in the MDT are reconstructed via a straight-line fit to the hits found in each layer, while in the CSC, segments are built using a combinatorial search in the η, ϕ plane. The search algorithm rejects cosmics and many other background sources by requiring a loose compatibility with the collision point. Segments generated in the middle layers of the detector (where more trigger hits are available) are then used to seed a track candidate. This seed is then fitted with hits from segments in different layers using a combinatorial search. At least two matching segments are required to build a track, except in the barrel end-cap transition region where a single high-quality segment with η and ϕ information can be used to build a track. ATLAS is then able to fully reconstruct muons by combining the information from each sub-detector. From this, there are four types of reconstructed muons available for use in an ATLAS analysis:

- Combined muons (CB) - reconstructed using hits from independently found tracks in the ID and MS.
- Segment-Tagged muons (ST) - reconstructed using an ID track extrapolated to the MS.
- Calorimeter-Tagged muons (CT) - reconstructed using ID track extrapolated to energy deposit in calorimeter (these are used in the region $|\eta_\mu| < 0.1$, where the MS is only partially instrumented).
- Standalone muons (SA) - reconstructed using hits in MS only.

More details on muon reconstruction can be found in Ref. [296].

The Muon Combined Performance Group (MCP) then provides 4 WPs of different selections on the variables used to isolate signal muons. These are; **medium**, **loose**, **tight** [297], and **high-$\mathbf{p_T}$** [298]. The first three of these (medium, loose and tight) are inclusive selections, so that each category includes the events of all tighter selections. The high-p_T selection is a subset of the medium WP, designed to enhance the momentum performance.

To isolate a muon for use in a physics analysis (i.e. to select prompt muons with a high efficiency, while suppressing background), one must apply identification requirements, track reconstruction requirements, and trigger requirements, as will be discussed in this section. The muons used in this analysis are defined as stated in Table 5.2.

[4]These are implemented in the higher pseudo rapidity ranges of $2 < |\eta| < 2.7$, as they have a finer granularity, and a higher time resolution, allowing them to cope with the increased track densities.

[5]Each MDT or CSC chamber is composed of multiple layers or "stations", with each chamber providing 6 - 8 η measurements along the muon trajectory.

Muon selection	
Requirement	Criteria
η Cut	< 2.7
pT Cut	> 27 GeV
Selection Working Point	`HighPt` - ($p_T(\mu) > 800$ GeV) `Medium` - ($p_T(\mu) < 800$ GeV)
Isolation	`FixedCutLooseIso`
d0 Significance Cut	3
$\lvert z0\rvert \sin(\theta)$ Cut	0.5 mm

Table 5.2: Muon selection requirements (the tighter selection on d_0^{Sig} and $|\Delta z_0 sin(\theta)|$ ensures that cosmic muons are discarded).

For this analysis, we require muons to be in the region $|\eta| < 2.7$. We then use two WP's provided by MCP (these are documented in Ref. [296]) to reconstruct muons in different regions of p_T. This is done to maximise our muon selection efficiency for all p_T regions. The `isMedium` WP is used to reconstruct muons with a $p_T < 800$ GeV, which is the default selection for muons in ATLAS. This WP used both CB and SA muons. As such, the η coverage of this WP is $|\eta| < 2.7$. The efficiency of this WP is more than 98% for muons with $p_T > 40$ GeV. For the high p_T region ($p_T > 800$ GeV)[6] we use the `HighPt` WP. This WP exclusively requires CB muons, and as such, the η coverage of this WP is $|\eta| < 2.5$. This WP optimizes the momentum resolution for tracks with $p_T > 100$ GeV. This is done by requiring CB muons which pass the `Medium` selection and have at least three hits in three different MS sites[7] and rejects tracks from specific regions of the MS where the alignment is sub-optimal. High p_T muons are also required to have a q/P significance of less than 7 where q/P, or the "charge-to-momentum ratio", is a variable introduced to help understand the curvature of a track, based on the absolute value of its 3-momentum P ($P = |\vec{p}|$) and electromagnetic charge, q. The q/P significance therefore gives the relative uncertainty of the q/P measurement, defined as the absolute value of the difference between the ratio of the charged momentum of the muons measured in the ID and MS divided by the sum in quadrature of the corresponding uncertainties, as seen in Equation 5.2.1.

$$\left| \frac{(q/P)_{ID} - (q/P)_{MS}}{\sqrt{\sigma(q/P)^2_{ID} + (q/P)^2_{MS}}} \right| \tag{5.2.1}$$

This means that a tight q/P significance cut will reject the tails of the $\Delta p_T/p_T$ distribution, which removes any spurious muon momentum measurements.

While this selection reduces the reconstruction efficiency by about 20%, it is seen that it

[6]The choice of applying this WP above 800 GeV was arrived at and validated in agreement with the MCP as a way to minimise any loss in efficiency due to the tighter selection, whilst also preventing any exposure to the reconstruction of spurious muons.

[7]This is required such as to improve the sagitta measurement.

also improves the p_T resolution of muons above 1.5 TeV by approximately 30%, and avoids badly measured muons. Our muon definition also includes the "`isFixedCutLooseIso`" working point of the track-based muon isolation tool provided by MCP.

5.2.3 Jet Definition

This analysis uses `AntiKt` [299] with a radius parameter of $R = 0.4$.[8] These are reconstructed using topological clusters of energy depositions in the calorimeters called topo-clusters [300]. The reconstruction of a topo-cluster begins with a "seed", which is identified as "cells with an energy deposit four times higher than the noise level". The neighbouring cells with an energy deposit two times above the threshold are added to the cluster and finally the adjacent cells with non-zero energy deposit are added. These topo-clusters are then used by the anti-k_T jet-reconstruction algorithm with a radius parameter of $R = 0.4$. A visualisation of what this clustering looks like for an $R = 1$ jet reconstructed with the anti-k_T algorithm is presented in Figure 5.2.

The anti-k_T algorithm is an example of an infrared (IR) and collinear safe[9] jet clustering algorithm that uses the sequential recombination of pairs of particles to reconstruct the jet. This algorithm first focuses on the recombination of the high p_T contributions, and considers the soft terms at the end, leading to a naturally IR safe algorithm with a well defined cone shape that is not skewed by the soft and collinear branching.

A calibration of the jet energy scale (JES) is evaluated. This is then applied to both simulation and data. The calibration applied to data is derived using in situ measurements, using well-measured reference objects, including photons, Z bosons, and calibrated jets. These account for differences in the jet response between data and MC, arising from the imperfect description of the detector response and detector material in simulation, as well as the hard scatter, UE, pile-up, jet formation and detector interaction. A detailed discussion of the methods used is provided in Ref. [302]. A full definition of jets used in this analysis is provided in Table 5.3. Jet cleaning is then performed on these via the JetCleaning tool, which is discussed in more detail in Section 5.2.3. In order to suppress jets arising from pileup a likelihood-based discriminant is used called the Jet Vertex Tagger (JVT [303]). This uses information about the primary vertex, the jet p_T and the track p_T to construct a likelihood of the jet originating from pileup. The JVT is only applied in the region of phase space in which it was trained (20 GeV $< p_T <$ 120 GeV and $|\eta| < 2.4$). This JVT is then applied in the "Medium" WP, providing a selection efficiency of 92%.

[8] Where R, the distance parameter of the `AntiKt` algorithm, regulates how far from the jet axis a cluster may be, for it to be considered for addition to the jet.

[9] The requirement that the observable does not change in the case of a collinear splitting or in the case of the emission of a soft particle

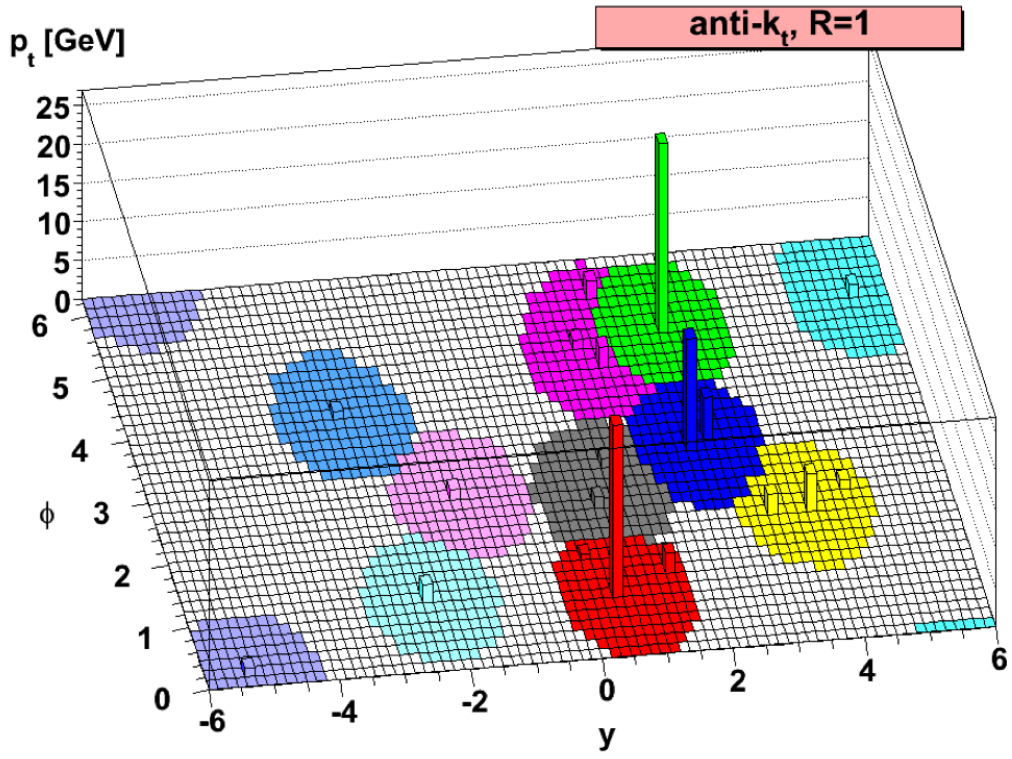

Figure 5.2: [299] Jet clustering of parton-level events, reconstructed with the anti-k_T algorithm. These inputs are generated with the HERWIG 6.5 [301] event generator. The different colours are used to represent the different jets and their areas. It can be seen that the anti-k_T algorithm reconstructs conical jets that emphasise hard radiation, with only the softer jets having more complex shapes. This property translates into reliable results for various quantitative properties of the reconstructed jets, as outlined in Ref. [299].

Selection requirements	
Observable	Requirement
Jet cleaning	LooseBad
BatMan cleaning	No
pT	>45 GeV
$\|\eta\|$	<2.5
JVT	>0.59 for p_T <60 GeV , $\|\eta\|$<2.4

Table 5.3: Selection requirements for `AntiKt4EMTopoJets`

Jet Cleaning

Presented here is a summary of the instructions provided for implementing jet cleaning into an analysis. The full instructions are documented in Ref. [304]. Jets that are reconstructed in the ATLAS detector can originate from a hard scatter proton collision or a non-collision background process. Since both can be reconstructed as real physics objects in the detector, it is important to have a set of selection criteria that can distinguish between them. In ATLAS, the development and implementation of these criteria is known as jet cleaning. Additionally, the presence of an unclean jet in an event can affect many other features of that event, including but not limited to the E_T^{miss} calculation and calorimeter behavior. Thus it is necessary to apply a second level of cleaning, designed to veto events that have one or more unclean jets. Application of the cleaning criteria to all jets in an event and using the jet-level information to make a cleaning decision at event-level is called event cleaning. This analysis follows the 2017 recommendations for jet cleaning as set out in Ref. [305]. This procedure is applied after the overlap removal (see Section 5.2.4) and p_T selection of $p_T(j_1), p_T(j_2) > 45$ GeV. This analysis uses the `Loose` working point of the jet cleaning tool. The jet cleaning tool will reject events that does not pass the `Loose` cleaning criteria. The exception to this is events (in the phase space of $20 < p_T^{jet} < 60$ & $|\eta| < 2.4$) in which an event is only rejected if it contains a jet which does not pass the cleaning criteria but also passes the Jet Vertex Tagger cut of JVT > 0.59, i.e. the event is only rejected if the "un-clean" jet is not considered to originate from pile-up.

b-Tagged Jets

The identification of jets originating from the fragmentation of a b quark (b-tagging) is possible due to the relative stability of B hadrons, which have a lifetime of roughly 1.5 ps. This longevity means that the decay of a B hadron will produce a secondary vertex that is significantly displaced from the primary. As such, measurement of the Impact parameter

(IP)[10] of a considered track to the primary vertex is a useful tool in identifying b-jets. A visualisation of this displaced vertex, and of how the measurement of the IP is constructed, can be seen in Figure 5.3. Additionally, around 70% of the b-quark's energy [306] will be transmitted to the primary hadron in the b-jet. Moreover, the decay topology of a B meson has characteristic properties, including a much higher decay ratio to c-hadrons than light quarks ($|V_{cb}| \gg |V_{ub}|$).

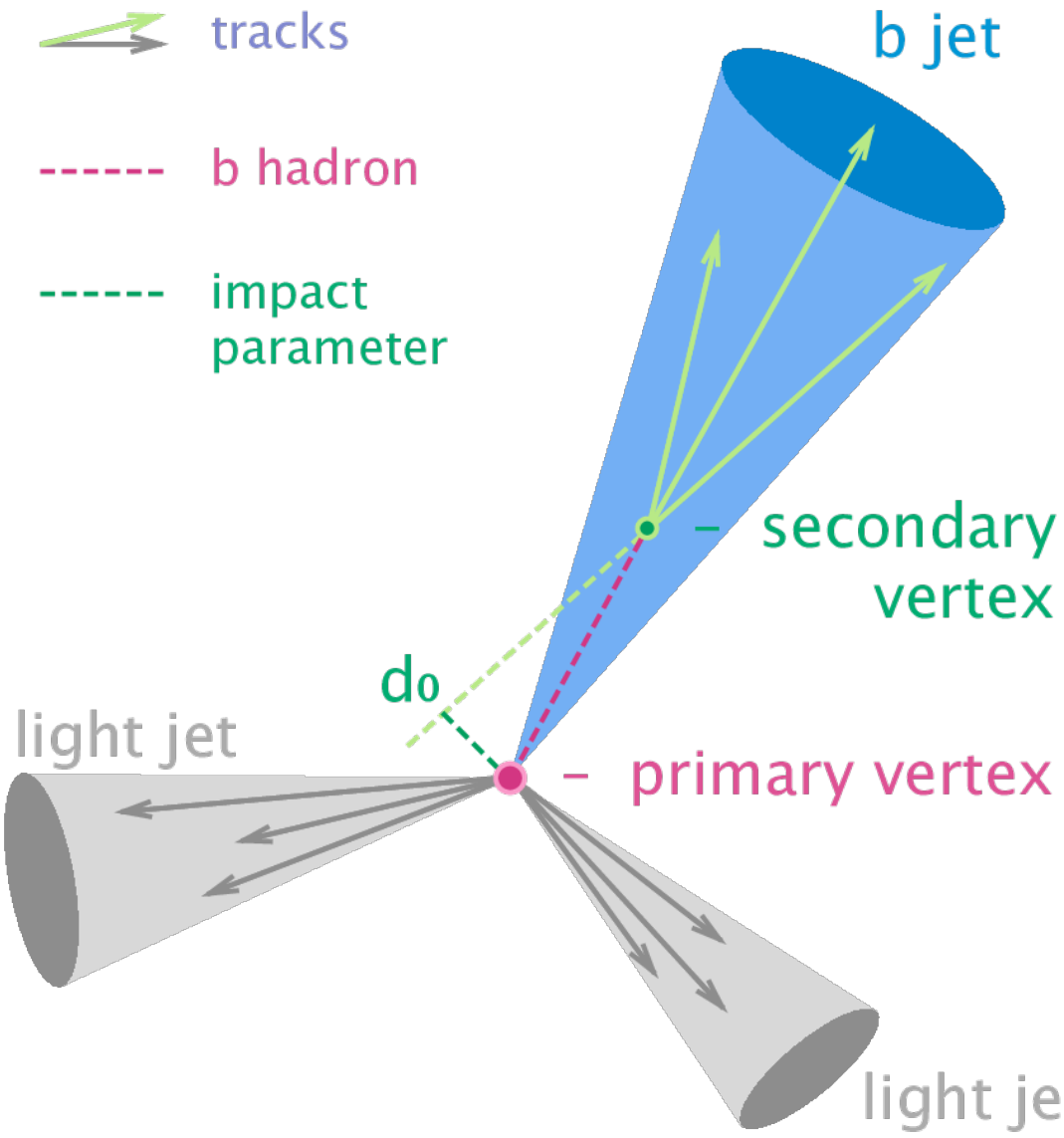

Figure 5.3: [307] A schematic showing the decay of a b-quark within a jet, and illustrating some of the parameters used in its identification, including the displaced secondary vertex.

The b-tagging strategy employed in this analysis uses the higher level b-tagging algo-

[10]The IP is defined as the signed point of closest approach in longitudinal and transverse plane, where it is positive if crossing the jet axis in front of primary vertex.

rithm "MV2" [308]. The MV2 algorithm is a multi-variate b-tagging algorithm, which uses lower level variables, such as the p_T and η of the jet, as well as the information from a series of lower-level algorithms, including IP2D, IP3D, SV1 [309, 310] and JET FITTER [311]. These are used to provide information about; the transverse and longitudinal impact parameter, details of the secondary vertex, and the relation between the primary and secondary vertices. These inputs are then used in a Boosted Decision Tree (BDT) algorithm,[11] using the ROOT Toolkit for Multivariate Data Analysis (TMVA) [312]. The performance of this variant of the MV2 tagger can be seen in Table 5.4.

BDT Cut Value	b-jet Efficiency [%]	c-jet Rejection	Light-jet Rejection	τ Rejection
0.9349	60	34	1538	184
0.8244	70	12	381	55
0.6459	77	6	134	22
0.1758	85	3.1	33	8.2

Table 5.4: Performance of the MV2C10 b-tagging algorithm at the WPs with 60%, 70%, 77% and 85% selection efficiency, including benchmark numbers for the efficiency and rejections rates (the inverse of the efficiencies). These are calculated using $t\bar{t}$ events, with the main selection requirement being for jet p_T to be greater than 20 GeV.

The algorithm is trained on a hybrid training sample, composed of both $t\bar{t}$ and Z'[12] events. In total, 8 million events have been used for the training; 5 million $t\bar{t}$ and 3 million Z'. Jets are required to pass the JVT and η requirements discussed in Section 5.2.3. Jets from these samples are reconstructed using the `AntiKt4EMTopoJets` Jet collection, as discussed in Section 5.2.3. The training has been performed with b-jets as signal and a mixture of 93% light-jet and 7% c-jets as background. In this analysis, the WP of MV2C10 with a 70% selection efficiency is chosen. This WP allows us a good rejection of light jets, with a large b-jet efficiency. The exact definition of b-jets used in this analysis can be seen in Table 5.5

b-tagging selection	
Jet collection	AntiKt
Algorithm	MV2c10
Operating point	Eff = 70%

Table 5.5: Summary table of b-jet definitions

The performance of b-tagging algorithms is optimized and evaluated using dedicated MC

[11] A BDT is a type of supervised machine learning architecture, that employs ensemble learning to improve performance by combining the predictions of many subsidiary decision trees in series, where each tree attempts to minimise the errors of previous tree.

[12] Z' is a BSM particle that has the same physics as the SM Z boson, but is much heavier. This particle is chosen as it results in b-jets, with a much larger p_T than are produced in $t\bar{t}$ decays.

samples. These samples are expected to be an imperfect description of all the relevant effects that impact the performance of b-tagging algorithms in data. As such, the flavour-tagging algorithms are calibrated by importing an ATLAS internal flavour tagging Calibration Data Interface (CDI). These calibrations aim to reduce / eliminate the bias of different simulations by providing data-to-MC scale factors (SFs). These are weights that reflect the b-tagging efficiency as measured in data compared to MC, and can then be used to correct the tagging efficiency in MC to that observed in data at the event level. The specific weights used in this process are stored in the efficiency maps of the b-tagging algorithm. These are determined by evaluating the performance of the algorithm using various nominal samples (e.g. POWHEG $t\bar{t}$, SHERPA W+jets, and SHERPA Z+jets samples) after a basic set of event level selections.

C-Tagged Jets

Charm Tagging. The discrimination of jets originating from the fragmentation of a charm quark is a much more challenging task than identifying the fragmentation of a b quark. This is because the decay topology of a charm quark has similar features to that of the b quark, but is less distinct in all aspects. Its mass is less separated from the lighter quarks, the lifetime of a charm hadron is ≤ 1 ps [110] (0.5 ps less than that of a B hadron), and the track multiplicity inside the jet of charmed meson decays is similarly less distinct. Both flavours of heavy quarks have much harder fragmentations (compared to the light quarks and massless gluons), with large fragmentation fractions into the weakly decaying charmed hadrons [313] (D^0, D^+, D_s^+ and Λ_c^+). Additionally, the fragmentation of a c-quark can be distinguished from that of a b-quark based on the topology of it's subsequent decay, as reconstructed via the JETFITTER algorithm. In this way, similar variables that are used in b-tagging are also useful in c-tagging, but are liable to yield poorer efficiencies.

Charm tagging is achieved using a combination of the DL1 [314] and MV2c10 discriminants. Both algorithms use a similar combination of lower level variables and algorithms (IP2D, IP3D, SV1 and JETFITTER) as well as the p_T and η of the jet. The DL1 tagging algorithm uses these lower level discriminants as an input to a Deep Neural Network (DNN) [315, 316][13] to produce three outputs, corresponding to the probabilities of a: charm flavoured jet (p_c), b flavoured jet, (p_b) or light flavoured jet (p_{light}). Each output is given a probability between 0 and 1, with the probabilities summing to 1 ($p_b + p_c + p_{light} = 1$). The DNN is then trained on the same hybrid training sample used to train the MV2c10 algorithm, as outlined in Section 5.2.3.

While primarily designed for b-jet identification, the DL1 outputs are used following the Neyman-Pearson lemma to define a one dimensional discriminant, applicable for c-tagging, as expressed in Equation 5.2.2

[13] A DNN is a supervised machine learning architecture that passes input parameters through many layers of weights and biases to arrive at a predicted value. It then iteratively adjusts these weights and biases to minimise the error in it's prediction.

$$DL1 = \ln\left(\frac{p_c}{f p_b + (1-f) \times p_{light})}\right) \tag{5.2.2}$$

where f corresponds to a weight attributed to the probabilities p_b and p_{light}.[14]

Working Point. A working point is a tuned set of an algorithms parameters that has been validated and recommended for use. The optimised c-tagging working point used in this analysis (discussed in detail in Ref. [317]) is labeled as CTag_Tight_Veto_MV2c10_FixedCutBEff_70. This WP was developed for the ongoing VH(cc) analysis [317]. This WP is found to have a c-jet selection efficiency of 27% a b-jet rejection of 12 and a light-jet rejection of 59.[15] A summary of the requirements applied to charm tagged jets is provided in Table 5.6.

c-tagging selection	
Jet collection	AntiKt4EMTopo
Jet selection	$p_T > 45$ GeV $\|\eta\| < 2.5$ $JVT < 0.59$
Algorithm	MV2c10 (Veto) DL1 (CTag)
Operating point	FixedCutBEff_70 (Veto) CTag_Tight_Veto_MV2c10_FixedCutBEff_70 (CTag)
CDI	2017-21-13TeV-MC16-CDI-2019-07-30_v1_CustomMaps(Veto) 2017-21-13TeV-MC16-CDI-July10_2019(CTag)

Table 5.6: Summary table of c-jet definitions

The c-tagging WP used in this analysis is designed to veto the presence of b-jets using the same 70% b-selection efficiency WP of MV2c10, as discussed in Section 5.2.3. Therefore the DL1 selection is only applied once a jet has failed the b-tagging requirement of the MV2c10 algorithm. As both the MV2c10 and DL1 algorithms are used in tandem in this strategy, the derivation of the relevant data-to-MC SFs (as previously discussed) requires a dedicated flavour tagging calibration.

Application of Charm Tagging in a search for LQ Pair production. In the c-tagging strategy employed by this analysis, there are three bins containing the different flavours of jets that can be identified using flavour tagging methods. These label individual jets as originating from the fragmentation of either a b-quark, c-quark or a light quark. Three categories are then defined to ensure that all events containing a charm tagged jet are grouped together, and labelled as c-tag. Subsequently, all remaining events that have a

[14] This value is correlated to the fraction of c-jets in the training sample

[15] Rejection factors are quoted as the probability of a tagged event originating from a differently flavoured jet. i.e. a light jet has a efficiency of being identified as c-tagged of 1/59

b-tagged jet are then labelled as b-tag and finally, all events with 0 tagged jets are labelled as "un-tagged". This is summarised in Table 5.7.

	c-tag	b-tag	un-tagged
cq	✓	✗	✗
cb	✓	✗	✗
cc	✓	✗	✗
bb	✗	✓	✗
bq	✗	✓	✗
qq	✗	✗	✓

Table 5.7: Categorisation of c-, b- and un-tagged jets, based on the targeted flavour of the leading hadronised quark, labelled as q for up, down and strange quarks, c for charm quarks and b for bottom quarks.

Truth-Tagged Jets

Due to the very high rejection of light and charm tagged jets, when using the MV2c10 flavour tagger it is possible to improve the statistical precision of our MC by applying a weight to each event based on the number of jets, tagging efficiencies and scale factors, as opposed to rejecting events that fail the cut. This procedure in ATLAS is rather unhelpfully called 'truth-tagging'.

In this analysis truth-tagging is only used for 2 tagged events for the Z and W MCs, where there are no true b-jets in the event.

Truth-tagging uses two components of each event; the event weight (ω_{TT}) and exact number, m, of tagged jets, out of the total n-jets contained within the event. Therefore, for a set of n-jets, the possible configurations of tagging the sub-set of m-jets can be denoted as $\binom{n}{m}$. For a given tagged configuration, referred to as the i^{th} combination, and denoted as $\binom{n}{m}_i$, the total number of remaining configurations is:

$$\overline{\binom{n}{m}} = \binom{n}{m} - \binom{n}{m}_i = \binom{n}{m} - 1 \tag{5.2.3}$$

The efficiency and inefficiency products are therefore:

$$\epsilon\left(\binom{n}{m}_i, x, f\right) = \prod_{j \epsilon m} \epsilon_x^f(j) \tag{5.2.4}$$

and

$$\epsilon_{in}\left(\binom{n}{m}_i, x, f\right) = \prod_{j \epsilon n-m} (1 - \epsilon_x^f(j)). \tag{5.2.5}$$

Where $\epsilon_x^f(j)$ is the tagging efficiency for jet, j, of flavour, f, at an efficiency working point, x, and $j\epsilon m(n-m)$ refers to the pool of (non-)tagged jets. Therefore, the event weight for m truth-tagged jets can be expressed as;

$$\omega_{TT}(x) = \sum_i^{\left|\binom{n}{m}\right|} P_i(x) \tag{5.2.6}$$

where

$$P_i(x) = \epsilon\left(\binom{n}{m}_i, x\right)\epsilon_{in}\left(\binom{n}{m}_i, x\right). \tag{5.2.7}$$

Consequentially, each i^{th} combination of m tagged-jets has the probability $P_i(x)/\omega_{TT}(x)$ of being truth-tagged, meaning a single truth-tagged combination can be randomly selected based on this probability. Once a single combination is selected and the jets tagged, the event is then scaled by the factor ω_{TT}. Subsequently, a comparison of this method to the direct tagging approach[16] was made, and the two methods were found to have good closure, justifying the decision not to apply additional systematic uncertainty on this method.

5.2.4 Overlap removal

Objects are reconstructed and identified separately and independently. As such, it is possible for multiple types of objects to be reconstructed from the same detector input, leading to falsely reconstructed final state objects. To reduce the effects of this, an overlap removal procedure is applied to remove any double counting. The procedure followed for doing this is the same as that followed by the VH $\rightarrow bb$ analysis [318], and follows the ATLAS recommendations prescribed in Ref. [319].

A summary of the procedure goes as follows;

- electron-electron: remove the lower p_T electron if two share the same track.
- electron-muon: remove the electron if it shares the same ID track with a muon OR remove the muon if it is a calo-muon.
- electron-jet 1: remove jets within $\Delta R = 0.2$ of any surviving electron.
- electron-jet 2: remove electrons within $\Delta R = min(0.4, 0.04 + \frac{10\text{ GeV}}{p_T^{electron}})$ of the surviving jet.
- muon-jet 1: remove jets within $\Delta R = 0.2$ of any surviving muon if the jet has less than three associated tracks with $p_T > 500$ MeV or both of the following conditions

[16] In which no truth tagging weights are applied, and events are rejected if they do not pass the relevant tagging selection

are met: the p_T ratio of the muon and jet is larger than 0.5 ($\frac{p_T^{\mu}}{p_T^{jet}} > 0.5$) and the ratio of the muon p_T to the sum of p_T of tracks with $p_T > 500$ MeV associated to the jet is larger than 0.7.

- muon-jet 2: remove muons within $\Delta R = min(0.4, 0.04 + \frac{10 \text{ GeV}}{p_T^{muon}})$ of the surviving jet.

5.3 Profile Likelihood Method

The axiomatic foundations of the field of modern probability theory were first laid out by Kolmogorov in 1933 [320]. The expansion into this new field of mathematics provided a methodology by which we can obtain knowledge of random processes. These are processes by which the outcome cannot be predicted with certainty, and for which repeated identical experiments have a finite chance of providing different results. In particle-physics applications, the reason for this inconsistency in experimentation can be attributed (simply speaking) to either true reflections of the fundamental physics, or limitations of the experiment. These can be considered in the field of probability as sources of uncertainty. These limitations in the experiment can be further divided into either reducible[17] or irreducible sources of uncertainty. The field of probability outlines methods by which we can then make statements about the characteristics of these random processes, and assign levels of uncertainty to these statements.

This Section describes the frequentist approach to deriving statistical tests of the compatibility of observed data with simulated theoretical models. The use of frequentist statistics in the derivation of confidence intervals of physical parameters in New Physics (NP) searches at particle physics experiments has been strongly advocated since Feldman and Cousins' paper in 1997 [321]. This approach of presenting confidence-interval and exclusion-interval based interpretations of a frequentist statistical analysis is now popular in many far ranging analyses of HEP data.

The notation used herein follows that used in the lecture course on probability and statistics presented at the AEPSHEP2012 physics school [322], which provides a useful resource for further studies on the subject.

5.3.1 Likelihood

A Probability Distribution Function (PDF) is used to determine the probability of a measurement, "X" of a distribution, x, to be within a range of values. This is done by integrating the PDF, "$\mathcal{P}(x)$", over said range;

$$\mathcal{P}(X \text{ in the range } [x, x + dx]) = \mathcal{P}(x)dx \tag{5.3.1}$$

[17] Limitations in the design of the experimental apparatus

PDFs that can be wholly described by a finite set of parameters (θ), are termed "parametric-PDFs". Here, a PDF will give the probability of arriving at measurement "X" given the values of each θ. The shape of a parametric-PDF can then be determined as a function of its variables, "x_i", and parameters "θ_i", "$\mathcal{P}(x_i;\theta_i)$". The shape of this PDF can be derived through a sequential estimation of its parameters. Taking a n-dimensional PDF with k parameters, $\mathcal{P}(x_1,...,x_n;\theta_1,...,\theta_k)$, we can estimate the parameters, θ_k, with estimators denoted $\widehat{\theta_k}$, where we can assign a confidence interval to our estimator, of $\mathcal{P}(\theta_a < \widehat{\theta} < \theta_b) = \alpha$. To determine these estimators, we can turn to the Maximum Likelihood (ML) theorem, whereby we first must formulate the likelihood as a function of these parameters ($\mathcal{L}(\theta_k)$), using the PDF, as shown in Equation 5.3.2,[18] where the index, "N" represents the analytical region considered.

$$\mathcal{L}(\theta_1,...,\theta_n;x) = \prod_{i=1}^{N} \mathcal{P}(x;\theta_1,...,\theta_n) \tag{5.3.2}$$

We then assign estimators ($\widehat{\theta}$) of the θ values that maximize this function, and give the greatest probability of producing the observed data. These estimators are taken to form Gaussian distributions, with variances $\hat{\sigma}_\theta$ that are extracted from the covariance of $\mathcal{L}$ around its maximum.

$$\mathcal{L}(\widehat{\theta_k};x) = \max_\theta \mathcal{L}(\theta_k) \tag{5.3.3}$$

Exact analytical solutions for equation 5.3.3 are constrained to only a few situations. More commonly, an evaluation of the likelihood around the parameter space is performed, to find the estimator $\widehat{\theta}$ that minimises $-\ln\mathcal{L}$ (the "negative log-likelihood",or NLL). Statistical errors on these estimates can be calculated using the co-variance matrix where, in general,

$$-2\Delta\ln\mathcal{L} = -2\left[\ln\mathcal{L}(\theta) - \ln\mathcal{L}(\widehat{\theta})\right] = \sum(\theta_i - \widehat{\theta_i})\sum\nolimits^{-1}_{i,j}(\theta_i - \widehat{\theta_j}) \tag{5.3.4}$$

This co-variance matrix, $\sum^{-1}_{i,j}$, maps contours of variance σ_θ which relate to the confidence intervals around the ML point. Here, the contours around the estimator $\widehat{\theta}$, taken in the region of $-2\Delta\ln\mathcal{L} < 1$ for a single parameter likelihood function would define a 68% confidence interval around the ML point. Therefore the Maximum Likelihood estimation of the parameter θ would be quoted as $\widehat{\theta} \pm \hat{\sigma}_\theta$. This co-variance, however, only estimates statistical sources of uncertainty. In experimentation, we must also evaluate other, systematic sources of uncertainty. To do this, we re-consider the parameterisation of our parametric-PDFs. Here, we distinguish the parameters of interest (POI) that we search for, denoted "μ", from those that hinder our measurement but must also be estimated, the nuisance

[18] Here, we have made a subtle change; the PDF, $\mathcal{P}(x;\theta)$ gives the probability observing the data, x, with the model parameters, θ, where as the Likelihood function $\mathcal{L}(\theta;x)$ gives the likelihood of the parameters taking certain values given that we've observed the dataset, x

parameters (NP). These NPs are categorised as either Type I for which the data set can be used to constrain the parameter, such as the normalisation of a certain background, and Type II, for which the uncertainty is due to model assumptions or uncontrollable limitations of the data. Notably, Type I NPs can be constrained (reduced) by a larger data set, whereas Type II are independent of the sample size. By modifying the likelihood function to reflect the separation of NPs and POIs, Type I NPs can be assessed by introducing a control sample, "y", to constrain these NPs, and assigning a specific likelihood to the NPs, and then profiling this specific parameter for a fixed value of μ.

$$\mathcal{L}(\mu,\theta) = \mathcal{L}_\mu(\mu,\theta)\mathcal{L}_\theta(\theta)\mathcal{L}(x,y;\mu,\theta) = \mathcal{L}_\mu(x;\mu,\theta)\mathcal{L}_\theta(y;\theta) \tag{5.3.5}$$

We then maximise the likelihood with respect to the NP, θ, for a given value of μ. By sequentially profiling all the NPs in this way, we arrive at a function that depends only on μ. This procedure is known as the Profile Likelihood Method (PLM).

Profile Likelihood Fit To relate how this likelihood fit is performed in practice, we first consider a histogram, "N", with i bins, which is composed of both a background content, and an un-known signal content; we can write the expected contents of each bin as

$$E[n_i] = \mu s_i + b_i. \tag{5.3.6}$$

Where μ is a parameter that modifies the strength of the signal, with no signal given by $\mu = 0$ and the full signal content given by $\mu = 1$. Here, the probability of the signal and background contents of the i^{th} bin (s_i and b_i respectively) are calculated by integrating their PDFs. These can subsequently be seen in Equations 5.3.7 and 5.3.8 for signal and background respectively.

$$s_i = s_{tot}\int_i f_s(x;\theta_s)dx, \tag{5.3.7}$$

$$b_i = b_{tot}\int_i f_b(x;\theta_b)dx, \tag{5.3.8}$$

Where f_s and f_b are the signal and background PDFs (paramaterised by θ_s and θ_b respectively) and s_{tot} and b_{tot} are the total mean numbers of signal and background events predicted by MC for signal and background respectively. The likelihood function can then be constructed as the product of Poisson probabilities for all bins.

$$\mathcal{L}(\mu,\theta) = \prod_{j=1}^{N} \frac{(\mu s_j + b_j)^{n_j}}{n_j!} e^{-(\mu s_j + b_j)} \tag{5.3.9}$$

By modifying the Likelihood function to reflect the separation of NPs and POIs, Type I NPs can be assessed by introducing a control sample, in the form of a dedicated histogram,

"M", of k bins, which is enriched in the process that is to be controlled. Again, as was shown in Equation 5.3.6, the expected contents of each bin can be written as,

$$E[m_k] = u_k(\theta), \tag{5.3.10}$$

where again, u_k is the PDF of the control sample, described by parameters θ. This histogram is then used to constrain these NPs by assigning a specific likelihood to the NPs, and then profiling this specific parameter for a fixed value of μ. These NPs then contribute Poisson probability terms to the Likelihood function, of;

$$\prod_{k=1}^{M} \frac{u_k^{m_k}}{m_k!} e^{-u_k} \tag{5.3.11}$$

5.3.2 CL_s method

In Section 5.3.1, we discussed methods used in parameterising functions to describe the PDF of a variable, and the likelihood of different observations of this variable. We will now go on to discuss the different hypotheses that can be used to explain these observations, and the statistical tests that can be performed to test said hypotheses. The tool which is used to assess the agreement of a hypothesis with observations is called a test statistic, usually denoted "q", which is used to compare data with the expectation of the null hypothesis. The outcome of the hypothesis test is presented in terms of a p-value, which gives the probability of a hypothesis producing an agreement which is worse than the one reported. p-values are used to indicate the validity of the null hypothesis. They present the probability of observing a result or one more extreme given the null hypothesis to be true. If this probability is low, it provides an indication that the null hypothesis is in fact unlikely, and subsequently motivates an alternative hypothesis. These tests can be visualised by plotting the PDF of the test statistic, as shown in Figure 5.4. We then find the p-value of a more extreme measurement than the observation under the null hypothesis. In this application, we consider one-sided hypothesis tests, whereby we only consider the probability of a measurement that is greater than the observation. This is calculated by integrating the PDF of the test statistic for all real values greater than the observed.

Both confidence levels and exclusion / discovery potential are achievable when performing hypothesis tests using the frequentist "CL_s method" [323, 324] which derives these values from the PDFs of the test statistic, as defined in Equation 5.3.12;

$$q = -2\ln(Q), \quad \text{where} \quad Q = \frac{\mathcal{L}(s+b)}{\mathcal{L}(b)} \tag{5.3.12}$$

or "the ratio of likelihoods for the two hypotheses of interest". Here, "b" denotes the null hypothesis, in which the data is described by the known background processes. In the event that the data allows the null hypothesis to be rejected to a high level of confidence,

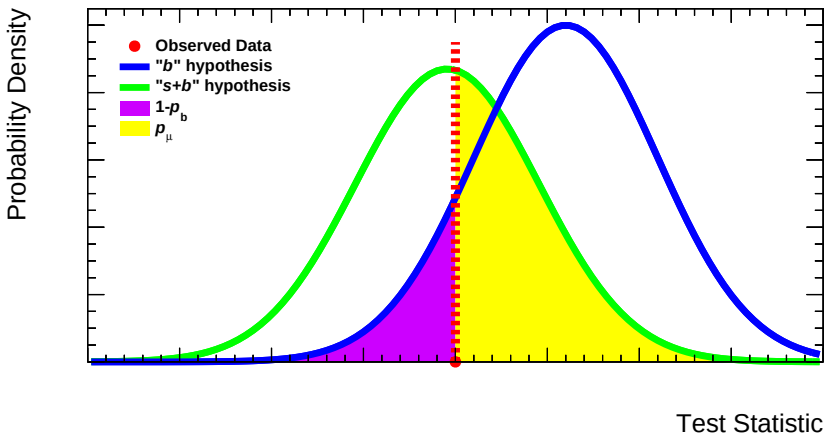

Figure 5.4: Example of the PDF distributions for both the background only (blue line) and the signal + background (green line) hypotheses, for a considered test statistic. Here, the integral of the PDF from the observed point (red), to infinity, gives the CL_{s+b} of the signal + background hypothesis, here filled in yellow and labelled as p_μ. Additionally, the integral from the observed point (red), to minus infinity indicates the $1-\mathrm{CL}_b$ value of the background-only hypothesis, filled in purple and labelled as $1-p_b$. These are related to the probabilities, under the assumption of each hypothesis, of an observation at the point measured, or one that is more extreme. As such, it is likely in this instance that the signal hypothesis will be accepted, as the p-value, p_μ, is large.

an alternative hypothesis can be suggested, in which both known backgrounds, and New Physics is required to explain the data. This is then denoted as the signal+background ("$s + b$") hypothesis. By defining the test statistic as in Equation 5.3.12 we find that, roughly speaking, positive values of q are consistent with a "background-like" scenario, and negative values indicate a "signal-plus-background" scenario, while all values close to zero indicate a poor sensitivity, so that we cannot distinguish clearly between the two scenarios. This method outlines a framework which allows confidence levels to be ascertained by calculating the p-value for each of these hypothesis, denoted as the CL_b and CL_{s+b} confidences, respectively, with an approximate[19] confidence in a signal-only hypothesis denoted as CL_s.[20] Calculation of the CL_{s+b} performs well when computing the expected fraction of signal+background experiments with counts $n_{s+b} < n_{observed}$, but only for experiments in which the contribution from the background is $n_b \leq n_{observed}$. A simultaneous downward fluctuation in both signal and background can lead the standard 95% benchmark for confidence intervals to report an exclusion of the signal in such situations. To resolve this, a modification of the p-values, "CL_s", is introduced, as shown in Equation 5.3.13.

$$\mathrm{CL}_s(\mu) = \frac{p_\mu}{1 - p_b} = \frac{CL_{s+b}}{CL_b} \tag{5.3.13}$$

Although not technically a p-value (a ratio of probabilities is not a probability), this serves as a useful definition, as it protects from statistically limited situations in which data fluctuates downward with respect to the background-only prediction. Such a situation may exclude any signal model with high confidence, and suggest a greater sensitivity than is available. Note therefore that the CL_s method gives a conservative limit. CL_s will always be greater than CL_{s+b}, resulting in a weaker upper limit. Many ATLAS and CMS searches for exotic particles now, in keeping with the recommendations from the LHC Higgs Combination Group [325], use the profiled likelihood ratio as the test statistic, calculated as;

$$\tilde{q}_\mu = \begin{cases} -2\ln\frac{L(\mu,\hat{\hat{\boldsymbol{\theta}}}(\mu))}{L(0,\hat{\hat{\boldsymbol{\theta}}}(0))} & \hat{\mu} < 0 \\ -2\ln\frac{L(\mu,\hat{\hat{\boldsymbol{\theta}}}(\mu))}{L(\hat{\mu},\hat{\boldsymbol{\theta}})} & 0 \leq \hat{\mu} \leq \mu \\ 0 & \hat{\mu} > \mu \end{cases} \tag{5.3.14}$$

Which tends to a χ^2 distribution, with 1 d.o.f. Here, $\hat{\hat{\theta}}$ are the fitted values of the NPs at fixed values of the signal strength, and the POI, μ, is taken to be the signal strength

[19] This can only ever be an approximation of a signal-only hypothesis, for as long as there is background in the experiment.

[20] In scenarios in which the PDFs of the $s+b$ and b hypothesis are well separated, then the $\mathrm{CL}_s \approx \mathrm{CL}_{s+b}$, however, in scenarios in which the PDF of the signal and background hypothesis are highly overlapping, the confidence interval quoted for any physical parameter must be clearly understood as the compatibility of the observed data with the signal considered, and not the other way around (i.e. the signal-only hypothesis ("s") is increasingly misleading, the more that the PDF of the "b" hypothesis contaminates that of the "s" hypothesis).

modifier, calculated as the ratio of the observed and expected cross sections ($\mu = \sigma/\sigma_{SM}$). $\hat{\mu}$ and $\hat{\theta}$ are the fitted values when both μ and NPs are all free to vary in the ML fit. This definition of the $\tilde{q}_\mu$ provides estimates of the compatibility of the data with the μ hypothesis. For the case of q_0, a one sided prescription is used, in which we assign $\tilde{q}_\mu = 0$ if the value of $\hat{\mu}$ is found to be above the hypothesis. Additionally, for cases in which $\hat{\mu} < 0$, we take μ to be 0, to avoid technical issues with negative PDFs. The numerator of Equation 5.3.14 is the conditional maximum-likelihood estimator of θ, where $\hat{\hat{\theta}}$ is the value of θ that maximises $\mathcal{L}$ for a given value of μ. The denominator of Equation 5.3.14 is then the unconditional ML function, where $\hat{\mu}$ and $\hat{\theta}$ are the ML estimators. p-values can then be calculated for both the null (p_b) and alternative (p_μ) hypothesis,

$$p_\mu = \int_{\tilde{q}_\mu^{obs}}^{\infty} f(\tilde{q}_\mu|\mu, \hat{\theta}_\mu^{obs})\, d\tilde{q}_\mu, \tag{5.3.15}$$

$$1 - p_b = \int_{q_0^{obs}}^{\infty} f(\tilde{q}_\mu|0, \hat{\theta}_0^{obs})\, d\tilde{q}_\mu, \tag{5.3.16}$$

where $\hat{\theta}_0^{obs}$ and $\hat{\theta}_\mu^{obs}$ are the nuisance parameters after fitting with data, $f(\tilde{q}_\mu|\mu, \hat{\theta}_\mu^{obs})$ and $f(\tilde{q}_\mu|0, \hat{\theta}_0^{obs})$ are sampling functions.

Calculating both the significance for a specific data set and the expected significance for a given hypothesis can require computationally expensive Monte Carlo calculations (colloquially known as Toys). It is shown in Ref. [326], however, that using the results of Wilks [327] and Wold [328] in the large sample limit approximation we can use an asymptotic formula to quickly and accurately evaluate p-values, with studies showing good closure between the asymptotic approximation and the Toys evaluation of these values. To do this, we must construct an artificial data set denoted the "Asimov data set" , which we define so that the estimators it evaluates for all parameters are the true parameter values.

As mentioned previously, the frequentist approach, and more specifically, the PLM is strongly advocated in the search for New Physics. CL_s based confidence intervals are frequently used to establish constraints on physical parameters of exotic BSM candidates, and the method has been used in the reporting of significant discoveries such as the Higgs discovery [9]. We will proceed to discuss the implementation of the PLM in this Thesis in Section 7.1.

Chapter 6

Search for scalar LQ pair production

This Chapter discusses the "cut-and-count" based approach to reconstructing and selecting potential candidates for the pair production of leptoquarks from 139 fb^{-1} of ATLAS data. The final states considered in this analysis contain charged leptons of the first or second generation (electrons or muons) and all quarks, excluding the top quark (u, d, s, c, b). For simplicity, it is assumed that both LQs decay via the same decay mode. This search is the first to consider LQ models in which the LQ can decay between leptons and quarks of different generations, e.g. decaying to both a 3^{rd} generation quark (b) and a 1^{st} generation lepton (e) in the process $LQLQ \to bebe$. This is also the first time in ATLAS that Leptoquarks have been searched for using both dedicated b- and c- flavour-tagging techniques. The publication documenting this analysis and its findings can be seen in Ref. [1]. This Chapter presents the implementation of the statistical method, as outlined in Section 5.3 of Chapter 5, where signal like events are excluded from ATLAS data to within a 95% confidence level.

The structure of this Chapter is as follows; An overview of the analysis is first presented in Section 6.1. The basic Preselection of candidate events is then outlined in Section 6.2, with the specific definitions of the analysis regions used in the isolation of different processes discussed in Section 6.3. Finally, the overall analysis strategy including the background contributions, modeling challenges and systematics strategy is then presented in Section 6.4.

6.1 Event Reconstruction and Selection

In selecting events to be considered in this analysis, one first applies a "preselection". This requires events to have the correct topology, and to contain objects that pass the basic requirements of the object definitions. These selections largely follow those of Ref. [176]. The preselection also encompasses the trigger selection and data quality checks.

The subsequent stage in event selection is to design requirements on final state objects in such a way as to maximise signal yield, and the removal of background processes. This

is done by constructing a Signal Region (SR) that identifies the kinematics of the signal Monte Carlo that best distinguish it from background processes. Similarly, Control Regions (CRs) can also be developed to isolate certain backgrounds from other processes, allowing us to study them in detail, and constrain them in the fit. The construction of these regions is discussed in Section 6.3.1.

6.2 Preselection

All data events must pass the GRL selection in order to reject periods of unstable beam or detector conditions. In order to reject events with jets reconstructed from calorimeter noise or beam halo background, events are vetoed based on a few discriminating variables of the calorimeter clusters such as LAr signal shape or total energy of cells that have negative energy.

Additionally, events are required to contain at least one primary vertex. Lastly, based on the final state signature, we can apply a basic event selection that defines the signal process. It is evident that we will require at least 2 jets ($n_{\text{jet}} \geq 2$), and exactly 2 oppositely charged, same flavour (OSSF) leptons ($n_\ell = 2$), that are required to be above the lepton trigger threshold. Due to the large mass constraints placed on the LQ candidates, as discussed in Section 2.8, it can also be inferred that the p_T of the leading and sub-leading lepton (p_T ($\ell_{1,2}$)) and the leading and sub-leading jet (p_T ($\text{jet}_{1,2}$)) will be large. Finally, an additional cut is implemented on the mass of the dilepton system ($m_{\ell\ell} > 130$ GeV) to avoid the mass peak of Z boson decays.

As such the following initial selection is applied:

- $n_\ell = 2$
- $n_{\text{jet}} \geq 2$
- p_T ($\ell_{1,2}$) ≥ 27 GeV
- p_T ($\text{jet}_{1,2}$) ≥ 45 GeV

a further cut is applied on the transverse momentum of the two lepton system of $p_T(\ell\ell) \geq 75$ GeV. This cut removes a large fraction of the Z+jets background while keeping the majority of the signal. Additionally, backgrounds from W and top processes can be suppressed by rejecting events with large E_T^{miss}. The resolution of the reconstructed E_T^{miss} increases with p_T, so applying a fixed cut can produce a smaller signal efficiency at large m_{LQ}. As such, we choose to apply a selection on the significance of the E_T^{miss} in the event, defined as $E_T^{\text{miss}}/\sqrt{H_T}$, which we require to be less than 3.5 $\text{GeV}^{1/2}$. In the reconstruction of this variable, we use an event based calculation of the E_T^{miss}, defined as the imbalance in the

total transverse momentum of all leptons and jets. This calculation also accounts for a track-based soft term [329] that provides the contribution from particles from the collision (tracks that are associated to the primary vertex), which are not already included in the E_T^{miss} calculation. H_T is defined as the scalar sum of the p_T of all lepton candidates and selected jets in the event. This variable effectively produces a looser cut on E_T^{miss} as m_{LQ} increases.

It is evident that this method of determining the $E_T^{\text{miss}}/\sqrt{H_T}$ is dependent on a good reconstruction of the E_T of all final state objects. This is problematic in the muon channel, however, where the E_T is reconstructed from the curvature of the muon track. As such, at higher p_T, where the curvature of muons is reduced, the E_T reconstruction performs poorly. In the high mass region this translates to a worse performance of the $E_T^{\text{miss}}/\sqrt{H_T}$ cut in the muon channel with respect to the electron channel (where the E_T^{miss} reconstruction is provided by the EM calorimeter). This can be seen in Figure 6.1. It is evident, therefore, that this reflects a limitation in the event selection for the muon channel of this analysis, and has a material impact on the performance of the limits derived in this channel. It is recommended that future iterations of this analysis avoid this selection, and find an alternative way to control their W and top background contributions for so long as there is no improvement in the reconstruction of the momentum of high p_T muons.

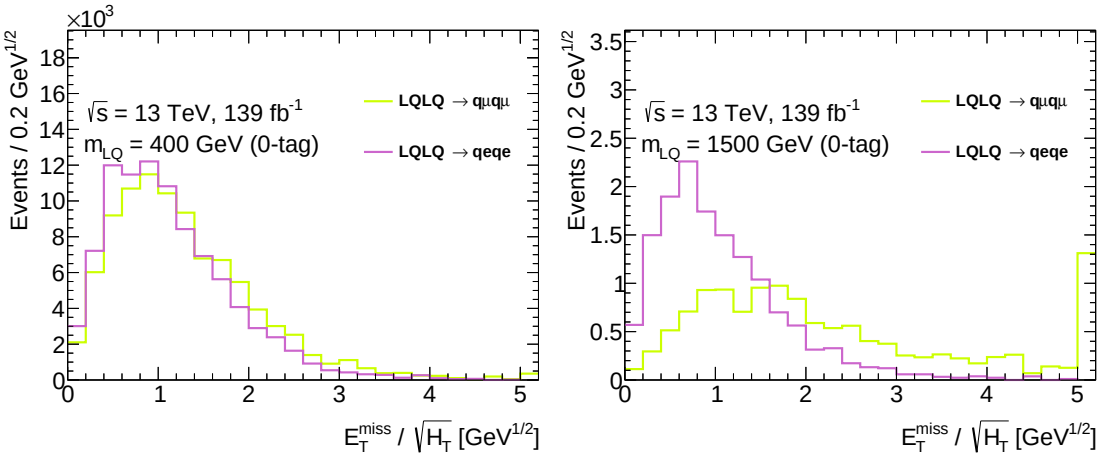

Figure 6.1: $E_T^{\text{miss}}/\sqrt{H_T}$ distribution in the 0 b-tag Signal Region, showing the $LQ \to se$ and $LQ \to s\mu$ signals for both a low mass ($m_{LQ} = 400$ GeV) and high mass ($m_{LQ} = 1500$ GeV) signal. In these plots, the $E_T^{\text{miss}}/\sqrt{H_T} < 3.5$ GeV$^{1/2}$ requirement has been relaxed for illustrative purposes, and the overflow bin is populated with events outside the x-axis range. From these plots, it can be seen that the $E_T^{\text{miss}}/\sqrt{H_T}$ is well described in both channels at low m_{LQ}, but performs considerably worse in the muon channel at high m_{LQ}, due to the poor momentum reconstruction of muons at high p_T.

6.2.1 Trigger Selection and Data Cleaning

Events considered in this analysis are triggered by at least one of the un-prescaled single lepton triggers (SLT) (electron or muon). It is required that one of the selected leptons must have fired the trigger. For the electron channel, events are required to have at least one electron with $p_T > 24$ GeV, which satisfy the 'medium' identification criteria and 'loose' isolation requirements (in later data-taking periods the p_T threshold is raised to 26 GeV and identification changed to 'tight'), or at least one electron with $p_T > 60$ GeV that applies the 'medium' identification criteria but makes no requirements on the isolation, or at least one electron with $p_T > 120$–140 GeV (depending on the data-taking period) that satisfies the 'loose' identification criteria. In summary, the lowest p_T un-prescaled single electron triggers in each data collection period is used. These are summarised in Table 6 of Ref. [330].

For the muon channel, events are required to have a muon with $p_T > 20$–26 GeV (depending on the data-taking period) and satisfy a 'loose' isolation criteria or at least one muon with $p_T > 50$ GeV without other requirements. The list of the lowest un-prescaled single muon triggers used in each data collection period are presented in Table 7 of Ref. [330].

6.3 Event Selection

A ranking is applied to the jets used in the reconstruction of leptoquarks. This is done to ensure that in events with one or two tags, the leptoquark that is reconstructed is comprised of the tagged jet(s) used in its identification. For the $LQ \to be$ and $LQ \to b\mu$ channels a tagged jet means it is b-tagged. For the $LQ \to ce$ and $LQ \to c\mu$ channels a tagged jet means it is either b- or c-tagged, where jets are first tested to be b-tagged, and then c-tagged. The selection of jets to be used for the leptoquark reconstruction is as follows: for events with 0 tagged jets, the leading and sub-leading jet are used in the leptoquark reconstruction. For events with one tagged jet, the tagged jet is taken to be the leading jet, and the leading non-tagged jet is taken to be the sub-leading jet. For events with two tagged jets, the leading and sub-leading b-tagged jets are considered for physics analysis.

6.3.1 Region Definition

Events can be categorised based on the multiplicity of tagged jets observed in the event. Different strategies are implemented when categorising the tag multiplicity in the event. The different strategies are designed to provide optimal sensitivity for the quark flavour composition of the LQ decay being targeted. Firstly, a b-tagging strategy is applied when targeting LQ decays involving a b-quark or a light-quark, using the b-tagging algorithm and definitions outlined in Section 5.2.3. Here, for decays involving a b-quark, events are sub divided into 0-, 1- and 2-tag categories, while decays involving a light-quark group these categories, along with the $>$ 2-tag category. We label this as the "pretag" category.

Secondly, a c-tagging strategy is applied when targeting LQ decays involving a c-quark. This strategy uses the c-tagging algorithm as outlined in Section 5.2.3, and categorises events to be either c-tagged, b-tagged or untagged.

Signal processes in this analysis are required to decay to a final state consisting of two lepton-jet pairs, where the leptons are of the opposite charge and are required to be of the same flavour (OSSF). As such, leptoquarks used in this analysis are reconstructed by finding the two lepton-jet pairs with the minimal mass difference. These two lepton-jet pairs are then ordered in mass, and taken to be the high and low mass LQs. We then calculate the asymmetry of the mass of these two lepton-jet pairs, as shown in Equation 6.3.1.

$$M_{\ell j}^{asym} = \frac{m_{\ell j}^{0} - m_{\ell j}^{1}}{m_{\ell j}^{0} + m_{\ell j}^{1}}. \tag{6.3.1}$$

Where $m_{\ell j}^{1}$ ($m_{\ell j}^{0}$) are the low (high) mass lepton - jet pair. This is based on the approach used in Ref. [178]. This variable is then used to define the signal region (SR), and two control regions. Additionally, the average mass of the two reconstructed lepton-jet pairs is selected as the discriminating variable on which to measure the observed and expected production cross sections.

$$m_{LQ}^{Av} = \frac{m_{\ell j}^{max} + m_{\ell j}^{min}}{2} \tag{6.3.2}$$

The SR is defined as $|M_{\ell j}^{asym}| < 0.2$, the sideband (SB) is defined as $0.2 < M_{\ell j}^{asym} < 0.4$ and the extended SB is defined as $|M_{\ell j}^{asym}| > 0.4$. Figure 6.2 demonstrates these three regions graphically.

These regions outlined in Figure 6.2 then play an important role in isolating signal processes and in validating our data / MC description (prior to the un-blinding of the analysis). We find that the distribution of the $M_{\ell j}^{asym}$ variable is well described for all values, by MC events, as shown in Figures 6.3 & 6.4, where we show all three regions (SR, SB & extended SB) with a 1 TeV $LQ \to b\ell$ signal in the muon and electron channel respectively.

A control region with a high purity of $t\bar{t}$ background (top CR) is defined by mimicking the SR selection, but modifying the lepton selection to require exactly 1 electron and 1 muon of opposite charge, changing the requirement from OSSF leptons to instead require Opposite Sign, Opposite Flavour (OSOF) leptons. This selection is used to normalise the top background and estimate the systematic uncertainty on the modelling of the top background (as discussed in Section 6.4.3).

Additionally, a Z control region (Z CR) is selected by placing a requirement on the invariant mass of the two leptons to be between 70 GeV and 110 GeV. As with the SR, SB and extended SB, these leptons are required to be OSSF. This selection is used to estimate the systematic uncertainty on the modelling of the Z background (as discussed in Section 6.4.3).

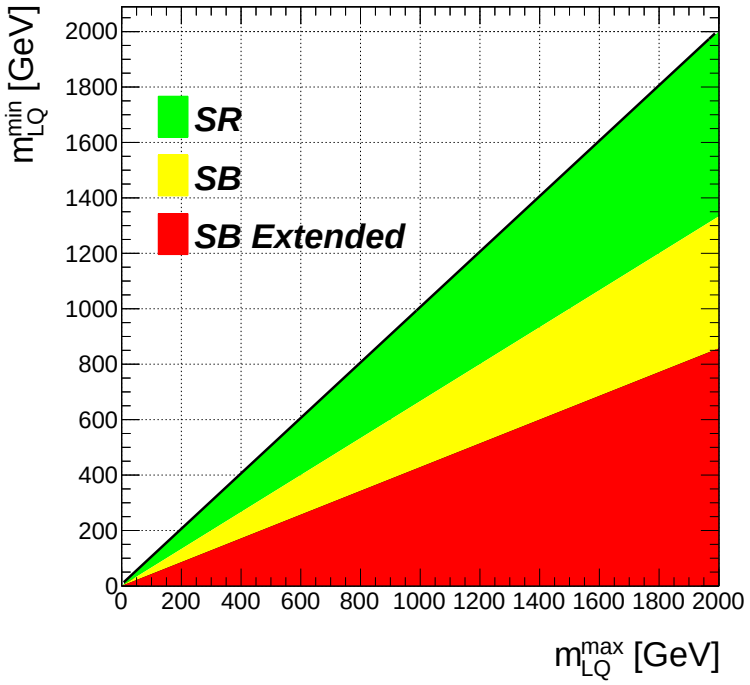

Figure 6.2: Definition of SR, SB and extended SB regions based on mass asymmetry, as defined in Equation 6.3.1, where $m^0_{\ell j}$ ($m^1_{\ell j}$) are the low (high) mass lepton - jet pair.

Z CR	Extended SB	SB	SR	Top CR
$n_\ell = 2$ $n_{\text{jet}} \geq 2$ $p_T(\ell_{1,2}) > 27$ GeV $p_T(\text{jet}_{1,2}) > 45$ GeV $p_T(\ell\ell) > 75$ GeV $E_T^{\text{miss}}/\sqrt{H_T} < 3.5$ GeV$^{1/2}$				
$70 < m_{ll} < 110$ GeV	$m_{\ell\ell} > 130$ GeV			
OSSF				OSOF
N/A	$\lvert m_{\ell j}^{Asym}\rvert > 0.4$	$0.2 < m_{\ell j}^{Asym} < 0.4$	$\lvert m_{\ell j}^{Asym}\rvert < 0.2$	

Table 6.1: Summary of the preselection and region-specific selections applied.

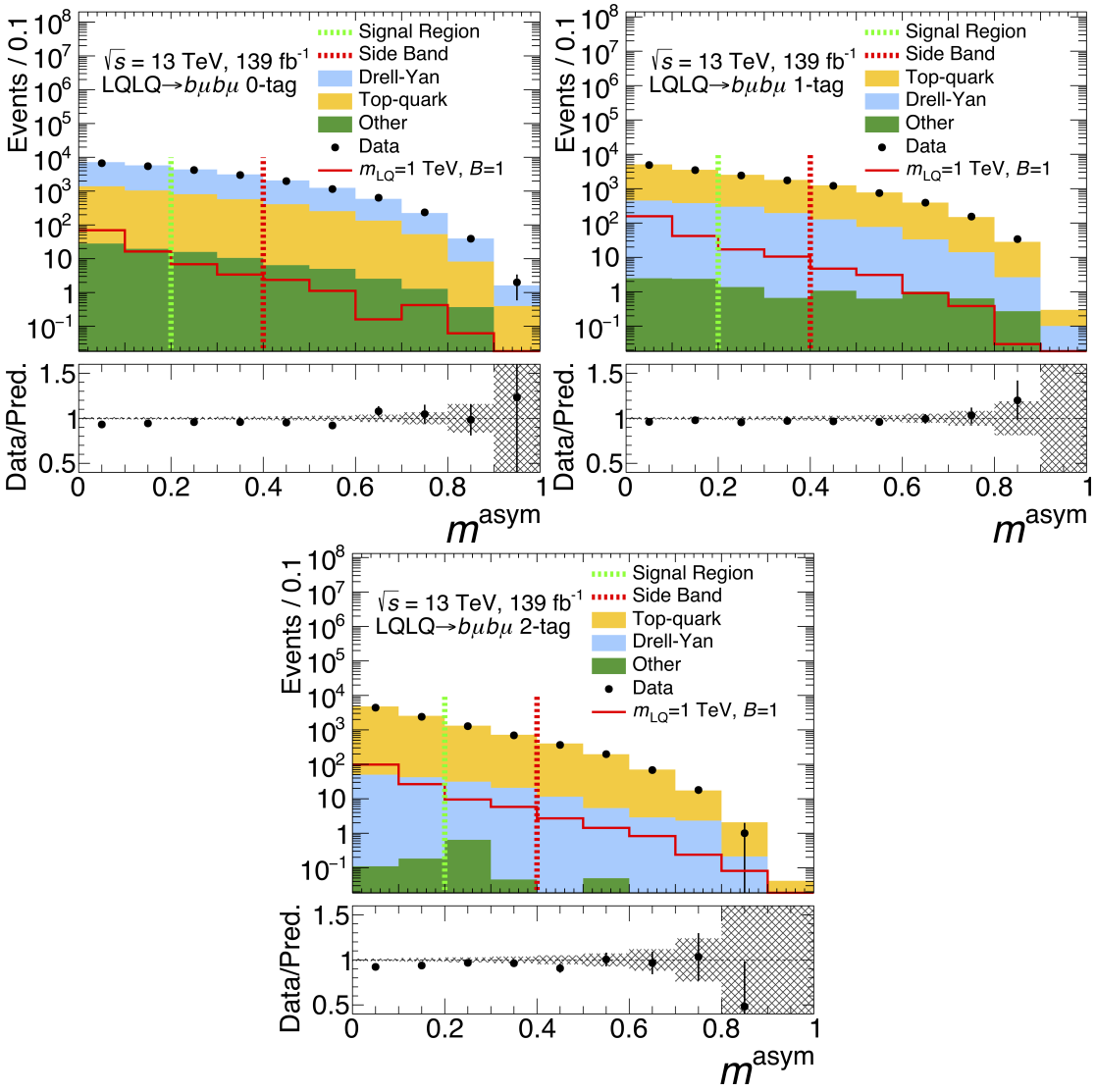

Figure 6.3: The asymmetry of the leading and sub-leading reconstructed LQ mass is shown in the muon channel. This combines the signal, sideband and extended sideband regions. The full discussion of these regions is provided in Section 6.3.1. This distribution is shown in the 0, 1 and 2 b-tagged channels, and with a 1 TeV $LQ \to b\mu$ signal. Also shown is the ratio of data against the MC prediction of the full SM background, with the statistical uncertainty on the simulated backgrounds, shown in hatched.

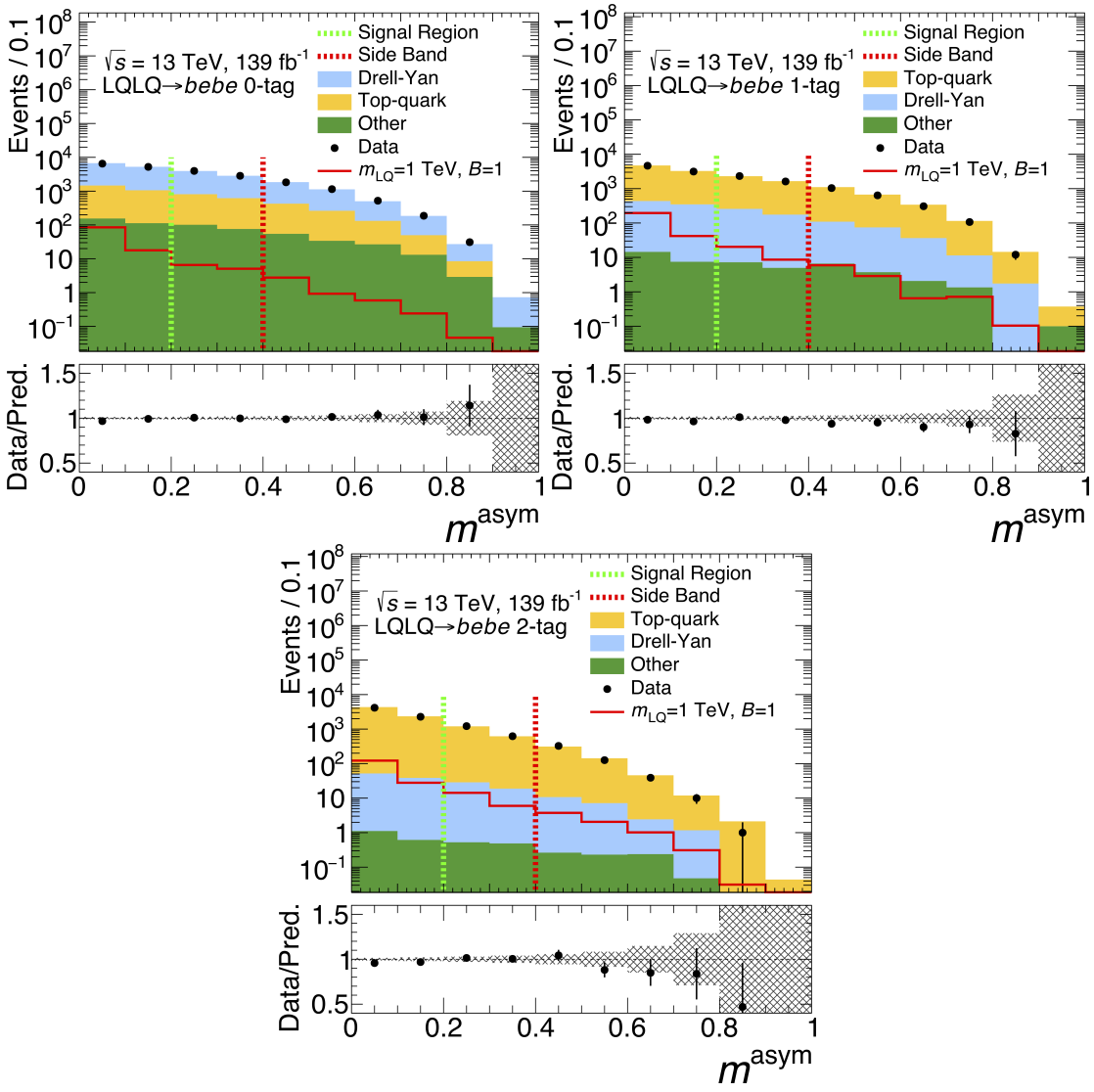

Figure 6.4: The asymmetry of the leading and sub-leading reconstructed LQ mass is shown in the electron channel. This combines the signal, sideband and extended sideband regions. The full discussion of these regions is provided in Section 6.3.1. This distribution is shown in the 0, 1 and 2 b-tagged channels, and with a 1 TeV $LQ \to be$ signal. Also shown is the ratio of data against the MC prediction of the full SM background, with the statistical uncertainty on the full SM measurement shown in hatched.

The effect of this sequence of cuts on the event yields in the Electron channel is presented in Table 6.2 and Table 6.3 presents the muon channel.

selection	LQ→ qe		LQ→ ce		LQ→ be	
	N (weighted)	N (unweighted)	N (weighted)	N (unweighted)	N (weighted)	N (unweighted)
initial	—	30000	—	30000	—	50000
event cleaning	—	29862	—	29875	—	49810
$p_T^\ell > 7$ GeV, $\lvert\eta_\ell\rvert < 2.47$ (2.7) e (μ), $N_\ell = 2$	—	6262	—	6224	—	15491
$p_T^j > 20$ GeV, $\lvert\eta_j\rvert < 4.5$, $N_j \geq 2$	—	6230	—	6203	—	15324
medium electrons	—	6093	—	6045	—	15025
remove true top decays	—	6093	—	6045	—	10514
trigger	—	6092	—	6045	—	10514
$p_T^\ell > 27$ GeV	28.872	6067	29.626	6023	30.600	10495
opposite sign, same flavour leptons	26.521	5592	27.316	5561	28.385	9765
$p_T^j > 45$ GeV, $\lvert\eta_j\rvert < 2.5$	26.215	5538	27.065	5519	28.059	9674
$p_T^{\ell\ell} > 75$ GeV	26.025	5500	26.800	5473	27.893	9601
$m_{\ell\ell} > 130$ GeV	25.971	5489	26.659	5452	27.821	9580
$E_T^{Miss}/\sqrt{H_T} < 3.5$ GeV$^{1/2}$	25.325	5377	24.299	4939	22.350	7666
$m^{\text{asym}} < 0.2$ (= pretag)	21.857	4548	19.400	3923	18.372	6300
0-tag / untagged	20.761	4336	13.812	2629	5.751	1802
1-tag / b-tag	0.963	184	2.409	529	8.745	2973
2-tag / c-tag	0.129	27	3.180	765	3.641	1414

Table 6.2: Cutflow table for all electron channels considering signal samples with LQ mass of 1 TeV. The initial statistics of the samples is 50000 events. The $q\ell$ samples are generated assuming $q = s$. All samples are generated assuming β=0.5 hence they include LQ decays into neutrinos and, in the $b\ell$ case, events with LQ $\to t\nu$ are present. Only events with both LQs decaying into electrons or muons are retained and an explicit requirement, indicated by the cut "remove true top decays", is applied on the samples used for the $b\ell$ channels.

selection	LQ→ $q\mu$		LQ→ $c\mu$		LQ→ $b\mu$	
	N (weighted)	N (unweighted)	N (weighted)	N (unweighted)	N (weighted)	N (unweighted)
initial	—	30000	—	30000	—	50000
event cleaning	—	29862	—	29832	—	49776
$p_T^\ell > 7$ GeV, $\lvert\eta_\ell\rvert < 2.47$ (2.7) e (μ), $N_\ell = 2$	—	6440	—	6319	—	15679
$p_T^j > 20$ GeV, $\lvert\eta_j\rvert < 4.5$, $N_j \geq 2$	—	6424	—	6294	—	15508
medium / high-p_T muons	—	5356	—	5240	—	13358
remove true top decays	—	5356	—	5240	—	9152
trigger	—	5162	—	5053	—	8798
$p_T^\ell > 27$ GeV	23.520	5133	23.784	5025	24.747	8770
opposite sign, same flavour leptons	23.473	5118	23.655	4997	24.702	8753
$p_T^j > 45$ GeV, $\lvert\eta_j\rvert < 2.5$	23.302	5083	23.430	4958	24.487	8674
$p_T^{\ell\ell} > 75$ GeV	23.162	5054	23.309	4931	24.309	8602
$m_{\ell\ell} > 130$ GeV	22.932	5015	23.065	4888	24.128	8547
$E_T^{Miss}/\sqrt{H_T} < 3.5$ GeV$^{1/2}$	17.583	3904	16.531	3564	15.180	5388
$m^{\text{asym}} < 0.2$ (= pretag)	15.183	3290	13.364	2821	12.568	4437
0-tag / untagged	14.362	3131	9.778	1966	3.843	1243
1-tag / b-tag	0.745	139	1.589	375	6.096	2154
2-tag / c-tag	0.062	18	1.998	480	2.446	964

Table 6.3: Cutflow table for all muon channels considering signal samples with LQ mass of 1 TeV. The initial statistics of the samples is 50000 events. The $q\ell$ samples are generated assuming $q = s$. All samples are generated assuming β=0.5 hence they include LQ decays into neutrinos and, in the $b\ell$ case, events with LQ $\to t\nu$ are present. Only events with both LQs decaying into electrons or muons are retained and an explicit requirement, indicated by the cut "remove true top decays", is applied on the samples used for the $b\ell$ channels.

6.4 Analysis Strategy

This section discusses the strategy employed in properly describing the considered signal and background processes with a detailed modelling of the associated uncertainties, as well as the targeting of signal processes to procure a high signal selection efficiency.

6.4.1 Backgrounds and Uncertainties

The dominant background contributions in this analysis vary based on the tag multiplicity, with DY+jets as leading, and top as sub-leading in the 0-tag regions, and the reverse being true for all tagged regions. Other backgrounds (dibosons, W and single top) provide a small but non-negligible contribution also. Fake background where both leptons are misidentified as jets or non-prompt leptons is neglected. To support this decision, an estimate of the fake contribution is presented in Section 6.4.2, where it is found to be small in all regions. Any residual fake background is absorbed into the Z+jets or $t\bar{t}$ normalisation factors and included in the data-driven modelling systematics discussed in Section 6.4.3.

As discussed in Section 2.7, the dominant background processes relevant to this final state signature are the $t\bar{t}$ and Z/DY+jets processes. It is worth noting that the MC generation of the Z+jets processes is divided into different samples, based on the flavour of the leading hadronised quark. The dominant production modes are $Z + l$X, $Z + c$X and $Z + b$X in that order (where l reflects the light quarks). Tables 6.4, 6.5 and 6.6 quantify the data and background contribution for each background processes in every tagging category for the pretag, c-tag and b-tag strategies respectively in both the electron and muon channels.

	LQ $\to qe$	LQ $\to q\mu$
$t\bar{t}$	1790 ± 220	1910 ± 240
Single top	390 ± 110	430 ± 120
DY+light-jets	2820 ± 180	3040 ± 180
DY+c-jets	521 ± 93	528 ± 90
DY+b-jets	233 ± 44	252 ± 46
W+jets	126 ± 32	8.5 ± 2.2
Diboson	31.8 ± 9.6	12.4 ± 3.7
Fitted SM background events	5910 ± 67	6185 ± 77
Observed events	5881	6169
Signal ($m_{\mathrm{LQ}} = 1$)	591 ± 45	503 ± 27
Signal ($m_{\mathrm{LQ}} = 1.5$)	22.1 ± 1.7	15.4 ± 1.0

Table 6.4: Observed and expected numbers of events in pretag SRs for LQ $\to q\ell$, where SM predictions are the result of fits performed using 139 fb^{-1} of data. The uncertainties quoted for the fitted SM background include both the statistical and systematic components. Yields for two LQ scenarios are also shown for comparison.

	LQ → ce			LQ → $c\mu$		
	untagged	b-tag	c-tag	untagged	b-tag	c-tag
$t\bar{t}$	291 ± 18	964 ± 51	227 ± 14	293 ± 16	1049 ± 50	237 ± 14
Single top	35 ± 11	129 ± 39	28.7 ± 9.0	37 ± 10	166 ± 46	38 ± 11
DY+light-jets	2872 ± 74	32.3 ± 8.6	101 ± 11	3120 ± 71	29.0 ± 9.4	123 ± 13
DY+c-jets	367 ± 49	80 ± 12	135 ± 17	340 ± 46	67 ± 10	155 ± 20
DY+b-jets	39.4 ± 5.7	166 ± 24	31.5 ± 4.8	40.4 ± 5.7	165 ± 23	35.1 ± 5.2
W+jets	101 ± 26	10.2 ± 2.7	7.5 ± 2.0	6.3 ± 1.6	1.39 ± 0.36	0.81 ± 0.21
Diboson	23.5 ± 7.2	2.58 ± 0.79	3.6 ± 1.1	9.0 ± 2.7	1.21 ± 0.37	1.45 ± 0.44
Fitted SM events	3728 ± 53	1384 ± 26	534 ± 17	3846 ± 55	1478 ± 26	591 ± 18
Observed events	3714	1366	535	3824	1484	591
Signal ($m_{\mathrm{LQ}} = 1$)	312 ± 26	71 ± 12	129 ± 13	265 ± 17	58.0 ± 9.1	111.5 ± 9.5
Signal ($m_{\mathrm{LQ}} = 1.5$)	13.7 ± 1.2	2.33 ± 0.38	3.10 ± 0.30	9.72 ± 0.69	1.49 ± 0.28	1.99 ± 0.20

Table 6.5: Observed and expected numbers of events in untagged, c- and b-tag SRs for LQ → $c\ell$, where SM predictions are the result of fits performed using 139 fb^{-1} of data. The uncertainties quoted for the fitted SM background include both the statistical and systematic components. Yields for two LQ scenarios are also shown for comparison.

	LQ → be			LQ → $b\mu$		
	0-tag	1-tag	2-tag	0-tag	1-tag	2-tag
$t\bar{t}$	469 ± 22	919 ± 33	255 ± 11	487 ± 22	1001 ± 35	295 ± 12
Single top	51 ± 11	109 ± 24	48 ± 10	48 ± 10	122 ± 25	49 ± 10
DY+light-jets	3035 ± 95	29.2 ± 8.0	0.105 ± 0.057	3318 ± 93	36 ± 11	0.099 ± 0.059
DY+c-jets	479 ± 77	92 ± 15	1.68 ± 0.34	464 ± 75	75 ± 13	1.61 ± 0.33
DY+b-jets	54.2 ± 7.7	165 ± 23	25.9 ± 3.6	52.5 ± 7.6	151 ± 22	21.1 ± 3.0
W+jets	113 ± 29	9.4 ± 2.4	1.02 ± 0.27	7.5 ± 1.9	0.97 ± 0.25	0.110 ± 0.028
Diboson	27.8 ± 8.5	2.63 ± 0.81	0.33 ± 0.10	10.8 ± 3.2	1.21 ± 0.37	0.141 ± 0.043
Fitted SM events	4229 ± 57	1326 ± 25	332.4 ± 9.0	4389 ± 59	1387 ± 25	367.1 ± 9.3
Observed events	4214	1314	316	4367	1408	340
Signal ($m_{\mathrm{LQ}} = 1$)	102 ± 13	237 ± 19	149 ± 13	87 ± 11	200 ± 12	124.1 ± 8.7
Signal ($m_{\mathrm{LQ}} = 1.5$)	5.69 ± 0.90	8.72 ± 0.76	3.57 ± 0.33	3.89 ± 0.61	6.11 ± 0.50	2.38 ± 0.20

Table 6.6: Observed and expected numbers of events in 0-, 1- and 2-tag SRs for LQ → $b\ell$, where SM predictions are the result of fits performed using 139 fb^{-1} of data. The uncertainties quoted for the fitted SM background include both the statistical and systematic components. Yields for two LQ scenarios are also shown for comparison.

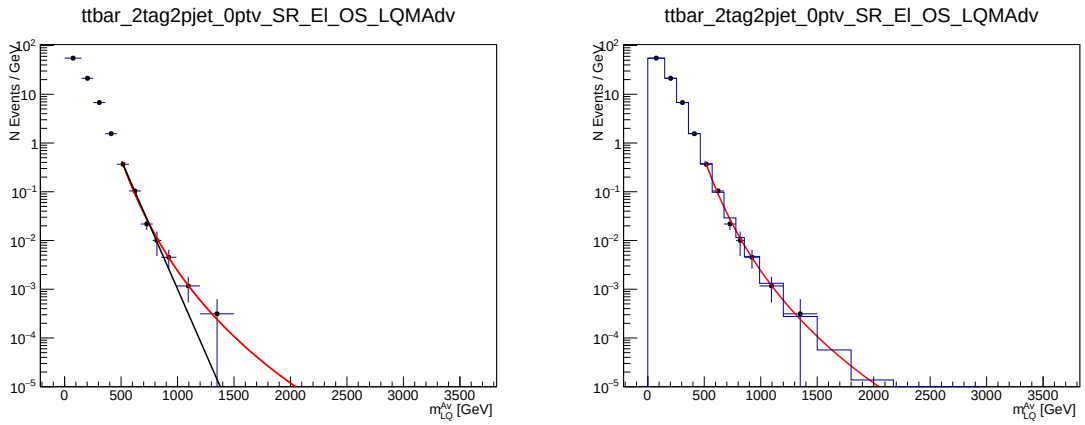

(a) Fits are shown using a power law (red) and exponential (black).

(b) Closure test of the power law fit, to the MC distribution

Figure 6.5: Fits and closure test of the $t\bar{t}$ MC distribution in the signal region. The fits and test is performed in the region $m_{\mathrm{LQ}}^{\mathrm{Av}} > 500$ GeV

Functional form for $t\bar{t}$ extrapolation

The MC prediction of most processes is generally less well described in the high p_T tails (and correlated variables such as m_{LQ}^{Av}). This is because the cross-section is low in these regions, meaning that it is expensive to generate sufficient MC statistics. To compensate for this, we perform an extrapolation of the m_{LQ}^{Av} distribution for the $t\bar{t}$ process into the high m_{LQ}^{Av} tails. This is done by fitting a functional form to the $t\bar{t}$ process in the low mass region of the m_{LQ}^{Av} distribution, and then using this functional form to evaluate the predicted number of events present in the high mass tails.

Different functional forms were tested in the description of the m_{LQ}^{Av} distribution of the $t\bar{t}$ process, with the best fit to MC in all regions being found for the following function

$$f^{t\bar{t}}(m_{\mathrm{LQ}}^{\mathrm{Av}}) = a(m_{\mathrm{LQ}}^{\mathrm{Av}})^{b}.$$

An exponential function, also depending on $m_{\mathrm{LQ}}^{\mathrm{Av}}$, is used to assess the uncertainty on the fit. Distributions for SR selections are shown in Figure 6.5a.

To ensure good closure between this function and MC, we perform a check, where bins in the original histogram (which uses a 5 GeV binning) that have $m_{\mathrm{LQ}}^{\mathrm{Av}} > 500$ GeV are replaced with $5 \times f^{t\bar{t}}(m_{\mathrm{LQ}}^{\mathrm{Av}})$. The MC is compared with the histogram formed from the function in Figure 6.5b. From this test, good agreement is observed. For the search limits only bins with $m_{\mathrm{LQ}}^{\mathrm{Av}} > 800$ GeV are replaced with the functional histogram and the MC is used for the remaining bins.

6.4.2 Fake Estimation

The distinguishing characteristic of an electron signature in the ATLAS detector is that of a track in the ID which aligns with an energy deposit in the electromagnetic calorimeter. This signature can, however, be created from numerous other processes occurring in the ATLAS detector. These additional processes are therefore considered "fake" electrons, and are considered to be a reducible background process.

One such source of "fake" electrons that is difficult to accurately model in Monte Carlo arises from the W+Jet(s) background (where a W boson is produced in association with a jet). In this process, the "Fake" arises from the mis-identification of a jet as a lepton. This process is signal-like when the W decays leptonically ($W \rightarrow \ell\nu_\ell$). This background can therefore be greatly reduced by the $E_T^{\text{miss}}/\sqrt{H_T} < 3.5$ GeV$^{1/2}$ requirement. Furthermore, in ATLAS, the jet suppression is at the level of 10^{-5} [331], so only jets in the tails of the detector response are misidentified as leptons. However, due to the large production cross-section of jets at the LHC, it is possible that the background is non-negligible. Such events, in which a "fake" or non-prompt electron signature is produced, can be studied by looking at the di-electron events with the same electron charge (same sign). A thorough discussion of Fake electron signals at the ATLAS detector is presented in Ref. [332].

Additional sources of same sign electron events can arise from the mis-identification of the electron charge. Primary sources of this mis-identification of the electron charge can be the matching of an incorrect track to the electron candidate, or a mis-measurement of the curvature of the primary electron track. The charge of the electron is reconstructed by measuring the curvature of the electron track in the strong magnetic fields in the ID. The curvature of a track as the inverse of its radius can be calculated using Equation 6.4.1.

$$C = \frac{1}{R} = B_z \frac{q}{p_T} \tag{6.4.1}$$

where B_z is the magnetic field strength in the direction of the beam axis and the charge of the electron, $q, \in -1, 1$. From Equation 6.4.1, it can be seen that C is inversely proportional to the p_T of the electron. Therefore, at large values of p_T, the curvature of the track can become small. Any scattering processes within the detector leading to an alteration of the track of the electron could lead to a false measurement of the signage of the curvature, and as such, a mis-identification of the charge of the electron. The measurement and suppression of charge mis-identification is fully discussed in Ref. [333].

The contribution of same sign events is studied in the Signal, Sideband and Extended Sideband regions. The exact same selections are applied as those described in Table 6.1, with the exception that the OSSF selection is reversed, to require same sign, same flavour (SSSF) leptons. These regions are then combined to maximise the statistics. Additionally, events are required to have $m_{LQ}^{Av} > 400$ GeV. This selection is imposed such that the fake estimate is not driven by low p_T contribution, ensuring that the estimate is relevant in the

high m_{LQ} region in which we set our limits. The same sign m_{LQ} distribution is shown in Figure 6.6, in which it can be seen that the prediction from MC is in good agreement with the data. The majority of fakes in the MC come from the W+jets sample. The other backgrounds arise due to the charge of one electron being reconstructed wrongly (charge flip), as previously mentioned.

No evidence is shown for a non-negligible contribution from multi-jet events (where both electrons are fake). Additionally, the this contribution was checked and found to be negligible for muons in other, similar analyses [318]. As such, this process is not considered, however the error on the fakes from the W+jets is adjusted to include a possible contribution. The total data from Figure 6.6 is $N_{\text{data}} = 213$ compared with a total expectation of $N_{\text{Tot}} = 203$ of which the number from the W+jets MC is $N_W = 81$. The fractional statistical error on the fakes is $\sqrt{(N_{\text{data}})}/N_W = 0.19$.

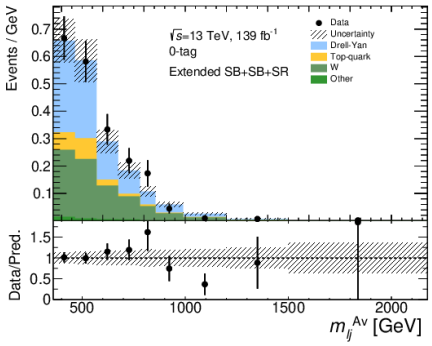

Figure 6.6: Distributions of m_{LQ}^{Av} in the 0 tag same sign signal region for the electron channel in the combined extended SB, SB and SR.

The contribution from Z+jets, $t\bar{t}$ and di-boson processes is not precisely known, as the probability of charge flip may not be accurately simulated. This is studied in the same sign Z CR, shown in Figure 6.7. The fake rate is very small due to the large Z contribution, with the agreement being within 10%. This is therefore applied as a systematic uncertainty on the determination of the fakes, i.e. the systematic fake contribution is $0.1(N_{\text{Tot}} - N_Z)/N_Z = 0.16$.

The combination of these two errors in quadrature therefore provides the total error on the fake contribution assigned to the W+jets MC as $\sqrt{0.16^2 + 0.19^2} = 25\%$.

6.4.3 Systematic uncertainties on the Background Modelling

A data driven approach is used to determine the uncertainty on the MC prediction of the Z/DY+jets and $t\bar{t}$ background processes. A data driven approach was chosen as it provides a real and direct insight into the mis-modelling of these processes specific to our analysis

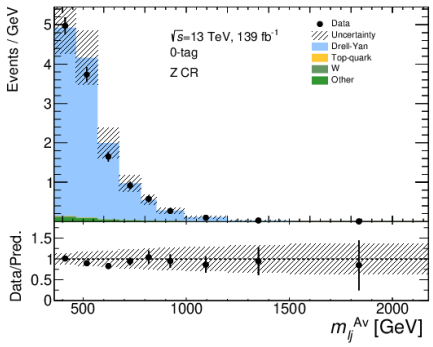

Figure 6.7: Distributions of m_{LQ}^{Av} in the 0 tag same sign Z CR for the electron channel.

regions, in a way that encompasses all sources of experimental and theoretical discrepancies. This method therefore is used in place of some of the experimental uncertainties. This is because the discrepancy between data and the MC estimate is due, at least in part, to these sources, such as the uncertainty on the jet energy resolution, or the lepton specific systematics (energy scale, identification and reconstruction etc). These uncertainties are therefore not evaluated for the Z/DY+jets and $t\bar{t}$ processes to avoid the double counting of such errors. The Flavour Tagging (FTAG) uncertainties, however, could still change the normalisation between the different regions of tag multiplicity. These effects are not accounted for in this study, and as such FTAG uncertainties are separately evaluated for the Z/DY+jets and $t\bar{t}$ processes. The procedure for evaluating these uncertainties is the same as is discussed in Section 6.4.5

The SB, Extended SB and Z CR regions were used to derive the uncertainty on the Z/DY+jets process. Of these, the regions dominated by the Z/DY+jets process were studied, and the region presenting the largest discrepancy between data and MC was then used to derive the uncertainty on this process. In this way, the error evaluated should reflect the most conservative estimate.

Figure 6.8 shows the mass distribution of the higher mass LQ candidate $m_{\ell j}^{max\,1}$ in the 0, 1 and 2-tag Z CRs. In these plots the Z+jets components have been scaled by a factor of 1.1 for illustrative purposes.

From these distributions, it is evident that the Z/DY+jets process is not well described in MC, and this is shown to be an effect that increases with $m_{\ell j}^{max}$. Therefore, based on the discrepancy observed in these distributions, two logarithmic error functions were derived empirically, of;

$$\sigma = \pm 0.2 \log(m_{LQ}/800\,\text{GeV}) \tag{6.4.2}$$

[1]The variable, $m_{\ell j}^{max}$ was chosen, as it maximises the statistics in the higher mass region, in which the uncertainty is expected to be of greatest importance.

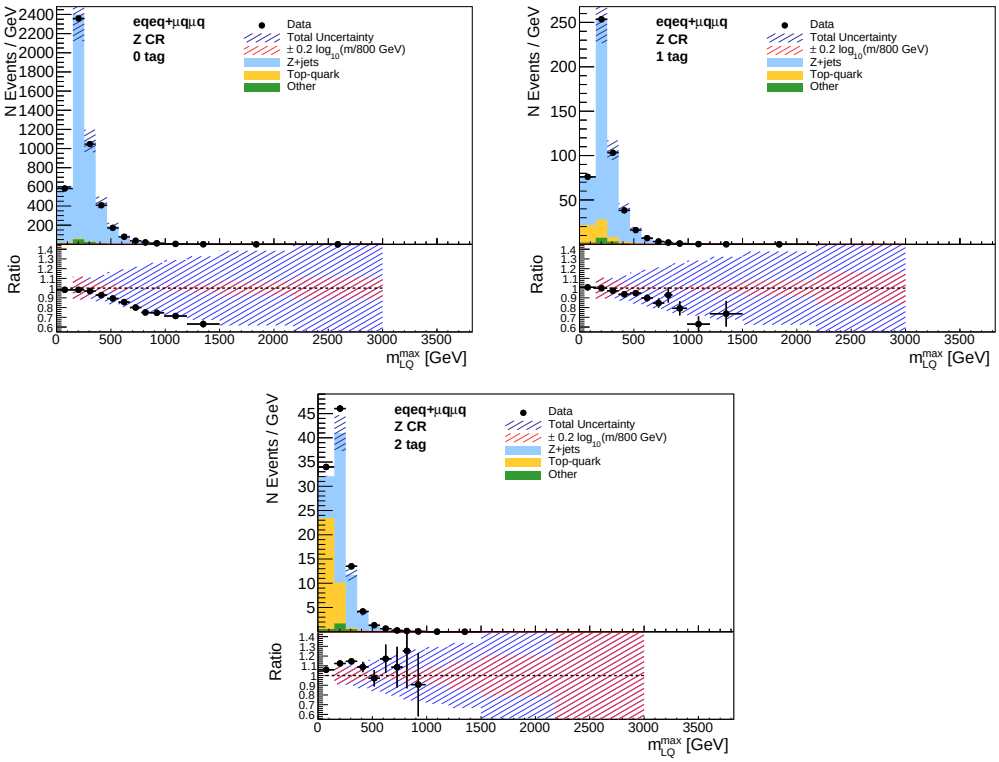

Figure 6.8: Distributions of m_{LQ}^{max} in the 0 tag, 1 tag and 2 tag Z control regions. The ratio shown is Data / MC. The electron and muon channels are combined in these plots. The Z+jets MC has been scaled by 1.1 for illustrative purposes. The total uncertainty (blue hatched) shown is formed of the two components $\sigma = \pm 0.2 \log(m_{LQ}/800\,\text{GeV})$ (red hatched) and $\sigma = \pm 0.4 \log(m_{LQ}/200\,\text{GeV})$.

and

$$\sigma = \pm 0.4 \log(m_{LQ}/200\,\text{GeV}). \tag{6.4.3}$$

The combination of these errors in quadrature is shown to cover the total disagreement between data and MC, as shown by the blue uncertainty band in Figure 6.8. The decision to split the uncertainty into two components was taken such as to provide an additional degree of freedom in the form of an additional nuisance parameter in the profile likelihood fit. This decision also provides an additional pivot point in the formulation of the total uncertainty, such that the combined error function does not reach '0' at any point of the distribution.

The other regions dominated by the Z/DY+jets process are the 0-tag extended SB and SB regions, as shown in Figure 6.9. It is found from these distributions that, as the uncertainty derived in the 0-tag Z CR is maximal, this error is then sufficient to describe any uncertainty on this process in all other regions also. The trend, shown in these plots, of an improving data / MC agreement continues towards the SR.

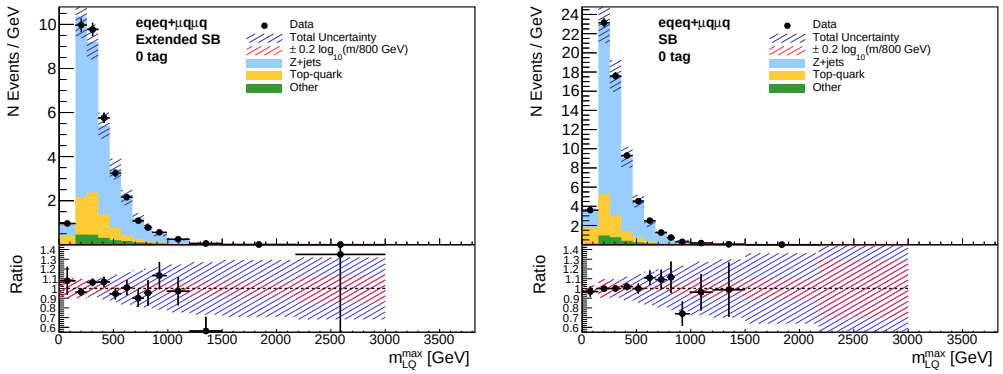

Figure 6.9: Distributions of m_{LQ}^{max} in the 0 tag extended SB and 0 tag SB regions. The ratio shown is Data / MC. The electron and muon channels are combined in these plots. The Z+jets MC has been scaled by 1.1 for illustrative purposes. The total uncertainty (blue hatched) shown is formed of the two components $\sigma = \pm 0.2 \log(m_{LQ}/800\,\text{GeV})$ (red hatched) and $\sigma = \pm 0.4 \log(m_{LQ}/200\,\text{GeV})$.

The modelling uncertainty derived herein on the Z/DY+jets process is taken to be uncorrelated between the different Z processes simulated, of Z+light, $Z + cX$ and $Z + bX$.

The modelling uncertainty on top-quark modelling is derived in a similar way. Here, we find that the 1 and 2 tag Top CRs have the largest top contribution of all regions. As seen in Figure 6.10, the agreement between data and MC is much better for this process than that of the Z/DY+jets. As such, an alternative error is proposed, of;

$$\sigma = \pm 0.5 \log(m_{LQ}/200\,\text{GeV}), \tag{6.4.4}$$

which covers any discrepancy between data and MC. The normalisation of the $t\bar{t}$ process is then floated as a free parameter in the profile likelihood fit. In the 0-tag Top CR, an

additional 30% error is assigned which covers the difference between data and Monte Carlo in this region, as shown in Figure 6.10.

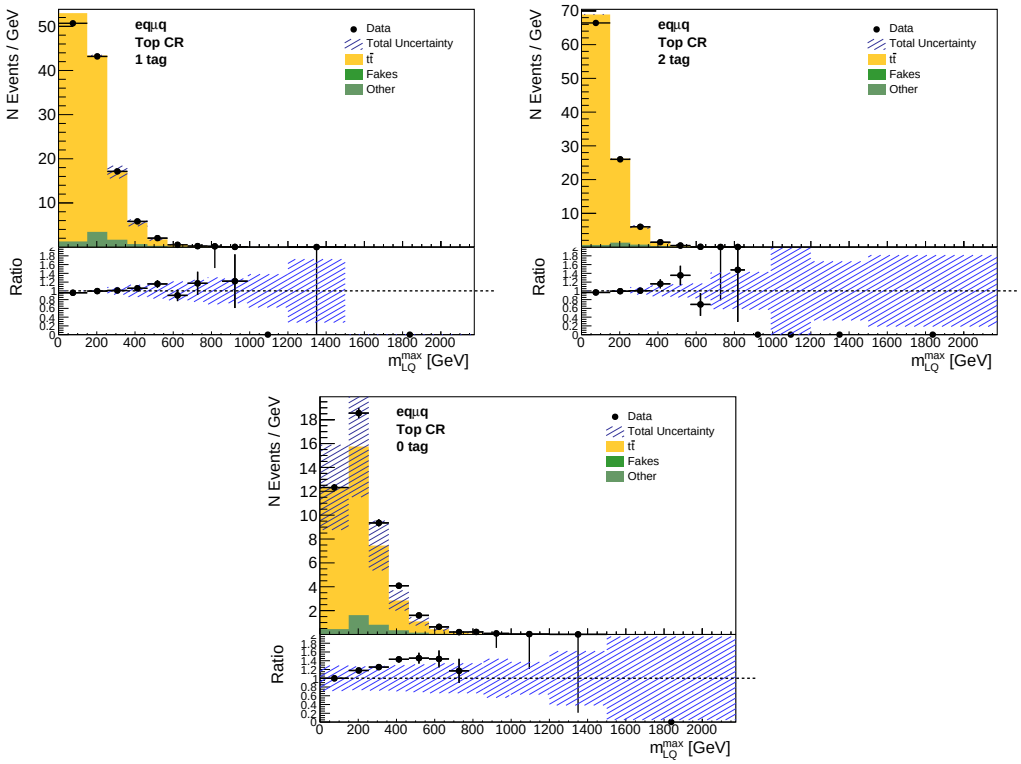

Figure 6.10: Distributions of m_{LQ}^{max} in the 1 and 2-tag Top CRs (top) and 0-tag Top CR (bottom). The ratio shown is Data / MC. The uncertainty shown is $\sigma = \pm 0.5 \log(m_{LQ}/200\,\text{GeV})$. In the 0 tag plot, the additional 30% uncertainty is also shown.

Single top theory uncertainty

Single top-quark production in association with a W boson is common in ATLAS with large cross-sections at 13 TeV, as shown in Table 6.7 [171].

Single top decay processes constitute a sub-dominant background in all regions of the analysis. In the 1 and 2-tag SRs and Top CRs, the contribution is at most $\mathcal{O} \sim 10\%$, and is negligible in the 0-tag region. In the 1- and 2-tag SB regions, however, the Wt contribution is significantly larger, and constitutes $\sim 40\%$ of the total background. This background is evaluated using MC, and a global uncertainty is applied to single top production. This uncertainty arises as the combination of various sources of theoretical uncertainties in the simulation of the Wt-mode of the single top processes, summed in quadrature. The decomposition of this uncertainty includes;

- uncertainties on the NLO cross-section (6%);
- shape variations due to changes on the renormalisation and factorization scales. The

impact of the latter is a few percent and is reported in Table 6.8. The full study in which these uncertainties were assessed can be found in the supporting documentation [339].

- different generator: a newly produced set of Sherpa 2.2.7 samples with correct W-line shape has been compared at truth-level to estimate differences in shape.[2] Differences in the range 400 - 2000 GeV are between 8% and 30%, the latter being found for light jets in the SR.

- interference model: an uncertainty due to the treatment of the interference between $t\bar{t}$ and Wt channels can be evaluated either considering the difference between diagram removal (DR) and diagram subtraction (DS) scheme [340][3] or considering the difference between nominal Wt+$t\bar{t}$ and $WWbb$ LO samples. The latter approach has been used in the R parity violating stop search, which is focused on the same event topology as considered in this analysis. This paper reports an uncertainty as large as 20% [178].

Therefore, a global uncertainty of 35% is applied to the normalisation of the Wt-mode production of the single top process. This is chosen as a conservative estimate of the uncertainty, taking the sum, in quadrature, of the upper estimates of each constituent source of uncertainty listed above.

Single top unc for variations of μ_R		
region	% Up	% Down
Electron Channel		
SR	4.17	1.81
Z CR	1.73	-9.6
SB	-2.41	-12.51
SB Extended	2.26	1.31
Muon Channel		
SR	9.6	-4.59
Z CR	3.03	-0.8
SB	1.89	-8.88
SB Extended	7.77	-5.57

Table 6.8: Evaluation of the uncertainty in the single top process due to variations in the factorization scale μ_R. The full study in which these uncertainties were assessed can be found in the supporting documentation [339].

[2] A bug has been recently identified on the nominal Powheg samples, with the W-line shape of the directly produced W boson being on shell only (narrow). The impact of this effect is analysis-dependent and it is taken here as part of the generator uncertainty.

[3] DR involves removing the LO $t\bar{t}$ modes from the Wt process at the amplitude level, and DS involves removing them at the cross-section level. The difference between these two approaches reflects the interference between the two production modes.

Summary of Modelling Uncertainties

In this section, we have discussed sources of systematic uncertainty due to fake leptons (to which we assigned a global 25% uncertainty on the W+jets normalization), modelling uncertainties in the Z/DY+jets and Top processes, to which we assigned the error functions presented in Equations 6.4.2 - 6.4.4, and an uncertainty on the extrapolation of the $t\bar{t}$ process to the high m_{LQ}^{Av} region, as well as theoretical uncertainties in the description of the single top process, to which we assign a normalization uncertainty of 35%.

In addition to the errors discussed, the $Z + cX$ and $Z + bX$ processes are each assigned a 10% normalisation uncertainty. This represents the largest difference between data and MC, after an overall scale is applied, which is observed in the Z control region for any number of b tags. For the smaller backgrounds a normalisation error of 30% is used for the total of the di-boson expectation. The full set of errors discussed in this section, are summarised in Table 6.9.

6.4.4 Signal studies

The signal Monte Carlo for the pair production of scalar LQs used in this analysis was generated using MADGRAPH5AMC@NLO version 2.6.0 [341] and showered using PYTHIA 8.230 [342] with the `A14N30NLO` UE tune [343]. The ME calculation was performed at tree level and combined with the PS using the CKKW-L prescription, with the matching scale set to $\frac{1}{4}$ of the m_{LQ}. For the Parton Distribution Function (PDF), the NNPDF2.3 LO set [344] was used. These samples were generated with their Yukawa coupling's set to $\lambda = 0.3$ and with a branching ratio of 0.5 to charged leptons. A subsequent re-scaling was performed to provide the statistics equivalent to the model assumption used in this analysis, which is a branching ratio of 1. This re-scaling is discussed in Section 6.4.4. The samples analysed are then normalised to the cross-sections calculated for direct top-squark pair production. These are produced via the same channels as LQ pair production, and both are massive, coloured, scalar particles. The calculations for top-squark pair production are made at approximate NNLO in QCD with resummation of next-to-next-to-leading-logarithm soft gluon terms (NNLO+NNLL) [345], as this is the "best" available cross-section calculation for this process. Variations of key parameters used in this calculation are used to evaluate the uncertainty. Parameters considered include the factorization and renormalisation scales, α_S, and PDF variations. A discussion of the top-squark pair production is provided in Section 6.4.4.

NNLO+NNLL $\tilde{t}$ pair production cross-section

LQ pair production is topologically identical to the pair production of the super symmetric top quark ($\tilde{t}$), as can be seen in Figure 6.11. As such, the theoretical calculation of the pair-produced $\tilde{t}$ production calculated at NNLO + NNLL in Ref. [345] can be used in

the comparison to the observed and expected cross-sections determined in this analysis, and in the re-scaling of signal yields. The $\tilde{t}$ pair-production cross-sections calculated in this paper were calculated using the 68% C.L. ranges of the `CTEQ6.6` (following `PDF4LHC` recommendations). This includes the evaluation of the uncertainty in the scale of α_S with `MSTW2008` PDF sets and variations of μ_R and μ_F. A nominal cross-section is then obtained using the midpoint of the envelope and the uncertainty is taken to be half the full width of the envelope. The determined uncertainties range from 6.65% for a mass of 300 GeV, to 24.38% for a mass of 2 TeV. The full list of cross-section calculations and the uncertainties are listed in Table 6.10, and these are the values then used in the comparison to the limits.

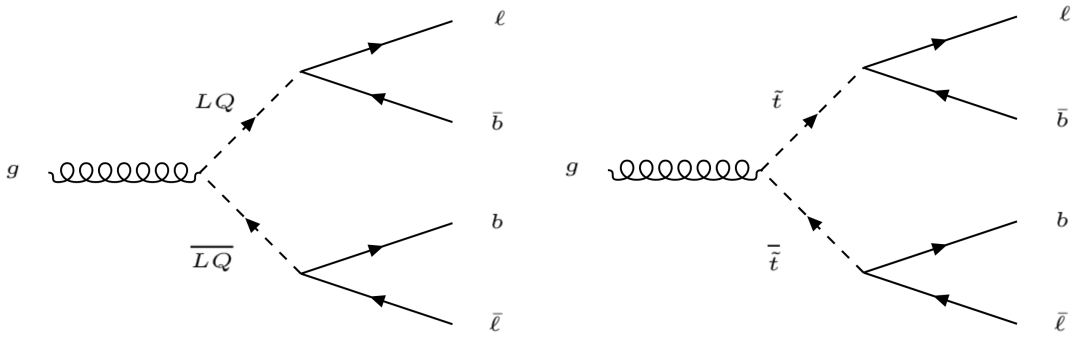

Figure 6.11: Figure showing the pair production of the up type LQs (left) and the pair production of the supersymmetric top quark (right).

Theoretical uncertainties on the Signal MC

Table 6.10 presents the cross-sections calculated to NNLO+NNLL, with an evaluation of the uncertainties on the cross-section due to effects from the variations of factorization and renormalisation scales μ_R, μ_F, of α_S, and PDF variations. In addition to these sources of uncertainty in the theoretical calculation of LQ cross-sections, uncertainties are evaluated to take into account the impact on the acceptance due to variations in the scales and shower parameters of the MC samples. These sources of uncertainty were evaluated by generating specific MC samples of 20,000 events with the "up" and "down" values of each considered parameter. For the scale factors, the values of μ_R and μ_F were varied by a factor of 2 (1/2) for the up (down) variation. For the shower (FSR) variations, samples were generated with a version of the `A14` tune which uses the `Var3c` [343] set of variations.[4] These dedicated samples are then compared to the nominal MC samples. The values for the up and down shift on the signal due to each source of uncertainty is then documented in Table 6.11 for representative LQ mass samples. An overall uncertainty of 3% is assigned for signals

[4]These represent variations to the set of tuned generator parameters that are defined in the `A14` tune. Importantly, this includes variations on the value of α_S. The full parameter set can be found in Ref. [343].

with $m_{LQ} < 1$ TeV and 5% for those with $m_{LQ} > 1$ TeV. Figures 6.12 and 6.13 show the invariant mass and transverse momentum of candidate LQs for a representative mass value.

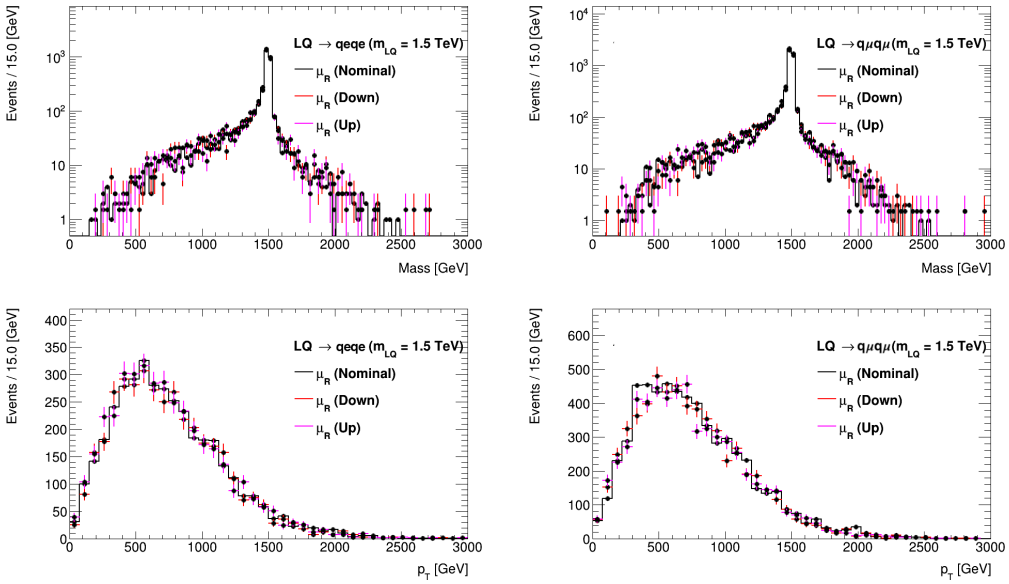

Figure 6.12: Mass and p_T of the leading LQ candidate from MC, as reconstructed in the Signal Region for a LQ signal of a 1.5 TeV LQ decaying as $LQ \to se(\mu)$ left (right). This is shown for the nominal sample used, as well as for samples generated with the value of the renormalisation μ_R and factorisation μ_F scales varied to 0.5 (Down) and 2 (Up).

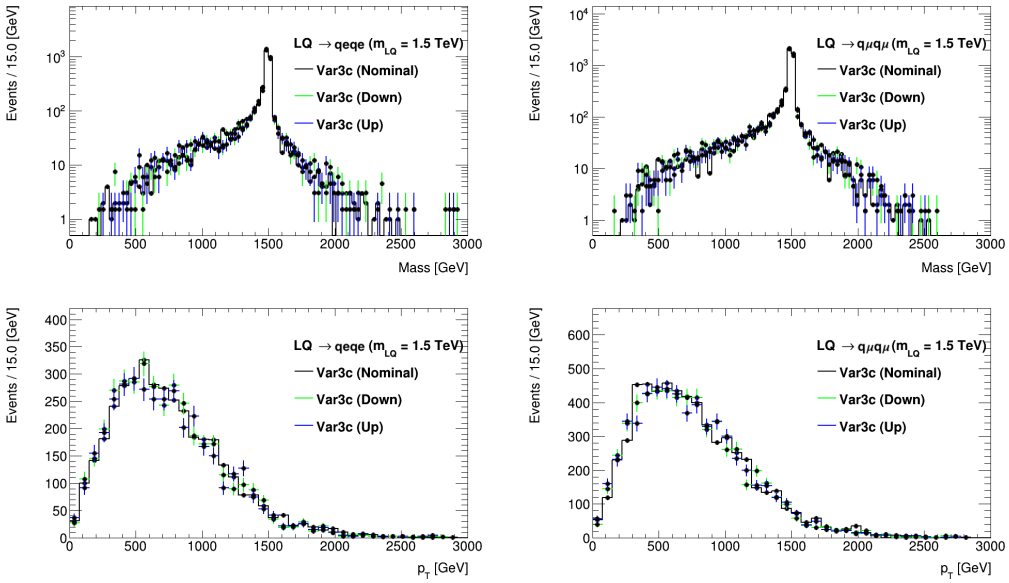

Figure 6.13: Mass and p_T of the leading LQ candidate from MC, as reconstructed in the Signal Region for a LQ signal of a 1.5 TeV LQ decaying as $LQ \to se(\mu)$ left (right). This is shown for the nominal sample used, as well as for samples generated with the Up and Down of the Var3c variants of the `A14` tune

β, BR Discrepancy

The Signal MC samples used in this analysis are produced with a setting of $\beta = 0.5$, a re-weighting procedure is applied to the events, to be able to study the whole range of possible β values, which follows the procedure outlined in Ref. [166]:

$$w(qvqv) = \frac{y^2}{x^2} \tag{6.4.5}$$

$$w(q\ell q\ell) = \frac{(1-y^2)}{(1-x^2)} \tag{6.4.6}$$

$$w(q\ell qv) = \frac{2y(1-y^2)}{2x(1-x^2)} \tag{6.4.7}$$

where $x = BR(LQ \to qv)$ and y is the target branching ratio (in this case, 1).

For decays to the heavy flavour quarks, the branching ratio must first be calculated for the signal LQ mass following the procedure outlined in Section 2.5. The sample compositions are then checked at `TRUTH` level for LQ masses of 400 GeV, 1 TeV and 1.5 TeV to estimate gamma. The exact weightings calculated can be seen in Table 6.12.

6.4.5 Experimental Systematics

Experimental uncertainties on the signal yields are incurred when selecting the objects used in the reconstruction of our LQ candidates. The dominant sources of uncertainty vary in the different LQ signal channels. In the reconstruction of the light signals ($LQ \to q\ell$), uncertainties due to the lepton identification and jet energy scale and resolution are dominant. In the reconstruction of the other considered processes ($LQ \to b(c)\ell$), flavour tagging (FTAG) efficiencies and mis-tagging rates are more prevalent. A thorough discussion of how these uncertainties are evaluated follows.

Electron Systematics The energy of electrons measured in MC is weighted to replicate the energy scale measured in data. This is achieved using weights provided by the e/γ working group (WG) [346]. A smearing is also applied to the energies measured in MC to replicate the limited resolution available in data. The e/γ WG also provide the $\pm 1\sigma$ variations of these weights, to be applied as the up and down systematic uncertainties. The efficiencies associated to the triggering, reconstruction, isolation and identification of electrons are measured in data using a tag-and-probe selection.[5] These measurements are then compared to simulation, and corresponding weights are determined for each efficiency, such as to correct each simulated event to data. Again, these weights are supplied by the

[5] In this method, $Z \to ee$ and $J/\Psi \to ee$ decays are used to evaluate efficiencies. This is done by defining a "*tag*" electron with strict selection criteria, and then measuring the efficiencies of the different criteria using the secondary "*probe*" electron.

e/γ WG. In this way, a separate uncertainty is provided for each of the efficiencies, as well as the reconstruction, identification, trigger and isolation scale factors. Uncertainties on the aforementioned scale factors are at a level of less than 6% [296, 347]. Details of the methods used in the evaluation of these weights and uncertainties can be found in Ref. [348].

Muon Systematics Similarly, calibrations and uncertainties are evaluated for the muon momentum scale, resolution, and each efficiency scale factor. These measurements are provided by the Muon Combined Performance (MCP) group [349], and are obtained by evaluating the invariant mass distributions of $Z \to \mu\mu$ and $J/\Psi \to \mu\mu$ decays in MC to those observed in data [350]. Uncertainties on the identification efficiency, trigger efficiency, isolation efficiency, energy scale and resolution account for as much as 10% [296, 347] of the total MC estimate.

Jet Systematics Uncertainties pertaining to the Jet energy scale and resolution are evaluated based on their respective measurements in data [351, 352]. This has 23 scale and 8 resolution uncertainties, with the total uncertainty accounting for up to 2% of the signal yield. An additional uncertainty on the efficiency of the JVT is also considered.

Flavour Tagging Systematics Scale factors are evaluated for the efficiency of both b and c tagging, as well as the probability of mis-tagging such as to calibrate simulation to data, as mentioned in Section 5.2.3. Uncertainties on these flavour tagging (FTAG) scale factors are then evaluated by varying the p_T- and flavour-dependent scale factors applied to each jet in the simulation within a range that reflects the systematic uncertainty in the measured tagging efficiency and mis-tag rates in data [353]. FTAG uncertainties on the efficiencies and mis-tagging rates dominate in all regions requiring at least one flavour-tagged jet. Uncertainties on b- and c-tagging are found to be up to 16% for $c\ell$ channels and 19% for the $b\ell$ channels.

Pileup reweighting The uncertainty in the re-weighting of samples to match the modelled pile-up profile is typically less than 1% [354].

Luminosity The luminosity measurement has a total uncertainty for the combined 2015–2018 dataset of 1.7% [189], obtained using the LUCID-2 detector [355].

6.4.6 Summary of Systematics

In this section, we have evaluated each background process contributing to the considered analysis channels, and discussed the methodology for evaluating any uncertainty on said processes. This is done as a mix of data-driven approaches, conventional methods as prescribed by the Combined Performance groups within ATLAS and some detailed modelling

of theoretical uncertainties in the parameters used in the Monte Carlo models. These uncertainties are then considered as additional "nuisance" parameters in the evaluation of the parameter of interest, μ, from the profile-likelihood fit.

NPs are parameters that introduce additional degrees of freedom in the fit. These NPs are evaluated in all regions considered in the fit, and the total scale of each NP can be modified by the fit to improve the data / MC agreement and to reduce the impact of the systematics. Using the Profile Likelihood method, we construct estimations of all NPs that are profiled out of our fit. These values form a Gaussian distribution around the measured nominal value, with a quoted uncertainty of $\pm 1\sigma$. This nominal value is nominally either 1 for a normalisation of a background, or 0 for a systematic uncertainty. These NPs are then modified by the fit to optimize agreement with the data. The modification of a NP can be in the form of a constraint of this uncertainty, or a pull of the scaling value away from 0 (1). This modification is performed when the measurement of a NP in a specific region either requires a scaling factor different from the nominal, or provides a constraint on the uncertainty quoted. These NPs then provide a freedom in the fit to ease such tensions that otherwise might prevent the fit from converging. These NPs can be ranked by the order of how much they are pulled away from there nominal value, as is shown in Figures 6.14 - 6.16, here showing the ranked effect on the μ value at a mass of $m_{LQ} = 1$ TeV. To help in understanding this plot, a mapping of the Systematic name, and the corresponding variation is provided in Table 6.13.

Channel		σ^{theory} [pb]	$\sigma^{observed}$ [pb]
$t\bar{b}$, $\bar{t}b$	(s-channel) (results at 8 TeV)	5.61 ± 0.22 (NLO+NNLL)	$4.8 \pm 0.8(\text{stat.})^{+1.6}_{-1.3}(\text{syst.})$
tW^-, $\bar{t}W^+$	(Wt-mode)	71.7 ± 3.8 (NLO+NNLL)	$94 \pm 10(\text{stat.})^{+28}_{-23}(\text{syst.})$
tq	(t-channel)	$136.0^{+5.4}_{-4.6}$ (NLO)	$156 \pm 5(\text{stat.}) \pm 24(\text{syst.})$
$\bar{t}q$		$81.0^{+4.1}_{-3.6}$ (NLO)	$91 \pm 4(\text{stat.}) \pm 14(\text{syst.})$

Table 6.7: Theoretical predictions [263, 334, 335] and ATLAS measurements [336–338] for the inclusive cross-sections of t-channel, s-channel and Wt-mode single top production. The uncertainties on the theoretical predictions include variations of the μ_R and μ_F, and PDF functions. The uncertainties on the measurements are driven by statistical and experimental systematic uncertainties.

Systematic Errors			
Process		Normalisation Uncertainty	Floated Normalisation
Z/DY+jets	Modelling Unc	Equations 6.4.2 & 6.4.3	yes
	$Z + (c)bX$	10%	no
Top	0-tag	30%	no
	other	Equation 6.4.4	yes
single top		35%	no
Fakes		25%	no
Diboson		30%	no

Table 6.9: Overview of systematic uncertainties derived in Section 6.4, and how they are treated in the Profile Likelihood Fit.

LQ_{Mass} [GeV]	σ_{LO}	$\sigma_{NNLO+NNLL}$	Error
400	$1.88\times10^{+00}$	$2.15\times10^{+00}$	6.99%
500	4.97×10^{-01}	6.09×10^{-01}	7.53%
600	1.64×10^{-01}	2.05×10^{-01}	8.12%
700	7.30×10^{-02}	7.83×10^{-02}	8.80%
800	2.93×10^{-02}	3.26×10^{-02}	9.53%
850	1.52×10^{-02}	2.16×10^{-02}	9.93%
900	1.20×10^{-02}	1.45×10^{-02}	10.33%
950	8.12×10^{-03}	9.91×10^{-03}	10.76%
1000	5.08×10^{-03}	6.83×10^{-03}	11.20%
1050	3.99×10^{-03}	4.76×10^{-03}	11.65%
1100	2.61×10^{-03}	3.35×10^{-03}	12.12%
1150	1.75×10^{-03}	2.38×10^{-03}	12.62%
1200	1.33×10^{-03}	1.70×10^{-03}	13.13%
1250	9.19×10^{-04}	1.22×10^{-03}	13.66%
1300	6.93×10^{-04}	8.87×10^{-04}	14.21%
1350	4.92×10^{-04}	6.46×10^{-04}	14.78%
1400	3.54×10^{-04}	4.73×10^{-04}	15.37%
1450	2.65×10^{-04}	3.48×10^{-04}	15.99%
1500	1.62×10^{-04}	2.57×10^{-04}	16.63%
1550	1.55×10^{-04}	1.91×10^{-04}	17.28%
1600	1.11×10^{-04}	1.42×10^{-04}	17.96%
1700	6.13×10^{-05}	7.96×10^{-05}	19.40%
1800	3.32×10^{-05}	4.51×10^{-05}	20.94%
1900	1.76×10^{-05}	2.58×10^{-05}	22.60%

Table 6.10: The Signal cross-section is shown for each mass hypothesis generated. Shown is the cross-section taken from the 2nd generation down type LQ signal, generated at Leading Order, with a branching fraction to charged leptons of $\beta = 0.5$. The cross-sections of the other LQ signals considered in this paper are the same to within a few percent. Also shown is the theory cross-section calculated at next-to-next-to-leading-order + next-to-next-to-leading-log (NNLO+NNLL) (with respective errors). The cross-sections shown here are a subset of the full cross-section calculation documented in [345].

Var3c				μ_R & μ_F			
Mass	Channel	Up	Down	Mass	Channel	Up	Down
2 TeV	sese	0.008	0.002	2 TeV	sese	-0.015	-0.039
	$s\mu s\mu$	-0.009	-0.021		$s\mu s\mu$	-0.003	0.003
	$cece$	0.019	0.108		$cece$	0.039	-0.037
	$c\mu c\mu$	-0.014	-0.031		$c\mu c\mu$	-0.056	-0.003
	$bebe$	-0.013	-0.035		$bebe$	0.067	0.027
	$b\mu b\mu$	-0.079	-0.048		$b\mu b\mu$	-0.052	-0.054
1.5 TeV	sese	0.003	-0.028	1.5 TeV	sese	0.025	-0.013
	$s\mu s\mu$	-0.011	-0.019		$s\mu s\mu$	-0.024	-0.022
	$cece$	-0.094	-0.02		$cece$	-0.072	-0.089
	$c\mu c\mu$	-0.003	0.009		$c\mu c\mu$	0.041	0.018
	$bebe$	-0.003	-0.076		$bebe$	-0.034	0.008
	$b\mu b\mu$	-0.011	-0.026		$b\mu b\mu$	-0.046	0.02
1 TeV	sese	-0.031	-0.034	1 TeV	sese	0.012	0.012
	$s\mu s\mu$	-0.013	-0.028		$s\mu s\mu$	-0.013	0.003
	$cece$	-0.098	0.021		$cece$	-0.046	-0.015
	$c\mu c\mu$	-0.041	-0.005		$c\mu c\mu$	0.018	0.008
	$bebe$	-0.053	-0.021		$bebe$	-0.052	0.036
	$b\mu b\mu$	-0.01	0.03		$b\mu b\mu$	-0.04	-0.011
0.4 TeV	sese	0.037	0.009	0.4 TeV	sese	-0.012	-0.019
	$s\mu s\mu$	0.012	0.01		$s\mu s\mu$	0.021	-0.014
	$cece$	-0.065	-0.078		$cece$	-0.08	0.001
	$c\mu c\mu$	-0.072	0.026		$c\mu c\mu$	-0.008	0.055

Table 6.11: Theory uncertainty on the Signal for variations of μ_R and Var3c. Measurements are taken in the Signal Region, as defined in Table 6.1

.

Mass [GeV]	N_{lep}	Number of Events	Analytical BR		Sample	
			$t+v$	$b+e$	$t+v$	$b+e$
400	2 Lepton	3602	0.399239	0.600761	0.398999	0.600167
1000	2 Lepton	2666	0.484999	0.515001	0.480625	0.516333
1500	2 Lepton	2529	0.493387	0.506613	0.5004	0.502892

Table 6.12: Summary of the branching ratio re-weightings calculated for three mass hypotheses.

SigAcc	MExtrap	MLQ*	FT*	norm*
The signal acceptance uncertainty	The uncertainty on the extrapolation of the $t\bar{t}$ background, as documented in Section 6.4.1	The modeling uncertainty on the different backgrounds, as documented in Section 6.4.3	Flavour tagging uncertainties	Background scale normalisations

Table 6.13: Summary of the naming convention used to describe the systematic variations in the pull and ranking plots. In this table, "*" refers to GNU globbing or a "wildcard".

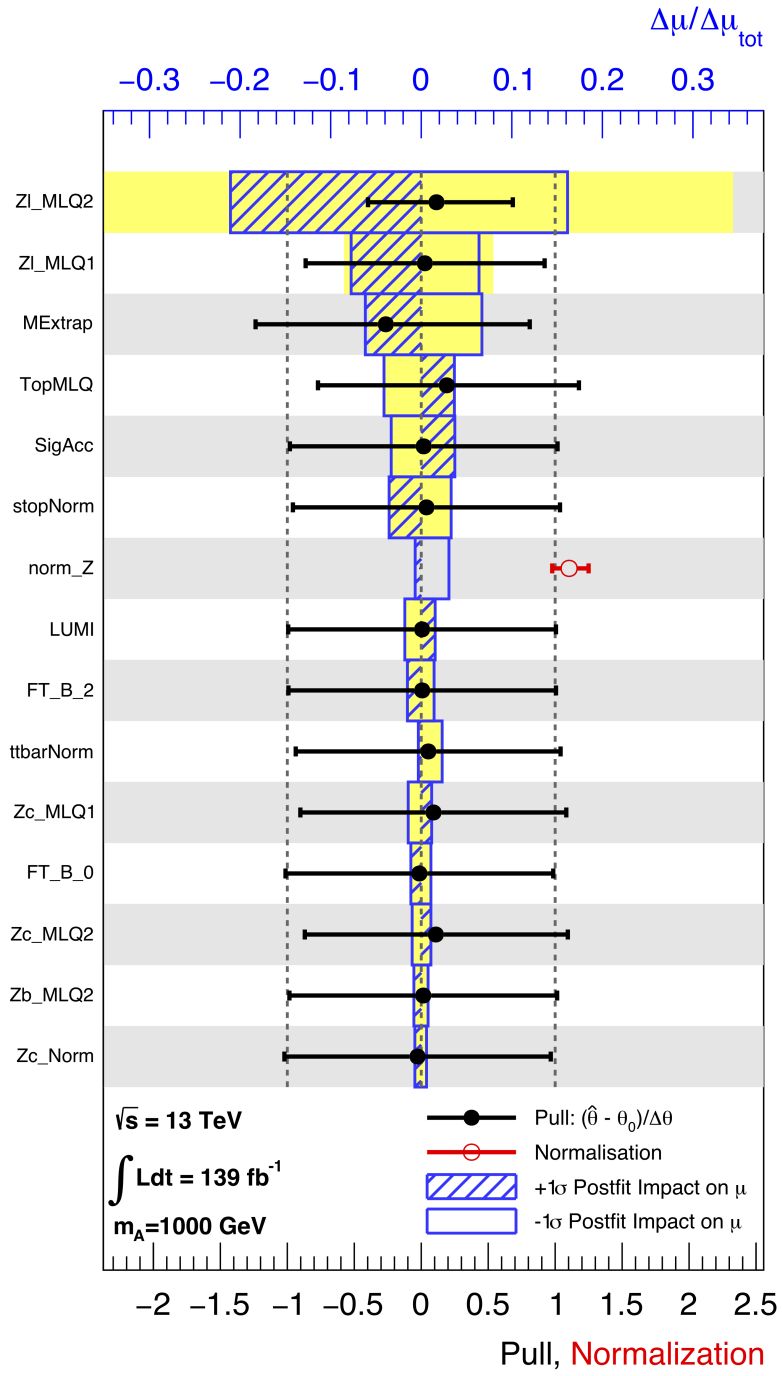

Figure 6.14: Effects of nuisance parameters on the signal strength ordered by effect on the measured μ value for the $s\mu s\mu$ channel with $m_{\mathrm{LQ}} = 1000$ GeV.

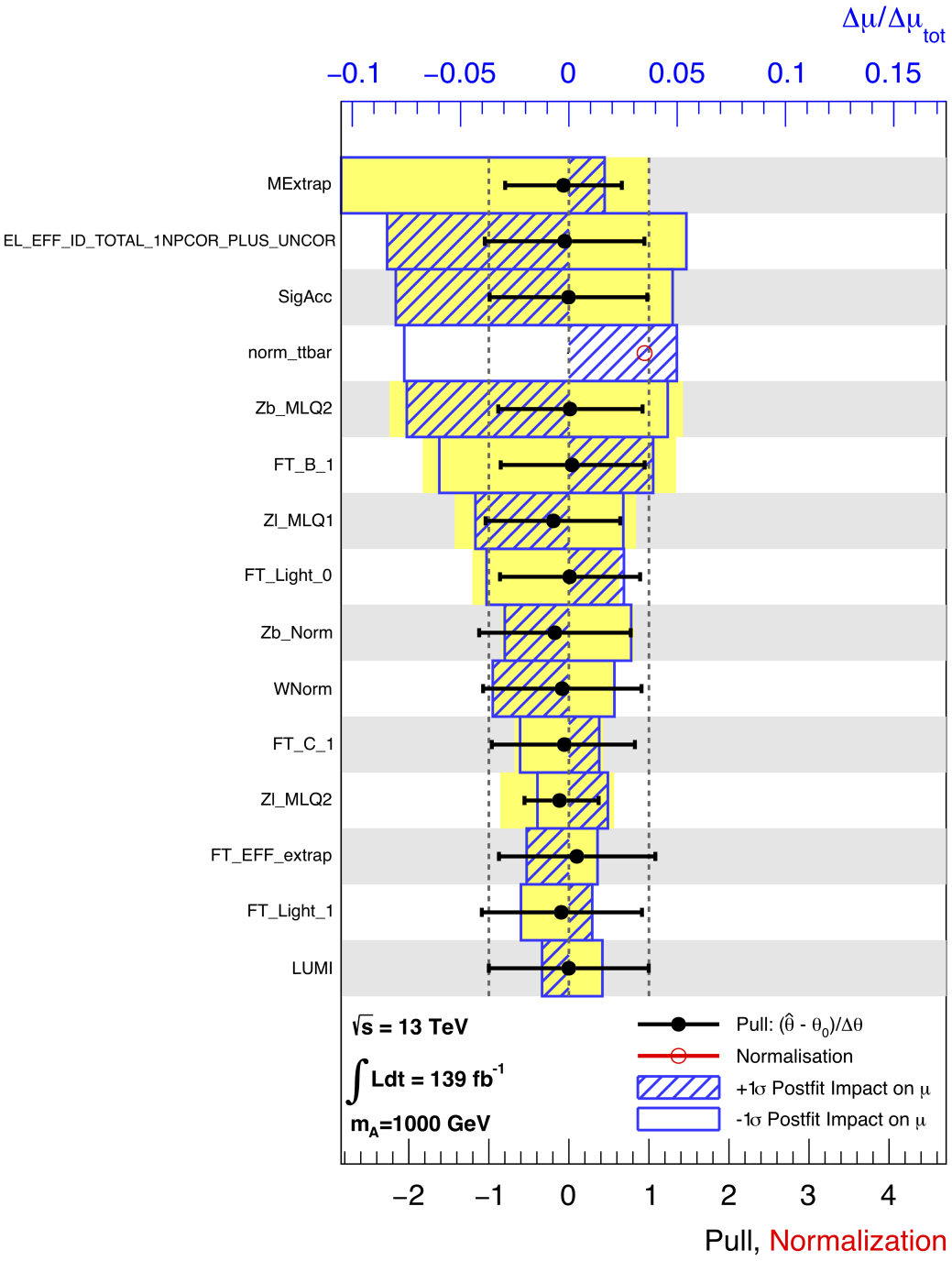

Figure 6.15: Effects of nuisance parameters on the signal strength ordered by effect on the measured μ value for the *bebe* channel with $m_{\mathrm{LQ}} = 1000$ GeV.

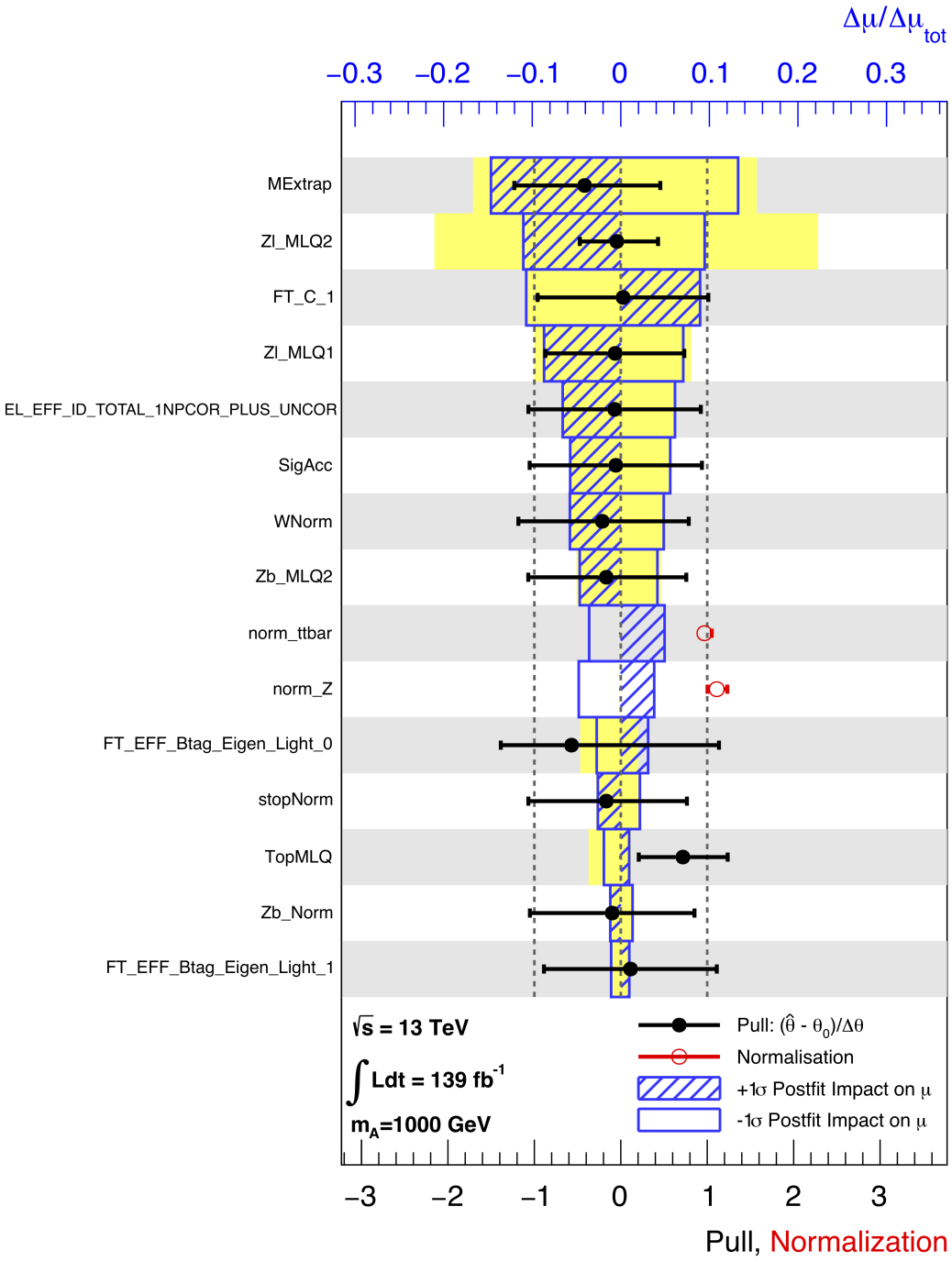

Figure 6.16: Effects of nuisance parameters on the signal strength ordered by effect on the measured μ value for the *cece* channel with $m_{\mathrm{LQ}} = 1000$ GeV.

Chapter 7

Results and Conclusions

In this Chapter, we shall present the statistical analysis of the data and Monte Carlo events selected in the search for leptoquark pair production. We shall then see the results of this analysis in Section 7.2, as well as the combination of these results with recent findings from other LQ searches in ATLAS, documented in Section 7.2.1. The subsequent conclusions are presented in Section 7.4. Additionally, we present the preservation of this analysis framework in Section 7.3, where we discuss the RECAST framework, and the public availability of the results via HEPData. This is done so that future analysts and theorists can easily use our results and re-interpret our work to new phenomenological models.

7.1 Fit Strategy

The main result of this analysis comes from the evaluation of the profile-likelihood fit, the details of which are discussed in Section 5.3 of Chapter 5, and follows the recommendations prescribed in the ATLAS statistics forum in Ref. [356]. Here, the signal distribution of the average mass of the two reconstructed LQ candidates is fitted to data. This is done to establish exclusion limits on the cross-section and mass of various LQ signal candidates. The variable m_{LQ}^{Av} is chosen, as it provides a better resolution of the mass peak than either of the separate reconstructed masses. As discussed in Section 6.4.6 the various sources of uncertainty in this measurement are treated as nuisance parameters in the fit whose values are unknown. As such, the values of these NPs are profiled out of the fit by estimating their values using the Maximum Likelihood theorem. For all fits, the Z+jets and $t\bar{t}$ normalisations are treated as free parameters. All other backgrounds (di-bosons, W and single top) are fixed to the MC expectation.

As discussed, separate analysis strategies have been developed in order to maximise the sensitivity of this search to each of the considered LQ decay modes. Separate fits are then performed for each of the LQ decay hypotheses, with the inclusion of different regions tailored to the strategy used in analysing each of the target LQ signals. For decays to the light quarks ($LQ \to q\ell$), the selection is agnostic to the multiplicity of tagged jets in the

event. In the fit of these decays, the pretag SR, SB and top CR are all used. For fits to decays to bottom quarks ($LQ \to b\ell$), events are selected based on the multiplicity of b-tagged jets. In this fit, the SR and SB in 0-, 1- and 2-tag categories are used together with the top CR in 1- and 2-tag region. For fits to decays to charm quarks ($LQ \to c\ell$), the selection targets events based on the multiplicity of both c- and b-tagged jets in the event. To fit these signals, the SR and SB in the untagged, c-tagged and b-tagged categories are used together with the top CR in the c-tagged and b-tagged categories.

As no statistically significant excess of data events were found in this search, upper exclusion limits were determined on the production cross-section as a function of the LQ mass for each considered signal hypothesis. This was accomplished by calculating frequentist CL_s values, following the methodology outlined in Section 5.3.2. The parameter of interest used in deriving these limits is the signal strength parameter "μ", which is defined as the ratio of measured number of signal events to the number of expected signal events from the leptoquark model. As mentioned in this section, following the results of Wilks [327] and Wold [328], it is shown that an asymptotic approximation can be used to reduce the complexity of these calculations. This approximation holds true in the large sample limit, taken to be for samples of $\mathcal{O} \sim 10$ events. However, bins in some SRs in this analysis approach this limit and, as such, it is important to verify the results found against the more computationally expensive Monte Carlo calculations, colloquially known as "Toys". This is presented in Section 7.1, and only small deviations from the asymptotic approximation are found in the higher mass region. Hence, the results presented in this analysis are determined using the asymptotic approximation.

Limits at 95% confidence level on the value of the signal strength μ are then computed by scanning values of the μ hypothesis, computing the CL_s exclusions and identifying the μ_{up} for which this value equals 0.05.

7.1.1 Limit comparison

According to Wilks' theorem [357], the distribution of $f(\tilde{q}_{\mu_{sig}}|\mu_{sig}|\theta)$ approximates to a χ^2 distribution with one degree of freedom in the high statistics region. This high statistics assumption holds well until around $\mathcal{O}$ 10 events. With sufficient statistics, the asymptotic method is used to approximate the p-value of the hypothesis test for each test statistic. However, in the high m_{LQ} bins of the distributions shown in Section 7.2, it is evident that the statistics are smaller so the validity of this approximation must be tested. As such, a comparison was made of the asymptotic approximation in this region, against the approach of performing pseudo experiments for each value of μ_{sig} (referred to as toys). This comparison was performed using the statistical framework package; "HistFitter", as documented in Ref. [358]. In this approach, work-spaces produced in the calculation of the asymptotic limit were applied in the HistFitter framework, with no modification. Signals of $m_{LQ} = 1$ and 1.8 TeV were then tested, for the decay process $LQ \to se$. These

tests are documented in Tables 7.1 and 7.2 with 5,000 and 10,000 pseudo experiments[1] used respectively.[2]

Limit	Asymptotic Limit	Toys Limit
Observed	0.05359	0.05426 ± 0.00044
Expected	0.03333	0.03315
+1 σ	0.04638	0.04733
-1 σ	0.02401	0.02355
+2 σ	0.06218	0.06488
-2 σ	0.01789	0.01669

Table 7.1: Comparison of 95% CL limits as calculated using the asymptotic method of approximating the p-values, against the HistFitter approach using pseudo experiments for each value of μ_{sig}. This is shown for a LQ at $m_{LQ} = 1$ TeV, decaying as $LQ \to se$. 5,000 pseudo experiments were performed for the calculation of the p-values using HistFitter.

Limit	Asymptotic Limit	Toys Limit
Observed	1.111	1.289 ± 0.034
Expected	1.222	1.431
+1 σ	1.701	2.253
-1 σ	0.881	1.010
+2 σ	2.280	40.000
-2 σ	0.656	0.844

Table 7.2: Comparison of 95% CL limits as calculated using the asymptotic method of approximating the p-values, against the HistFitter approach using pseudo experiments for each value of μ_{sig}. This is shown for a LQ at $m_{LQ} = 1.8$ TeV, decaying as $LQ \to se$. 10,000 pseudo experiments were performed for the calculation of the p-values using HistFitter.

It was found that at an m_{LQ} of 1 TeV, the limit is found to be in agreement with the asymptotic approximation. Figure 7.1 shows the distribution of the p-values calculated for a scan of μ_{sig} values for the 1 TeV $LQ \to se$ signal. For $m_{LQ} = 1.8$ TeV, as seen in Figure 7.2, we find that the limit agrees with the asymptotic approximation to within 1 σ, and so to minimise computational expenditure, it was decided to proceed with the asymptotic method. It is also found that the +2 σ limit at 1.8 TeV does not work with the present statistics.

[1] Pseudo-experiments are a "brute force" method of determining the distribution of our test statistic (q_μ). In this method, we generate pseudo data to populate the bins of our POI. We then normalize the resulting histogram, and use it as an approximation of the test statistic distribution. From this, we can calculate the observed value of our pseudo data. By repeating this process for a very large number of iterations, we may arrive at a reliable approximation of the distribution of q_μ.

[2] Fewer experiments were used at 1 TeV due to the increased computational load.

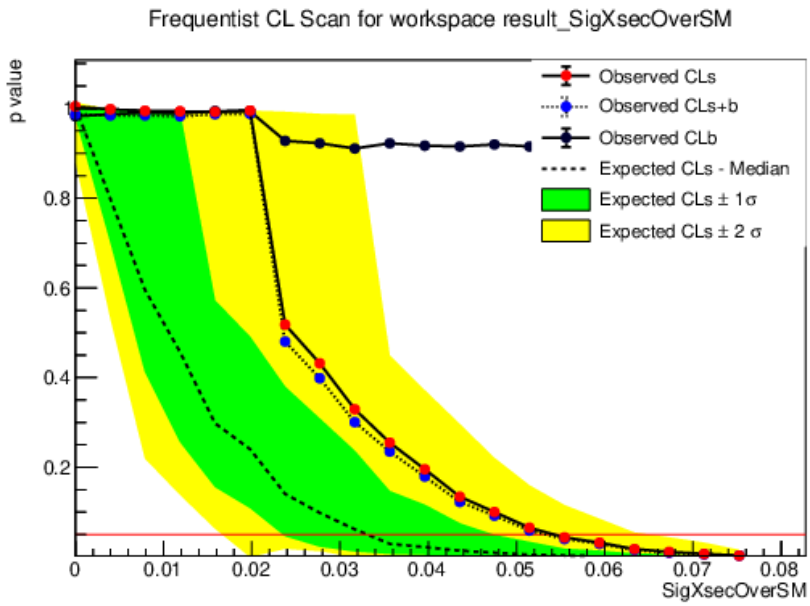

Figure 7.1: p-values calculated using 5,000 pseudo experiments, shown for a LQ at $m_{LQ} =$ 1 TeV, decaying as $LQ \to se$.

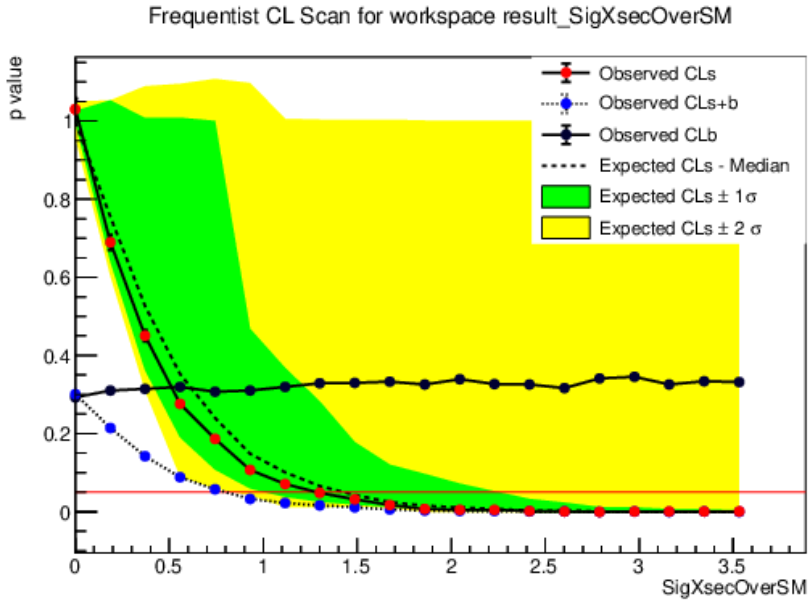

Figure 7.2: p-values calculated using 10,000 pseudo experiments, shown for a LQ at $m_{LQ} = 1.8$ TeV, decaying as $LQ \to se$.

7.2 Results

Profile likelihood fits are therefore performed following the statistical analysis documented in Section 7.1. Data / MC compatibility can be tested by performing a background-only fit, in which the signal strength, μ is fixed to 0. The post-fit plots are shown, for various analysis regions, in Figures 7.3 - 7.7 These plots, also show a signal LQ process with $m_{LQ} = 1$ TeV, at $\mu = 1$. Good agreement between data and the total SM prediction is observed in all SRs. No evidence is indicated for a leptoquark resonant within the mass range that the analysis is sensitive to.

Fits performed with no constraint on the signal strength are used to derive the expected cross-section limits on the signal, as discussed in Section 7.1. These results are shown in Figure 7.8. Here, limits are shown as a function of the LQ mass. Additionally, the fit can also be expressed as limits on the branching ratio to charged leptons, calculated as $\sqrt{(}\sigma_{\text{obs}}/\sigma_{\text{theory}})$, where σ_{obs} is the observed leptoquark pair production cross-section limit with $\beta = 1$ and σ_{theory} is the theory cross-section. These results are shown for each considered LQ decay, in Figure 7.9. This calculation is made using the assumption that there is zero acceptance to LQ decays involving neutrinos in the present analysis.

It can be seen that in the high mass region, limits in the electron channel consistently outperform those in the muon channel. This is due to the better electron resolution at high p_T which, as discussed in Section 6.2, leads to a worse performance of the $E_T^{\text{miss}}/\sqrt{H_T}$ cut in the muon channel. Additionally, decays involving b quarks have lower cross-section limits over most of the mass range due to the smaller backgrounds in the 1 and 2 tag categories.

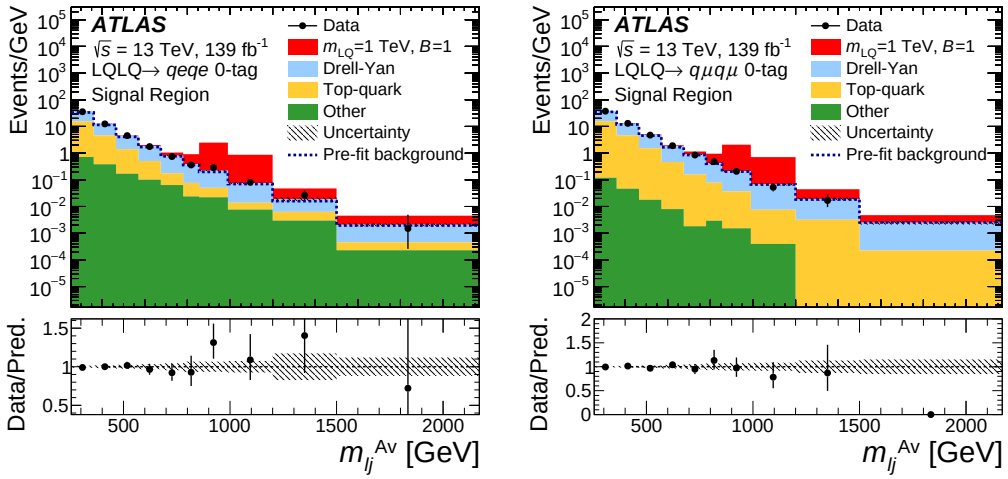

Figure 7.3: Post-fit distributions of $m_{\ell j}^{\text{Av}}$ in the signal regions pretag for the qe (left) and $q\mu$ (right) channels. The expected signals, shown for $m_{\text{LQ}} = 1$ TeV and $\mathcal{B}(LQ \to qe/q\mu) = 1$, are shown for illustrative purposes. The category "Other" refers to di-boson and W+jet production. The category "Top-quark" includes both $t\bar{t}$ and single-top processes. Data and predictions outside the depicted mass range are not used in the fit and are not shown.

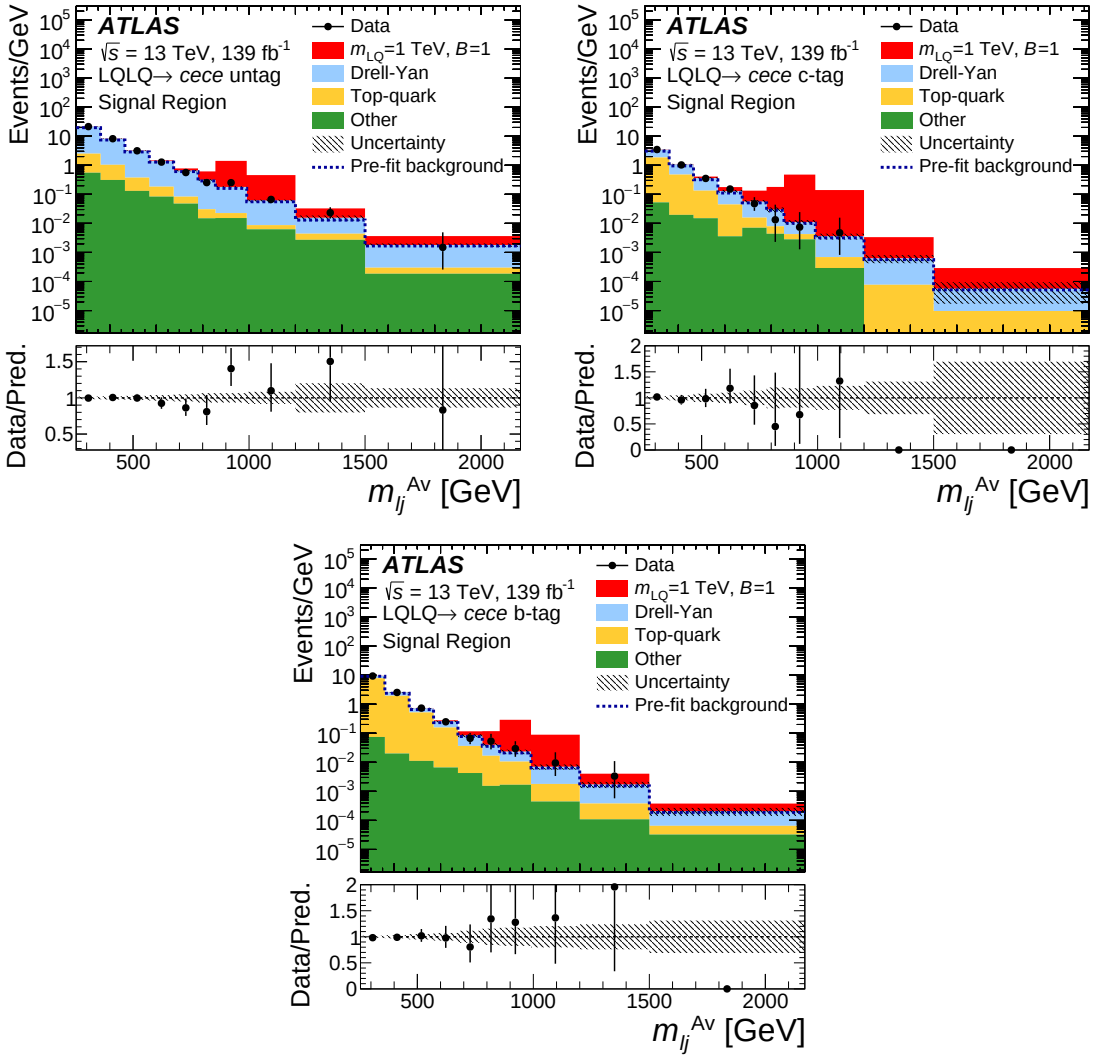

Figure 7.4: Post-fit distributions of $m_{\ell j}^{\mathrm{Av}}$ in the signal regions untagged (left), c-tag (middle), b-tag (right). The expected signals, shown for $m_{\mathrm{LQ}} = 1$ TeV and $\mathcal{B}(LQ \to ce) = 1$, are shown for illustrative purposes. The category "Other" refers to di-boson and W+jet production. Data and predictions outside the depicted mass range are not used in the fit and are not shown.

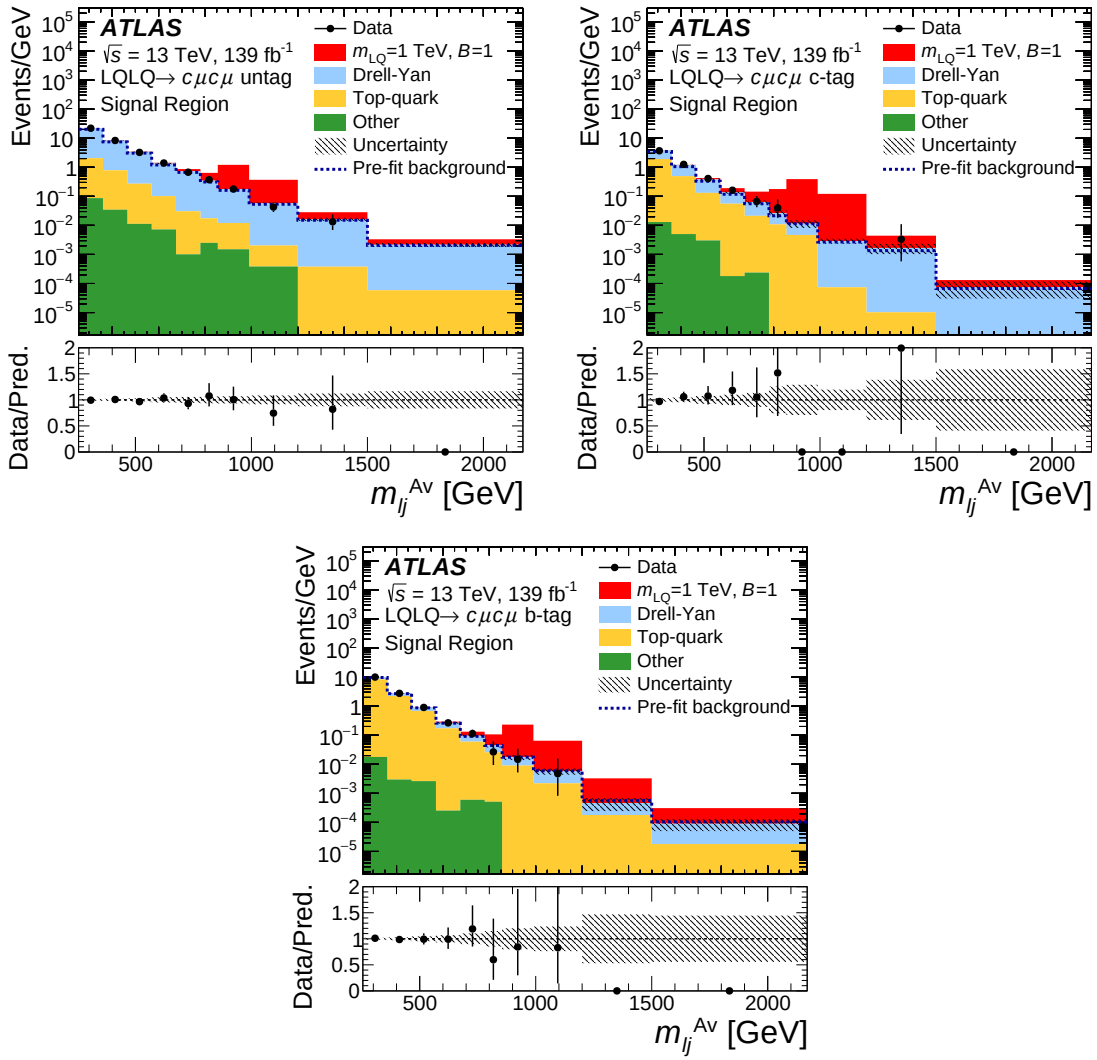

Figure 7.5: Post-fit distributions of $m_{\ell j}^{\mathrm{Av}}$ in the signal regions untagged (left), c-tag (middle), b-tag (right). The expected signals, shown for $m_{\mathrm{LQ}} = 1$ TeV and $\mathcal{B}(LQ \to c\mu) = 1$, are shown for illustrative purposes. The category "Other" refers to di-boson and W+jet production. Data and predictions outside the depicted mass range are not used in the fit and are not shown.

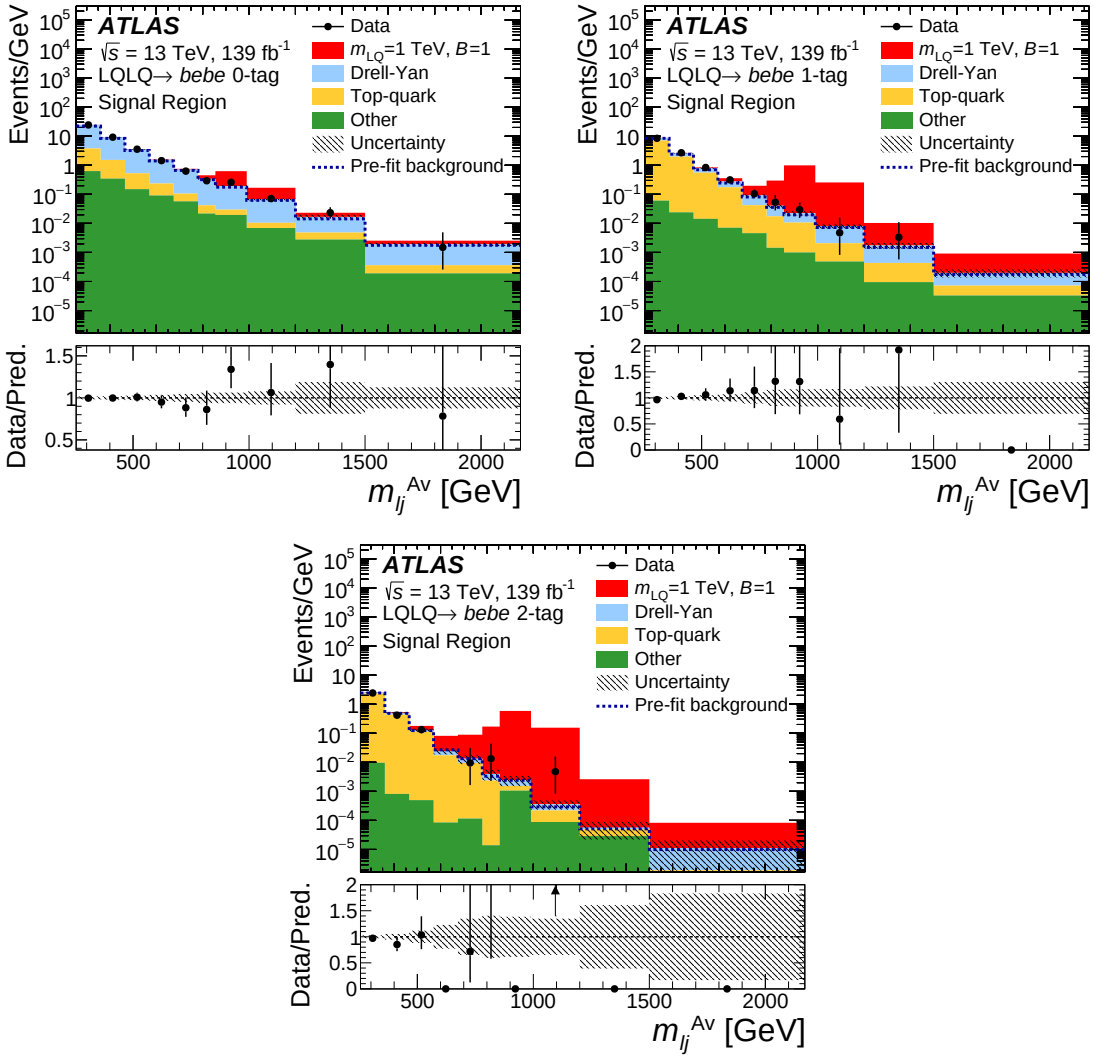

Figure 7.6: Post-fit distributions of $m_{\ell j}^{\mathrm{Av}}$ in the signal regions 0-tag (left), 1-tag (middle), 2-tag (right). The expected signals, shown for $m_{\mathrm{LQ}} = 1$ TeV and $\mathcal{B}(LQ \to be) = 1$, are shown for illustrative purposes. The category "Other" refers to diboson and W+jet production. Data and predictions outside the depicted mass range are not used in the fit and not shown.

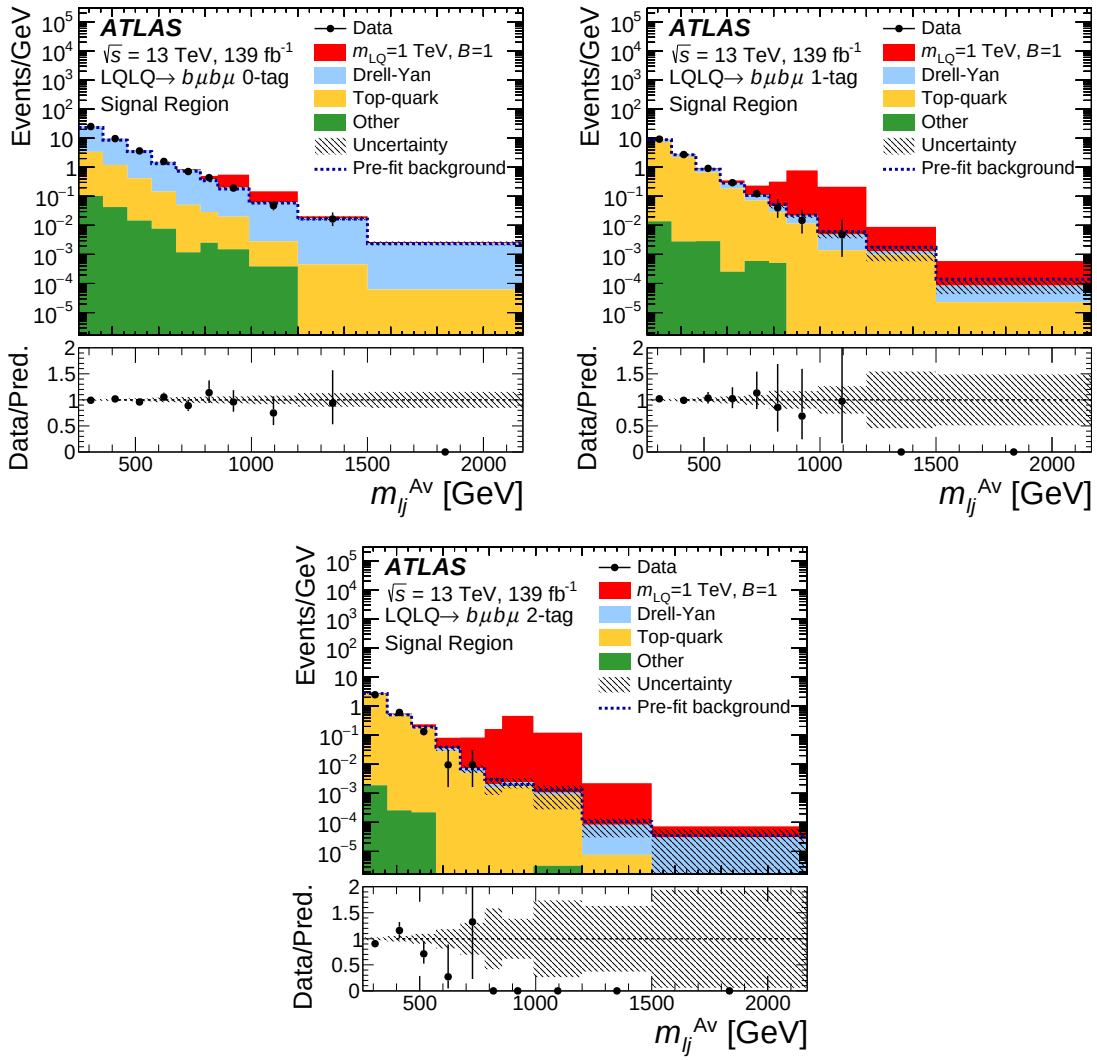

Figure 7.7: Post-fit distributions of $m_{\ell j}^{\mathrm{Av}}$ in the signal regions 0-tag (left), 1-tag (middle), 2-tag (right). The expected signals, shown for $m_{\mathrm{LQ}} = 1$ TeV and $\mathcal{B}(LQ \to b\mu) = 1$, are shown for illustrative purposes. The category "Other" refers to di-boson and W+jet production. Data and predictions outside the depicted mass range are not used in the fit and are not shown.

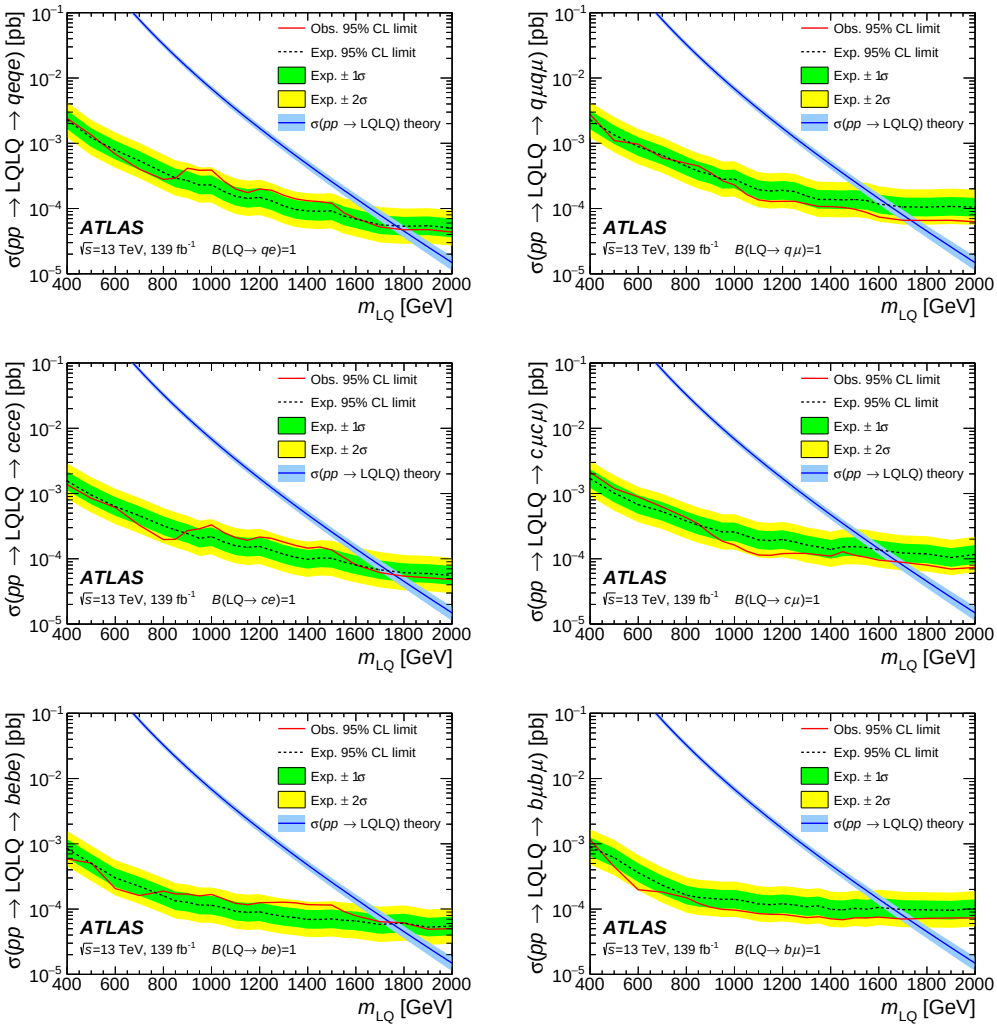

Figure 7.8: The observed and expected limit on the leptoquark pair production cross-section at 95% C.L for a branching fraction to charged leptons of 1, shown as a function of m_{LQ} for the different leptoquark channels. Also included on the plots is the expected theoretical cross-section.

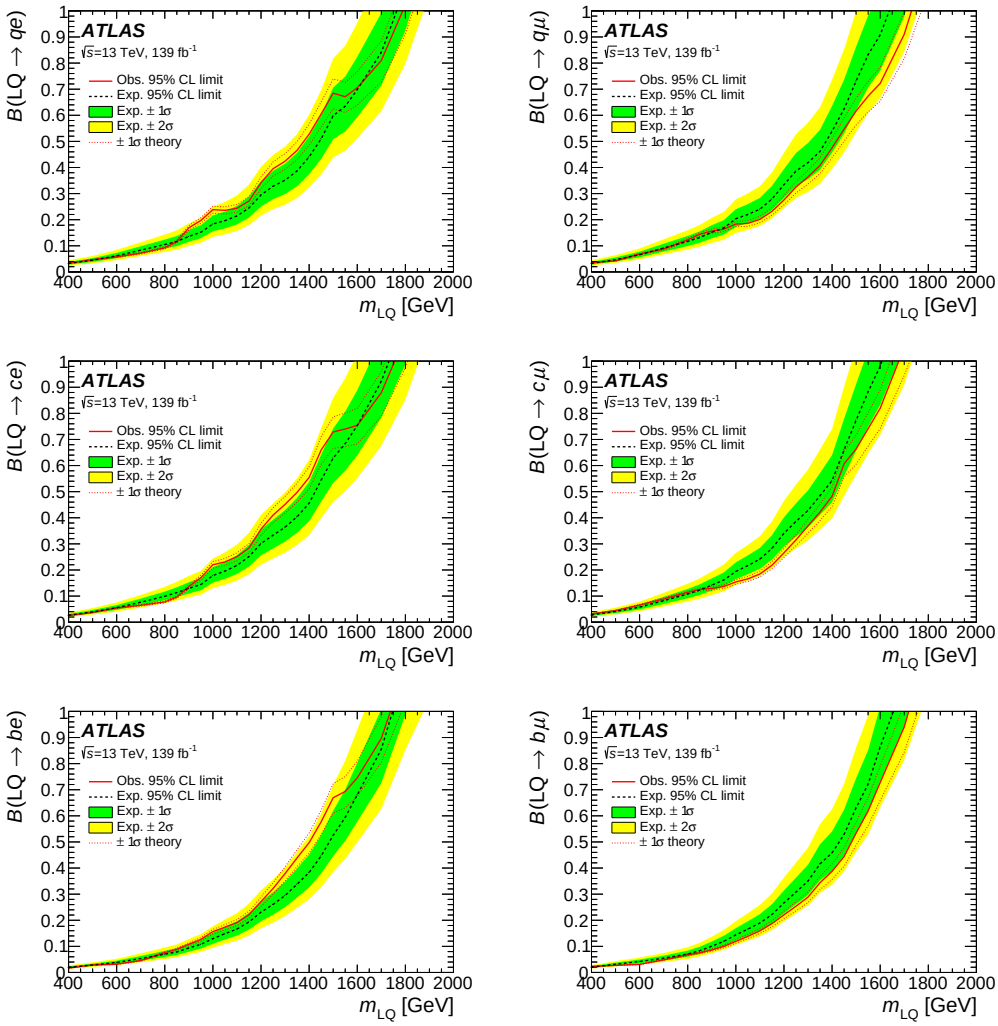

Figure 7.9: The observed and expected limit on the leptoquark branching ratio, $\mathcal{B}$, at 95% C.L, shown as a function of m_{LQ} for the different leptoquark channels.

7.2.1 Combination

Work is ongoing to perform a combination of this result with other LQ searches performed using the full Run II dataset of the ATLAS detector, some of which have been described in Section 2.8. Currently this combination work is still in its early stages, but an overlay of the published and un-published limits on the branching fraction to charged leptons has been produced, as shown in Figure 7.11. This Figure presents both cross-generational and 3^{rd} generation LQ searches, for all b-tagged channels. Of these limits, the 3^{rd} generation limits may be directly compared to the early Run II limits, performed using 36.1 fb^{-1} of data recorded by the ATLAS detector in 2015-16, as shown in Figure 7.11. From this comparison, it can be seen that the updated limits, using the full Run II data set, extend the constraints on the mass of the LQ by around 250 GeV.

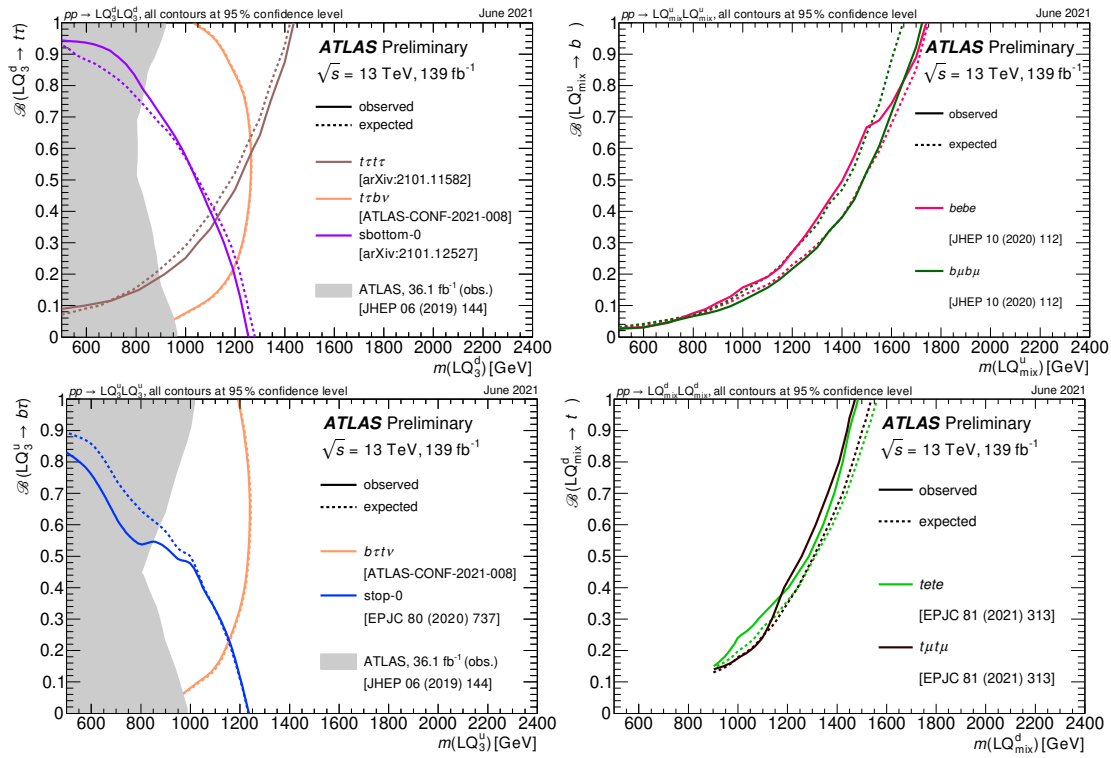

Figure 7.10: [359] Limits on the branching ratio into charged leptons for scalar LQ models decaying to b- or t-quarks plus leptons. Limits are shown for both cross-generational (right) and 3^{rd} generation LQ models for both down-type (top) and up-type LQs (bottom). Here, stop-0 and sbottom-0 are the result of reinterpretations of supersymmetry searches. Additionally, the limits labelled $b\tau b\nu$ and $b\tau t\nu$ are from a supersymmetry search for the pair production of supersymmetric top squarks. The rest are dedicated analyses, indicated by the final state of the leptoquark decays.

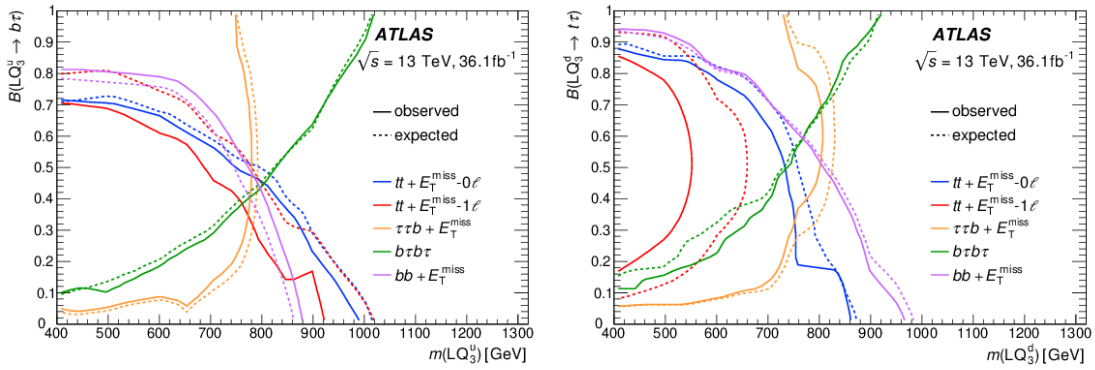

Figure 7.11: [166] Limits on the branching ratio into charged leptons for scalar third-generation up-type (left) and down-type (right) leptoquark pair production, produced using the early Run II dataset of the ATLAS detector, recorded in the years 2015 and 2016.

7.3 Analysis Preservation

In order to extend the scope of an ATLAS analysis, it is useful for it to be presented in such a way that alternative models may be tested. This can be achieved by re-using estimates of the backgrounds, systematic uncertainties and observations in the data, as taken from the original search, to quickly and easily determine limits on alternative signal hypotheses. As such, it is important that the analytical framework is retained as a re-usable and openly available resource to interested parties. To this end, there has been a recent drive in the ATLAS community to develop the "RECAST" (Request Efficiency Computation for Alternative Signal Theories) [360] framework, based on software images preserved in Docker [361, 362]. These are containerised processes, which provide the full root file-system, which provides all the software dependencies required to execute a given task. It is then the job of the analyser to encapsulate the workflow of their analysis. This is done using the "workflow description language" `yadage` [363]. These workflows are then stored remotely via GitLab. The repository for the RECAST efforts of this analysis can be found at the link `https://gitlab.cern.ch/recast-atlas/exotics/ana-exot-2019-013`.

In addition to the analysis preservation provided by Docker, the specific results of this analysis, with the stated signal model, are also stored and made openly available via the HEPData web-page hosted by Durham University. This contains the data presented in the publication in an accessible way, such that it can be accessed and re-used by theorists. This process has also become standard ATLAS policy for recent publications in the interest of increasing the usability and shelf-life of an analysis. The HEPData records for the analysis discussed in this Thesis can be found at the link `https://www.hepdata.net/record/95211`.

7.4 Conclusions

In this Thesis, I have presented the search for a new-physics signature of lepton-jet resonances using the full Run II dataset recorded by the ATLAS detector, corresponding to an integrated luminosity of 139 fb^{-1} of $\sqrt{s} = 13$ TeV pp collisions at the LHC. This search considers pair-production of scalar leptoquarks following a modification of the theoretical prescriptions of the W. Buchmüller, R. Rückl and D. Wyler model documented in Ref. [168]. Candidate events are required to contain exactly two electrons or muons and two or more jets, with a flavour tagging selection imposed on the jets, intended to identify jets arising from the fragmentation of b-quarks (b-jets) and, for the first time, of c-quarks (c-jets). Separate constraints are determined on both the LQ mass and the LQ mass as a function of the branching ratio.

Leptoquarks were searched for in the mass range $400 \leq m_{LQ} \leq 2000$ GeV. No statistically significant excess of events was observed beyond the considered SM background processes. As such, Leptoquarks with masses below 1.8 TeV and 1.7 TeV are excluded in

the electron and muon channels respectively for a branching ratio into a charged lepton and a quark of $\mathcal{B} = 100\%$, with minimal dependency on the quark flavour. In addition, LQs with masses of up to around 800 GeV can be excluded for branching ratios into charged leptons as low as 0.1, assuming that there is zero acceptance for LQ decays involving neutrinos or top quarks, and that only one charged lepton plus quark decay mode at one time is possible. Additionally, the reinterpretation of this study with new BSM models is made available via the RECAST framework, using Docker.

This analysis was statistics limited in the high m_{LQ} tails, and as such, it is expected that in the high-lumi LHC, these results may be improved upon. In addition, it is hoped that upgrades to the MS [364] may provide improved reconstruction of muon p_T in Run III, enabling an improved sensitivity in the muon channel.

These findings improve upon previous studies for scalar LQ production by around 300-400 GeV of LQ mass and establish for the first time limits on cross-generational LQ decays using dedicated c- and b-jet identification algorithms. These results come in the context of a wider group of LQ studies in ATLAS that search for scalar LQ pair production to a range of final states. A combination of these results is underway.

Appendices

Appendix A

Implementation of merged multi-leg $t\bar{t}$ samples at NLO accuracy using the Matchbox framework in Herwig 7

A.1 Rivet Analysis

In this study, we compare event samples generated using Herwig 7.1.3 in the Athena framework, against 13 TeV pp collisions recorded by the ATLAS detector. The comparisons are made using Rivet 2.6.1 [365] with the routines discussed in Sections A.1.1 and A.1.2. Rivet is a HEP MC Tool hosted by HepForge [366] for the validation of Monte Carlo event generators.

The "MC_XS" routine is also used to record the total cross-section, number of generated events and the ratio of events with positive and negative weights for MC samples. As it is a truth level evaluation of the event information, it is suitable for any process or experimental setup.

A.1.1 Single lepton Rivet routine

The "Single lepton" Rivet routine was produced to analyse Monte Carlo samples with the selection of the "Measurements of top-quark pair differential cross-sections in the lepton+jets channel in pp collisions at $\sqrt{s} = 13$ TeV using the ATLAS detector" analysis [367]. This routine was developed using 3.2 fb^{-1} of 13 TeV pp collisions as recorded by ATLAS. Measurements are then provided of the differential cross-sections of top-quark pair production as a function of the top-quark transverse momentum and rapidity, as well as the $t\bar{t}$ transverse momentum, rapidity and invariant mass.The analysis requires events with exactly one electron or muon and at least two b-tagged jets in the final state. Jets used in this analysis are identified using the anti-k_t algorithm with a radius parameter of $R = 0.4$. This algorithm uses topological clusters of energy depositions in the calorimeters called

topo-clusters. Jets are accepted within the range $p_T > 25$ GeV and $|\eta| < 2.5$. Jets originating from pile-up are suppressed using a multivariate jet-vertex-tagger (JVT). It then defines b-jets using a multivariate discriminant, which uses track impact parameters, track invariant mass, track multiplicity and secondary vertex information to identify b-jets with a 77% efficiency. Two separate selections are then applied which each focus on different top-quark momentum regions, that form the resolved and boosted topologies of the $t\bar{t}$ final state.

From this routine, predictions of the differential cross-sections of the top-quark pair production will be shown. These will be plotted as a function of the mass of the $t\bar{t}$ system, as well as the rapidity, $|y|$ and p_T of both the leading hadronized top quark, and the $t\bar{t}$ system.

A.1.2 Dilepton RIVET routine

The "Dilepton" RIVET routine was produced to analyse Monte Carlo samples with the selection of the "Measurement of jet activity produced in top-quark events with an electron, a muon and two b-tagged jets in the final state in pp collisions at $\sqrt{s} = 13$ TeV with the ATLAS detector" analysis [368]. This analysis measures the jet activity in top-quark pair events produced using 3.2 fb^{-1} of 13 TeV pp collisions as recorded by ATLAS. This routine selects oppositely charged e/μ events and two b-tagged jets to be in the final state. Jets and b-tagged jets are identified in the same way as described in Section A.1.1. From this, the normalised differential cross-sections of top-quark pair production are presented as functions of additional-jet multiplicity, transverse momentum, p_T and the gap fraction as a function of the p_T threshold for additional jets.

Two types of gap fraction are used; the first is measured as a ratio between the number of events n(Q_0) with no additional jet with $p_T > Q_0$, and the total number of selected events ($N_{t\bar{t}}$), as expressed in Equation A.1.1.

$$f_{Gap}(Q_0) = \frac{n(Q_0)}{N_{t\bar{t}}} \tag{A.1.1}$$

The second gap fraction as expressed in Equation A.1.2 calculates the fraction of events in which the scalar p_T sum of all additional jets (within the defined veto region) does not exceed a given threshold (Q_{sum}), where the subset of events that meet this criteria are labeled n(Q_{sum}).

$$f_{Gap}(Q_{sum}) = \frac{n(Q_{sum})}{N_{t\bar{t}}} \tag{A.1.2}$$

From this routine, predictions of the number of additional jets after a p_T cut of $p_T > 25$ GeV will be shown, as well as the p_T of the leading (sub-leading) b-jet, and the p_T of the additional leading jet. The gap fractions calculated in Equations A.1.1 and A.1.2 will also be shown, in the rapidity vetoes of $0.8 < |y| < 1.5$ and $1.5 < |y| < 2.1$.

A.2 ATLAS Nominal Samples

ATLAS hosts a range of validated, high statistic $t\bar{t}$ samples, available for use in ATLAS analysis. We report briefly on the setup of nominal MC generator samples generated with PowhegBox [223, 255, 256, 369] v2 generator, and interfaced to Pythia 8 [342] and Herwig 7 for the PS. These samples will be used to compare with the ATLAS data and the Herwig 7 generated samples.

The nominal Powheg + Pythia 8 sample (DSID 410472) was generated using the PowhegBox v2 generator which provides matrix elements at next-to-leading order (NLO) in the strong coupling constant α_S with the NNPDF3.0NLO [260] parton distribution function (PDF) and the h_{damp} parameter[1] set to 1.5 time the mass of the top quark (m_{top}) [268]. The functional form of the renormalisation (μ_R) and factorisation (μ_F) scale is set to the default scale $\sqrt{m_{\text{top}}^2 + p_{\text{T}}^2}$. The events are interfaced with Pythia8.230 for the parton shower and hadronization, using the A14 set of tuned parameters [343] and the `NNPDF23LO` PDF set. The decays of bottom and charm hadrons are simulated using the EvtGen v1.6.0 program [370].

The NLO $t\bar{t}$ inclusive production cross-section is corrected to the theory prediction at NNLO in QCD including the resummation of next-to-next-to-leading logarithmic (NNLL) soft-gluon terms calculated using Top++2.0 [247, 371–376]. For proton–proton collisions at a centre-of-mass energy of $\sqrt{s} = 13$ TeV, this cross-section corresponds to $\sigma(t\bar{t})_{\text{NNLO+NNLL}} = 832 \pm 51$ pb using a top-quark mass of $m_{\text{top}} = 172.5$ GeV.

The nominal Powheg + Herwig 7 sample (DSID 410558) uses the same un-showered events generated with PowhegBox as discussed previously. The Les Houches Events [377] (LHE) are then interfaced with Herwig 7.04 [271, 272], using the H7UE set of tuned parameters [272] and the MMHT2014LO PDF set [49].

A.3 Job Options

The Job Option (JO) is used to steer the Herwig 7 generator by passing commands using the "`generator.add_commands`" function. This is used to build a run card which passes arguments to the Herwig 7 program. Section A.3.1 describes how the underlying process is set, and how the additional jets are merged to the ME. Section A.3.2 describes the different renormalisation and factorisation scales that can be selected in Herwig 7. Section A.3.3 then describes how different leptonic filters can be applied, allowing us to "cheaply" generate events with a higher effective luminosity. Herwig 7 is then steered in three different modes; `build`, `integrate` and `run`. The matrix elements are constructed and sub-processes generated in the `build` stage. This creates a set of loop integration jobs,

[1] The h_{damp} parameter controls the transverse momentum p_T of the first additional emission beyond the leading-order Feynman diagram in the parton shower and therefore regulates the high-p_T emission against which the $t\bar{t}$ system recoils.

where the amplitudes are compiled, and the sub-processes are integrated over, which is performed by the `integrate` stage. The interactions are then combined into a `.tar` file, which can be exported to a computing cluster to perform the computationally intensive process of generating and showering the events in the `run` stage.

A.3.1 Process Selection

The $t\bar{t}$ events are generated by selecting a process decaying to t and $\bar{t}$, plus the desired multiplicity of additional merged jets with the line;

```
do MergingFactory:Process p p -> t tbar [ j j ]
```

where we see that here we have selected 2 additional jets to be merged to the hard ME.

The order of perturbation (above the born process) that the hard ME will be calculated to is then selected by the line;

```
set MergingFactory:NLOProcesses 2
```

where we see that we have requested the process to be calculated to the NLO. There is one caveat however, in the selection of the order of perturbation, and the process selection. The settings described above choose a $pp \to t\bar{t}$ process with 2 additional jets, to be calculated at the NLO. This corresponds to calculating the process:

$$t\bar{t} \text{ at NLO} + 1 \text{ jet at NLO} + 2 \text{ jets at LO} \tag{A.3.1}$$

if the order of `NLOProcesses` was set to 3, then this would correspond to

$$t\bar{t} \text{ at NNLO} + 1 \text{ jet at NNLO} + 2 \text{ jets at NLO} + 0 \text{ jets at LO.} \tag{A.3.2}$$

Therefore, the order of `NLOProcesses` cannot be set to be larger than the number of additional jets chosen to be merged to the hard ME.

It is then necessary to determine a scale at which the merging of the additional jets to the ME will be performed. This is set using the lines;

```
set Merger:MergingScale 20.*GeV
set Merger:MergingScaleSmearing 0.1
```

This is the scale at which the parton shower is separated from the matrix element. The Herwig 7 authors recommend this to be between 10 and 30 GeV for the LHC. As such, a merging scale of 20 GeV is used in the following.

The PDF set used is the `MMHT2014nlo68cl` [258] PDF set (which is optimized for use in multi-jet matching and merging), and the `FiveFlavourNoBMassScheme` is chosen.

A.3.2 Scale Settings

Herwig 7 offers two dedicated options for setting the re-normalisation and factorisation scales that are tuned to the $t\bar{t}$ process. These include the '`TopPairMass`' scale and the

'TopPairMT scale' which can be set with the following lines:

```
set Factory:ScaleChoice Scales/TopPairMassScale
set Factory:ScaleChoice Scales/TopPairMTScale
```

The TopPairMass scale is a scale based on the invariant mass of the $t\bar{t}$ system. This will set the renormalisation scale and the factorisation scale to:

$$\mu_R^2 \;=\; \mu_F^2 \;=\; (p_t \;+\; p_{\bar{t}})^2 \tag{A.3.3}$$

where p_t ($p_{\bar{t}}$) is the momentum of the top (anti-top) quark.

The TopPairMT scale will set these scales to be:

$$\mu_R^2 \;=\; \mu_F^2 \;=\; (m_{T,t}^2 + m_{T,\bar{t}}^2) \tag{A.3.4}$$

where $m_{T,t}$ ($m_{T,\bar{t}}$) is the transverse mass of the top (anti-top) quark.
In this document, both scales are tested for comparison.

A.3.3 Leptonic Filters

We apply a custom designed lepton filter such that we can run larger effective luminosity samples. This is useful for comparisons to the Dilepton Rivet routine.

This filter is implemented as follows:

```
##################################################
##Di-Lepton Filter
##################################################
do /Herwig/Particles/t:SelectDecayModes /Herwig/Particles/t/t->nu_e,e+,b; /
    Herwig/Particles/t/t->nu_mu,mu+,b;
do /Herwig/Particles/tbar:SelectDecayModes /Herwig/Particles/tbar/tbar->
    nu_ebar,e-,bbar; /Herwig/Particles/tbar/tbar->nu_mubar,mu-,bbar;
```

We then have to rescale the cross-section to account for the change in Branching Ratio (β):

```
##################################################
##Re-weight x-section for the change in BR
##taken from : https://twiki.cern.ch/twiki/bin/view/AtlasProtected/
    Herwig7ForAtlas
##################################################
create Herwig::BranchingRatioReweighter /Herwig/Generators/BRReweighter
insert /Herwig/Generators/EventGenerator:EventHandler:
    PostHadronizationHandlers 0 /Herwig/Generators/BRReweighter
```

It is then possible to print out the exact decay modes of each process:

```
##################################################
##Print decay modes
##################################################
do /Herwig/Particles/t:PrintDecayModes
```

```
5 do /Herwig/Particles/tbar:PrintDecayModes
```

From this, it is found that the branching ratio for the t and $\bar{t}$ decays (after selecting the decay modes of the Dileptonic filter) are:

- $t \to (n_l/\bar{l}) + b = 0.108059$
- $\bar{t} \to (n_{\bar{l}}/l) + \bar{b} = 0.108059$

Bibliography

[1] Georges Aad et al., *Search for pairs of scalar leptoquarks decaying into quarks and electrons or muons in $\sqrt{s} = 13$ TeV pp collisions with the ATLAS detector*, (2020), arXiv: 2006.05872 [hep-ex] (cit. on pp. ii, 102).

[2] G. Arnison et al., *Experimental Observation of Isolated Large Transverse Energy Electrons with Associated Missing Energy at s**(1/2) = 540-GeV*, Phys. Lett. B **122** (1983) 103 (cit. on p. 1).

[3] G. Arnison et al., *Experimental Observation of Lepton Pairs of Invariant Mass Around 95-GeV/c**2 at the CERN SPS Collider*, Phys. Lett. B **126** (1983) 398 (cit. on p. 1).

[4] Christoph Berger et al., *Jet Analysis of the Υ (9.46) Decay Into Charged Hadrons*, Phys. Lett. B **82** (1979) 449 (cit. on p. 1).

[5] S. Abachi et al., *Observation of the top quark*, Phys. Rev. Lett. **74** (1995) 2632, arXiv: hep-ex/9503003 (cit. on p. 1).

[6] F. Abe et al., *Observation of top quark production in $\bar{p}p$ collisions*, Phys. Rev. Lett. **74** (1995) 2626, arXiv: hep-ex/9503002 (cit. on p. 1).

[7] J.J. Aubert et al., *Experimental Observation of a Heavy Particle J*, Phys. Rev. Lett. **33** (1974) 1404 (cit. on p. 1).

[8] J.E. Augustin et al., *Discovery of a Narrow Resonance in e^+e^- Annihilation*, Phys. Rev. Lett. **33** (1974) 1406 (cit. on p. 1).

[9] ATLAS Collaboration, *Observation of a new particle in the search for the Standard Model Higgs boson with the ATLAS detector at the LHC*, Physics Letters B **716** (2012) 1, ISSN: 0370-2693, URL: http://dx.doi.org/10.1016/j.physletb.2012.08.020 (cit. on pp. 1, 17, 101).

[10] CMS Collaboration, *Observation of a new boson at a mass of 125 GeV with the CMS experiment at the LHC*, Physics Letters B **716** (2012) 30, ISSN: 0370-2693, URL: http://dx.doi.org/10.1016/j.physletb.2012.08.021 (cit. on pp. 1, 17).

[11] Cliff P Burgess and Guy D Moore, *The Standard Model: A Primer*, Cambridge Univ. Press, 2007, URL: https://cds.cern.ch/record/1003111 (cit. on p. 4).

[12] Paul Langacker, *The standard model and beyond; 2nd ed.* High energy physics, cosmology and gravitation, CRC Press, 2017, URL: https://cds.cern.ch/record/2256595 (cit. on p. 4).

[13] Dave Goldberg, *The standard model in a nutshell*, Princeton University Press, 2017, URL: https://cds.cern.ch/record/2244785 (cit. on p. 4).

[14] F. Halzen and Alan D. Martin, *QUARKS AND LEPTONS: AN INTRODUCTORY COURSE IN MODERN PARTICLE PHYSICS*, 1984, ISBN: 978-0-471-88741-6 (cit. on p. 4).

[15] W.N. Cottingham and D.A. Greenwood, *An introduction to the standard model of particle physics*, Cambridge University Press, 2007, ISBN: 978-0-511-27136-6, 978-0-521-85249-4 (cit. on p. 4).

[16] Robert B. Mann, *An introduction to particle physics and the standard model*, CRC Press, 2010 (cit. on p. 4).

[17] D.E. Littlewood, *Lie Algebras and Representations of Continuous Groups*, Int. J. Theor. Phys. **14** (1976) 97 (cit. on p. 4).

[18] Emmy Noether, *Invariant variation problems*, Transport Theory and Statistical Physics **1** (1971) 186, eprint: https://doi.org/10.1080/00411457108231446, URL: https://doi.org/10.1080/00411457108231446 (cit. on p. 4).

[19] Katherine Brading and Harvey R. Brown, *Noether's theorems and gauge symmetries*, (2000), arXiv: hep-th/0009058 (cit. on p. 4).

[20] Paul A.M. Dirac, *On the Theory of quantum mechanics*, Proc. Roy. Soc. Lond. A **112** (1926) 661 (cit. on p. 6).

[21] Enrico Fermi, *On the Quantization of the Monoatomic Ideal Gas*, (1999), arXiv: cond-mat/9912229 (cit. on p. 6).

[22] Bose, *Plancks Gesetz und Lichtquantenhypothese*, Zeitschrift fur Physik **26** (1924) 178 (cit. on p. 6).

[23] P.A. Zyla et al., *Review of Particle Physics*, PTEP **2020** (2020) 083C01 (cit. on pp. 7, 12, 74).

[24] C.S. Wu, E. Ambler, R.W. Hayward, D.D. Hoppes, and R.P. Hudson, *Experimental Test of Parity Conservation in β Decay*, Phys. Rev. **105** (1957) 1413 (cit. on p. 7).

[25] W.H. Furry, *On transition probabilities in double beta-disintegration*, Phys. Rev. **56** (1939) 1184 (cit. on pp. 8, 27).

[26] Y. Fukuda et al., *Evidence for oscillation of atmospheric neutrinos*, Phys. Rev. Lett. **81** (1998) 1562, arXiv: hep-ex/9807003 (cit. on pp. 10, 26).

[27] Q.R. Ahmad et al., *Direct evidence for neutrino flavor transformation from neutral current interactions in the Sudbury Neutrino Observatory*, Phys. Rev. Lett. **89** (2002) 011301, arXiv: nucl-ex/0204008 (cit. on pp. 10, 26).

[28] K. Eguchi et al., *First results from KamLAND: Evidence for reactor anti-neutrino disappearance*, Phys. Rev. Lett. **90** (2003) 021802, arXiv: hep-ex/0212021 (cit. on pp. 10, 26).

[29] T.P. Cheng and Ling-Fong Li, $\mu \to e\gamma$ *in Theories With Dirac and Majorana Neutrino Mass Terms*, Phys. Rev. Lett. **45** (1980) 1908 (cit. on p. 10).

[30] S.T. Petcov, *The Processes mu –> e Gamma, mu –> e e anti-e, Neutrino' –> Neutrino gamma in the Weinberg-Salam Model with Neutrino Mixing*, Sov. J. Nucl. Phys. **25** (1977) 340, [Erratum: Sov.J.Nucl.Phys. 25, 698 (1977), Erratum: Yad.Fiz. 25, 1336 (1977)] (cit. on p. 10).

[31] Steven Weinberg, *A Model of Leptons*, Phys. Rev. Lett. **19** (1967) 1264 (cit. on p. 11).

[32] Abdus Salam, *Weak and Electromagnetic Interactions*, Conf. Proc. C **680519** (1968) 367 (cit. on p. 11).

[33] Sheldon L. Glashow, *The renormalizability of vector meson interactions*, Nucl. Phys. **10** (1959) 107 (cit. on p. 11).

[34] F. Englert and R. Brout, *Broken Symmetry and the Mass of Gauge Vector Mesons*, Phys. Rev. Lett. **13** (1964) 321, ed. by J.C. Taylor (cit. on p. 14).

[35] Peter W. Higgs, *Broken symmetries, massless particles and gauge fields*, Phys. Lett. **12** (1964) 132 (cit. on p. 14).

[36] Peter W. Higgs, *Broken Symmetries and the Masses of Gauge Bosons*, Phys. Rev. Lett. **13** (1964) 508, ed. by J.C. Taylor (cit. on p. 14).

[37] Peter W. Higgs, *Spontaneous Symmetry Breakdown without Massless Bosons*, Phys. Rev. **145** (1966) 1156 (cit. on p. 14).

[38] G.S. Guralnik, C.R. Hagen, and T.W.B. Kibble, *Global Conservation Laws and Massless Particles*, Phys. Rev. Lett. **13** (1964) 585, ed. by J.C. Taylor (cit. on p. 14).

[39] John Ellis, Mary K Gaillard, and Dimitri V Nanopoulos, *A Historical Profile of the Higgs Boson. An Updated Historical Profile of the Higgs Boson*, (2015) 22 p, URL: https://cds.cern.ch/record/2012465 (cit. on p. 15).

[40] Chen-Ning Yang and Robert L. Mills, *Conservation of Isotopic Spin and Isotopic Gauge Invariance*, Phys. Rev. **96** (1954) 191, ed. by Jong-Ping Hsu and D. Fine (cit. on p. 18).

[41] C. Patrignani et al., *Review of Particle Physics*, Chin. Phys. C **40** (2016) 100001 (cit. on pp. 19, 20).

[42] Claudia Glasman, *Precision measurements of alpha(s) at HERA*, J. Phys. Conf. Ser. **110** (2008) 022013, ed. by Roger Barlow, arXiv: 0709.4426 [hep-ex] (cit. on p. 20).

[43] Hideki Yukawa, *On the Interaction of Elementary Particles I*, Proc. Phys. Math. Soc. Jap. **17** (1935) 48 (cit. on p. 21).

[44] S.D. Drell and Tung-Mow Yan, *Partons and their Applications at High-Energies*, Annals Phys. **66** (1971) 578 (cit. on pp. 21, 38).

[45] W Kwong, J L Rosner, and C Quigg, *Heavy-Quark Systems*, Annual Review of Nuclear and Particle Science **37** (1987) 325, eprint: https://doi.org/10.1146/annurev.ns.37.120187.001545, URL: https://doi.org/10.1146/annurev.ns.37.120187.001545 (cit. on p. 21).

[46] V.N. Gribov and L.N. Lipatov, *Deep inelastic e p scattering in perturbation theory*, Sov. J. Nucl. Phys. **15** (1972) 438 (cit. on p. 22).

[47] Yuri L. Dokshitzer, *Calculation of the Structure Functions for Deep Inelastic Scattering and e+ e- Annihilation by Perturbation Theory in Quantum Chromodynamics.*, Sov. Phys. JETP **46** (1977) 641 (cit. on p. 22).

[48] Guido Altarelli and G. Parisi, *Asymptotic Freedom in Parton Language*, Nucl. Phys. B **126** (1977) 298 (cit. on p. 22).

[49] L. A. Harland-Lang, A. D. Martin, P. Motylinski, and R. S. Thorne, *Parton distributions in the LHC era: MMHT 2014 PDFs*, Eur. Phys. J. C **75** (2015) 204, arXiv: 1412.3989 [hep-ph] (cit. on pp. 22, 153).

[50] Bo Andersson, G. Gustafson, G. Ingelman, and T. Sjostrand, *Parton Fragmentation and String Dynamics*, Phys. Rept. **97** (1983) 31 (cit. on pp. 23, 67).

[51] B.R. Webber, *A QCD Model for Jet Fragmentation Including Soft Gluon Interference*, Nucl. Phys. B **238** (1984) 492 (cit. on pp. 23, 67).

[52] Jogesh C. Pati and Abdus Salam, *Unified Lepton-Hadron Symmetry and a Gauge Theory of the Basic Interactions*, Phys. Rev. D **8** (4 1973) 1240, URL: https://link.aps.org/doi/10.1103/PhysRevD.8.1240 (cit. on p. 24).

[53] Barbara Schrempp and Fridger Schrempp, *LIGHT LEPTOQUARKS*, Phys. Lett. B **153** (1985) 101 (cit. on p. 24).

[54] W. Buchmuller and D. Wyler, *Constraints on SU(5) Type Leptoquarks*, Phys. Lett. B **177** (1986) 377 (cit. on p. 24).

[55] Howard Georgi and S. L. Glashow, *Unity of All Elementary-Particle Forces*, Phys. Rev. Lett. **32** (8 1974) 438, URL: https://link.aps.org/doi/10.1103/PhysRevLett.32.438 (cit. on p. 24).

[56] Jogesh C. Pati and Abdus Salam, *Lepton Number as the Fourth Color*, Phys. Rev. D **10** (1974) 275, [Erratum: Phys.Rev.D 11, 703–703 (1975)] (cit. on p. 24).

[57] R. Barbier et al., *R-parity violating supersymmetry*, Phys. Rept. **420** (2005) 1, arXiv: hep-ph/0406039 (cit. on p. 24).

[58] Pran Nath and Pavel Fileviez Perez, *Proton stability in grand unified theories, in strings and in branes*, Phys. Rept. **441** (2007) 191, arXiv: hep-ph/0601023 (cit. on p. 24).

[59] I. Doršner, S. Fajfer, A. Greljo, J.F. Kamenik, and N. Košnik, *Physics of leptoquarks in precision experiments and at particle colliders*, Phys. Rept. **641** (2016) 1, arXiv: 1603.04993 [hep-ph] (cit. on pp. 24, 30, 36).

[60] JoAnne L. Hewett and Thomas G. Rizzo, *Much ado about leptoquarks: A comprehensive analysis*, Phys. Rev. D **56** (9 1997) 5709, URL: https://link.aps.org/doi/10.1103/PhysRevD.56.5709 (cit. on p. 24).

[61] Sacha Davidson, David C. Bailey, and Bruce A. Campbell, *Model independent constraints on leptoquarks from rare processes*, Z. Phys. C **61** (1994) 613, arXiv: hep-ph/9309310 (cit. on pp. 24, 37).

[62] M.J. Duff, *M theory (The Theory formerly known as strings)*, Int. J. Mod. Phys. A **11** (1996) 5623, arXiv: hep-th/9608117 (cit. on p. 25).

[63] M.J. Duff, "A Layman's guide to M theory", *Abdus Salam Memorial Meeting*, 1997 10, arXiv: hep-th/9805177 (cit. on p. 25).

[64] Michael J. Duff, ed., *The world in eleven-dimensions: Supergravity, supermembranes and M theory*, 1999 (cit. on p. 25).

[65] A.J. Buras, John R. Ellis, M.K. Gaillard, and Dimitri V. Nanopoulos, *Aspects of the Grand Unification of Strong, Weak and Electromagnetic Interactions*, Nucl. Phys. B **135** (1978) 66 (cit. on p. 25).

[66] Graham G. Ross, *GRAND UNIFIED THEORIES*, 1985 (cit. on p. 25).

[67] James M. Cline, M.E. Knutt, G.D. Mahlon, and Guy D. Moore, eds., *Toward the theory of everything. Proceedings, 20th Annual Meeting on High-Energy Physics, MRST'98, Montreal, Canada, May 13-15, 1998*, 1998 (cit. on p. 25).

[68] R. Descartes, *Principia philosophiae*, apud Ludovicum Elzevirium, 1644, URL: https://books.google.co.uk/books?id=lHpbAAAAQAAJ (cit. on p. 25).

[69] R.N. Mohapatra and Jogesh C. Pati, *A Natural Left-Right Symmetry*, Phys. Rev. D **11** (1975) 2558 (cit. on p. 26).

[70] Rabindra N. Mohapatra and Goran Senjanovic, *Neutrino Mass and Spontaneous Parity Nonconservation*, Phys. Rev. Lett. **44** (1980) 912 (cit. on p. 26).

[71] Murray Gell-Mann, Pierre Ramond, and Richard Slansky, *Complex Spinors and Unified Theories*, Conf. Proc. C **790927** (1979) 315, arXiv: 1306.4669 [hep-th] (cit. on p. 26).

[72] Peter Minkowski, $\mu \to e\gamma$ *at a Rate of One Out of* 10^9 *Muon Decays?*, Phys. Lett. B **67** (1977) 421 (cit. on p. 26).

[73] J. Schechter and J.W.F. Valle, *Neutrinoless Double beta Decay in SU(2) x U(1) Theories*, Phys. Rev. D **25** (1982) 2951 (cit. on p. 27).

[74] G.W. Bennett et al., *Final Report of the Muon E821 Anomalous Magnetic Moment Measurement at BNL*, Phys. Rev. D **73** (2006) 072003, arXiv: hep-ex/0602035 (cit. on p. 27).

[75] T. Aoyama et al., *The anomalous magnetic moment of the muon in the Standard Model*, (2020), arXiv: 2006.04822 [hep-ph] (cit. on p. 27).

[76] Tatsumi Aoyama, Masashi Hayakawa, Toichiro Kinoshita, and Makiko Nio, *Complete Tenth-Order QED Contribution to the Muon* $g-2$, Phys. Rev. Lett. **109** (2012) 111808, arXiv: 1205.5370 [hep-ph] (cit. on p. 27).

[77] Tatsumi Aoyama, Toichiro Kinoshita, and Makiko Nio, *Theory of the Anomalous Magnetic Moment of the Electron*, Atoms **7** (2019) 28 (cit. on p. 27).

[78] Andrzej Czarnecki, William J. Marciano, and Arkady Vainshtein, *Refinements in electroweak contributions to the muon anomalous magnetic moment*, Phys. Rev. **D67** (2003) 073006, [Erratum: Phys. Rev. **D73**, 119901 (2006)], arXiv: hep-ph/0212229 [hep-ph] (cit. on p. 27).

[79] C. Gnendiger, D. Stöckinger, and H. Stöckinger-Kim, *The electroweak contributions to* $(g-2)_\mu$ *after the Higgs boson mass measurement*, Phys. Rev. **D88** (2013) 053005, arXiv: 1306.5546 [hep-ph] (cit. on p. 27).

[80] Michel Davier, Andreas Hoecker, Bogdan Malaescu, and Zhiqing Zhang, *Reevaluation of the hadronic vacuum polarisation contributions to the Standard Model predictions of the muon* $g-2$ *and* $\alpha(m_Z^2)$ *using newest hadronic cross-section data*, Eur. Phys. J. **C77** (2017) 827, arXiv: 1706.09436 [hep-ph] (cit. on p. 27).

[81] Alexander Keshavarzi, Daisuke Nomura, and Thomas Teubner, *Muon* $g-2$ *and* $\alpha(M_Z^2)$*: a new data-based analysis*, Phys. Rev. **D97** (2018) 114025, arXiv: 1802.02995 [hep-ph] (cit. on p. 27).

[82] Gilberto Colangelo, Martin Hoferichter, and Peter Stoffer, *Two-pion contribution to hadronic vacuum polarization*, JHEP **02** (2019) 006, arXiv: 1810.00007 [hep-ph] (cit. on p. 27).

[83] Martin Hoferichter, Bai-Long Hoid, and Bastian Kubis, *Three-pion contribution to hadronic vacuum polarization*, JHEP **08** (2019) 137, arXiv: 1907.01556 [hep-ph] (cit. on p. 27).

[84] M. Davier, A. Hoecker, B. Malaescu, and Z. Zhang, *A new evaluation of the hadronic vacuum polarisation contributions to the muon anomalous magnetic moment and to* $\boldsymbol{\alpha(m_Z^2)}$, Eur. Phys. J. **C80** (2020) 241, [Erratum: Eur. Phys. J. **C80**, 410 (2020)], arXiv: 1908.00921 [hep-ph] (cit. on p. 27).

[85] Alexander Keshavarzi, Daisuke Nomura, and Thomas Teubner, *The* $g-2$ *of charged leptons,* $\alpha(M_Z^2)$ *and the hyperfine splitting of muonium*, Phys. Rev. **D101** (2020) 014029, arXiv: 1911.00367 [hep-ph] (cit. on p. 27).

[86] Alexander Kurz, Tao Liu, Peter Marquard, and Matthias Steinhauser, *Hadronic contribution to the muon anomalous magnetic moment to next-to-next-to-leading order*, Phys. Lett. **B734** (2014) 144, arXiv: 1403.6400 [hep-ph] (cit. on p. 27).

[87] Kirill Melnikov and Arkady Vainshtein, *Hadronic light-by-light scattering contribution to the muon anomalous magnetic moment revisited*, Phys. Rev. **D70** (2004) 113006, arXiv: hep-ph/0312226 [hep-ph] (cit. on p. 27).

[88] Pere Masjuan and Pablo Sánchez-Puertas, *Pseudoscalar-pole contribution to the* $(g_\mu - 2)$*: a rational approach*, Phys. Rev. **D95** (2017) 054026, arXiv: 1701.05829 [hep-ph] (cit. on p. 27).

[89] Gilberto Colangelo, Martin Hoferichter, Massimiliano Procura, and Peter Stoffer, *Dispersion relation for hadronic light-by-light scattering: two-pion contributions*, JHEP **04** (2017) 161, arXiv: 1702.07347 [hep-ph] (cit. on p. 27).

[90] Martin Hoferichter, Bai-Long Hoid, Bastian Kubis, Stefan Leupold, and Sebastian P. Schneider, *Dispersion relation for hadronic light-by-light scattering: pion pole*, JHEP **10** (2018) 141, arXiv: 1808.04823 [hep-ph] (cit. on p. 27).

[91] Antoine Gérardin, Harvey B. Meyer, and Andreas Nyffeler, *Lattice calculation of the pion transition form factor with* $N_f = 2 + 1$ *Wilson quarks*, Phys. Rev. **D100** (2019) 034520, arXiv: 1903.09471 [hep-lat] (cit. on p. 27).

[92] Johan Bijnens, Nils Hermansson-Truedsson, and Antonio Rodríguez-Sánchez, *Short-distance constraints for the HLbL contribution to the muon anomalous magnetic moment*, Phys. Lett. **B798** (2019) 134994, arXiv: 1908.03331 [hep-ph] (cit. on p. 27).

[93] Gilberto Colangelo, Franziska Hagelstein, Martin Hoferichter, Laetitia Laub, and Peter Stoffer, *Longitudinal short-distance constraints for the hadronic light-by-light contribution to* $(g-2)_\mu$ *with large-*N_c *Regge models*, JHEP **03** (2020) 101, arXiv: 1910.13432 [hep-ph] (cit. on p. 27).

[94] Thomas Blum et al., *The hadronic light-by-light scattering contribution to the muon anomalous magnetic moment from lattice QCD*, Phys. Rev. Lett. **124** (2020) 132002, arXiv: 1911.08123 [hep-lat] (cit. on p. 27).

[95] Gilberto Colangelo, Martin Hoferichter, Andreas Nyffeler, Massimo Passera, and Peter Stoffer, *Remarks on higher-order hadronic corrections to the muon $g-2$*, Phys. Lett. **B735** (2014) 90, arXiv: 1403.7512 [hep-ph] (cit. on p. 27).

[96] Richard H. Parker, Chenghui Yu, Weicheng Zhong, Brian Estey, and Holger Müller, *Measurement of the fine-structure constant as a test of the Standard Model*, Science **360** (2018) 191, arXiv: 1812.04130 [physics.atom-ph] (cit. on pp. 27, 32).

[97] J. Grange et al., *Muon (g-2) Technical Design Report*, (2015), arXiv: 1501.06858 [physics.ins-det] (cit. on p. 27).

[98] Graziano Venanzoni, *The New Muon g-2 experiment at Fermilab*, Nucl. Part. Phys. Proc. **273-275** (2016) 584, ed. by M Aguilar-Benitez, J Fuster, S Marti-Garcia, and A Santamaria, arXiv: 1411.2555 [physics.ins-det] (cit. on p. 27).

[99] M. Abe et al., *A New Approach for Measuring the Muon Anomalous Magnetic Moment and Electric Dipole Moment*, PTEP **2019** (2019) 053C02, arXiv: 1901.03047 [physics.ins-det] (cit. on p. 27).

[100] Tsutomu Mibe, *Measurement of muon g-2 and EDM with an ultra-cold muon beam at J-PARC*, Nucl. Phys. B Proc. Suppl. **218** (2011) 242, ed. by George Lafferty and Stefan Soldner-Rembold (cit. on p. 27).

[101] Richard Massey, Thomas Kitching, and Johan Richard, *The dark matter of gravitational lensing*, Rept. Prog. Phys. **73** (2010) 086901, arXiv: 1001.1739 [astro-ph.CO] (cit. on p. 28).

[102] V. C. Rubin, N. Thonnard, and W. K. Ford Jr., *Rotational properties of 21 SC galaxies with a large range of luminosities and radii, from NGC 4605 /R = 4kpc/ to UGC 2885 /R = 122 kpc/*, Astrophys. J. **238** (1980) 471 (cit. on p. 28).

[103] Vera C. Rubin and W. Kent Ford Jr., *Rotation of the Andromeda Nebula from a Spectroscopic Survey of Emission Regions*, Astrophys. J. **159** (1970) 379 (cit. on p. 28).

[104] K. G. Begeman, A. H. Broeils, and R. H. Sanders, *Extended rotation curves of spiral galaxies: Dark haloes and modified dynamics*, Mon. Not. Roy. Astron. Soc. **249** (1991) 523 (cit. on p. 28).

[105] Douglas Clowe et al., *A direct empirical proof of the existence of dark matter*, Astrophys. J. Lett. **648** (2006) L109, arXiv: astro-ph/0608407 (cit. on p. 28).

[106] P. A. R. Ade et al., *Planck 2015 results. XIII. Cosmological parameters*, Astron. Astrophys. **594** (2016) A13, arXiv: 1502.01589 [astro-ph.CO] (cit. on p. 28).

[107] P.A.R. Ade et al., *Planck 2013 results. I. Overview of products and scientific results*, Astron. Astrophys. **571** (2014) A1, arXiv: 1303.5062 [astro-ph.CO] (cit. on p. 28).

[108] R. Adam et al., *Planck 2015 results. I. Overview of products and scientific results*, Astron. Astrophys. **594** (2016) A1, arXiv: 1502.01582 [astro-ph.CO] (cit. on p. 28).

[109] R.S. Hill et al., *Five-Year Wilkinson Microwave Anisotropy Probe (WMAP)Observations: Beam Maps and Window Functions*, Astrophys. J. Suppl. **180** (2009) 246, arXiv: 0803.0570 [astro-ph] (cit. on p. 28).

[110] M. Tanabashi et al., *Review of Particle Physics*, Phys. Rev. D **98** (2018) 030001 (cit. on pp. 28, 91).

[111] Sean M. Carroll, *The Cosmological constant*, Living Rev. Rel. **4** (2001) 1, arXiv: astro-ph/0004075 (cit. on p. 28).

[112] Simon White, C. Frenk, and Marc Davis, *Clustering in a neutrino-dominated universe*, The Astrophysical Journal **274** (1983) L1 (cit. on p. 28).

[113] D. S. Akerib et al., *First results from the LUX dark matter experiment at the Sanford Underground Research Facility*, Phys. Rev. Lett. **112** (2014) 091303, arXiv: 1310.8214 [astro-ph.CO] (cit. on p. 28).

[114] E. Aprile et al., *First Dark Matter Search Results from the XENON1T Experiment*, Phys. Rev. Lett. **119** (2017) 181301, arXiv: 1705.06655 [astro-ph.CO] (cit. on p. 28).

[115] F. Donato, D. Maurin, P. Brun, T. Delahaye, and P. Salati, *Constraints on WIMP Dark Matter from the High Energy PAMELA $\bar{p}/p$ data*, Phys. Rev. Lett. **102** (2009) 071301, arXiv: 0810.5292 [astro-ph] (cit. on p. 28).

[116] F. Aharonian et al., *H.E.S.S. observations of the Galactic Center region and their possible dark matter interpretation*, Phys. Rev. Lett. **97** (2006) 221102, [Erratum: Phys.Rev.Lett. 97, 249901 (2006)], arXiv: astro-ph/0610509 (cit. on p. 28).

[117] M. G. Aartsen et al., *Search for dark matter annihilations in the Sun with the 79-string IceCube detector*, Phys. Rev. Lett. **110** (2013) 131302, arXiv: 1212.4097 [astro-ph.HE] (cit. on p. 28).

[118] ATLAS Collaboration, *Search for large missing transverse momentum in association with one top-quark in proton-proton collisions at $\sqrt{s} = 13$ TeV with the ATLAS detector*, JHEP **05** (2019) 041, arXiv: 1812.09743 [hep-ex] (cit. on p. 28).

[119] CMS Collaboration, *Search for dark matter produced in association with a single top quark or a top quark pair in proton-proton collisions at $\sqrt{s} = 13$ TeV*, JHEP **03** (2019) 141, arXiv: 1901.01553 [hep-ex] (cit. on p. 28).

[120] LHCb Collaboration, *Search for Dark Photons Produced in 13 TeV pp Collisions*, Phys. Rev. Lett. **120** (2018) 061801, arXiv: 1710.02867 [hep-ex] (cit. on p. 28).

[121] N. Aghanim et al., *Planck 2018 results. VI. Cosmological parameters*, Astron. Astrophys. **641** (2020) A6, arXiv: 1807.06209 [astro-ph.CO] (cit. on p. 29).

[122] A.D. Sakharov, *Violation of CP Invariance, C asymmetry, and baryon asymmetry of the universe*, Sov. Phys. Usp. **34** (1991) 392 (cit. on p. 29).

[123] J. C. Pati, A. Salam, and J. Strathdee, *On fermion number and its conservation*, Il Nuovo Cimento A (1971-1996) **26** (1975) 72, URL: https://doi.org/10.1007/BF02849600 (cit. on p. 29).

[124] W. Buchmüller, R. Rückl, and D. Wyler, *Leptoquarks in lepton-quark collisions*, Physics Letters B **191** (1987) 442, ISSN: 0370-2693, URL: http://www.sciencedirect.com/science/article/pii/037026938790637X (cit. on pp. 30, 31, 37).

[125] A. Djouadi, T. Kohler, M. Spira, and J. Tutas, *(e b), (e t) TYPE LEPTOQUARKS AT e p COLLIDERS*, Z. Phys. C **46** (1990) 679 (cit. on p. 30).

[126] JoAnne L. Hewett and Thomas G. Rizzo, *Much ado about leptoquarks: A Comprehensive analysis*, Phys. Rev. D **56** (1997) 5709, arXiv: hep-ph/9703337 (cit. on p. 30).

[127] G. Gabrielse, D. Hanneke, T. Kinoshita, M. Nio, and Brian C. Odom, *New Determination of the Fine Structure Constant from the Electron g Value and QED*, Phys. Rev. Lett. **97** (2006) 030802, [Erratum: Phys.Rev.Lett. 99, 039902 (2007)] (cit. on p. 32).

[128] Ilja Doršner, Svjetlana Fajfer, and Shaikh Saad, *$\mu \to e\gamma$ selecting scalar leptoquark solutions for the $(g-2)_{e,\mu}$ puzzles*, Phys. Rev. D **102** (2020) 075007, arXiv: 2006.11624 [hep-ph] (cit. on p. 32).

[129] Ilja Doršner, Svjetlana Fajfer, and Olcyr Sumensari, *Muon $g-2$ and scalar leptoquark mixing*, JHEP **06** (2020) 089, arXiv: 1910.03877 [hep-ph] (cit. on p. 32).

[130] Innes Bigaran and Raymond R. Volkas, *Getting chirality right: single scalar leptoquark solution/s to the $(g-2)_{e,\mu}$ puzzle*, Phys. Rev. D **102** (2020) 075037, arXiv: 2002.12544 [hep-ph] (cit. on p. 32).

[131] Ufuk Aydemir, Djordje Minic, Chen Sun, and Tatsu Takeuchi, *B-decay anomalies and scalar leptoquarks in unified Pati-Salam models from noncommutative geometry*, JHEP **09** (2018) 117, arXiv: 1804.05844 [hep-ph] (cit. on p. 33).

[132] LHCb Collaboration, "Observation of CP violation in charm decays at LHCb", *54th Rencontres de Moriond on Electroweak Interactions and Unified Theories (Moriond EW 2019) La Thuile, Italy, March 16-23, 2019*, 2019, arXiv: 1905.05428 [hep-ex] (cit. on pp. 32, 34).

[133] LHCb Collaboration, *Test of lepton universality with $B^0 \to K^{*0}\ell^+\ell^-$ decays*, JHEP **08** (2017) 055, arXiv: 1705.05802 [hep-ex] (cit. on pp. 32, 33).

[134] LHCb Collaboration, *Measurement of the ratio of branching fractions $\mathcal{B}(\bar{B}^0 \to D^{*+}\tau^-\bar{\nu}_\tau)/\mathcal{B}(\bar{B}^0 \to D^{*+}\mu^-\bar{\nu}_\mu)$*, Phys. Rev. Lett. **115** (2015) 111803, [Erratum: Phys.Rev.Lett. 115, 159901 (2015)], arXiv: 1506.08614 [hep-ex] (cit. on p. 32).

[135] Ben Gripaios, Marco Nardecchia, and S. A. Renner, *Composite leptoquarks and anomalies in B-meson decays*, JHEP **05** (2015) 006, arXiv: 1412.1791 [hep-ph] (cit. on p. 32).

[136] Marat Freytsis, Zoltan Ligeti, and Joshua T. Ruderman, *Flavor models for* $\bar{B} \to D^{(*)}\tau\bar{\nu}$, Phys. Rev. **D92** (2015) 054018, arXiv: 1506.08896 [hep-ph] (cit. on p. 32).

[137] Martin Bauer and Matthias Neubert, *Minimal Leptoquark Explanation for the* $R_{D^{(*)}}$ *,* R_K *, and* $(g-2)_g$ *Anomalies*, Phys. Rev. Lett. **116** (2016) 141802, arXiv: 1511.01900 [hep-ph] (cit. on p. 32).

[138] Luca Di Luzio and Marco Nardecchia, *What is the scale of new physics behind the B-flavour anomalies?*, Eur. Phys. J. **C77** (2017) 536, arXiv: 1706.01868 [hep-ph] (cit. on p. 32).

[139] Dario Buttazzo, Admir Greljo, Gino Isidori, and David Marzocca, *B-physics anomalies: a guide to combined explanations*, JHEP **11** (2017) 044, arXiv: 1706.07808 [hep-ph] (cit. on p. 32).

[140] Roel Aaij et al., *Test of lepton universality using* $B^+ \to K^+\ell^+\ell^-$ *decays*, Phys. Rev. Lett. **113** (2014) 151601, arXiv: 1406.6482 [hep-ex] (cit. on p. 32).

[141] M. Huschle et al., *Measurement of the branching ratio of* $\overline{B} \to D^{(*)}\tau^-\overline{\nu}_\tau$ *relative to* $\overline{B} \to D^{(*)}\ell^-\overline{\nu}_\ell$ *decays with hadronic tagging at Belle*, Phys. Rev. D **92** (7 2015) 072014, URL: https://link.aps.org/doi/10.1103/PhysRevD.92.072014 (cit. on p. 32).

[142] Y. Sato et al., *Measurement of the branching ratio of* $\overline{B}^0 \to D^{*+}\tau^-\overline{\nu}_\tau$ *relative to* $\overline{B}^0 \to D^{*+}\ell^-\overline{\nu}_\ell$ *decays with a semileptonic tagging method*, Phys. Rev. D **94** (7 2016) 072007, URL: https://link.aps.org/doi/10.1103/PhysRevD.94.072007 (cit. on p. 32).

[143] S. Hirose et al., *Measurement of the* τ *Lepton Polarization and* $R(D^*)$ *in the Decay* $\overline{B} \to D^*\tau^-\overline{\nu}_\tau$, Phys. Rev. Lett. **118** (21 2017) 211801, URL: https://link.aps.org/doi/10.1103/PhysRevLett.118.211801 (cit. on p. 32).

[144] J. P. Lees et al., *Evidence for an Excess of* $\overline{B} \to D^{(*)}\tau^-\overline{\nu}_\tau$ *Decays*, Phys. Rev. Lett. **109** (10 2012) 101802, URL: https://link.aps.org/doi/10.1103/PhysRevLett.109.101802 (cit. on p. 32).

[145] J. P. Lees et al., *Measurement of an excess of* $\overline{B} \to D^{(*)}\tau^-\overline{\nu}_\tau$ *decays and implications for charged Higgs bosons*, Phys. Rev. D **88** (7 2013) 072012, URL: https://link.aps.org/doi/10.1103/PhysRevD.88.072012 (cit. on p. 32).

[146] LHCb Collaboration, *Test of lepton universality in beauty-quark decays*, (2021), arXiv: 2103.11769 [hep-ex] (cit. on pp. 32, 33).

[147] R. Aaij et al., *Test of Lepton Flavor Universality by the measurement of the $B^0 \to D^{*-}\tau^+\nu_\tau$ branching fraction using three-prong τ decays*, Phys. Rev. D **97** (2018) 072013, arXiv: 1711.02505 [hep-ex] (cit. on pp. 32, 33).

[148] ATLAS Collaboration, *Test of the universality of τ and μ lepton couplings in W-boson decays from $t\bar{t}$ events with the ATLAS detector*, (2020), arXiv: 2007.14040 [hep-ex] (cit. on p. 33).

[149] Svjetlana Fajfer, Jernej F. Kamenik, and Ivan Nisandzic, *On the $B \to D^*\tau\bar{\nu}_\tau$ Sensitivity to New Physics*, Phys. Rev. D **85** (2012) 094025, arXiv: 1203.2654 [hep-ph] (cit. on p. 33).

[150] David M. Straub, *flavio: a Python package for flavour and precision phenomenology in the Standard Model and beyond*, (2018), arXiv: 1810.08132 [hep-ph] (cit. on p. 33).

[151] Marzia Bordone, Gino Isidori, and Andrea Pattori, *On the Standard Model predictions for R_K and R_{K^*}*, Eur. Phys. J. C **76** (2016) 440, arXiv: 1605.07633 [hep-ph] (cit. on p. 33).

[152] Christoph Bobeth, Gudrun Hiller, and Giorgi Piranishvili, *Angular distributions of $\bar{B} \to \bar{K}\ell^+\ell^-$ decays*, JHEP **12** (2007) 040, arXiv: 0709.4174 [hep-ph] (cit. on p. 33).

[153] Sébastien Descotes-Genon, Lars Hofer, Joaquim Matias, and Javier Virto, *Global analysis of $b \to s\ell\ell$ anomalies*, JHEP **06** (2016) 092, arXiv: 1510.04239 [hep-ph] (cit. on p. 33).

[154] Gudrun Hiller, Dennis Loose, and Ivan Nišandžić, *Flavorful leptoquarks at hadron colliders*, Phys. Rev. D **97** (2018) 075004, arXiv: 1801.09399 [hep-ph] (cit. on p. 34).

[155] José Eliel Camargo-Molina, Alejandro Celis, and Darius A. Faroughy, *Anomalies in Bottom from new physics in Top*, Phys. Lett. B **784** (2018) 284, arXiv: 1805.04917 [hep-ph] (cit. on p. 34).

[156] Heinrich Päs and Erik Schumacher, *Common origin of R_K and neutrino masses*, Phys. Rev. **D92** (2015) 114025, arXiv: 1510.08757 [hep-ph] (cit. on p. 34).

[157] Ilja Doršner, Svjetlana Fajfer, and Nejc Košnik, *Leptoquark mechanism of neutrino masses within the grand unification framework*, Eur. Phys. J. **C77** (2017) 417, arXiv: 1701.08322 [hep-ph] (cit. on p. 34).

[158] Oleg Popov and Graham A White, *One Leptoquark to unify them? Neutrino masses and unification in the light of $(g-2)_\mu$, $R_{D^{(\star)}}$ and R_K anomalies*, Nucl. Phys. **B923** (2017) 324, arXiv: 1611.04566 [hep-ph] (cit. on p. 34).

[159] K. S. Babu and J. Julio, *Two-Loop Neutrino Mass Generation through Leptoquarks*, Nucl. Phys. **B841** (2010) 130, arXiv: 1006.1092 [hep-ph] (cit. on p. 34).

[160] Vernon D. Barger and King-man Cheung, *Atomic parity violation, leptoquarks, and contact interactions*, Phys. Lett. **B480** (2000) 149, arXiv: hep-ph/0002259 [hep-ph] (cit. on p. 34).

[161] Bernard Aubert et al., *Search for CP violation in the decays $D^0 \to K^-K^+$ and $D^0 \to \pi^-\pi^+$*, Phys. Rev. Lett. **100** (2008) 061803, arXiv: 0709.2715 [hep-ex] (cit. on p. 34).

[162] M. Staric et al., *Measurement of CP asymmetry in Cabibbo suppressed D^0 decays*, Phys. Lett. **B670** (2008) 190, arXiv: 0807.0148 [hep-ex] (cit. on p. 34).

[163] Miriam Leurer, *A Comprehensive study of leptoquark bounds*, Phys. Rev. D **49** (1994) 333, arXiv: hep-ph/9309266 (cit. on pp. 34, 37).

[164] Miriam Leurer, "New bounds on leptoquarks", *5th International Symposium on Heavy Flavor Physics*, 1993 93, arXiv: hep-ph/9309288 (cit. on p. 34).

[165] B. Dion, L. Marleau, and G. Simon, *Scalar and vector leptoquark pair production at hadron colliders: Signal and backgrounds*, Phys. Rev. D **59** (1999) 015001, arXiv: hep-ph/9808413 (cit. on p. 35).

[166] Morad Aaboud et al., *Searches for third-generation scalar leptoquarks in $\sqrt{s} = 13$ TeV pp collisions with the ATLAS detector*, JHEP **06** (2019) 144, arXiv: 1902.08103 [hep-ex] (cit. on pp. 36, 41, 44, 126, 147).

[167] Celine Degrande et al., *UFO - The Universal FeynRules Output*, Comput. Phys. Commun. **183** (2012) 1201, arXiv: 1108.2040 [hep-ph] (cit. on pp. 37, 67).

[168] Tanumoy Mandal, Subhadip Mitra, and Satyajit Seth, *Pair Production of Scalar Leptoquarks at the LHC to NLO Parton Shower Accuracy*, Phys. Rev. **D93** (2016) 035018, arXiv: 1506.07369 [hep-ph] (cit. on pp. 37, 38, 148).

[169] J H Christenson et al., *Observation of massive muon pairs in hadron collisions*, Phys. Rev. Lett. **25** (1970) 1523, URL: https://cds.cern.ch/record/350316 (cit. on p. 38).

[170] ATLAS Collaboration, *Measurement of the cross section for isolated-photon plus jet production in pp collisions at $\sqrt{s} = 13$ TeV using the ATLAS detector*, Phys. Lett. B **780** (2017) 578, 40 pages in total, author list starting page 24, 5 figures, 1 table, published in Physics Letters B, All figures including auxiliary figures are available at http://atlas.web.cern.ch/Atlas/GROUPS/PHYSICS/PAPERS/STDM-2017-01/, URL: https://cds.cern.ch/record/2299162 (cit. on p. 38).

[171] ATLAS Collaboration, *Single Top-Quark Production Cross Section Using the ATLAS Detector at the LHC*, tech. rep. ATL-PHYS-PROC-2016-216, CERN, 2016, URL: https://cds.cern.ch/record/2231834 (cit. on pp. 39, 121).

[172] CMS Collaboration, *The CMS Experiment at the CERN LHC*, JINST **3** (2008) S08004 (cit. on pp. 40, 46).

[173] CMS Collaboration, *Search for pair production of first-generation scalar leptoquarks at $\sqrt{s}$ = 13 TeV*, Phys. Rev. D **99** (2019) 052002, arXiv: 1811.01197 [hep-ex] (cit. on pp. 40–42).

[174] CMS Collaboration, *Search for pair production of second-generation leptoquarks at $\sqrt{s}$ = 13 TeV*, Phys. Rev. D **99** (2019) 032014, arXiv: 1808.05082 [hep-ex] (cit. on pp. 40–42).

[175] CMS Collaboration, *Searches for physics beyond the standard model with the M_{T2} variable in hadronic final states with and without disappearing tracks in proton-proton collisions at $\sqrt{s}$ = 13 TeV*, Eur. Phys. J. C **80** (2020) 3, arXiv: 1909.03460 [hep-ex] (cit. on p. 40).

[176] ATLAS Collaboration, *Searches for scalar leptoquarks and differential cross-section measurements in dilepton-dijet events in proton-proton collisions at a centre-of-mass energy of $\sqrt{s}$ = 13 TeV with the ATLAS experiment*, (2019), arXiv: 1902.00377 [hep-ex] (cit. on pp. 40, 41, 43, 102).

[177] ATLAS Collaboration, *Search for a scalar partner of the top quark in the all-hadronic $t\bar{t}$ plus missing transverse momentum final state at $\sqrt{s}$=13 TeV with the ATLAS detector*, (2020), arXiv: 2004.14060 [hep-ex] (cit. on p. 41).

[178] Morad Aaboud et al., *Search for B-L R -parity-violating top squarks in $\sqrt{s}$ =13 TeV pp collisions with the ATLAS experiment*, Phys. Rev. **D97** (2018) 032003, arXiv: 1710.05544 [hep-ex] (cit. on pp. 41, 106, 122).

[179] ATLAS Collaboration, *Search for pair production of scalar leptoquarks decaying into first- or second-generation leptons and top quarks in proton-proton collisions at $\sqrt{s}$ = 13 TeV with the ATLAS detector*, (2020), arXiv: 2010.02098 [hep-ex] (cit. on p. 41).

[180] Tianqi Chen and Carlos Guestrin, *XGBoost*, Proceedings of the 22nd ACM SIGKDD International Conference on Knowledge Discovery and Data Mining (2016), URL: http://dx.doi.org/10.1145/2939672.2939785 (cit. on p. 41).

[181] *Search for pair production of third-generation scalar leptoquarks decaying into a top quark and a tau-lepton in pp collisions at $\sqrt{s}$ = 13 TeV with the ATLAS detector*, (2020) (cit. on p. 41).

[182] ATLAS Collaboration, *The ATLAS Experiment at the CERN Large Hadron Collider*, JINST **3** (2008) S08003 (cit. on p. 46).

[183] Oliver Sim Brüning et al., *LHC Design Report*, CERN Yellow Reports: Monographs, CERN, 2004, URL: http://cds.cern.ch/record/782076 (cit. on p. 46).

[184] Lyndon Evans and Philip Bryant, *LHC Machine*, JINST **3** (2008) S08001 (cit. on p. 46).

[185] *LEP design report*, Copies shelved as reports in LEP, PS and SPS libraries, CERN, 1984, URL: https://cds.cern.ch/record/102083 (cit. on p. 46).

[186] LHCb Collaboration, *The LHCb Detector at the LHC*, JINST **3** (2008) S08005 (cit. on p. 46).

[187] ALICE Collaboration, *The ALICE experiment at the CERN LHC*, JINST **3** (2008) S08002 (cit. on p. 46).

[188] Esma Mobs, *The CERN accelerator complex - 2019. Complexe des accélérateurs du CERN - 2019*, (2019), General Photo, URL: https://cds.cern.ch/record/2684277 (cit. on p. 47).

[189] *Luminosity determination in pp collisions at $\sqrt{s} = 13$ TeV using the ATLAS detector at the LHC*, tech. rep. ATLAS-CONF-2019-021, CERN, 2019, URL: http://cds.cern.ch/record/2677054 (cit. on pp. 48–50, 127).

[190] ATLAS Collaboration, *The new LUCID-2 detector for luminosity measurement and monitoring in ATLAS*, JINST **13** (2018) P07017 (cit. on pp. 49, 58).

[191] ATLAS Collaboration, *Reconstruction of primary vertices at the ATLAS experiment in Run 1 proton–proton collisions at the LHC*, Eur. Phys. J. C **77** (2017) 332, arXiv: 1611.10235 [physics.ins-det] (cit. on pp. 49, 82).

[192] *Characterization of Interaction-Point Beam Parameters Using the pp Event-Vertex Distribution Reconstructed in the ATLAS Detector at the LHC*, tech. rep. ATLAS-CONF-2010-027, CERN, 2010, URL: http://cds.cern.ch/record/1277659 (cit. on p. 49).

[193] ATLAS Collaboration, *ATLAS data quality operations and performance for 2015–2018 data-taking*, JINST **15** (2020) P04003, arXiv: 1911.04632 [physics.ins-det] (cit. on pp. 49, 50).

[194] ATLAS Collaboration, *The ATLAS Experiment at the CERN Large Hadron Collider*, JINST **3** (2008) S08003 (cit. on p. 51).

[195] ATLAS Collaboration, "Computer generated image of the whole ATLAS detector", 2008, URL: http://cds.cern.ch/record/1095924 (cit. on p. 52).

[196] *ATLAS magnet system: Technical design report*, (1997) (cit. on pp. 52, 53).

[197] ATLAS Collaboration, "Computer generated image of the ATLAS inner detector", 2008, URL: http://cds.cern.ch/record/1095926 (cit. on p. 53).

[198] ATLAS Collaboration, *The upgraded Pixel detector and the commissioning of the Inner Detector tracking of the ATLAS experiment for Run-2 at the Large Hadron Collider*, PoS **EPS-HEP2015** (2015) 261, arXiv: 1608.07850 [physics.ins-det] (cit. on p. 53).

[199] *Technical Design Report for the ATLAS Inner Tracker Pixel Detector*, tech. rep. CERN-LHCC-2017-021. ATLAS-TDR-030, CERN, 2017, URL: https://cds.cern.ch/record/2285585 (cit. on p. 54).

[200] ATLAS Collaboration, *ATLAS Insertable B-Layer Technical Design Report*, tech. rep. CERN-LHCC-2010-013. ATLAS-TDR-19, 2010, URL: https://cds.cern.ch/record/1291633 (cit. on p. 54).

[201] ATLAS Collaboration, *The ATLAS semiconductor tracker*, Nucl. Instrum. Methods Phys. Res., A **466** (2001) 243, URL: http://cds.cern.ch/record/516841 (cit. on p. 54).

[202] ATLAS Collaboration, "The ATLAS transition radiation tracker", *8th International Conference on Advanced Technology and Particle Physics (ICATPP 2003): Astroparticle, Particle, Space Physics, Detectors and Medical Physics Applications*, 2003 497, arXiv: hep-ex/0311058 (cit. on p. 54).

[203] ATLAS Collaboration, "Computer Generated image of the ATLAS calorimeter", 2008, URL: http://cds.cern.ch/record/1095927 (cit. on p. 56).

[204] *ATLAS liquid argon calorimeter: Technical design report*, (1996) (cit. on p. 56).

[205] ATLAS Collaboration, *Energy linearity and resolution of the ATLAS electromagnetic barrel calorimeter in an electron test-beam*, Nucl. Instrum. Meth. A **568** (2006) 601, arXiv: physics/0608012 (cit. on p. 56).

[206] ATLAS Collaboration, *The ATLAS liquid argon hadronic end-cap calorimeter: Construction and selected beam test results*, Nucl. Phys. B Proc. Suppl. **150** (2006) 102, ed. by C. Bosio, P.S. Marrocchesi, F.L. Navarria, M. Paganoni, and P.G. Pelfer, arXiv: physics/0407026 (cit. on p. 56).

[207] *ATLAS tile calorimeter: Technical design report*, (1996) (cit. on p. 56).

[208] *ATLAS muon spectrometer: Technical design report*, (1997) (cit. on p. 57).

[209] ATLAS Collaboration, "Computer generated image of the ATLAS Muons subsystem", 2008, URL: http://cds.cern.ch/record/1095929 (cit. on p. 58).

[210] ATLAS Collaboration, *ATLAS high-level trigger, data-acquisition and controls: Technical Design Report*, Technical Design Report ATLAS, CERN, 2003, URL: https://cds.cern.ch/record/616089 (cit. on p. 58).

[211] *ATLAS level-1 trigger: Technical Design Report*, Technical Design Report ATLAS, CERN, 1998, URL: https://cds.cern.ch/record/381429 (cit. on p. 58).

[212] ATLAS Collaboration, *Operation of the ATLAS trigger system in Run 2*, (2020), arXiv: 2007.12539 [physics.ins-det] (cit. on p. 58).

[213] ATLAS Collaboration, *The ATLAS Level-1 Topological Processor: from design to routine usage in Run-2*, tech. rep. ATL-DAQ-PROC-2018-044, CERN, 2018, URL: https://cds.cern.ch/record/2649959 (cit. on p. 58).

[214] ATLAS Collaboration, *Minimum Bias Trigger Scintillators in ATLAS Run II*, JINST **9** (2014) C10020 (cit. on p. 58).

[215] ATLAS Collaboration, *Zero Degree Calorimeters for ATLAS*, tech. rep. CERN-LHCC-2007-001. LHCC-I-016, CERN, 2007, URL: https://cds.cern.ch/record/1009649 (cit. on p. 58).

[216] ATLAS Collaboration, *Operation of the upgraded ATLAS Central Trigger Processor during the LHC Run 2*, tech. rep. ATL-DAQ-PROC-2015-050. 02, CERN, 2015, URL: https://cds.cern.ch/record/2063035 (cit. on p. 58).

[217] ATLAS Collaboration, *Performance of the ATLAS trigger system in 2015*, Eur. Phys. J. C **77** (2017) 317, arXiv: 1611.09661 [hep-ex] (cit. on p. 59).

[218] ATLAS Collaboration, *The ATLAS Data Acquisition system in LHC Run 2*, tech. rep. ATL-DAQ-PROC-2017-007. 3, CERN, 2017, URL: https://cds.cern.ch/record/2244345 (cit. on p. 59).

[219] T. Gleisberg et al., *Event generation with SHERPA 1.1*, JHEP **02** (2009) 007, arXiv: 0811.4622 [hep-ph] (cit. on pp. 63, 65, 67, 68).

[220] H. Bethe and W. Heitler, *On the Stopping of fast particles and on the creation of positive electrons*, Proc. Roy. Soc. Lond. A **A146** (1934) 83 (cit. on p. 64).

[221] V.V. Sudakov, *Vertex parts at very high-energies in quantum electrodynamics*, Sov. Phys. JETP **3** (1956) 65 (cit. on p. 64).

[222] Stafano Frixione and Bryan R. Webber, *The MC@NLO 3.3 Event Generator*, (2006), arXiv: hep-ph/0612272 (cit. on p. 65).

[223] Paolo Nason, *A New method for combining NLO QCD with shower Monte Carlo algorithms*, JHEP **11** (2004) 040, arXiv: hep-ph/0409146 (cit. on pp. 65, 68, 153).

[224] F. Krauss, *Matrix elements and parton showers in hadronic interactions*, JHEP **08** (2002) 015, arXiv: hep-ph/0205283 (cit. on pp. 65, 67).

[225] S. Catani, F. Krauss, R. Kuhn, and B.R. Webber, *QCD matrix elements + parton showers*, JHEP **11** (2001) 063, arXiv: hep-ph/0109231 (cit. on pp. 65, 67).

[226] S. Catani, Yuri L. Dokshitzer, M.H. Seymour, and B.R. Webber, *Longitudinally invariant K_t clustering algorithms for hadron hadron collisions*, Nucl. Phys. B **406** (1993) 187 (cit. on p. 65).

[227] S. Catani, Yuri L. Dokshitzer, M. Olsson, G. Turnock, and B.R. Webber, *New clustering algorithm for multi - jet cross-sections in e+ e- annihilation*, Phys. Lett. B **269** (1991) 432 (cit. on p. 65).

[228] Leif Lönnblad and Stefan Prestel, *Merging Multi-leg NLO Matrix Elements with Parton Showers*, JHEP **03** (2013) 166, arXiv: 1211.7278 [hep-ph] (cit. on pp. 65, 70).

[229] Nils Lavesson and Leif Lonnblad, *W+jets matrix elements and the dipole cascade*, JHEP **07** (2005) 054, arXiv: hep-ph/0503293 (cit. on p. 65).

[230] Leif Lonnblad, *Correcting the color dipole cascade model with fixed order matrix elements*, JHEP **05** (2002) 046, arXiv: hep-ph/0112284 (cit. on p. 65).

[231] ATLAS Collaboration, *The ATLAS Monte Carlo Project*, tech. rep. ATL-SOFT-INT-2010-002, CERN, 2010, URL: https://cds.cern.ch/record/1239901 (cit. on p. 65).

[232] S. Agostinelli et al., *GEANT4–a simulation toolkit*, Nucl. Instrum. Meth. A **506** (2003) 250 (cit. on p. 65).

[233] S. Guatelli, Dean Cutajar, B. Oborn, and Anatoly Rosenfeld, *Introduction to the Geant4 Simulation toolkit*, AIP Conference Proceedings **1345** (2011) 303 (cit. on p. 65).

[234] ATLAS Collaboration, *The new ATLAS Fast Calorimeter Simulation*, PoS **ICHEP2016** (2016) 184 (cit. on p. 66).

[235] ATLAS Collaboration, *The ATLAS Simulation Infrastructure*, Eur. Phys. J. C **70** (2010) 823, arXiv: 1005.4568 [physics.ins-det] (cit. on p. 66).

[236] Simulation Group, *Public Plots*, https://atlas.web.cern.ch/Atlas/GROUPS/PHYSICS/PLOTS/SIM-2019-002/, Accessed: 2020-08-20 (cit. on p. 66).

[237] Tanju Gleisberg and Stefan Höche, *Comix, a new matrix element generator*, JHEP **12** (2008) 039, arXiv: 0808.3674 [hep-ph] (cit. on pp. 67, 68).

[238] Fabio Cascioli, Philipp Maierhofer, and Stefano Pozzorini, *Scattering Amplitudes with Open Loops*, Phys. Rev. Lett. **108** (2012) 111601, arXiv: 1111.5206 [hep-ph] (cit. on pp. 67, 68).

[239] Steffen Schumann and Frank Krauss, *A Parton shower algorithm based on Catani-Seymour dipole factorisation*, JHEP **03** (2008) 038, arXiv: 0709.1027 [hep-ph] (cit. on pp. 67, 68, 70).

[240] Stefan Höche, Frank Krauss, Marek Schönherr, and Frank Siegert, *QCD matrix elements + parton showers: The NLO case*, JHEP **04** (2013) 027, arXiv: 1207.5030 [hep-ph] (cit. on pp. 67, 68).

[241] Federico Buccioni et al., *OpenLoops 2*, Eur. Phys. J. C **79** (2019) 866, arXiv: 1907.13071 [hep-ph] (cit. on p. 67).

[242] Ansgar Denner, Stefan Dittmaier, and Lars Hofer, *Collier: A fortran-based complex one-loop library in extended regularizations*, Comput. Phys. Commun. **212** (2017) 220, arXiv: 1604.06792 [hep-ph] (cit. on p. 67).

[243] F. Krauss, R. Kuhn, and G. Soff, *AMEGIC++ 1.0: A Matrix element generator in C++*, JHEP **02** (2002) 044, arXiv: hep-ph/0109036 (cit. on p. 67).

[244] R. Kuhn, F. Krauss, B. Ivanyi, and G. Soff, *APACIC++: A PArton Cascade In C++, version 1.0*, Comput. Phys. Commun. **134** (2001) 223, arXiv: hep-ph/0004270 (cit. on p. 67).

[245] F. Krauss, A. Schalicke, and G. Soff, *APACIC++ 2.0: A Parton cascade in C++*, Comput. Phys. Commun. **174** (2006) 876, arXiv: hep-ph/0503087 (cit. on p. 67).

[246] Jan-Christopher Winter, Frank Krauss, and Gerhard Soff, *A Modified cluster hadronization model*, Eur. Phys. J. C **36** (2004) 381, arXiv: hep-ph/0311085 (cit. on p. 67).

[247] Michal Czakon and Alexander Mitov, *Top++: A Program for the Calculation of the Top-Pair Cross-Section at Hadron Colliders*, Compt/ Phys. Commun. (2014) 2930, arXiv: 1112.5675 [hep-ph] (cit. on pp. 67–69, 153).

[248] Torbjorn Sjöstrand, Stephen Mrenna, and Peter Z. Skands, *PYTHIA 6.4 Physics and Manual*, JHEP **05** (2006) 026, arXiv: hep-ph/0603175 (cit. on p. 67).

[249] Bo Andersson, "THE LUND STRING MODEL", *7th European Symposium on Antiproton Interactions: From LEAR to the Collider and Beyond*, 1986 447 (cit. on p. 67).

[250] Adam Alloul, Neil D. Christensen, Céline Degrande, Claude Duhr, and Benjamin Fuks, *FeynRules 2.0 - A complete toolbox for tree-level phenomenology*, Comput. Phys. Commun. **185** (2014) 2250, arXiv: 1310.1921 [hep-ph] (cit. on p. 67).

[251] J.M. Butterworth, Jeffrey R. Forshaw, and M.H. Seymour, *Multiparton interactions in photoproduction at HERA*, Z. Phys. C **72** (1996) 637, arXiv: hep-ph/9601371 (cit. on p. 67).

[252] J.M. Butterworth and M.H. Seymour, *JIMMY4: Multiparton Interactions in HERWIG for the LHC.*, tech. rep., 2004 (cit. on p. 67).

[253] Stefano Frixione and Bryan R. Webber, *Matching NLO QCD computations and parton shower simulations*, JHEP **06** (2002) 029, arXiv: hep-ph/0204244 [hep-ph] (cit. on p. 68).

[254] Stefano Frixione, Fabian Stoeckli, Paolo Torrielli, Bryan R. Webber, and Chris D. White, *The MCaNLO 4.0 Event Generator*, (2010), arXiv: 1010.0819 [hep-ph] (cit. on p. 68).

[255] Stefano Frixione, Paolo Nason, and Carlo Oleari, *Matching NLO QCD computations with Parton Shower simulations: the POWHEG method*, JHEP **11** (2007) 070, arXiv: 0709.2092 [hep-ph] (cit. on pp. 68, 153).

[256] Simone Alioli, Paolo Nason, Carlo Oleari, and Emanuele Re, *A general framework for implementing NLO calculations in shower Monte Carlo programs: the POWHEG BOX*, JHEP **06** (2010) 043, arXiv: 1002.2581 [hep-ph] (cit. on pp. 68, 153).

[257] Carlo Oleari, *The POWHEG-BOX*, Nucl. Phys. B Proc. Suppl. **205-206** (2010) 36, ed. by Johannes Blümlein, Sven-Olaf Moch, and Tord Riemann, arXiv: 1007.3893 [hep-ph] (cit. on p. 68).

[258] J. Alwall et al., *The automated computation of tree-level and next-to-leading order differential cross sections, and their matching to parton shower simulations*, JHEP **07** (2014) 079, arXiv: 1405.0301 [hep-ph] (cit. on pp. 68, 154).

[259] D. J. Lange, *The EvtGen particle decay simulation package*, Nucl. Instrum. Meth. A **462** (2001) 152 (cit. on p. 68).

[260] Richard D. Ball et al., *Parton distributions for the LHC Run II*, JHEP **04** (2015) 040, arXiv: 1410.8849 [hep-ph] (cit. on pp. 68, 153).

[261] Nikolaos Kidonakis, *Next-to-next-to-leading-order collinear and soft gluon corrections for t-channel single top quark production*, Phys. Rev. **D83** (2011) 091503, arXiv: 1103.2792 [hep-ph] (cit. on pp. 68, 69).

[262] Nikolaos Kidonakis, *Two-loop soft anomalous dimensions for single top quark associated production with a W- or H-*, Phys. Rev. **D82** (2010) 054018, arXiv: 1005.4451 [hep-ph] (cit. on pp. 68, 69).

[263] Nikolaos Kidonakis, *NNLL resummation for s-channel single top quark production*, Phys. Rev. D **81** (2010) 054028, arXiv: 1001.5034 [hep-ph] (cit. on pp. 68, 129).

[264] Stefano Catani, Leandro Cieri, Giancarlo Ferrera, Daniel de Florian, and Massimiliano Grazzini, *Vector boson production at hadron colliders: A Fully exclusive QCD calculation at NNLO*, Phys.Rev.Lett. **103** (2009) 082001, arXiv: 0903.2120 [hep-ph] (cit. on p. 68).

[265] Torbjörn Sjöstrand et al., *An introduction to PYTHIA 8.2*, Computer Physics Communications **191** (2015) 159, ISSN: 0010-4655, URL: http://dx.doi.org/10.1016/j.cpc.2015.01.024 (cit. on p. 69).

[266] Peter Zeiler Skands, *Tuning Monte Carlo Generators: The Perugia Tunes*, Phys. Rev. D **82** (2010) 074018, arXiv: 1005.3457 [hep-ph] (cit. on p. 69).

[267] J. Pumplin et al., *New generation of parton distributions with uncertainties from global QCD analysis*, JHEP **07** (2002) 012, arXiv: hep-ph/0201195 (cit. on p. 69).

[268] ATLAS Collaboration, *Studies on top-quark Monte Carlo modelling for Top2016*, ATL-PHYS-PUB-2016-020, 2016, URL: https://cds.cern.ch/record/2216168 (cit. on pp. 69, 153).

[269] ATLAS Collaboration, *Comparison of Monte Carlo generator predictions for gap fraction and jet multiplicity observables in $t\bar{t}$ events*, ATL-PHYS-PUB-2014-005, 2014, URL: https://cds.cern.ch/record/1703034 (cit. on p. 69).

[270] ATLAS Collaboration, *Multi-Boson Simulation for 13 TeV ATLAS Analyses*, ATL-PHYS-PUB-2017-005, 2017, URL: https://cds.cern.ch/record/2261933 (cit. on p. 69).

[271] M. Bahr et al., *Herwig++ Physics and Manual*, Eur. Phys. J. C **58** (2008) 639, arXiv: 0803.0883 [hep-ph] (cit. on pp. 69, 153).

[272] Johannes Bellm et al., *Herwig 7.0/Herwig++ 3.0 release note*, Eur. Phys. J. C **76** (2016) 196, arXiv: 1512.01178 [hep-ph] (cit. on pp. 69, 153).

[273] Johannes Bellm et al., *Herwig 7.1 Release Note*, (2017), arXiv: 1705.06919 [hep-ph] (cit. on p. 69).

[274] Simon Platzer and Stefan Gieseke, *Dipole Showers and Automated NLO Matching in Herwig++*, Eur. Phys. J. **C72** (2012) 2187, arXiv: 1109.6256 [hep-ph] (cit. on p. 69).

[275] Adam Elliott Jaspan, *Implementation of merged multi-leg $t\bar{t}$ samples at NLO accuracy using Matchbox framework in Herwig 7*, tech. rep. ATL-COM-PHYS-2019-1300, CERN, 2019, URL: https://cds.cern.ch/record/2692863 (cit. on pp. 70, 73, 74).

[276] Leif Lonnblad and Stefan Prestel, *Unitarising Matrix Element + Parton Shower merging*, JHEP **02** (2013) 094, arXiv: 1211.4827 [hep-ph] (cit. on p. 70).

[277] Rikkert Frederix and Stefano Frixione, *Merging meets matching in MC@NLO*, JHEP **12** (2012) 061, arXiv: 1209.6215 [hep-ph] (cit. on p. 70).

[278] Johannes Bellm, Stefan Gieseke, and Simon Plätzer, *Merging NLO Multi-jet Calculations with Improved Unitarization*, Eur. Phys. J. **C78** (2018) 244, arXiv: 1705.06700 [hep-ph] (cit. on p. 70).

[279] Simon Plätzer, *Controlling inclusive cross sections in parton shower + matrix element merging*, JHEP **08** (2013) 114, arXiv: 1211.5467 [hep-ph] (cit. on p. 70).

[280] Gavin Cullen et al., *Automated One-Loop Calculations with GoSam*, Eur. Phys. J. **C72** (2012) 1889, arXiv: 1111.2034 [hep-ph] (cit. on p. 70).

[281] R. Keith Ellis and Giulia Zanderighi, *Scalar one-loop integrals for QCD*, JHEP **02** (2008) 002, arXiv: 0712.1851 [hep-ph] (cit. on p. 70).

[282] J. Baglio et al., *VBFNLO: A Parton Level Monte Carlo for Processes with Electroweak Bosons – Manual for Version 2.7.0*, (2011), arXiv: 1107.4038 [hep-ph] (cit. on p. 70).

[283] T. Kinoshita, *Mass singularities of Feynman amplitudes*, J. Math. Phys. **3** (1962) 650 (cit. on p. 71).

[284] T.D. Lee and M. Nauenberg, *Degenerate Systems and Mass Singularities*, Phys. Rev. **133** (1964) B1549, ed. by G. Feinberg (cit. on p. 71).

[285] Christian Bierlich et al., *Robust Independent Validation of Experiment and Theory: Rivet version 3*, SciPost Phys. **8** (2020) 026, arXiv: 1912.05451 [hep-ph] (cit. on p. 71).

[286] Simone Amoroso et al., *Challenges in Monte Carlo Event Generator Software for High-Luminosity LHC*, Comput. Softw. Big Sci. **5** (2021) 12, ed. by Andrea Valassi, Efe Yazgan, and Josh McFayden, arXiv: 2004.13687 [hep-ph] (cit. on p. 74).

[287] ATLAS Collaboration, "Development of ATLAS Primary Vertex Reconstruction for LHC Run 3", *Connecting the Dots and Workshop on Intelligent Trackers*, 2019, arXiv: 1910.08405 [hep-ex] (cit. on p. 80).

[288] ATLAS Collaboration, "Track Simulation and Reconstruction in the ATLAS experiment", 2008, URL: https://cds.cern.ch/record/2224514 (cit. on p. 80).

[289] Manuella Vincter, *Event Displays from Run 2 physics analyses*, https://twiki.cern.ch/twiki/bin/view/AtlasPublic/EventDisplayRun2Physics, Accessed: 2020-08-25 (cit. on p. 80).

[290] ATLAS Collaboration, "ATLAS collision event from the first LHC fill with stable beam on 17th April 2018", General Photo, 2018, URL: https://cds.cern.ch/record/2313779 (cit. on p. 80).

[291] ATLAS Collaboration, *The new ATLAS track reconstruction (NEWT)*, J. Phys. Conf. Ser. **119** (2008) 032014, ed. by Randall Sobie, Reda Tafirout, and Jana Thomson (cit. on p. 81).

[292] R. Fruhwirth, *Application of Kalman filtering to track and vertex fitting*, Nucl. Instrum. Meth. A **262** (1987) 444 (cit. on p. 81).

[293] *Particle Identification Performance of the ATLAS Transition Radiation Tracker*, tech. rep. ATLAS-CONF-2011-128, CERN, 2011, URL: https://cds.cern.ch/record/1383793 (cit. on p. 82).

[294] ATLAS Collaboration, *Electron reconstruction and identification in the ATLAS experiment using the 2015 and 2016 LHC proton–proton collision data at* $\sqrt{s} = 13$ *TeV*, Eur. Phys. J. (2019), arXiv: 1902.04655 [hep-ex] (cit. on p. 83).

[295] ATLAS Collaboration, *Electron efficiency measurements with the ATLAS detector using 2012 LHC proton–proton collision data*, Eur. Phys. J. C **77** (2017) 195, arXiv: 1612.01456 [hep-ex] (cit. on p. 83).

[296] ATLAS Collaboration, *Muon reconstruction performance of the ATLAS detector in proton–proton collision data at* $\sqrt{s} = 13$ *TeV*, Eur. Phys. J. C **76** (2016) 292, arXiv: 1603.05598 [hep-ex] (cit. on pp. 84, 85, 127).

[297] ATLAS Collaboration, *Muon reconstruction performance of the ATLAS detector in proton–proton collision data at $\sqrt{s}$ =13 TeV*, Eur. Phys. J. C **76** (2016) 292, arXiv: 1603.05598 [hep-ex] (cit. on p. 84).

[298] ATLAS Collaboration, *Reconstruction and identification of high-pT muons in $\sqrt{s}$ = 13 TeV proton-proton collisions with the ATLAS detector*, tech. rep. ATL-PHYS-PROC-2019-110, CERN, 2019, URL: https://cds.cern.ch/record/2691453 (cit. on p. 84).

[299] Matteo Cacciari, Gavin P. Salam, and Gregory Soyez, *The anti-k_t jet clustering algorithm*, JHEP **04** (2008) 063, arXiv: 0802.1189 [hep-ph] (cit. on pp. 86, 87).

[300] ATLAS Collaboration, *Topological cell clustering in the ATLAS calorimeters and its performance in LHC Run 1*, Eur. Phys. J. C **77** (2017) 490, arXiv: 1603.02934 [hep-ex] (cit. on p. 86).

[301] G. Corcella et al., *HERWIG 6.5 release note*, (2002), arXiv: hep-ph/0210213 (cit. on p. 87).

[302] ATLAS Collaboration, *Jet energy scale measurements and their systematic uncertainties in proton-proton collisions at $\sqrt{s} = 13$ TeV with the ATLAS detector*, Phys. Rev. D **96** (2017) 072002, arXiv: 1703.09665 [hep-ex] (cit. on p. 86).

[303] ATLAS Collaboration, *Tagging and suppression of pileup jets with the ATLAS detector*, ATLAS-CONF-2014-018, 2014, URL: https://cds.cern.ch/record/1700870 (cit. on p. 86).

[304] Julia Gonski, *How To Clean Jets 2017*, https://twiki.cern.ch/twiki/bin/viewauth/AtlasProtected/HowToCleanJets2017, Accessed: 2019-09-18 (cit. on p. 88).

[305] Julia Gonski, *Jet Cleaning in 2016 and the Event Level Cleaning Tool*, tech. rep. ATL-COM-PHYS-2017-982, CERN, 2017, URL: https://cds.cern.ch/record/2272136 (cit. on p. 88).

[306] Michael Feindt, *b quark fragmentation*, (1995) 6 p, URL: https://cds.cern.ch/record/282482 (cit. on p. 89).

[307] Wikimedia Commons, *File:B-tagging diagram.png — Wikimedia Commons, the free media repository*, [Online; accessed 27-August-2020], 2016, URL: %5Curl%7Bhttps://commons.wikimedia.org/w/index.php?title=File:B-tagging_diagram.png&oldid=216090609%7D (cit. on p. 89).

[308] ATLAS Collaboration, *Optimisation of the ATLAS b-tagging performance for the 2016 LHC Run*, ATL-PHYS-PUB-2016-012, 2016, URL: https://cds.cern.ch/record/2160731 (cit. on p. 90).

[309] *Commissioning of the ATLAS high-performance b-tagging algorithms in the 7 TeV collision data*, tech. rep. ATLAS-CONF-2011-102, CERN, 2011, URL: https://cds.cern.ch/record/1369219 (cit. on p. 90).

[310] *Expected performance of the ATLAS b-tagging algorithms in Run-2*, tech. rep. ATL-PHYS-PUB-2015-022, CERN, 2015, URL: https://cds.cern.ch/record/2037697 (cit. on p. 90).

[311] ATLAS Collaboration, *A new inclusive secondary vertex algorithm for b-jet tagging in ATLAS*, J. Phys. Conf. Ser. **119** (2008) 032032, ed. by Randall Sobie, Reda Tafirout, and Jana Thomson (cit. on p. 90).

[312] Andreas Hocker et al., *TMVA - Toolkit for Multivariate Data Analysis*, (2007), arXiv: physics/0703039 (cit. on p. 90).

[313] Leonid Gladilin, *Fragmentation fractions of c and b quarks into charmed hadrons at LEP*, Eur. Phys. J. C **75** (2015) 19, arXiv: 1404.3888 [hep-ex] (cit. on p. 91).

[314] Marie Christine Lanfermann, Tobias Golling, and Andrea Coccaro, *Deep Neural Network based higher level flavour tagging algorithm at the ATLAS experiment*, tech. rep. ATL-COM-PHYS-2017-1596, CERN, 2017, URL: https://cds.cern.ch/record/2290144 (cit. on p. 91).

[315] Ian Goodfellow, Yoshua Bengio, and Aaron Courville, *Deep Learning*, http://www.deeplearningbook.org, MIT Press, 2016 (cit. on p. 91).

[316] Yann LeCun, Yoshua Bengio, and Geoffrey Hinton, *Deep learning*, Nature **521** (2015), URL: https://doi.org/10.1038/nature14539 (cit. on p. 91).

[317] Andrew Chisholm et al., *Search for $H \to c\bar{c}$ decays in associated VH production with the ATLAS experiment: Internal Supporting Document*, tech. rep. ATL-COM-PHYS-2020-013, CERN, 2020, URL: https://cds.cern.ch/record/2706457 (cit. on p. 92).

[318] ATLAS Collaboration, *Observation of $H \to b\bar{b}$ decays and VH production with the ATLAS detector*, Phys. Lett. **B786** (2018) 59, arXiv: 1808.08238 [hep-ex] (cit. on pp. 94, 117).

[319] ATLAS Collaboration, *Recommendations of the Physics Objects and Analysis Harmonisation Study Groups 2014*, tech. rep. ATL-PHYS-INT-2014-018, CERN, 2014, URL: https://cds.cern.ch/record/1743654 (cit. on p. 94).

[320] *Publications of A. N. Kolmogorov*, Ann. Probab. **17** (1989) 945, URL: https://doi.org/10.1214/aop/1176991252 (cit. on p. 95).

[321] Gary J. Feldman and Robert D. Cousins, *A Unified approach to the classical statistical analysis of small signals*, Phys. Rev. D **57** (1998) 3873, arXiv: physics/9711021 (cit. on p. 95).

[322] *2012 Asia-Europe-Pacific School of High-Energy Physics: Fukuoka, Japan 14 - 27 Oct 2012. 1st Asia-Europe-Pacific School of High-Energy Physics*, Comments: 8 lectures, 285 pages, published as CERN Yellow Report https://cds.cern.ch/record/1443909, CERN, CERN, 2014, URL: https://cds.cern.ch/record/1443909 (cit. on p. 95).

[323] A L Read, *Modified frequentist analysis of search results (the CL_s method)*, (2000), URL: https://cds.cern.ch/record/451614 (cit. on p. 98).

[324] Alexander L. Read, *Presentation of search results: The CL(s) technique*, J. Phys. G **28** (2002) 2693, ed. by M.R. Whalley and L. Lyons (cit. on p. 98).

[325] *Procedure for the LHC Higgs boson search combination in Summer 2011*, tech. rep. CMS-NOTE-2011-005. ATL-PHYS-PUB-2011-11, CERN, 2011, URL: https://cds.cern.ch/record/1379837 (cit. on p. 100).

[326] Glen Cowan, Kyle Cranmer, Eilam Gross, and Ofer Vitells, *Asymptotic formulae for likelihood-based tests of new physics*, Eur. Phys. J. C **71** (2011) 1554, [Erratum: Eur.Phys.J.C 73, 2501 (2013)], arXiv: 1007.1727 [physics.data-an] (cit. on p. 101).

[327] S.S. Wilks, *The Large-Sample Distribution of the Likelihood Ratio for Testing Composite Hypotheses*, Annals Math. Statist. **9** (1938) 60 (cit. on pp. 101, 136).

[328] Abraham Wald, *Tests of Statistical Hypotheses Concerning Several Parameters When the Number of Observations is Large*, Transactions of the American Mathematical Society **54** (1943) 426, ISSN: 00029947, URL: http://www.jstor.org/stable/1990256 (cit. on pp. 101, 136).

[329] ATLAS Collaboration, *Performance of missing transverse momentum reconstruction with the ATLAS detector using proton–proton collisions at $\sqrt{s} = 13$ TeV*, Eur. Phys. J. C **78** (2018) 903, arXiv: 1802.08168 [hep-ex] (cit. on p. 104).

[330] Adrian Buzatu and Stephen Jiggins, *Object Definitions and Selections for Standard Model $VH \to ll/l\nu/\nu\nu + b\bar{b}$ Analysis*, tech. rep. ATL-COM-PHYS-2018-517, CERN, 2018, URL: https://cds.cern.ch/record/2317182 (cit. on p. 105).

[331] ATLAS Collaboration, *Expected Performance of the ATLAS Experiment - Detector, Trigger and Physics*, (2009), arXiv: 0901.0512 [hep-ex] (cit. on p. 116).

[332] John Alison, "The Road to Discovery: Detector Alignment, Electron Identification, Particle Misidentification, WW Physics, and the Discovery of the Higgs Boson", Presented 08 Nov 2012, 2015, URL: https://cds.cern.ch/record/1536507 (cit. on p. 116).

[333] ATLAS Collaboration, *Electron reconstruction and identification in the ATLAS experiment using the 2015 and 2016 LHC proton-proton collision data at $\sqrt{s} = 13$ TeV*, Eur. Phys. J. C **79** (2019) 639. 40 p, URL: https://cds.cern.ch/record/2657964 (cit. on p. 116).

[334] Nikolaos Kidonakis, "Top Quark Production", *Helmholtz International Summer School on Physics of Heavy Quarks and Hadrons*, 2014 139, arXiv: 1311.0283 [hep-ph] (cit. on p. 129).

[335] P. Kant et al., *HatHor for single top-quark production: Updated predictions and uncertainty estimates for single top-quark production in hadronic collisions*, Comput. Phys. Commun. **191** (2015) 74, arXiv: 1406.4403 [hep-ph] (cit. on p. 129).

[336] ATLAS Collaboration, *Evidence for single top-quark production in the s-channel in proton-proton collisions at $\sqrt{s}$ =8 TeV with the ATLAS detector using the Matrix Element Method*, Phys. Lett. B **756** (2016) 228, arXiv: 1511.05980 [hep-ex] (cit. on p. 129).

[337] *Measurement of the cross-section of the production of a W boson in association with a single top quark with ATLAS at $\sqrt{s} = 13$ TeV*, tech. rep. ATLAS-CONF-2016-065, CERN, 2016, URL: https://cds.cern.ch/record/2206207 (cit. on p. 129).

[338] *Measurement of the inclusive cross-section of single top-quark t-channel production in pp collisions at $\sqrt{s}$ = 13 TeV*, tech. rep. ATLAS-CONF-2015-079, CERN, 2015, URL: https://cds.cern.ch/record/2114851 (cit. on p. 129).

[339] Adam Elliott Jaspan, Monica D'Onofrio, and Andrew Mehta, *Supporting Documentation for search for pairs of leptoquarks decaying into quarks and electrons or muons in $\sqrt{s} = 13$ TeV pp collisions with the ATLAS delector*, tech. rep. ATL-COM-PHYS-2019-1195, CERN, 2019, URL: https://cds.cern.ch/record/2689896 (cit. on p. 122).

[340] Chris D. White, Stefano Frixione, Eric Laenen, and Fabio Maltoni, *Isolating Wt production at the LHC*, JHEP **11** (2009) 074, arXiv: 0908.0631 [hep-ph] (cit. on p. 122).

[341] Johan Alwall, Michel Herquet, Fabio Maltoni, Olivier Mattelaer, and Tim Stelzer, *MadGraph 5 : Going Beyond*, JHEP **06** (2011) 128, arXiv: 1106.0522 [hep-ph] (cit. on p. 123).

[342] Torbjörn Sjöstrand et al., *An Introduction to PYTHIA 8.2*, Comput. Phys. Commun. **191** (2015) 159, arXiv: 1410.3012 [hep-ph] (cit. on pp. 123, 153).

[343] *ATLAS Run 1 Pythia8 tunes*, tech. rep. ATL-PHYS-PUB-2014-021, CERN, 2014, URL: https://cds.cern.ch/record/1966419 (cit. on pp. 123, 124, 153).

[344] Richard D. Ball et al., *Parton distributions with LHC data*, Nucl. Phys. B **867** (2013) 244, arXiv: 1207.1303 [hep-ph] (cit. on p. 123).

[345] Christoph Borschensky et al., *Squark and gluino production cross sections in pp collisions at $\sqrt{s}$ = 13, 14, 33 and 100 TeV*, Eur. Phys. J. **C74** (2014) 3174, arXiv: 1407.5066 [hep-ph] (cit. on pp. 123, 130).

[346] ATLAS Collaboration, *ATLAS Electron Gamma Working Group*, https://twiki.cern.ch/twiki/bin/viewauth/AtlasProtected/ElectronGamma, Accessed: 2020-08-25 (cit. on p. 126).

[347] ATLAS Collaboration, *Electron and photon performance measurements with the ATLAS detector using the 2015-2017 LHC proton-proton collision data*, JINST **14** (2019) P12006, arXiv: 1908.00005 [hep-ex] (cit. on p. 127).

[348] ATLAS Collaboration, *Electron and photon performance measurements with the ATLAS detector using the 2015–2017 LHC proton-proton collision data*, JINST **14** (2019) P12006, arXiv: 1908.00005 [hep-ex] (cit. on p. 127).

[349] ATLAS Collaboration, *ATLAS Muon Combined Performance Working Group*, https://twiki.cern.ch/twiki/bin/view/AtlasProtected/MuonPerformance, Accessed: 2020-08-25 (cit. on p. 127).

[350] *Muon reconstruction performance in early $\sqrt{s} = 13$ TeV data*, tech. rep. ATL-PHYS-PUB-2015-037, CERN, 2015, URL: https://cds.cern.ch/record/2047831 (cit. on p. 127).

[351] ATLAS Collaboration, *Jet energy scale measurements and their systematic uncertainties in proton–proton collisions at $\sqrt{s} = 13$ TeV with the ATLAS detector*, Phys. Rev. D **96** (2017) 072002, arXiv: 1703.09665 [hep-ex] (cit. on p. 127).

[352] ATLAS Collaboration, *Jet energy resolution in proton–proton collisions at $\sqrt{s} = 7$ TeV recorded in 2010 with the ATLAS detector*, Eur. Phys. J. C **73** (2013) 2306, arXiv: 1210.6210 [hep-ex] (cit. on p. 127).

[353] ATLAS Collaboration, *ATLAS b-jet identification performance and efficiency measurement with $t\bar{t}$ events in pp collisions at $\sqrt{s} = 13$ TeV*, Eur. Phys. J. C **79** (2019) 970, arXiv: 1907.05120 [hep-ex] (cit. on p. 127).

[354] ATLAS Collaboration, *Measurement of the Inelastic Proton–Proton Cross Section at $\sqrt{s} = 13$ TeV with the ATLAS Detector at the LHC*, Phys. Rev. Lett. **117** (2016) 182002, arXiv: 1606.02625 [hep-ex] (cit. on p. 127).

[355] G. Avoni et al., *The new LUCID-2 detector for luminosity measurement and monitoring in ATLAS*, JINST **13** (2018) P07017 (cit. on p. 127).

[356] *Frequentist Limit Recommendation*, vol. 1.1, ATLAS statistics forum, 2011, URL: https://indico.cern.ch/event/126652/contributions/1343592/attachments/80222/115004/Frequentist%5C_Limit%5C_Recommendation.pdf (cit. on p. 135).

[357] S. S. Wilks, *The Large-Sample Distribution of the Likelihood Ratio for Testing Composite Hypotheses*, Ann. Math. Statist. **9** (1938) 60, URL: https://doi.org/10.1214/aoms/1177732360 (cit. on p. 136).

[358] M. Baak et al., *HistFitter software framework for statistical data analysis*, Eur. Phys. J. **C75** (2015) 153, arXiv: 1410.1280 [hep-ex] (cit. on p. 136).

[359] *Summary Plots from ATLAS Searches for Pair-Produced Leptoquarks*, tech. rep., All figures including auxiliary figures are available at https://atlas.web.cern.ch/Atlas/GROUPS/PHYSICS/PUB PHYS-PUB-2021-017: CERN, 2021, URL: http://cds.cern.ch/record/2771726 (cit. on p. 146).

[360] Kyle Cranmer and Itay Yavin, *RECAST: Extending the Impact of Existing Analyses*, JHEP **04** (2011) 038, arXiv: 1010.2506 [hep-ex] (cit. on p. 148).

[361] D. Bernstein, *Containers and Cloud: From LXC to Docker to Kubernetes*, IEEE Cloud Computing **1** (2014) 81 (cit. on p. 148).

[362] Dirk Merkel, *Docker: Lightweight Linux Containers for Consistent Development and Deployment*, Linux J. **2014** (2014), ISSN: 1075-3583 (cit. on p. 148).

[363] Kyle Cranmer and Lukas Heinrich, *Yadage and Packtivity - analysis preservation using parametrized workflows*, J. Phys. Conf. Ser. **898** (2017) 102019, ed. by Richard Mount and Craig Tull, arXiv: 1706.01878 [physics.data-an] (cit. on p. 148).

[364] *Technical Design Report for the Phase-II Upgrade of the ATLAS Muon Spectrometer*, tech. rep. CERN-LHCC-2017-017. ATLAS-TDR-026, CERN, 2017, URL: https://cds.cern.ch/record/2285580 (cit. on p. 149).

[365] Andy Buckley et al., *Rivet user manual*, Comput. Phys. Commun. **184** (2013) 2803, arXiv: 1003.0694 [hep-ph] (cit. on p. 151).

[366] A. Buckley et al., "HepForge: A Lightweight development environment for HEP software", *15th International Conference on Computing in High Energy and Nuclear Physics (CHEP 2006) Mumbai, Maharashtra, India, February 13-17, 2006*, 2006, arXiv: hep-ph/0605046 [hep-ph] (cit. on p. 151).

[367] ATLAS Collaboration, *Measurements of top-quark pair differential cross-sections in the lepton+jets channel in pp collisions at $\sqrt{s} = 13$ TeV using the ATLAS detector*, JHEP **11** (2017) 191, arXiv: 1708.00727 [hep-ex] (cit. on p. 151).

[368] ATLAS Collaboration, *Measurement of jet activity produced in top-quark events with an electron, a muon and two b-tagged jets in the final state in pp collisions at $\sqrt{s} =$ 13 TeV with the ATLAS detector*, Eur. Phys. J. C **77** (2017) 220, arXiv: 1610.09978 [hep-ex] (cit. on p. 152).

[369] S. Frixione et al., *A positive-weight next-to-leading-order Monte Carlo for heavy flavour hadroproduction*, JHEP **09** (2007) 126, arXiv: 0707.3088 [hep-ph] (cit. on p. 153).

[370] D. J. Lange, *The EvtGen particle decay simulation package*, Nucl. Instrum. Meth. A **462** (2001) 152 (cit. on p. 153).

[371] M. Beneke, P. Falgari, S. Klein, and C. Schwinn, *Hadronic top-quark pair production with NNLL threshold resummation*, Nucl. Phys. B **855** (2012) 695, arXiv: 1109.1536 [hep-ph] (cit. on p. 153).

[372] Matteo Cacciari, Michal Czakon, Michelangelo Mangano, Alexander Mitov, and Paolo Nason, *Top-pair production at hadron colliders with next-to-next-to-leading logarithmic soft-gluon resummation*, Phys. Lett. B **710** (2012) 612, arXiv: 1111.5869 [hep-ph] (cit. on p. 153).

[373] Peter Bärnreuther, Michal Czakon, and Alexander Mitov, *Percent Level Precision Physics at the Tevatron: First Genuine NNLO QCD Corrections to $q\bar{q} \to t\bar{t} + X$*, Phys. Rev. Lett. **109** (2012) 132001, arXiv: 1204.5201 [hep-ph] (cit. on p. 153).

[374] Michal Czakon and Alexander Mitov, *NNLO corrections to top-pair production at hadron colliders: the all-fermionic scattering channels*, JHEP **12** (2012) 054, arXiv: 1207.0236 [hep-ph] (cit. on p. 153).

[375] Michal Czakon and Alexander Mitov, *NNLO corrections to top pair production at hadron colliders: the quark-gluon reaction*, JHEP **01** (2013) 080, arXiv: 1210.6832 [hep-ph] (cit. on p. 153).

[376] Michal Czakon, Paul Fiedler, and Alexander Mitov, *The total top quark pair production cross-section at hadron colliders through $O(\alpha_S^4)$*, Phys. Rev. Lett. **110** (2013) 252004, arXiv: 1303.6254 [hep-ph] (cit. on p. 153).

[377] Johan Alwall et al., *A Standard format for Les Houches event files*, Comput. Phys. Commun. **176** (2007) 300, arXiv: hep-ph/0609017 [hep-ph] (cit. on p. 153).